Alma Mater Studiorum – Università degli studi di Bologna

DIPARTIMENTO DI FISICA E ASTRONOMIA
Corso di Dottorato di Ricerca in Astronomia
CICLO XXVII

The dynamics of early-type galaxies as a tool to understand their hot coronae and their IMF

Dottorando:
Silvia Posacki

Relatore:
Chiar.mo Prof. Luca Ciotti

Correlatore:
Chiar.ma Prof. Silvia Pellegrini

Coordinatore:
Chiar.mo Prof. Lauro Moscardini

Esame finale anno 2014

Settore Concorsuale: 02/C1 – Astronomia, Astrofisica, Fisica della Terra e dei Pianeti
Settore Scientifico-Disciplinare: FIS/05 – Astronomia e Astrofisica

To those who do not know mathematics it is difficult
to get across a real feeling as to the beauty,
the deepest beauty,
of nature.
If you want to learn about nature, to appreciate nature,
it is necessary to understand the language that she speaks in.

Richard Phillips Feynman

Contents

List of acronyms

CBE	Collisionless Boltzmann Equation
DF	Distribution Function
DM	Dark Matter
EO	Edge-on
ETGs	Early-Type Galaxies
FO	Face-on
HST	Hubble Space Telescope
IMF	Initial Mass Function
IS	Isotropic Rotator model
ISM	Interstellar Medium
JAM	Jeans Anisotropic MGE
MGE	Multi Gaussian Expansion
MN	Miyamoto-Nagai
NFW	Navarro Frenk White
SDSS	Sloan Digital Sky Survey
SIS	Singular Isothermal Sphere
SLACS	Sloan Lens ACS
SLs	Scaling Laws
SMBH	Super Massive Black Hole
SNIa	Type Ia Supernovae
VD	Velocity Dispersion supported model

Thesis outline

This thesis addresses and investigates different astrophysical problems regarding the family of early-type galaxies (ETGs), particularly exploiting information about the stellar dynamical properties of these objects. This is made possible through the construction of advanced dynamical models, that reproduce to a good level of accuracy the observed properties and light profiles of ETGs, and hence are representative of real galaxies.

The thesis is organized as follows. Chapter 1 introduces the concept of dynamical model, which is recurring throughout the thesis since it is at the basis of the methods used in all the works here presented. It contains a discussion about the use and the usefulness of dynamical models in astronomy, intended to give a brief overview of their potentialities in several research fields. There are also illustrated three kinds of galaxy models, based on different approaches, so as to scan the various possibilities allowed. Chapter 2 describes the main steps and capabilities of the pluri-tested numerical code, developed during this PhD project, that builds advanced and flexible dynamical models by solving the Jeans equations, and which has been exploited in several works. Chapter 3 presents a family of flexible and purely analytical dynamical models obtained from the analytical solution of the Jeans equations for the Miyamoto-Nagai disc embedded in the Binney logarithmic potential. Besides its potential applications, the solution is valuable as a test for the numerical code described in Chapter 2. Chapter 4 concerns the hot X-ray emitting coronae that surround ETGs. It addresses the long-standing issue of the X-ray coolness and under-luminosity of flat and rotating galaxies with respect to their rounder and dynamically hot counterparts. It provides explanations for the recently observed trends of the X-ray temperature and luminosity decrease with galaxy shape and rotation. This investigation is performed in a twofold manner, first recurring to energetic arguments based on realistic galaxy models, and then comparing the predictions with the results of 2D hydrodynamical simulations run for the same models. Chapter 5 is about the stellar initial mass function (IMF) of ETGs. Making use of high-quality photometric ($HST/\mathrm{ACS}/F814W$ images) and spectroscopic data (SDSS optical spectra), it investigates the mass normalization of the IMF for 55 galaxies of the SLACS sample by means of an analysis which simultaneously exploits information derived from gravitational lensing, stellar dynamics and stellar population synthesis models. Finally, Chapter 6 summarises the results and discuss possible future improvements of the works presented. Appendix A illustrates the Jeans equations, which constitute the basis of the models used in the works here presented. Appendix B reports the fluid equations in the presence of source terms, necessary to understand the relation between the stellar dynamical

configuration of a galaxy and the energy provided to its interstellar medium (ISM) by its evolving stellar population. Appendix C introduces the Multi-Gaussian Expansion (MGE) technique, and collects images and parameters of the MGE models built in Chapter 5.

Chapter 1

Introduction

Dynamical models provide a description of the motion of bodies under the action of a system of forces. In astronomy, the motion of a stellar system is governed by Newton's laws of motion and Newton's law of gravity, and the study of this behaviour is the branch of theoretical physics called stellar dynamics.

Galaxy dynamical models are widely exploited in astronomy, both to elucidate issues related to stellar dynamics, and to obtain estimates of dynamical quantities, useful for applications in many different research fields. Dynamical models are indeed very powerful, since they provide insights in the main dynamical properties and behaviours of real galaxies, even if they are generally an idealised and simplified version of these last. In fact, sometimes reality is so complex to interpret that the construction of a simple model can reveal itself to be the best approach to adopt to understand a dynamical problem, since it is able to explain the basic behaviours of the modelled object, and clarify what are the main driving agents.

Dynamical models have been extensively and successfully used to study several problems related to ETGs, which are the subject of the present thesis. For example, most of a galaxy mass is thought to reside in dark matter (DM) that can only be traced by its gravitational field, and this field can be mapped through the kinematics of stars. Constraining the shape and mass fraction of galaxy DM haloes is a long-standing problem that has been studied for decades, and is still a debated issue since a definite answer has not yet been achieved. N-body cosmological simulations converge towards an NFW (Navarro et al. 1997) density profile for the DM, but accurately probing this prediction is hard since it requires many observational constraints to account for all the free parameters at play. For example, a fundamental degeneracy, that always lies at the base of this kind of investigations, concerns the difficult disentanglement between the dark and luminous mass components by means of the (uncertain) stellar mass-to-light ratio. Other minor degeneracies are given by the stellar orbital anisotropy, or by the presence of a central massive black hole. However, degeneracies can be reduced or soothed in fortunate (rare) cases, when complementary constraints (e.g., from stellar spectra and gravitational lensing) are available, and can be placed within a consistent picture by means of dynamical models. Then, evidences are found that point towards a small DM fraction in the central light-dominated regions of galaxies, almost independently of the DM halo profile adopted for the modelling (e.g., Gerhard et al. 2001; Treu & Koopmans 2004; Thomas et al. 2005; Cappellari et al. 2006, 2012).

In addition to the study of DM haloes, dynamical models have been used also to search for and weigh super massive black holes at the centres of luminous spheroids, leading to the discovery of the well-known $M_{\rm BH} - \sigma_*$ relation between black-hole mass and spheroid velocity dispersion (Ferrarese & Merritt 2000; Gebhardt et al. 2000; Merritt & Ferrarese 2001).

Another important application concerns the study of the large-scale dynamics of ETGs, aimed at constraining again their mass and orbital distributions. In particular, the advent of integral-field spectrographs has rejuvenated the study of the internal dynamics of these galaxies, providing data that probe with unprecedented detail the stellar kinematics over a large part of the central galactic regions, typically extending to one effective radius or more (Bacon et al. 2001; Emsellem et al. 2007; Cappellari et al. 2011b). The quality of these data has revealed particular internal structures, such as kinematically decoupled or counter-rotating cores, central discs and velocity twists, and has discovered the existence of two broad classes of observed stellar velocity fields, with ETGs in one class exhibiting a clear large-scale rotation pattern, and those in the other showing no significant rotation. Such data can be interpreted and fitted essentially only with the aid of advanced dynamical models, which can help to understand the origin of these diverse configurations in the context of galaxy formation scenarios.

Thus, dynamical models have a fundamental role in achieving an elucidation of these open issues, and, more generally, in the study of ETGs.

The dynamical models mostly used in literature belong to three main kinds, based on three different approaches, but all of them rely on the assumption that galaxies are in states of dynamical equilibrium. Regarding ETGs, this assumption is good since they are collisionless stellar systems in virial equilibrium.

The first kind of models relies on the construction of the phase space distribution function (DF), which contains all the information about the physics of a collisionless stellar system. Using a descriptive approach, the DF can be derived from the galaxy density distribution, which is the quantity that is best constrained by the observations, under the assumption of a constant mass-to-light ratio and of a three-dimensional geometry of the system. This method assures that the projected density profile is reproduced, but there is no guarantee that the retrieved DF is positive definite or unique. A more rigorous approach, instead, consists in a physically based choice of the DF, which is able to predict detailed information about both the density distribution and the kinematical profiles of the system, starting from some physical arguments.

The second kind of models follows a more phenomenological approach based on the Schwarzschild's orbit-superposition technique (Schwarzschild 1979). Given a comprehensive orbit library for an assumed gravitational potential, this technique finds the linear sum of those orbits that best reproduces the available observations. This method is very general and free from most assumptions: even the required assumption of a given geometry for the gravitational potential is practically removed by the iterative nature of the technique, since it constructs Schwarzschild models for an entire grid of potentials, and finds out the one that best fits the data.

Finally, the third kind of models relies on the Jeans equations (Jeans 1919), which give the possibility to infer the velocity moments of the DF starting from stellar density profiles, but without recovering the DF itself. Thus, also in this case there

is no guarantee that the models built through this method admit a positive definite and physically plausible DF. However, the Jeans equations are valuable since they relate observationally accessible quantities, such as the stellar density distribution, streaming velocity and velocity dispersion. They are an incomplete set of equations, that can be closed in special circumstances, by making some assumptions on the velocity dispersion anisotropy and on the streaming motions.

In the present thesis we will focus on this last kind of dynamical models, exploiting them in different astrophysical contexts concerning ETGs. Thus, particular importance must be recognised to the numerical code developed during this PhD project, dedicated to the solution of the Jeans equations and to the building of state-of-the-art galaxy dynamical models.

The present thesis addresses two main current astrophysical problems in the research field of ETGs. The first one is the study of their X-ray emitting haloes: ETGs are indeed embedded in hot gaseous coronae with temperatures of the order of $10^6 - 10^7$ K. Observational evidences show that the properties of these haloes, like the X-ray luminosity and temperature, are very sensitive to major galaxy properties as the shape of the mass distribution, and the mean rotation velocity of the stellar component (Pellegrini 2012a). In particular, flat and rotating ETGs are X-ray fainter and cooler with respect to rounder and dynamically hot systems. The mass of the haloes is produced mainly by stellar winds, while its energy budget comes from Type Ia supernovae (SNIa) explosions and by the thermalization of stellar motions. In this scenario, the study of the dependence of this thermalization energy on the galaxy stellar structure and dynamics is mandatory to understand the observed trends. This can be attained with a general, systematic investigation that encompasses the construction and the analysis of wide families of state-of-the-art galaxy models, which explore the whole range of the observed ETGs' properties, as done in Chapter 4.

The second astrophysical problem addressed here concerns the stellar IMF of ETGs. Nowadays, this is a very controversial issue due to a growing number of works on ETGs, based on different and independent techniques, that show evidences of a systematic variation of the IMF normalization as a function of galaxy velocity dispersion or mass (e.g., Treu et al. 2010; Conroy & van Dokkum 2012; Cappellari et al. 2013a). The IMF of ETGs was instead previously thought to be the same as that of spiral galaxies, and hence universal throughout the whole large family of galaxies. A method, widely used in literature, to discriminate between different IMF normalisations is based on galaxy stellar mass estimates. However, as mentioned above, many degeneracies undermine a fair estimate of the stellar mass, so that this can be achieved only with the aid of either a good quantity of or good quality observational constraints. In this context, in Chapter 5 a sample of 55 gravitational lens galaxies is analysed by combining three independent diagnostics of mass, i.e. stellar populations synthesis models, gravitational lensing, and stellar dynamics. In particular, the constraints derived from these last two diagnostics are consistently taken into account by building advanced dynamical models, that also reproduce the observed galaxy surface brightness profiles in great detail.

Of course, dynamical models can be used in many other active fields of research. For example, current studies of the structure of the Milky Way are dominated by a series of major observational programs that collect tremendous amounts of as-

trometric, photometric, and spectroscopic data, e.g., the ESA's Hipparcos mission (Perryman et al. 1997), the Sloan Digital Sky Survey (SDSS; Abazajian et al. 2009), the RAVE survey (Steinmetz et al. 2006), and the Gaia-ESO survey (Perryman et al. 2001). Extracting science from these huge and diverse data-sets, and turning them into a consistent picture that maps the Galaxy's DM content, and unravels how the Galaxy was assembled are a difficult and ambitious goal. Dynamical models play a vital role in this achievement since they can combine constraints on the properties of the Galaxy from different surveys simultaneously, taking into account their selection effects, observational biases and measurement errors.

We note that the dynamical models present in this thesis are not suitable exclusively for ETGs, since they allow for ample generality, so that they can be applied (after proper modifications) also to this kind of investigations, and hence to spiral galaxies.

Chapter 2

The Jeans solver code

In this Chapter we present the main features of the numerical code (Posacki et al. 2013a,b), developed during this PhD project, which constructs advanced and flexible galaxy models, based on the solution of the Jeans equations.

2.1 Physical purpose

Starting from a given axisymmetric density distribution the code computes in terms of elliptic integrals the associated gravitational potential and vertical and radial forces. Then the Jeans equations in cylindrical coordinates (R, z, φ) are solved. For an axisymmetric density distribution $\rho_*(R, z)$ supported by a two-integral phase-space DF, the Jeans equations are

$$\frac{\partial \rho_* \sigma^2}{\partial z} = -\rho_* \frac{\partial \Phi_{\rm tot}}{\partial z}, \tag{2.1}$$

and

$$\frac{\partial \rho_* \sigma^2}{\partial R} + \rho_* \frac{\sigma^2 - \overline{v_\varphi^2}}{R} = -\rho_* \frac{\partial \Phi_{\rm tot}}{\partial R} \tag{2.2}$$

(see Appendix A), where $\Phi_{\rm tot}$ is the sum of the gravitational potentials of all the components (e.g. stars, DM halo, black hole). As well known, for a two-integral DF (1) the velocity dispersion tensor is diagonal and aligned with the coordinate system; (2) the radial and vertical velocity dispersions are equal, i.e. $\sigma_R = \sigma_z \equiv \sigma$; (3) the only non-zero streaming motion is in the azimuthal direction.

In order to control the amount of ordered azimuthal velocity $\overline{v}_\varphi$, we adopted the k-decomposition introduced by Satoh (1980)

$$\overline{v}_\varphi^2 = k^2(\overline{v_\varphi^2} - \sigma^2), \tag{2.3}$$

and then it follows

$$\sigma_\varphi^2 \equiv \overline{v_\varphi^2} - \overline{v}_\varphi^2 = \sigma^2 + (1 - k^2)(\overline{v_\varphi^2} - \sigma^2), \tag{2.4}$$

where $0 \leqslant k \leqslant 1$. The case $k = 1$ corresponds to the isotropic rotator, while for $k = 0$ no net rotation is present and all the flattening is due to the azimuthal velocity dispersion σ_φ. In principle, k can be a function of (R, z), and so more complicated (realistic) velocity fields can be realised (see also Ciotti & Pellegrini 1996; Negri et al. 2013).

The code then projects all the relevant kinematical fields, together with the stellar density. The projections along a general line of sight (l.o.s.) of the stellar density ρ_*, streaming velocity $\boldsymbol{v}$ and velocity dispersion tensor $\boldsymbol{\sigma}^2$ are

$$\Sigma_* = \int_{-\infty}^{+\infty} \rho_* \, {\rm d}l, \tag{2.5}$$

$$\Sigma_* v_{\rm los} = \int_{-\infty}^{+\infty} \rho_* \langle \boldsymbol{v}, \boldsymbol{n} \rangle \, {\rm d}l, \tag{2.6}$$

$$\Sigma_* \sigma_{\rm P}^2 = \int_{-\infty}^{+\infty} \rho_* \langle \boldsymbol{\sigma}^2 \boldsymbol{n}, \boldsymbol{n} \rangle \, {\rm d}l, \tag{2.7}$$

respectively, where $\langle , \rangle$ is the scalar product, $\boldsymbol{n}$ is the l.o.s. direction and l is the integration path along $\boldsymbol{n}$. Note that if a rotational support is present, then $\sigma_{\rm P}^2$ is not the l.o.s. (i.e. the observed) velocity dispersion $\sigma_{\rm los}^2$, given by

$$\sigma_{\rm los}^2 = \sigma_{\rm P}^2 + V_{\rm P}^2 - v_{\rm los}^2, \tag{2.8}$$

where $V_{\rm P}^2$ is the projection of $\langle \boldsymbol{n}, \boldsymbol{v} \rangle^2$ (Ciotti & Pellegrini 1996). In particular, the face-on projections are

$$\Sigma_* = 2 \int_0^\infty \rho_* \, \mathrm{d}z, \tag{2.9}$$

$$\Sigma_* \sigma_{\rm P}^2 = 2 \int_0^\infty \rho_* \sigma^2 \, \mathrm{d}z, \tag{2.10}$$

with $\sigma_{\rm los}^2 = \sigma_{\rm P}^2$. The edge-on projections are instead

$$\Sigma_* = 2 \int_R^\infty \frac{\rho_* \tilde{R} \, \mathrm{d}\tilde{R}}{\sqrt{\tilde{R}^2 - R^2}}, \tag{2.11}$$

$$\Sigma_* v_{\rm los} = 2R \int_R^\infty \frac{\rho_* \overline{v}_\varphi \, \mathrm{d}\tilde{R}}{\sqrt{\tilde{R}^2 - R^2}}, \tag{2.12}$$

$$\Sigma_* \sigma_{\rm P}^2 = 2 \int_R^\infty \left[(\tilde{R}^2 - R^2)\sigma^2 + R^2 \sigma_\varphi^2 \right] \frac{\rho_* \, \mathrm{d}\tilde{R}}{\tilde{R}\sqrt{\tilde{R}^2 - R^2}}, \tag{2.13}$$

$$\Sigma_* V_{\rm P}^2 = 2R^2 \int_R^\infty \frac{\rho_* \overline{v}_\varphi^2 \, \mathrm{d}\tilde{R}}{\tilde{R}\sqrt{\tilde{R}^2 - R^2}}, \tag{2.14}$$

where all the integrations are performed at fixed z.

After the projections, the code calculates the corresponding circularized effective radius $R_{\rm e}$. In practice, the stellar projected density is integrated on the isodensity curves, and $R_{\rm e}^2 = q_{\rm los} a_{\rm e}^2$, where $a_{\rm e}$ and $q_{\rm los}$ are the semi-major axis and the l.o.s. axial ratio of the ellipse of half projected luminosity, respectively. In general, $q_{\rm los}$ is a function of the l.o.s. inclination (Lanzoni & Ciotti 2003): for a face-on projection $q_{\rm los} = 1$, while for the edge-on case $q_{\rm los} = q$. Then, the corresponding luminosity averaged aperture velocity dispersion

$$\sigma_{\rm e8}^2 \equiv \frac{\int_0^{R_{\rm e}/8} \Sigma_* \sigma_{\rm los}^2 R \, \mathrm{d}R}{\int_0^{R_{\rm e}/8} \Sigma_* R \, \mathrm{d}R}, \tag{2.15}$$

is computed within a circular aperture of $R_{\rm e}/8$.

For comparison with other works, we followed also the approach of the ATLAS$^{\rm 3D}$ project (Cappellari et al. 2011a, 2013b), calculating the quantity

$$V_{\rm rms}^2 = \sigma_{\rm P}^2 + V_{\rm P}^2 = \sigma_{\rm los}^2 + v_{\rm los}^2, \tag{2.16}$$

and its corresponding luminosity averaged mean within $R_{\rm e}/8$, according to a definition analogous to Eq. (2.15). Finally, for a given model, the code evaluates a series of volume integrals related to the stellar kinetic energy and to the gravitational potential energy of the galaxy, by using a standard finite-difference scheme (these integrals will be introduced and used in Chapter 4, Sect. 4.3).

The code was developed with the aim of creating a generator of flexible galaxy models, which can be customised according to one's need. It is indeed possible to choose within several density profiles, both for the stellar component and the DM halo, and the implementation of new ones is straightforward. The possible presence of a supermassive black hole (SMBH) is also implemented. All output data are

divided between the different mass components (e.g. stars, DM halo, black hole), and are properly normalized to the total respective masses, so that, if needed, the model can be customised by any possible user in terms of mass normalisations. Also the kinematical configuration can be modified a posteriori, without the need to rerun the model.

2.2 Technical details

The code is written in Fortran 90 and has been parallelized with MPI procedures. It uses a principal grid on which all input and output quantities are computed, and other two secondary grids, staggered in R and z respectively, that serve to make the calculations since the code uses a centred finite-difference method to approximate the derivatives. All grids are slightly logarithmic to better resolve the central regions of the galaxy. Numerical integration is performed through the standard trapezoidal rule. Output data are stored in HDF5 files that allow portability between different operating systems, and quite low file sizes thanks to the binary format.

The boundary conditions for the solution of the vertical Jeans equation can be chosen between two options. If the system had infinite extent, then the natural boundary condition would be $\rho\sigma^2 \to 0$ for $|\mathbf{r}| \to \infty$, thus one option is to adopt a suitable large grid with respect to the galaxy size and use this boundary condition. The other option instead is to use the following expression

$$\rho_* \sigma^2(R, z_{\max}) = \int_{z_{\max}}^{\infty} \rho_* \frac{\partial \Phi_0}{\partial z} \, \mathrm{d}z, \tag{2.17}$$

where Φ_0 is the monopole term of the total gravitational potential.

2.3 Code testing

The code has been accurately tested multiple times both in spherical and cylindrical symmetry, by means of analytical formulae, and comparing its results with those of similar codes. For example, the code has been tested against the analytical formulae presented in Chapter 3, that give the exact solution of the Jeans equations for two-component axisymmetric galaxy models, made of the Miyamoto-Nagai (MN) disc embedded in the Binney logarithmic potential. The comparison between our analytical (left panel) and numerical (right panel) results for a given model is shown in Fig. 2.1, where the vertical velocity dispersion σ_z is shown in the inner 50 kpc of the numerical grid. The relative errors are of the order of $\sim 10^{-3}$ in the inner ~ 60 kpc of the computational domain for all the explored combinations of the model parameters, and they slightly increase for higher z values. It can be noticed in Fig. 2.1, that the upper numerical iso-velocity curve is less steep than the analytical one, and this is due to the adopted boundary condition $\rho\sigma_z^2 \to 0$ for $|\mathbf{r}| \to \infty$.

Another test has been performed against the JAM code of Cappellari (2008), that we exploit also in Chapter 5 to build axisymmetric galaxy models for the SLACS sample. The JAM (Jeans Anisotropic Multi gaussian expansion) method allows for a more generalised modelling, since it applies to axisymmetric stellar distributions described by a three-integral DF. This method assumes a velocity ellipsoid

aligned with the cylindrical coordinates (R, z, φ), and a constant vertical anisotropy parametrized by $\beta_z = 1 - \sigma_z^2/\sigma_R^2$. Thus, while the dynamical models built with our Jeans solver code are always semi-isotropic models (i.e., $\sigma_z^2 = \sigma_R^2$, because they are based on a two-integral DF), and they become isotropic ($\sigma_z^2 = \sigma_R^2 = \sigma_\varphi^2$) for a particular choice of the Satoh parameter ($k = 1$), the JAM models can be also completely anisotropic. However, for $\beta_z = 0$ the JAM method is equivalent to ours, so that we can compare the results. Note that the implementation of the vertical anisotropy in our code would be straightforward.

Figure 2.2 shows the projected velocity field $V_{\rm rms}$ (Eq. 2.16) for a one-component axisymmetric galaxy models, whose stellar distribution is described by the de Vaucouleurs (1948) law, by using the deprojection of Mellier & Mathez (1987), generalized for ellipsoidal axisymmetric distributions (see Chapter 4, Eqs. 4.1 and 4.2). The comparison between the JAM (left panel) and our (right panel) solution shows that the agreement between the two codes is very good: the relative errors in the inner 60 kpc of the numerical grid span from 0.1 per cent up to 4 per cent.

Further tests have been successfully carried out also against the analytical solutions for a two-component MN+MN model (Ciotti & Pellegrini 1996), and for the Ferrers ellipsoids (Lanzoni & Ciotti 2003).

2.4 Code applications

The code has been used to create several families of galaxy models, which have been extensively used for theoretical and numerical analyses in a series of works, which investigate the effects of galaxy shape and kinematical configuration on the hot ISM temperature and content of the X-ray haloes of ETGs (see Chapter 4; Posacki et al. 2013a,b; Negri et al. 2013, 2014a,b). These models allow for a full generality in the choice of the axisymmetric galaxy shape and of the stellar and DM profiles, that can be tailored to reproduce observational constraints. Furthermore, they can have different dynamical structures by properly using the Satoh (1980) decomposition. Indeed, as already mentioned in Section 2.1, it is possible to realise velocity fields that are more complicated than a velocity dispersion supported system (VD, $k = 0$) or an isotropic rotator (IS, $k = 1$). This can be accomplished by adopting a Satoh parameter k that is a function of (R, z) (in principle it can be any function).

For example, in Negri et al. (2014a) the code was exploited to build S0 galaxy models, tailored on the Sombrero galaxy, four different stellar kinematical configurations were explored, allowing also for counter-rotation. These models have two mass components: a spherical DM halo described by the Einasto (1965) density-potential pair, and a stellar distribution described by the Miyamoto & Nagai (1975) density-potential pair

$$\rho_*(R,z) = \frac{M_* b^2}{4\pi} \frac{aR^2 + (a+3\zeta)(a+\zeta)^2}{\zeta^3[R^2 + (a+\zeta)^2]^{5/2}}, \tag{2.18}$$

$$\Phi_*(R,z) = -\frac{GM_*}{\sqrt{R^2 + (a+\zeta)^2}}, \tag{2.19}$$

where a and b are scale-lengths, $\zeta \equiv \sqrt{z^2 + b^2}$, and $a = b = 1.6$ kpc. Besides the IS and VD configurations, shown in Fig. 2.3, the counter-rotating disc (CR) and

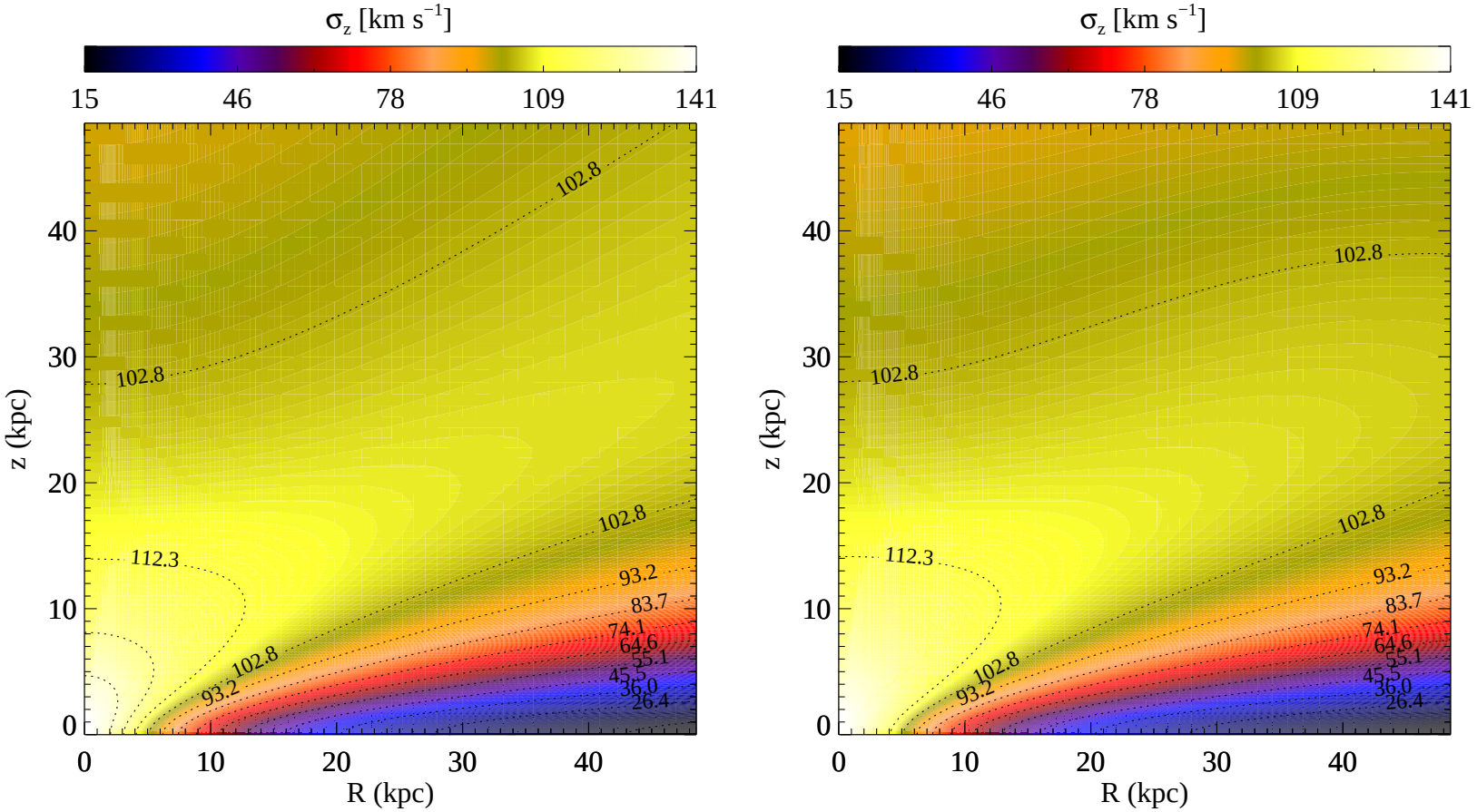

Figure 2.1: Vertical velocity dispersion σ_z field, in the inner 50 kpc, for a MN disc embedded in a Binney logarithmic potential. Left panel: exact analytic solution obtained with the formulae presented in Chapter 3 evaluated on a numerical grid, for the model parameters $M_* = 10^{11} M_\odot$, $v_\mathrm{h} = 200\,\mathrm{km\ s^{-1}}$, $b = 2$ kpc, $R_\mathrm{c} = 2b$, $q = 0.7$ and $s = 1$. Right panel: numerical solution obtained with our Jeans solver code for the same model.

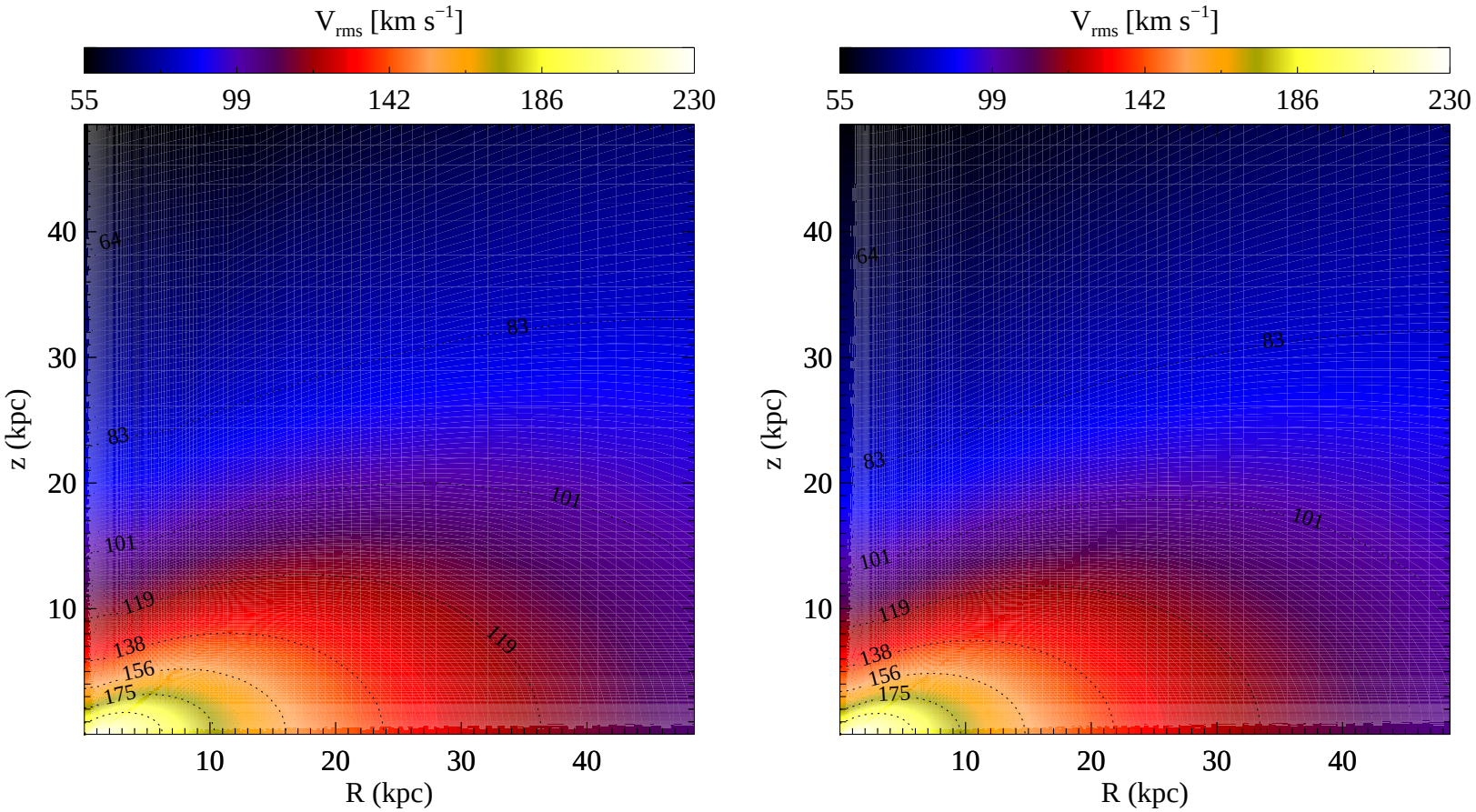

Figure 2.2: $V_{\rm rms}$ field (see Eq. 2.16), in the inner 50 kpc, for a one-component galaxy model, whose stellar distribution is described by the de Vaucouleurs (1948) law, by using the deprojection of Mellier & Mathez (1987), generalized for ellipsoidal axisymmetric distributions (see Chapter 4, Eqs. 4.1 and 4.2). Left panel: solution obtained with the JAM code of Cappellari (2008), for the model parameters $M_* = 3.35 \times 10^{11} M_\odot$, $R_{\rm e\,0} = 7.38$ kpc, and $q = 0.6$. Right panel: numerical solution obtained with our Jeans solver code for the same model.

a velocity dispersion supported system with an inner rotating disc were explored. These last models are built adopting the following functional form for the Satoh parameter

$$k(R,z) = k_{\rm ext} + \frac{\rho_*(R,z)}{\rho_*(0,0)}(k_{\rm int} - k_{\rm ext}), \tag{2.20}$$

where ρ_* is given by Eq. 2.18 with $a = 18$ kpc and $b = 4$ kpc. This choice leads to a very flattened rotating structure in the central regions of the galaxy, with $k(0,0) = k_{\rm int}$, and $k = k_{\rm ext}$ at large radii. In particular, the CR model is obtained for $k_{\rm int} = -1$ and $k_{\rm ext} = 1$, while the RD model has $k_{\rm int} = 1$ and $k_{\rm ext} = 0$. In this way, at large radii the CR and RD models become similar to the IS and VD models, respectively. This can be easily seen comparing Figs. 2.3 and 2.4, where meridional sections of the galaxy rotational field $\overline{v}_\varphi$ and of the stellar azimuthal velocity dispersion σ_φ are illustrated for the four kinds of models.

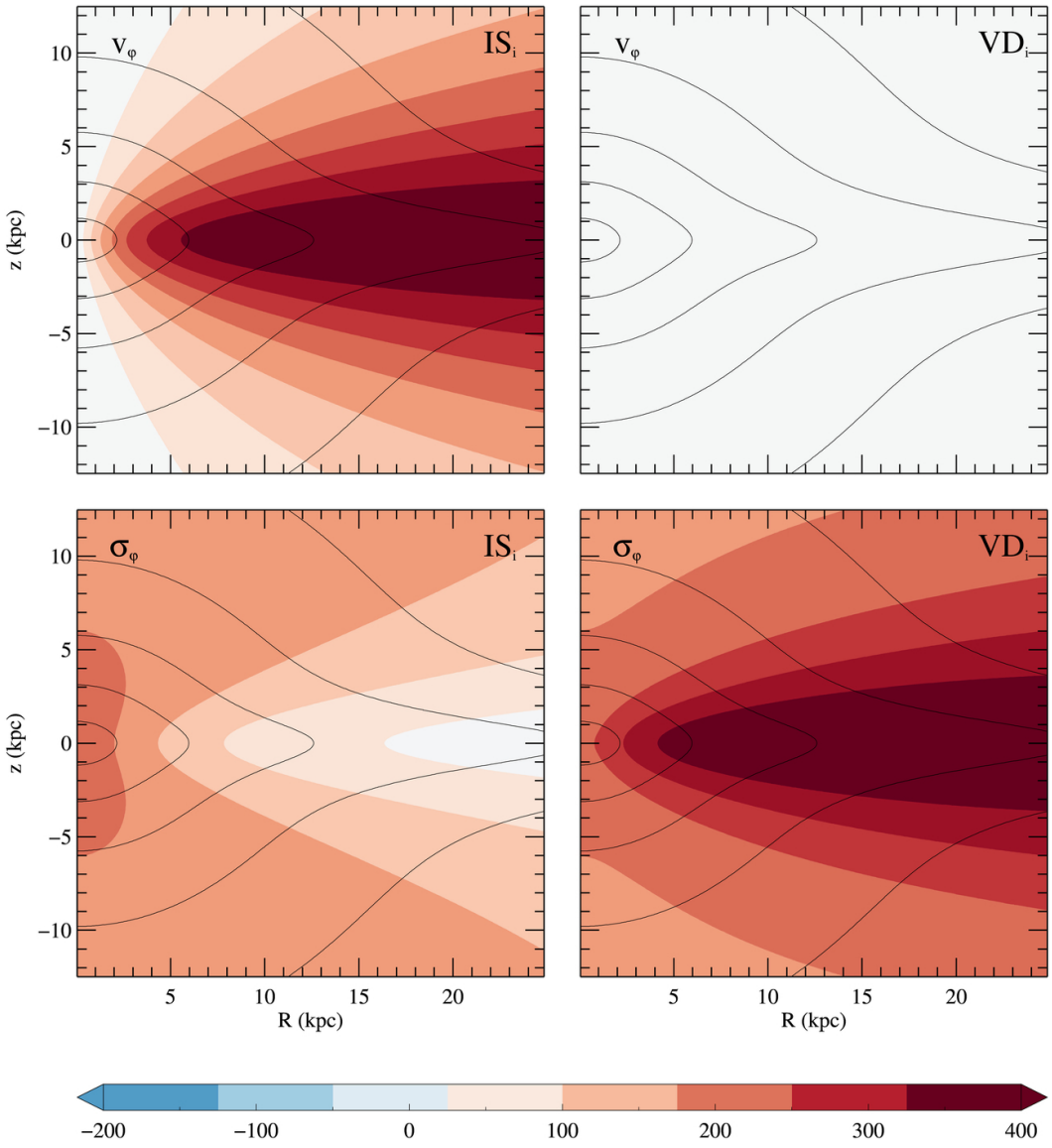

Figure 2.3: Meridional sections of the galaxy rotational field $\overline{v}_\varphi$ (top) and of the stellar azimuthal velocity dispersion σ_φ (bottom) for the IS (left) and VD (right) models. Note that, by construction, the velocity dispersion components $\sigma_R = \sigma_z = \sigma$ of the two models coincides with σ_φ of IS. The stellar isodensity contours are superimposed in black. Taken from Negri et al. (2014a).

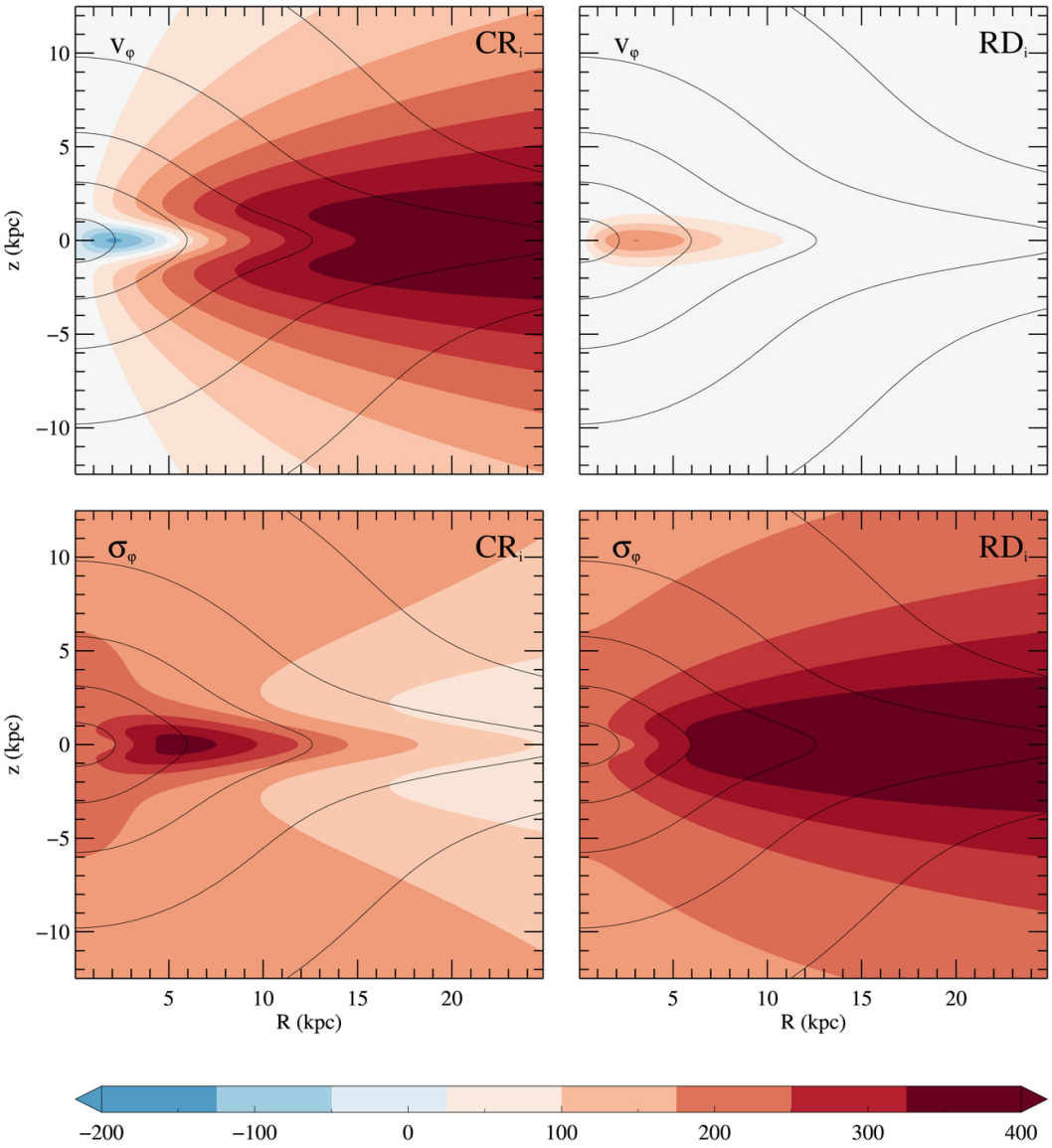

Figure 2.4: Analogue of Fig. 2.3 for the CR (left) and RD (right) models. Taken from Negri et al. (2014a).

Chapter 3

The solution of the Jeans equations for the Miyamoto-Nagai disc embedded in the Binney potential

Smet C. O., Posacki S., Ciotti L., 2014, MNRAS, submitted

In this Chapter we analytically solve the two-integrals Jeans equations for a new family of two-component galaxy models, given by a Miyamoto-Nagai stellar disc embedded in a DM Binney logarithmic halo, a cored generalisation of the singular isothermal sphere. This is done for all parameter values, thus providing a large flexibility of the models, e.g. from a disc galaxy to a spherical one. The obtained formulae have been tested against their asymptotic expansions, and, most importantly they have been used to test the numerical solutions obtained with our Jeans solver code (see Chapter 2).

3.1 Introduction

Spherical galaxy models are widely used in astrophysical applications and to elucidate concepts in stellar dynamics (e.g., see Binney & Tremaine 1987; Bertin 2000) due to their simplicity. The list of galaxy models for which the Jeans equations have been solved analytically is quite long, both for one and two-component systems (without attempting at completeness, see, e.g., Plummer 1911; Binney & Mamon 1982; Jaffe 1983; Dejonghe 1984, 1986; Sarazin & White 1987; Hernquist 1990; Renzini & Ciotti 1993; Dehnen 1993; Tremaine et al. 1994; Carollo et al. 1995; Ciotti et al. 1996; Zhao 1996; Ciotti 1996, 1999; Łokas & Mamon 2001; Ciotti et al. 2009; Van Hese et al. 2009). Even if a deeper understanding of the model properties can be obtained only by using a phase-space based approach (see e.g., Michie 1963; King 1966; Wilson 1975; Bertin & Stiavelli 1984; Trenti & Bertin 2005; Binney 2014; Williams et al. 2014), the moment approach (i.e., the solution of the Jeans equations) is still preferred in applications, due to the relatively simple method of solution. However, in the Jeans approach there is no guarantee that the underlying distribution function of the model is positive, and often an educated guess is needed to impose the closure relation (for example a prescribed anisotropy). Fortunately, in some cases it is possible to recover the underlying phase-space DF and check for its positivity (see, e.g., Eddington 1916; Osipkov 1979; Merritt 1985; Cuddeford 1991; Gerhard 1991; Ciotti & Pellegrini 1992; An & Evans 2006; Ciotti & Morganti 2009, 2010a,b).

The class of axisymmetric analytical galaxy models for which the Jeans equations can be explicitly solved is instead far less populated, and only a handful of two-component axisymmetric galaxy models are presently known. Some examples of one-component systems are the MN model (Miyamoto & Nagai 1975; Nagai & Miyamoto 1976), the Satoh (1980) disc, the family of Toomre (1982) tori, the flattened Isochrone (Evans et al. 1990), the Binney logarithmic halo (de Zeeuw et al. 1996), the homeoidally expanded systems (Ciotti & Bertin 2005), the Ferrers models (e.g., Lanzoni & Ciotti 2003), the systems obtained with the complex-shift method (Ciotti & Giampieri 2007), and the power-law systems (Evans 1994; Evans & de Zeeuw 1994). More recently, two new disc models have been presented (Evans & Bowden 2014; Evans & Williams 2014), obtained by a particular variation of the MN coordinate transformation. The situation is even worse for two-component systems: we recall here the two-component MN models (Ciotti & Pellegrini 1996, where the virial quantities can be expressed analytically), and the Evans (1993) phase-space decomposition of the Binney (1981) logarithmic halo.

In this Chapter we show that, quite surprisingly, the Jeans equations for the MN model embedded in the Binney logarithmic potential can be solved analytically for general choices of the parameters.

These models are very useful to test numerical codes dedicated to the solution of the Jeans equations, and indeed we used them to test our Jeans solver code, obtaining excellent agreement (see Chapter 2). Among other applications that can benefit from the models, we recall the hydrodynamical simulations of gas flows in ETGs, where the stellar velocity fields are a major ingredient of the energy and momentum budget of the ISM, injected by the evolving stellar populations (see, e.g., Chapter 4; Posacki et al. 2013b; Negri et al. 2014b; see also Pellegrini 2012b and references therein).

Another possible application of the present models is to quantify the effects of the relative shape of the stellar and DM distribution in disc galaxies on the vertical kinematics of stars, a quantity that can be used for DM measurements near the galactic plane (see, e.g., King et al. 1990). Further applications can also concern the study of the circular velocity of gas in the equatorial plane, and the building of hydrostatic, barotropic and baroclynic models for hot rotating models Barnabè et al. (2006). Finally, a curious application, that, at the best of our knowledge, has not been considered in the past, is proposed in Smet et al. (2014). In this paper, by means of the functions obtained in this Chapter, we study the asymmetric drift as a function of the models' parameters, and we propose a new mechanism for the formation of radial inflows of the ISM. In practice, at each radius, the gas injected by the stars has a lower specific angular momentum than the cold gas rotating with the local circular velocity, and this is able to produce a radial inflow of the ISM; using our models we get quantitative estimates of this effect which show that the mechanism is plausible.

The Chapter is organized as follows. The models are presented in Section 3.2. Sections 3.3 and 3.4 give the solution of the Jeans equations for the stellar disc alone and coupled with the DM halo, respectively. Section 3.5 shows the formulae for special cases, for which the solution can be simplified. Section 3.6 illustrates the main properties of the solutions, with particular attention to the behaviour of the velocity dispersion near the equatorial plane as a function of the stellar and DM halo parameters. Finally we mention some applications of our models, that are fully described in the paper of Smet et al. (2014)

3.2 The models

The models consist of two density components: a stellar MN disc and a DM halo characterized by the Binney logarithmic potential (Binney & Tremaine 1987). In particular, the MN potential-density pair is

$$\Phi_*(R,z) = -\frac{GM_*}{\sqrt{R^2+(a+\zeta)^2}}, \tag{3.1}$$

$$\rho_*(R,z) = \frac{M_* b^2}{4\pi}\frac{aR^2+(a+3\zeta)(a+\zeta)^2}{\zeta^3[R^2+(a+\zeta)^2]^{5/2}}, \tag{3.2}$$

where $\zeta = \sqrt{z^2+b^2}$ and (R,φ,z) are the standard cylindrical coordinates.

The Binney logarithmic family is defined by

$$\Phi_{\rm h}(R,z) = \frac{v_{\rm h}^2}{2}\ln\left(R_{\rm h}^2 + R^2 + \frac{z^2}{q^2}\right), \tag{3.3}$$

where q is the axis ratio of the equipotential surfaces, and $v_{\rm h}$ and $R_{\rm h}$ are constants related to the halo circular velocity in the equatorial plane as

$$v_{\rm circ}(R) = \frac{v_{\rm h} R}{\sqrt{R_{\rm h}^2+R^2}}. \tag{3.4}$$

Note that $v_{\rm circ}$ is independent of q, and that if $q < 1/\sqrt{2}$, the halo density is no longer everywhere positive, independently of the value of $R_{\rm h}$ (Binney & Tremaine 1987). Moreover, for zero flattening ($q = 1$) and $R_{\rm h} = 0$ we have the special case of the Singular Isothermal Sphere (SIS) [1]

$$\Phi_{\rm h}(r) = v_{\rm h}^2 \ln r, \tag{3.5}$$

where $r = \sqrt{R^2 + z^2}$ is the spherical radius, and $v_{\rm circ}(R) = v_{\rm h}$.

Note that this new two-component model allows a few interesting limiting cases: for example, one can consider a stellar component with spherical symmetry ($a = 0$) within a Binney logarithmic halo which has no spherical symmetry ($q \neq 1$), or alternatively a non-spherical stellar component ($a > 0$) within a spherical halo ($q = 1$). We can finally introduce the spherical symmetry in both components, by choosing $a = 0$ in the MN model and $q = 1$ in the Binney logarithmic halo.

In particular, the choice $a = 0$ gives the Plummer (1911) sphere, while for $b = 0$ we have the razor-thin Kuzmin (1956) disc. Since we do not consider the case of the Kuzmin disc[2], in the following treatment all the lengths will be normalized to b, and we will use the parameter $s = a/b$ to quantify the flattening of the MN disc.

3.3 The solution for the MN disc

We recall that, for an axisymmetric distribution $\rho_*(R, z)$ supported by a two-integrals phase-space DF $f(E, J_z)$, the Jeans equations are given by Eqs. (2.1) and (2.2), and the following properties hold: (1) the velocity dispersion tensor is diagonal and aligned with the coordinate system; (2) the radial and vertical velocity dispersions are equal, i.e., $\sigma_R = \sigma_z \equiv \sigma$; (3) the only non-zero streaming motion is in the azimuthal direction. These equations have been solved analytically both for the one-component MN model (Miyamoto & Nagai 1975), and for the family of two-components MN models with different flattening values s, but the same scale-length b (see Ciotti & Pellegrini 1996, where analytical expressions for the virial quantities are also derived). Easy algebra shows that

$$\rho_* \sigma_{**}^2 = \frac{G M_*^2}{8\pi b^4} \frac{(s+\zeta)^2}{\zeta^2 [R^2 + (s+\zeta)^2]^3}, \tag{3.6}$$

and

$$\rho_* (\overline{v_\varphi^2} - \sigma^2)_{**} = \frac{G M_*^2}{4\pi b^4} \frac{s R^2}{\zeta^3 [R^2 + (s+\zeta)^2]^3}. \tag{3.7}$$

We note that, since all the lengths are normalized to b, $\zeta = \sqrt{1 + z^2}$. The subscript "$_{**}$" indicates a quantity originated by the self-interaction of the stellar component, while "$_{*\rm h}$" will indicate the terms (to be computed in the next Section) due to the effect of the DM halo on the stellar component.

[1] Without loss of generality, in Eqs. (3.3) and (3.5) the argument of the logarithm is implicitly assumed normalized to some scale length.

[2] Formally, a razor-thin disc supported by a two-integrals phase-space DF can have only circular orbits.

3.4 The solution for the Binney logarithmic halo

3.4.1 The vertical Jeans equation

In the case of a Binney logarithmic halo, the halo contribution to the vertical and radial velocity dispersion is given by

$$\rho_* \sigma_{*\mathrm{h}}^2 = \int_z^\infty \rho_* \frac{\partial \Phi_\mathrm{h}}{\partial z'} dz' = \int_z^\infty \frac{v_\mathrm{h}^2 \, \rho_* z' \, dz'}{A + 1 + z'^2} = \frac{M_* v_\mathrm{h}^2}{4\pi b^3} I, \tag{3.8}$$

where $A \equiv q^2(R^2 + R_\mathrm{h}^2) - 1$, I is dimensionless, and, to avoid cumbersome notation, from now on R, R_h and z are intended normalized to b. Note that, given q and R_h, the minimum value for A is $q^2 R_\mathrm{h}^2 - 1$ and it is reached on the z-axis; for a core-less halo instead, $A \geq -1$. As we will see, the sign of A plays an important role in the treatment of Eq. (3.8). In fact, for $qR_\mathrm{h} > 1$, A is positive independently of R, while for $qR_\mathrm{h} < 1$ a radius $R_\mathrm{c} = \sqrt{1/q^2 - R_\mathrm{h}^2}$ exists so that for $R < R_\mathrm{c}$ the parameter A is negative. We call R_c the *critical radius*, and the region $R < R_\mathrm{c}$ the *critical cylinder*. In the special case of the SIS halo, $R_\mathrm{c} = 1$. The integral in Eq. (3.8) is quite complicated, especially considering the fact that ρ_* in Eq. (3.2) contains two nested irrationalities. However, in the following we show that this integral can be computed in terms of elementary functions. We stress that there are some special choices of the parameters for which the general treatment described below cannot be used (or can be significantly simplified), and the corresponding formulae can be obtained as limits of the general solution. Even if this procedure does not present conceptual difficulties, we prefer to list these special cases in Table 3.1, referring to the specific parts of Section 3.5, where the explicit formulae are provided.

In order to integrate Eq. (3.8) we begin by removing the inner irrationality with the substitution $\zeta = \sqrt{1 + z^2}$, so that

$$I \equiv \int_\zeta^\infty \frac{sR^2 + (s + 3\zeta')(s + \zeta')^2}{\zeta'^2 [R^2 + (s + \zeta')^2]^{5/2} (A + \zeta'^2)} d\zeta'. \tag{3.9}$$

Note that $\zeta \geq 1$, so that $A + \zeta^2 \geq 0$ everywhere: the equality holds at the origin only for a core-less halo, i.e., for $R_\mathrm{h} = 0$ (and so in particular for the SIS). In order to proceed with the integration, we remove the second irrationality with the change of variable $\mathrm{sh}\, x = (s + \zeta)/R$. This substitution is not valid on the z-axis, but in this case the integrand in Eq. (3.9) is a rational function of ζ' and its integration is elementary (see Table 3.1, first case). For $R \neq 0$ we obtain

$$I = \frac{1}{R^2} \int_{\mathrm{arcsh}\, \lambda}^\infty \frac{\left[s + (3R\, \mathrm{sh}\, x - 2s)\mathrm{sh}^{\,2} x\right] \, dx}{(R\, \mathrm{sh}\, x - s)^2 [A + (R\, \mathrm{sh}\, x - s)^2](1 + \mathrm{sh}^{\,2} x)^2}, \tag{3.10}$$

where $\mathrm{arcsh}\, x = \ln\left(x + \sqrt{1 + x^2}\right)$ and

$$\lambda \equiv \frac{s + \zeta}{R} = \frac{s + \sqrt{1 + z^2}}{R}. \tag{3.11}$$

Equation (3.10) is our starting point: a partial fraction decomposition, in terms of

Table 3.1: Special cases

Name	Condition	Section
z-axis	$R = 0$	3.5.1
critical cylinder	$R = R_\mathrm{c}$	3.5.2
spherical stellar density	$s = 0$	3.5.3

Notes: list of the special cases for which the treatment in Section 3.4 is no longer valid or can be greatly simplified. The corresponding formulae are given in Section 3.5.

$\mathrm{sh}\, x$, of its integrand proves the following identities

$$\begin{aligned} I &= \frac{1}{R^2}\int_{\mathrm{arcsh}\,\lambda}^{\infty} \frac{\alpha_0 + \alpha_1 \mathrm{sh}\, x + \alpha_2 \mathrm{sh}^{\,2} x + \alpha_3 \mathrm{sh}^{\,3} x}{(1+\mathrm{sh}^{\,2} x)^2} dx \\ &+ \frac{1}{R^2}\int_{\mathrm{arcsh}\,\lambda}^{\infty} \frac{\beta_0 + \beta_1 \mathrm{sh}\, x}{(R\mathrm{sh}\, x - s)^2} dx \\ &+ \frac{1}{R^2}\int_{\mathrm{arcsh}\,\lambda}^{\infty} \frac{\gamma_0 + \gamma_1 \mathrm{sh}\, x}{A + (R\mathrm{sh}\, x - s)^2} dx \\ &= \frac{I_\alpha + I_\beta + I_\gamma}{R^2}, \end{aligned} \tag{3.12}$$

where λ is defined in Eq. (3.11), and the meaning of I_α, I_β and I_γ is obvious.

Note that if $A = 0$ (i.e., for $R = R_\mathrm{c}$), two of the denominator factors in Eq. (3.10) coincide, and a different partial fraction decomposition is needed (Table 3.1, second case). Moreover, in the case of a spherical stellar distribution, we have $s = 0$ and the integrand in Eq. (3.9) simplifies (Table 3.1, third case). Leaving the special cases apart, we now focus on the evaluation of Eq. (3.10) in the case $R \neq 0, A \neq 0, s \neq 0$.

The integral I_α

The first integral in Eq. (3.12) is of trivial evaluation and the result is

$$I_\alpha = \frac{2\alpha_0 + \alpha_2}{3} + \frac{\alpha_3}{\sqrt{1+\lambda^2}} - \frac{\alpha_0 \lambda}{(1+\lambda^2)^{3/2}} - \frac{\alpha_3 - \alpha_1}{3(1+\lambda^2)^{3/2}} - \frac{(\alpha_2 + 2\alpha_0)\lambda^3}{3(1+\lambda^2)^{3/2}}. \tag{3.13}$$

The partial fraction decomposition coefficients of I_α in Eq. (3.13) for $R \neq 0$, $A \neq 0$, and $s \neq 0$ are given by

$$\begin{aligned}\frac{\alpha_0\alpha_d}{s} =& -17R^8 - 2R^6(11s^2 - 12A) + R^4(8s^4 + 19s^2A - 9A^2) \\ &+ 2R^2(s^2 + A)(7s^4 + A^2) + s^2(s^2 + A)^3,\end{aligned} \tag{3.14}$$

$$\begin{aligned}\frac{\alpha_1\alpha_d}{R} =& -6R^8 + R^6(14s^2 + 15A) + 2R^4(25s^4 - 4s^2A - 6A^2) \\ &+ R^2(34s^6 + 3s^4A + 4s^2A^2 + 3A^3) \\ &+ 2s^2(2s^6 + 5s^4A + 4s^2A^2 + A^3),\end{aligned} \tag{3.15}$$

$$\begin{aligned}\frac{\alpha_2\alpha_d}{s} =& -8R^8 + R^6(2s^2 + 3A) + 2R^4(13s^4 + 8s^2A + 3A^2) \\ &+ R^2(s^2 + A)(14s^4 + 9s^2A - A^2) - 2s^2(s^2 + A)^3,\end{aligned} \tag{3.16}$$

$$\begin{aligned}\frac{\alpha_3\alpha_d}{R} =& -3R^8 + 2R^6(7s^2 + 3A) + R^4(32s^4 + s^2A - 3A^2) \\ &+ 2s^2R^2(5s^4 - A^2) - s^2(5s^2 + A)(s^2 + A)^2,\end{aligned} \tag{3.17}$$

where

$$\alpha_d = (R^2 + s^2)^2[(A + s^2 - R^2)^2 + 4R^2s^2]^2. \tag{3.18}$$

The integral I_β

The partial fraction decomposition coefficients of I_β in Eq. (3.12) for $R \neq 0$, $A \neq 0$, and $s \neq 0$ are given by

$$\beta_0\beta_d = R^4s, \qquad \beta_1\beta_d = R^3s^2, \tag{3.19}$$

where

$$\beta_d = A(R^2 + s^2)^2. \tag{3.20}$$

For the computation of I_β we then use the standard substitution $y = \text{th}\,(x/2)$ to obtain

$$I_\beta = -\frac{2\beta_0}{s^2}\int_\mu^1 \frac{y^2 - 2sy/R - 1}{(y^2 + 2Ry/s - 1)^2}dy, \tag{3.21}$$

where the upper limit of integration in Eq. (3.12) has now become 1, while the lower limit of integration is

$$\mu \equiv \tanh\left(\frac{\text{arcsh}\,\lambda}{2}\right) = \sqrt{1 + \frac{1}{\lambda^2}} - \frac{1}{\lambda}. \tag{3.22}$$

It can be easily proved that the two real zeros of the denominator in Eq. (3.21) lie outside the integration domain. The rational integrand in Eq. (3.21) can be solved again by partial fraction decomposition, and elementary integration leads to the surprisingly simple expression

$$I_\beta = \frac{\beta_0}{R}\left(\frac{\sqrt{1 + \lambda^2}}{\zeta} - \frac{1}{R}\right). \tag{3.23}$$

The integral I_γ

The partial fraction decomposition coefficients of I_γ in Eq. (3.12) for $R \neq 0$, $A \neq 0$, and $s \neq 0$ are given by

$$\frac{\gamma_0\gamma_d}{R^2 s} = -R^6 - 2R^4(s^2 - 3A) - R^2(s^4 - 18s^2A - 3A^2) - 8A(s^2 + A)^2, \tag{3.24}$$

$$\frac{\gamma_1\gamma_d}{R^3} = -R^4(s^2 - 3A) - 2R^2(s^4 + 8s^2A + 3A^2) - (s^2 - 3A)(s^2 + A)^2, \tag{3.25}$$

where

$$\gamma_d = A[(A + s^2 - R^2)^2 + 4R^2s^2]^2. \tag{3.26}$$

At variance with I_α and I_β, I_γ is the most complicated integral, since the integration procedure now depends on the sign of A. Inspection of Eq. (3.12) suggests that an easy factorisation of the denominator of I_γ could be obtained in the case $A < 0$. However, as the same procedure cannot be applied to the case $A > 0$ without using complex numbers, we prefer to follow another approach that maximises the similarity of the treatment in the two cases.

We use the exponential substitution $y = e^x$, which leads to the following rational integrand

$$I_\gamma = \frac{2\gamma_1}{R^2} \int_\nu^\infty \frac{y^2 + Hy - 1}{\Delta(y)}\, dy, \tag{3.27}$$

where

$$H = 2\frac{\gamma_0}{\gamma_1}, \tag{3.28}$$

and

$$\Delta(y) = y^4 - \frac{4s}{R}y^3 + \left(\frac{4A}{R^2} + \frac{4s^2}{R^2} - 2\right)y^2 + \frac{4s}{R}y + 1. \tag{3.29}$$

With this substitution the upper limit of integration in Eq. (3.12) becomes ∞ in Eq. (3.27), while the lower limit is

$$\nu \equiv e^{\operatorname{arcsh}\lambda} = \lambda + \sqrt{1 + \lambda^2}. \tag{3.30}$$

In principle, we could use the antisymmetry of $\Delta(y)/y^2$ (after noticing that $y = 0$ is not a zero) to factorise it: it is readily seen that if y_1 is a zero of Δ, then so is $-1/y_1$. This implies that $\Delta(y)/y^2$ can be written as a quadratic polynomial in $t = y - 1/y$, from which the factorisation is immediate. However, if $A > 0$ the two roots of the quadratic polynomial in t are complex conjugates.

In practice this computation is not needed since any quartic polynomial with real coefficients can be factorised into two quadratic polynomials with real coefficients. Without loss of generality, we found it useful to adopt the factorisation

$$\Delta(y) = \left[(y - \Delta_+)^2 + \delta_+\right]\left[(y - \Delta_-)^2 + \delta_-\right]. \tag{3.31}$$

Expansion of Eq. (3.31) and comparison with Eq. (3.29) shows that

$$\Delta_\pm = \frac{s}{R} \pm \sqrt{\frac{s^2}{R^2} + \delta}, \qquad \delta_\pm = \frac{1 - \delta}{\delta}\Delta_\pm^2, \tag{3.32}$$

where

$$\delta = \frac{\sqrt{(A+s^2-R^2)^2+4R^2s^2}-(A+s^2-R^2)}{2R^2}. \tag{3.33}$$

Note that $\delta > 0, \Delta_+ > 0$ and $\Delta_- < 0$. If $A > 0$, then $0 < \delta < 1$ and hence $\delta_\pm > 0$, making the two quadratic polynomials in Eq. (3.31) irreducible over the reals. If $A < 0$, then $\delta > 1$ and hence $\delta_\pm < 0$, consistent with the fact that in this case Δ can be factorised into four linear factors over the reals.

Now we can proceed in the usual way, by a partial fraction decomposition. The coefficients in

$$\frac{y^2+Hy-1}{\Delta(y)} = \frac{\eta_+ y+\theta_+}{(y-\Delta_+)^2+\delta_+} + \frac{\eta_- y+\theta_-}{(y-\Delta_-)^2+\delta_-} \tag{3.34}$$

are given, after some simplification, by

$$\eta_\pm \sigma_d = \pm\, 2\delta\left(2\delta - \frac{Hs}{R}\right), \tag{3.35}$$

$$\theta_\pm \sigma_d = 2\Delta_\pm\left[\frac{s}{R}(\Delta_+-\Delta_-) \pm \delta\Delta_\pm(H+2\Delta_\mp)\right], \tag{3.36}$$

where

$$\sigma_d = 4(\Delta_+-\Delta_-)\left(\delta^2+\frac{s^2}{R^2}\right). \tag{3.37}$$

Finally, the constants above are linked by the following simple algebraic relations

$$\Delta_+^2\delta_- = \delta_+\Delta_-^2\,, \qquad \frac{\eta_+\Delta_+ + \theta_+}{\Delta_+} = \frac{\eta_-\Delta_- + \theta_-}{\Delta_-}, \tag{3.38}$$

which are useful to simplify the final expression of I_γ [3]

$$I_\gamma = \frac{\gamma_1\eta_+}{R^2}\ln\frac{(\nu-\Delta_-)^2+\delta_-}{(\nu-\Delta_+)^2+\delta_+} + \frac{2\gamma_1}{R^2}\frac{\theta_+ + \eta_+\Delta_+}{\sqrt{|\delta_+|}}\times$$
$$\begin{cases} \arctan\dfrac{\sqrt{\delta_+}(\nu-\Delta_-)-\sqrt{\delta_-}(\nu-\Delta_+)}{(\nu-\Delta_+)(\nu-\Delta_-)+\sqrt{\delta_+\delta_-}} & \text{if } A>0; \\ \operatorname{arctanh}\dfrac{\sqrt{|\delta_+|}(\nu-\Delta_-)-\sqrt{|\delta_-|}(\nu-\Delta_+)}{(\nu-\Delta_+)(\nu-\Delta_-)-\sqrt{\delta_+\delta_-}} & \text{if } A<0. \end{cases} \tag{3.39}$$

We stress again that all the formulae reported in this Section cannot be used in their present form to describe the velocity dispersion on the z-axis ($R = 0$), on the critical cylinder ($A = 0$, i.e., $R = R_c$), or in the case of a spherical stellar density ($s = 0$). As listed in Table 3.1, all these cases are treated in Section 3.5.

In Smet et al. (2014) we provide also asymptotic expansions of the above formulae, computed at selected places in the model (i.e., near the origin, along the z-axis, and in the equatorial plane for $R \to \infty$), in order to better illustrate the effects of

[3] The addition formulae used in Eq. (3.39) are $\operatorname{arctanh} u - \operatorname{arctanh} v = \operatorname{arctanh}\dfrac{u-v}{1-uv}$ and $\arctan u - \arctan v = \arctan\dfrac{u-v}{1+uv}$, where for $|x|<1$, $\operatorname{arctanh} x = \frac{1}{2}\ln\dfrac{1+x}{1-x}$.

the model parameters on the dynamical properties of the stellar population. We note that the asymptotic formulae have been verified numerically, thus giving an independent check of the analytical integration.

We conclude this Section by noticing that, quite remarkably, the integral in Eq. (3.10) can also be performed in closed form by using the Residue Theorem of Complex Analysis (see Smet et al. 2014 for further details). However, despite the elegance of this method, the number of poles, their multiplicity, and their complex nature do not reduce the amount of work needed to obtain the final (real) result when compared with the standard method in this Section 3.4.1.

3.4.2 The radial Jeans equation

In the previous Section we solved the vertical Jeans Eq. (2.1). For the radial Jeans Eq. (2.2), no further integration is needed, as only the radial derivative of I is required. Notice that from Eq. (3.9) it follows that I is an even function of R, hence $dI/dR = 0$ at $R = 0$. For $R > 0$ one can obtain an explicit expression for dI/dR performing explicit differentiation on Eq. (3.12). However, the easiest way to obtain dI/dR is to differentiate Eq. (3.10) with respect to R, and to perform the partial fraction decomposition on the resulting integrand. The resulting integrals are formally similar to the ones already computed, and they can be solved with the same techniques. In any case, we chose not to include these explicit expressions here, since any computer algebra system can easily perform the differentiation.

3.5 Special cases

In the following we give the explicit solution of Eq. (3.10) in the special cases $R = 0$, $A = 0$, $s = 0$, when the formulae in Section 3.4 cannot be used. We recall that $A = q^2(R^2 + R_{\rm h}^2) - 1$.

3.5.1 Velocity dispersion on the z-axis

For $R = 0$ (i.e., along the z-axis), Eq. (3.9) simplifies considerably, and its integration is elementary:

$$I = \frac{1}{As^2\zeta} + \frac{4s}{(A+s^2)^3}\ln\frac{(\zeta+s)^2}{\zeta^2+A} - \frac{A+5s^2}{s^2(A+s^2)^2(\zeta+s)} - \frac{1}{s(A+s^2)(\zeta+s)^2} + \frac{3A^2-6As^2-s^4}{A\sqrt{|A|}(A+s^2)^3}\begin{cases}\arctan\dfrac{\sqrt{A}}{\zeta} & \text{if } A>0;\\ \operatorname{arctanh}\dfrac{\sqrt{|A|}}{\zeta} & \text{if } -1\le A<0.\end{cases} \tag{3.40}$$

The cases $A = 0$ and $A = -s^2$ should be treated separately. For $A = 0$, i.e., when the critical cylinder coincides with the z-axis ($R_{\rm h} = 1/q$), then

$$I = \frac{8}{s^5}\ln\frac{\zeta+s}{\zeta} + \frac{s^4+2s^3\zeta-8s^2\zeta^2-36s\zeta^3-24\zeta^4}{3s^4\zeta^3(\zeta+s)^2}. \tag{3.41}$$

The case $A = -s^2$ is possible only for $s < 1$, so that $\zeta > s$, and

$$I = \frac{1}{4s^5} \ln \frac{\zeta + s}{\zeta - s} - \frac{6s^3 + 10s^2\zeta + 9s\zeta^2 + 3\zeta^3}{6s^4\zeta(\zeta + s)^3}. \tag{3.42}$$

Note that this solution is always finite, except at the origin ($z = 0$, i.e., $\zeta = 1$) for $s = 1$, so that $A = -1$ on the z-axis, which in turn implies $R_\mathrm{h} = 0$, i.e., when the DM potential is not cored.

3.5.2 Velocity dispersion on the critical cylinder

On the critical cylinder $R^2 = R_\mathrm{c}^2 \equiv q^{-2} - R_\mathrm{h}^2$, the parameter A vanishes, and two denominator factors in Eq. (3.10) coincide. Note that, if $qR_\mathrm{h} > 1$, there is no critical cylinder since $A > 0$ for every R. If $qR_\mathrm{h} < 1$, then R_c exists, and in particular $R_\mathrm{c} = 1$ for the SIS model. If $qR_\mathrm{h} = 1$, then the critical cylinder coincides with the z-axis, and the solution for I is given by Eq. (3.41).

On the critical cylinder the partial fraction decomposition in Eq. (3.12) is no longer valid, and instead we have that

$$I = \frac{I_\alpha + I_c}{R_\mathrm{c}^2}, \tag{3.43}$$

where I_α is as before and I_c can be written, without loss of generality, as

$$I_c = \sum_{i=1}^{4} \int_{\operatorname{arcsh} \lambda}^{\infty} \frac{\theta_i}{(R_\mathrm{c} \operatorname{sh} x - s)^i} dx. \tag{3.44}$$

Here no singularities are contained in the integration domain, and the coefficients θ_i can be found by the usual partial fraction decomposition technique. The substitution $y = e^x$ transforms the integrals in rational ones, and in particular

$$\int \frac{dx}{R_\mathrm{c} \operatorname{sh} x - s} = \frac{2}{R_\mathrm{c}} \int \frac{dy}{y^2 - 2\dfrac{s}{R_\mathrm{c}} y - 1} = -\frac{2}{\sqrt{R_\mathrm{c}^2 + s^2}} \operatorname{arctanh} \frac{\sqrt{R_\mathrm{c}^2 + s^2}}{R_\mathrm{c} - s}. \tag{3.45}$$

The other integrals for $i = 2, 3$, and 4 are more easily obtained by differentiating Eq. (3.45) with respect to s. The limits of integration for y are ν_c given by Eq. (3.30) evaluated at $R = R_\mathrm{c}$, and ∞. The final result for I_c is

$$\begin{aligned} I_c = &\frac{2R_\mathrm{c}^2(3R_\mathrm{c}^4 - 24R_\mathrm{c}^2 s^2 + 8s^4)}{(R_\mathrm{c}^2 + s^2)^{9/2}} \operatorname{arctanh} \frac{\sqrt{R_\mathrm{c}^2 + s^2}}{R_\mathrm{c}\nu_c - s} \\ &+ \frac{2R_\mathrm{c}^2 s}{3(R_\mathrm{c}^2 + s^2)^4} \frac{P_5(\nu_c, R_\mathrm{c})}{(R_\mathrm{c}\nu_c^2 - 2s\nu_c - R_\mathrm{c})^3}, \end{aligned} \tag{3.46}$$

where

$$\begin{aligned} P_5(\nu, R) = &\, 3R^2 s(4R^2 - 3s^2)\nu^5 + R(15R^4 - 54R^2 s^2 + 36s^4)\nu^4 \\ &+ s(-78R^4 + 100R^2 s^2 - 32s^4)\nu^3 + 6R(-4R^4 + 21R^2 s^2 - 10s^4)\nu^2 \\ &+ 3R^2 s(22R^2 - 13s^2)\nu + R^3(13R^2 - 8s^2). \end{aligned} \tag{3.47}$$

A careful treatment shows that in the special case where the critical cylinder coincides with the z-axis (i.e., $qR_\mathrm{h} = 1$ and $A = R = 0$), Eq. (3.43) coincides with Eq. (3.41).

3.5.3 Spherical stellar density

In the case of a spherical stellar density, i.e., when the MN model reduces to the Plummer sphere, Eq. (3.9) simplifies to

$$I = 3 \int_{\zeta}^{\infty} \frac{\zeta'}{(R^2 + \zeta'^2)^{5/2}(A + \zeta'^2)} d\zeta'. \tag{3.48}$$

The substitution $u = \sqrt{\zeta^2 + R^2}$ gives a rational integrand, and

$$\begin{aligned} I = & \frac{1}{(A - R^2)(R^2 + \zeta^2)^{3/2}} - \frac{3}{(A - R^2)^2 \sqrt{R^2 + \zeta^2}} \\ & + \frac{3}{|A - R^2|^{5/2}} \begin{cases} \arctan \sqrt{\dfrac{A - R^2}{R^2 + \zeta^2}} & \text{if } A > R^2; \\ \operatorname{arctanh} \sqrt{\dfrac{R^2 - A}{R^2 + \zeta^2}} & \text{if } A < R^2; \end{cases} \end{aligned} \tag{3.49}$$

while for $A = R^2$

$$I = \frac{3}{5(R^2 + \zeta^2)^{5/2}}. \tag{3.50}$$

3.6 General properties of the solution

The formulae reported in the Section 3.4 (and in Section 3.5 for special cases) are fully general and they can be easily implemented in numerical codes and in computer algebra systems to explore the behaviour of the kinematical fields of the models in all cases of interest. In particular, as the Jeans equations of the one component MN model has been already solved (see Eqs. 3.6 and 3.7), we now have a two-component, axisymmetric galaxy model, admitting a fully analytical solution for the Jeans equations relative to the stellar component. However, the obtained formulae are sufficiently cumbersome to avoid an immediate reading of their physical contents.

For this reason, a first qualitative illustration of the behaviour of the solutions in the meridional (R, z) plane is given in Fig. 3.1, for a moderately flattened MN stellar distribution ($s = 10$) of total mass $M_* = 10^{11} M_\odot$, and scale-length $b = 2$ kpc, embedded in a quite flattened DM logarithmic halo with $R_\mathrm{h} = 10$ kpc, $v_\mathrm{h} = 250\,\mathrm{km\ s^{-1}}$ and $q = 0.7$. Here we show the following velocity fields: σ_* (left panel), $\overline{v}_\varphi$ (central panel) and σ_φ (right panel). For reference, the solid lines shows the isodensities of the stellar distribution. As expected, the vertical velocity dispersion (independent of the specific decomposition of the azimuthal fields) near the equatorial plane declines for increasing R, due to fact that the MN stellar distribution becomes more and more flat. Of course, in the isotropic case the same behaviour is reflected by σ_φ, while the flattening of the stellar distribution is supported by ordered motions (central panel). Finally, in the fully velocity dispersion supported model, while σ_* remains unchanged, σ_φ takes the place of $\overline{v}_\varphi$, as can be seen by considering the right panel. Figure 3.1 can be compared with the analogous plots in Fig. 2.3, relative to a rounder stellar MN model (with $s = 1$), embedded in a Einasto DM halo (with exponent $n = 4$). The overall structure of the kinematical fields, both in the isotropic

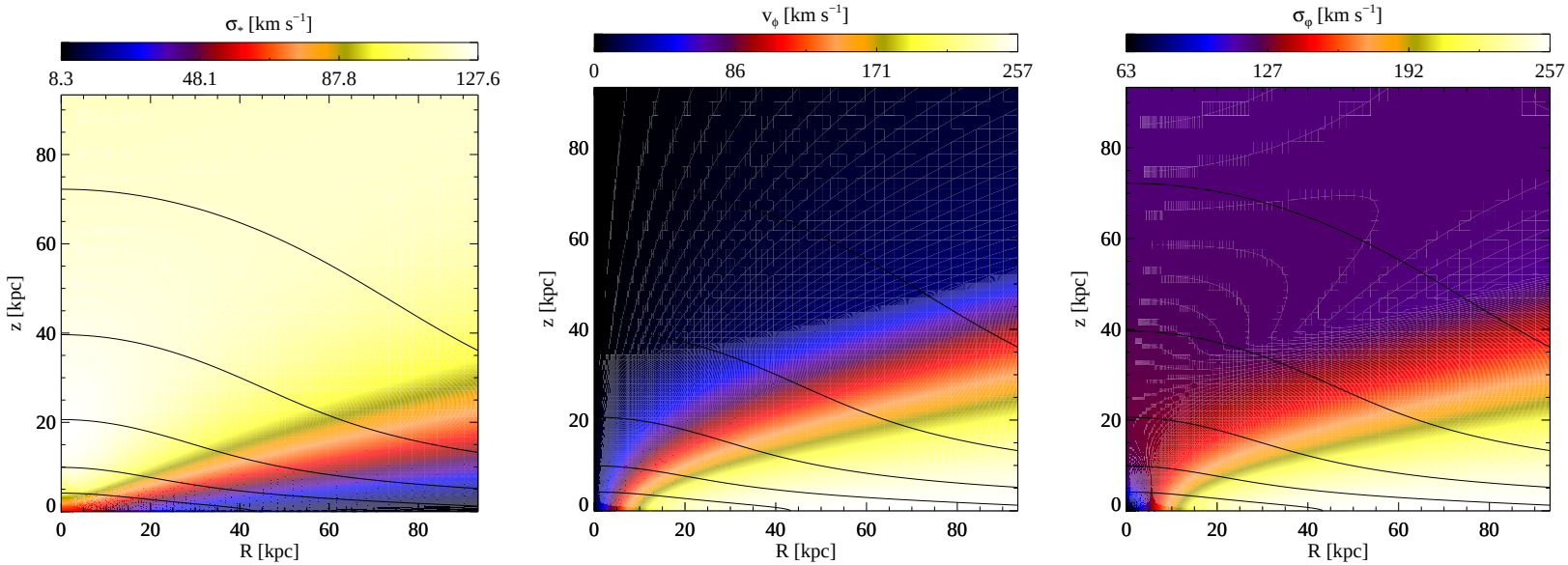

Figure 3.1: Two-dimensional maps of σ_*, $\overline{v}_\varphi$ (isotropic model, $k = 1$) and σ_φ (velocity dispersion supported model, $k = 0$) for the parameter values $M_* = 10^{11} M_\odot$, $b = 2$ kpc, $s = 10$, $v_\mathrm{h} = 250\,\mathrm{km\ s^{-1}}$, $R_\mathrm{h} = 5b$, $q = 0.7$. Solid lines represents isodensity contours of the stellar distribution.

($k = 1$) and fully velocity dispersion supported ($k = 0$) cases are very similar, with the exception of the central "hourglass" structure in the vertical and radial velocity dispersion that can be observed in Fig. 2.3. The hourglass shaped distribution of σ_{**} is a characteristic of the one-component MN model, and in the models in Fig. 3.1 is absent because of the contribution of the massive Binney halo adopted (at variance with the lighter Einasto halo in Fig. 2.3): for decreasing values of $v_{\rm h}$, this feature appears again, as soon as σ_{**} dominates over $\sigma_{*\rm h}$.

Additional information on the behaviour of the velocity dispersion field as a function of the various parameters of the models can be obtained from Fig. 3.2, where we plot σ_* in the equatorial plane for a selection of models. For reference, the black lines represent the velocity dispersion for the one-component MN model, σ_{**}. In particular, the plots show how the flattening of the stellar distribution, and the DM halo shape and concentration affect the vertical velocity dispersion of the stellar component, an observationally relevant quantity. As is well known, this is important for studies of DM densities in the solar neighbourhood, see e.g. King et al. (1990), Binney & Tremaine (1987). We can notice a few, obvious features. First, the velocity dispersion of the model without halo is - for each model - lower than the velocity dispersion in presence of the halo. Second, while the velocity dispersion declines at large radii for the MN model, it flattens to a constant value for models embedded in the logarithmic halo, as expected from the dominance of its quasi-isothermal profile at large radii. The effects of the halo and stellar flattenings are instead more interesting. In particular, it should be noted how, for a fixed stellar distribution, an increase of the halo flattening (at fixed $R_{\rm h}$ and $v_{\rm h}$) *increases* the stellar velocity dispersion at each radius (compare the red and blue lines in each panel). The velocity dispersion increase is a consequence of the increase of the vertical gravitational field of the halo, that is more and more equatorially concentrated for decreasing q. However, for a fixed halo, a more flattened stellar distribution (at fixed total stellar mass) leads to a *decrease* of the stellar velocity dispersion. This may appear a curious behaviour, as the same argument above about the strength of the vertical gravitational field applies, but it is not. In fact, the vertical gravitational field of the stellar distribution increases for increasing s, but the stellar population now has - by construction - a shorter vertical scale-length, so that its "temperature" decreases accordingly, and the two effects more than compensate, with a net effect of decreasing σ_*. This behaviour is by no means a peculiarity of the present models, and it can be easily cast in algebraic form by using the simpler family of oblate Ferrers ellipsoids (Ciotti & Lanzoni 1997). Finally, note how a decrease of $R_{\rm h}$ at fixed halo geometry and $v_{\rm h}$ leads to an increase of the velocity dispersion, due to the stronger concentration of the halo.

For the sake of completeness, we note that other dynamical quantities related to the rotational properties of the (isotropic) models in the equatorial plane, are illustrated in Smet et al. (2014) (Fig. 4), where particular attention is paid to the description of the effects of the models parameters (especially the stellar and halo flattenings) on the asymmetric drift $\mathrm{AD} \equiv v_{\rm circ} - \overline{v}_\varphi$ (Binney & Tremaine 1987). In particular, in the paper we consider the coupling between stellar mass losses and AD, and we propose it as a possible mechanism for the development of gaseous radial flows in disc galaxies. We also qualitatively estimate the magnitude of this effect obtaining an infall velocity of $v_{\rm infall} \simeq 1\,\mathrm{km\ s^{-1}}$, consistent with the estimates

required by chemical evolution models (see Smet et al. 2014 for further details).

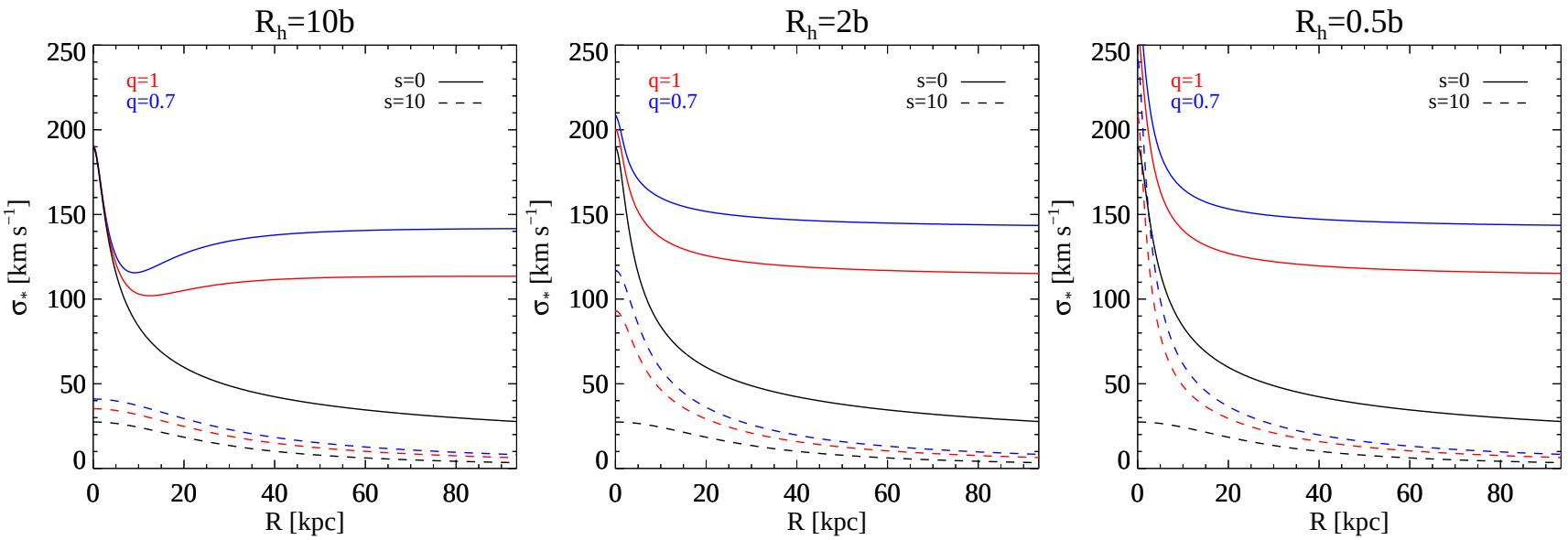

Figure 3.2: Radial trend of the vertical velocity dispersion σ_* in the equatorial plane for a model with $M_* = 10^{11} M_\odot$, $b = 2$ kpc, $v_\mathrm{h} = 250\,\mathrm{km\ s^{-1}}$, and different values of s, q, and R_h. In particular, solid lines refer to a spherical stellar distribution, while the dashed lines to a flattened MN disk. Red and blue lines correspond to spherical and flat equipotentials for the DM halo. The black curves represent the stellar contribution σ_{**}.

Chapter 4

The hot X-ray emitting coronae of ETGs: energetic and hydrodynamical analyses

Posacki S., Pellegrini S., Ciotti L., 2013, MNRAS, 433, 2259

Negri A., Posacki S., Pellegrini S., Ciotti L., 2014, MNRAS, 445, 1351

In this Chapter we address the problem of the X-ray under-luminosity and coolness of flat and rotating ETGs, following two different and complementary approaches, based on energetic estimates and hydrodynamical simulations respectively. Both methods rely on the construction of advanced galaxy models, built with the Jeans solver code illustrated in Chapter 2. The work here presented has been published in Posacki et al. (2013b) and Negri et al. (2014b).

4.1 Introduction

Before the late 1970s it was generally believed that ETGs were gas-poor systems, as observed in optical and radio wavebands. This was however at odd with our knowledge from stellar evolution: during their lives stars shed large amounts of mass that joins the ISM, so it is expected a certain amount of material to be ejected from an evolving stellar population. This apparent absence was justified speculating that this gas was heated and expelled in a supernova-driven galactic wind, thus several galactic winds models were developed in order to explain why most of these galaxies showed virtually no evidence of interstellar matter (e.g., Mathews & Baker 1971, for a full discussion see Mathews & Brighenti 2003).

Subsequently, with the advent of the *Einstein* Observatory, the first fully imaging X-ray telescope put into space, ETGs were discovered to be associated with a soft thermal X-ray emission. Since then, this emission has been extensively studied, especially with the aid of improving quality observations obtained with the subsequent X-ray satellites *ROSAT*, *ASCA*, *Chandra* and *XMM - Newton*, leading to the collection of numerous precious information.

The emission raises from both the presence of hot interstellar gas, especially in X-ray bright elliptical galaxies, and point sources, most of which appear to be Low Mass X-ray Binaries. From X-ray spectra and surface brightness profiles we can deduce that the emission from discrete sources dominates the total observed X-ray flux only in optically faint ETGs, while in the more luminous galaxies the bulk of the emission originates from the hot phase ($k_{\rm B}T \sim 0.3 - 0.8\,{\rm keV}$) of the ISM that emits via thermal bremsstrahlung.

Einstein observations found that ETGs have X-ray luminosities which range over $L_{\rm X} \sim 10^{40} - 10^{43}\,{\rm erg\,s^{-1}}$ and correlate with their blue luminosity $L_{\rm B}$ ($L_{\rm X} \propto L_{\rm B}^{1.5-2}$), though with a significant dispersion; taking the optical luminosity fixed, $L_{\rm X}$ can vary by more than two orders of magnitude. The total mass of the emitting gas is in the range $M_{gas} \sim 10^9 - 10^{11}\,M_\odot$, which is an amount comparable to the mass lost by stars over the past several billion years and, at the same time, it is a large enough range of mass to produce consistent scatter in $L_{\rm X}$.

This variation is related to the ISM evolution over cosmological time-scales, during which stellar mass losses and SNIa explosions provide gas and gas heating, respectively, to the hot haloes (possibly in conjunction with feedback from accretion on to the central SMBH). Modulo environmental effects like galaxy interactions or tidal stripping, the hot gas content and temperature fundamentally depend on the energy budget of the hot ISM, that in turn depends on the particular host galaxy structure and internal kinematics (e.g., Ciotti et al. 1991; Pellegrini 2011). For example, the luminous and DM content and distribution determine the potential well shape and depth, and so the binding energy of the gas and its dynamical state (e.g., Ciotti & Pellegrini 1996). Indeed, one of the discoveries that followed the analysis of first X-ray data of ETGs was the sensitivity of the hot gas content to major galaxy properties as the shape of the mass distribution, and the mean rotation velocity of the stars (see Pellegrini 2012a for a review). The investigation of the origin of this sensitivity is the goal of the present chapter.

A relation between the hot gas retention capability and the intrinsic galactic shape became apparent already in the X-ray sample of ETGs built from *Einstein*

observations: on average, at any fixed $L_{\rm B}$, rounder systems had larger total $L_{\rm X}$ and $L_{\rm X}/L_{\rm B}$, a measure of the galactic hot gas content, than flatter ETGs and S0 galaxies (Eskridge et al. 1995). Moreover, galaxies with axial ratio close to unity spanned the full range of $L_{\rm X}$, while flat systems had $L_{\rm X} \lesssim 10^{41}$erg s^{-1}. This result was not produced by flat galaxies having a lower $L_{\rm B}$, with respect to round ETGs, since it held even in the range of $L_{\rm B}$ where the two shapes coexist (Pellegrini 1999). The relationship between $L_{\rm X}$ and shape was reconsidered, confirming the above trends, for the *ROSAT* PSPC sample (Pellegrini 2012a), and for the *Chandra* sample (Li et al. 2011a). Therefore, there seems to be an empirical dependence of the hot gas content on the galactic shape, and it was suggested that a flatter shape by itself may be linked to a less negative binding energy for the gas (Ciotti & Pellegrini 1996). However, since flatter systems also possess a higher rotational support on average (e.g., Binney & Tremaine 1987), also the influence of galactic rotation on the hot gas was called into question. For example, in rotationally supported ETGs the gas may be less bound, compared to the ISM in non-rotating ETGs, leading rotating ETGs to be more prone to host outflowing regions. For these reasons, the effects on $L_{\rm X}$ of both galactic shape and rotation were studied for a sample of 52 ETGs with known maximum rotational velocity of the stars $V_{\rm max}$, and so with a measure of $V_{\rm max}/\sigma_{\rm c}$, an indicator of the importance of rotation (Pellegrini et al. 1997). It was found that $L_{\rm X}/L_{\rm B}$ can be high only for $V_{\rm max}/\sigma_{\rm c} < 0.4$, and is limited to low values for $V_{\rm max}/\sigma_{\rm c} > 0.4$. This trend was not produced by being the ETGs with high $V_{\rm max}/\sigma_{\rm c}$ confined to low $L_{\rm B}$. Sarzi et al. (2010) investigated again the relationship between X-ray emission (from *Einstein* and *ROSAT* data) and rotational properties for the ETGs of the *SAURON* sample, confirming that slowly rotating galaxies can exhibit much larger luminosities than fast-rotating ones.

Recently, renewed interest in the study of the hot gas haloes of ETGs has come from high-quality X-ray observations performed with the *Chandra* X-ray Observatory, which have produced a large body of data of unprecedented detail. In particular, the nuclear and the stellar (resolved and unresolved) contributions to the total X-ray emission could be subtracted, obtaining more accurate properties of the hot ISM than ever before. From a homogeneous and thorough X-ray analysis for the pure gaseous component, samples of ETGs have been built with an improved measurement of the X-ray average temperature $T_{\rm X}$ and luminosity $L_{\rm X}$ for the gas only (e.g., Boroson et al. 2011). This X-ray information allowed to revisit the $L_{\rm X} - L_{\rm K}$ correlation, and the previously known large variation of up to two orders of magnitude in $L_{\rm X}$ at the same $L_{\rm K}$ has been even extended, due to the inclusion of hot-gas poor ETGs in a larger fraction than previously possible (with $L_{\rm X}$ extending down to $\sim 10^{38}$ erg s^{-1}; Boroson et al. 2011).

In an investigation using *Chandra* and *ROSAT* data for the ATLAS$^{\rm 3D}$ sample, Sarzi et al. (2013) found that slow rotators generally have the largest $L_{\rm X}$ and $L_{\rm X}/L_{\rm K}$ values, and $T_{\rm X}$ values consistent just with the thermalisation of the stellar kinetic energy, estimated from $\sigma_{\rm e}$ (the stellar velocity dispersion averaged within the optical effective radius $R_{\rm e}$). Fast rotators, instead, have generally lower $L_{\rm X}$ and $L_{\rm X}/L_{\rm K}$ values, and the more so the larger their degree of rotational support. The $T_{\rm X}$ values of fast rotators keep below 0.4 keV and do not scale with $\sigma_{\rm e}$ (see also Boroson et al. 2011). Considering that fast rotators are likely to be intrinsically flatter than slow rotators, and that the few slow rotators with low $L_{\rm X}$ are also relatively flat, Sarzi

et al. (2013) supported the hypothesis whereby flatter galaxies have a harder time in retaining their hot gas (Ciotti & Pellegrini 1996). To explain why fast rotators seem confined to lower T_X than slow rotators, they suggest that the kinetic energy associated with the stellar ordered motions may be thermalised less efficiently (see Appendix B).

In order to help clarify what is the expected variation of the hot gas content and temperature, originating in a variation of shape and internal kinematics (and in its degree of thermalisation) of the host galaxy, we study the problem under two points of view, both based on the numerical construction of realistic, state-of-the-art (axisymmetric) galaxy models, built with the Jeans solver code described in Chapter 2. In order to derive robust conclusions, we perform a large-scale exploration of the parameter space, considering galaxy models characterized by different stellar mass, intrinsic flattening, distribution of DM, and internal kinematics. In particular, the galaxy flattening is supported by ordered rotation (isotropic rotators) or by tangential anisotropy, and all galaxy models are tailored to reproduce the observed properties and scaling laws of ETGs.

The first part the investigation is based on estimates of the temperature and energy budget for the gas, that can be associated with a galaxy model since they are derived from the given galaxy structure and kinematical configuration.

The second part of the investigation, instead, studies the evolution of the hot gas by means of high-resolution 2D hydrodynamical simulations, where the gas is subjected mainly to supernova heating, stellar winds and radiative cooling. These simulations are the outcome of a joint research collaboration, and are performed for a subset of galaxy models built with the Jeans solver code described in Chapter 2. In this way, in addition to the study of the gas flows, we are also allowed to test how much simple energetic estimates, such those of Ciotti & Pellegrini 1996 and especially the ones here computed (Posacki et al. 2013b), can be trustworthy in interpreting the global properties of the hot gaseous X-ray coronae.

The Chapter is organized as follows. In Section 4.2 we describe the different profiles adopted for the mass components of the galaxy models, the scaling laws considered to constrain the models to resemble real galaxies, the observable properties of the models in the optical band, and the procedure to obtain flat models. In Section 4.3 we define a set of mean temperatures for the models, some of which already introduced in Pellegrini (2011). Our main results obtained from the energetic analysis are presented in Section 4.4, together with a comparison with the observed X-ray properties of ETGs. Then in Section 4.5 the simulations are presented together with their main ingredients, such as the selected galaxy models and the output data necessary to make a comparison with the previous energetic analysis. The main results of the hydrodynamical analysis are described in Section 4.6. Finally Section 4.7 presents our main conclusions.

4.2 The galaxy models

The galaxy models used for the energetic estimates include three mass components: a stellar distribution, a DM halo, and a central SMBH. The stellar component is axisymmetric and can have different degrees of flattening, while for simplicity the DM halo is spherical. The SMBH is a central mass concentration with mass $M_{BH} =$

$10^{-3}M_*$, following the Magorrian et al. (1998) relation. Its effects are minor, but it is considered for completeness. For these models, the Jeans equations are solved under the standard assumption of a two-integral phase space DF (see Chapter 2 and Appendix A), so that, besides random motions, stars can have ordered motions only in the azimuthal direction. The decomposition of the azimuthal motions in velocity dispersion and streaming velocity is performed via the k-decomposition introduced by Satoh (1980); thus, the amount of rotational support is varied simply through the parameter k. With the adoption of the mass profiles detailed below for the stars and the DM, we built galaxy models that reproduce with a good level of accuracy the typical properties of the majority of ETGs. The models are then projected along two extreme lines of sight (corresponding to the face and edge-on views) and forced to resemble real galaxies as described in Section 4.2.3.

4.2.1 Stellar distribution

The stellar distribution is described by the de Vaucouleurs (1948) law, by using the deprojection of Mellier & Mathez (1987) generalized for ellipsoidal axisymmetric distributions

$$\rho_*(R,z) = \rho_0 \xi^{-0.855} \exp(-\xi^{1/4}), \tag{4.1}$$

with

$$\rho_0 = \frac{M_* b^{12}}{16\pi q R_{\mathrm{e}\,0}^3 \Gamma(8.58)}, \quad \xi = \frac{b^4}{R_{\mathrm{e}\,0}} \sqrt{R^2 + \frac{z^2}{q^2}}, \tag{4.2}$$

where (R, φ, z) are the cylindrical coordinates and $b \simeq 7.67$. The flattening is controlled by the parameter $q \leqslant 1$, so that the minor axis is aligned with the z axis. $R_{\mathrm{e}\,0}$ is the projected half mass radius (effective radius) when the galaxy is seen face-on; for an edge-on view, the circularized effective radius is $R_{\mathrm{e}} = R_{\mathrm{e}\,0}\sqrt{q}$ (see Section 4.2.4 and Chapter 2). We assume a constant stellar mass-to-light ratio Υ_* all over the galaxy, so that M_* is directly proportional to the luminosity L. Note that Eq. (4.2) guarantees that the total stellar mass (luminosity) of the model is independent of the choice of q and $R_{\mathrm{e}\,0}$.

4.2.2 Dark matter halo

Given the uncertainties affecting our knowledge of the density profile of DM haloes, we explored four families of DM profiles. The first one is the scale-free SIS

$$\rho_{\mathrm{h}}(r) = \frac{v_{\mathrm{c}}^2}{4\pi G r^2}, \qquad \Phi_{\mathrm{h}}(r) = v_{\mathrm{c}}^2 \ln r, \tag{4.3}$$

where v_{c} is the halo circular velocity. The gravitational potential of this profile diverges at small and large radii, thus it is truncated at a distance of 15 R_{e} to obtain a finite T_{g}^- (see Section 4.3.2).

A number of recent works are reconsidering the Einasto (1965) profile as appropriate to model DM haloes (e.g. Navarro et al. 2004; Merritt et al. 2006; Gao et al. 2008; Navarro et al. 2010). The density distribution of this profile is the three-dimensional analogue of the Sérsic law, widely used to fit the surface brightness profiles of ETGs. The density is described by

$$\rho_{\mathrm{h}}(r) = \rho_{\mathrm{c}} \exp(d_n - x), \tag{4.4}$$

where ρ_c is the density at the volume half-mass radius r_h, $x \equiv d_n(r/r_h)^{1/n}$, n is a free parameter, and d_n is well approximated by the relation

$$d_n \simeq 3n - \frac{1}{3} + \frac{8}{1215\ n}, \tag{4.5}$$

(Retana-Montenegro et al. 2012). Finally the gravitational potential is

$$\Phi_h(x) = -\frac{GM_h}{r}\left[1 - \frac{\Gamma(3n,x)}{\Gamma(3n)} + \frac{x^n\Gamma(2n,x)}{\Gamma(3n)}\right]. \tag{4.6}$$

The third family is based on the Hernquist (1990) profile

$$\rho_h(r) = \frac{M_h r_h}{2\pi r(r+r_h)^3}, \qquad \Phi_h(r) = -\frac{GM_h}{r+r_h}, \tag{4.7}$$

where M_h and r_h are the halo total mass and scale radius, respectively.

Lastly, we used also the NFW profile (Navarro et al. 1997)

$$\rho_h(r) = \frac{\rho_{crit}\ \delta_c r_h}{r\,(1+r/r_h)^2}, \tag{4.8}$$

where $\rho_{crit} = 3H^2/8\pi G$ is the critical density for closure. The total mass diverges, so it is common use to identify the characteristic mass of the model M_h with the mass enclosed within r_{200}, defined as the radius of a sphere of mean interior density 200 ρ_{crit}. Then, from the definition of r_{200}, the concentration $c \equiv r_{200}/r_h$ and the coefficient δ_c are linked as

$$\delta_c = \frac{200}{3}\frac{c^3}{\ln(1+c) - c/(1+c)}. \tag{4.9}$$

The gravitational potential of the NFW profile is

$$\Phi_h(r) = -4\pi G\rho_{crit}\ \delta_c r_h^3\ \frac{\ln(1+r/r_h)}{r}. \tag{4.10}$$

4.2.3 Linking the models to real ETGs

One of the most delicate steps of the present study is to have a sample of galaxy models, characterised by various degrees of flattening and rotational support, that closely resemble real ETGs, at least in a statistical sense. This is accomplished by flattening spherical models, that we call "progenitors".

In fact, the process of flattening a galaxy model is not trivial, and it is highly degenerate, as illustrated by the exploratory work of Ciotti & Pellegrini (1996), where the full parameter space of two-component MN models was explored. Here, we begin with a generic spherical galaxy model, and we impose that its effective radius R_e and aperture luminosity-weighted velocity dispersion within $R_e/8$, σ_{e8}, satisfy the most important observed scaling laws (SLs) of ETGs, the Faber–Jackson and the Size–Luminosity relations. In particular, we use the Faber–Jackson and the Size–Luminosity relations derived in the r band for $\approx 80\,000$ ETGs drawn from Data

Release 4 (DR4) of the SDSS (Desroches et al. 2007). These relations are quadratic best-fitting curves, with a slope varying with luminosity $L_{\rm r}$:

$$\log \sigma_{\rm e8} = -1.79 + 0.674 \log L_{\rm r} - 0.0234 \log^2 L_{\rm r}, \tag{4.11}$$

$$\log R_{\rm e} = 1.50 - 0.802 \log L_{\rm r} + 0.0805 \log^2 L_{\rm r}, \tag{4.12}$$

where $\sigma_{\rm e8}$ and $R_{\rm e}$ are in units of km s^{-1} and kpc respectively, and $L_{\rm r}$ is calibrated to the AB system (Desroches et al. 2007).

In practice, we fix a value for $\sigma_{\rm e8}$ in the range 150 km s^{-1} $\lesssim \sigma_{\rm e8} \lesssim$ 300 km s^{-1}, and then we derive $L_{\rm r}$ and $R_{\rm e}$ from Eqs. (4.11) and (4.12). After conversion of $L_{\rm r}$ to the V-band[1] ($L_{\rm V}$), we derive M_* adopting a (luminosity dependent) V-band mass-to-light ratio Υ_* appropriate for a 12 Gyr old stellar population with a Kroupa IMF (Maraston 2005). Following empirical evidences (Bender et al. 1992; Cappellari et al. 2006), we assume that $\Upsilon_* \propto L_{\rm V}^{0.26}$, obtaining $3.3 \lesssim \Upsilon_* \lesssim 4.7$. With this choice, the models need a DM halo to reproduce the assigned $\sigma_{\rm e8}$. We consider the four different families of (spherical) DM haloes in Section 4.2.2, whose parameters are fixed to reproduce the assigned $\sigma_{\rm e8}$. The simplest family is that with the SIS halo in Eq. (4.3), where we fix $v_{\rm c}$ so that the progenitor has the given $\sigma_{\rm e8}$. For the Einasto DM haloes, we fix $n = 6$ and $r_{\rm h} \simeq 7R_{\rm e}$ in Eq. (4.4), in order to obtain $r_{\rm h}$ values in the accepted range for ETGs (see, e.g., Merritt et al. 2006; Navarro et al. 2010), and to keep low the DM fraction $f_{\rm DM}$ in the central regions of the model (see below). $M_{\rm h}$, the only remaining free parameter, is then determined by the chosen $\sigma_{\rm e8}$. This procedure gives $M_{\rm h}$ values that are $\simeq 20$ percent larger than in the SIS case, due to the shallower density slope of the Einasto DM halo at small radii, which translates into a weaker effect on the stellar random motions, and then into a larger DM amount required to raise the central stellar velocity dispersion profile up to the chosen $\sigma_{\rm e8}$. Also for the Hernquist and NFW families we choose $r_{\rm h} \simeq 7R_{\rm e}$, and $M_{\rm h}$ is fixed to reproduce the assigned $\sigma_{\rm e8}$. For the Hernquist family, this request results in $1.8 \times 10^{12} M_\odot \lesssim M_{\rm h} \lesssim 4 \times 10^{12} M_\odot$, while for the NFW haloes we find $12 \lesssim c \lesssim 25$ (Binney & Tremaine 1987; Napolitano et al. 2009), corresponding to $10^{14} M_\odot \gtrsim M_{\rm h} \gtrsim 7.2 \times 10^{12} M_\odot$. For all models, the resulting $M_{\rm h}/M_*$ ratios agree with those given by cosmological simulations and galaxy mass functions (Narayanan & Davé 2013). A summary of the properties of some spherical progenitors, for SIS and Einasto DM haloes, is given in Table 4.1. An important quantity characterizing the models is the effective DM fraction, defined as the ratio of the DM mass to the total mass contained within a sphere of radius $R_{\rm e}$, $f_{\rm DM} = M_{\rm h}(R_{\rm e})/M_{\rm tot}(R_{\rm e})$. We compute $f_{\rm DM}$ a posteriori, to check that it agrees with the values found for well studied ETGs from stellar dynamics and gravitational lensing studies (that is, $f_{\rm DM} \sim 0.3$; Cappellari et al. 2006, Gerhard et al. 2001, Thomas et al. 2005, Treu & Koopmans 2004). In particular, for the NFW families we found quite high $f_{\rm DM}$ values (of the order of ~ 0.66 for the progenitor) due to the larger $M_{\rm h}$ values.

[1]The V-band luminosity $L_{\rm V}$ is computed using the standard transformation equations between SDSS magnitudes and other systems (http://www.sdss3.org/dr9/algorithms/sdssUBVRITransform.php), also assuming $B - V = 0.9$ as appropriate for ETGs (Donas et al. 2007).

Table 4.1: Fundamental galaxy parameters for the progenitors.

σ_{e8} (km s^{-1}) (1)	L_V ($10^{11} L_{V\odot}$) (2)	L_K ($10^{11} L_{K\odot}$) (3)	R_e (kpc) (4)	M_* ($10^{11} M_\odot$) (5)	Υ_* ($M_\odot L_{V\odot}^{-1}$) (6)	v_c (km s^{-1}) (7)	$M_h(15R_e)$ ($10^{11} M_\odot$) (8)	f_{DM} (9)	M_h ($10^{11} M_\odot$) (10)	f_{DM} (11)
300	1.66	6.64	11.79	7.80	4.7	237.3	26.57	0.32	31.53	0.49
250	0.78	3.12	7.04	3.35	4.3	189.4	10.10	0.30	11.99	0.46
200	0.33	1.32	4.09	1.25	3.8	151.9	3.78	0.30	4.48	0.46
150	0.12	0.47	2.29	0.39	3.3	113.0	1.17	0.29	1.39	0.45

Notes: (1) Stellar velocity dispersion, as the luminosity-weighted average within an aperture of radius $R_e/8$. (2) and (3): luminosities in the V band (derived as described in Section 4.2.3) and K band, from $L_K = 4L_V$ as appropriate for a 12 Gyr old stellar population with a Kroupa IMF and solar metallicity (Maraston 2005). (4) Effective radius. (5) Stellar mass. (6) V band stellar mass-to-light ratio. (7) – (9) Circular velocity, DM mass within a sphere of radius 15 R_e, and DM fraction within R_e, for the SIS halo. (10) – (11) DM mass and DM fraction within R_e for the Einasto halo.

4.2.4 From spherical to flat ETGs

In principle, realistic flat and rotating galaxy models could be constructed with a Monte-Carlo approach, where all the model parameters are randomly extracted from large ranges, the resulting models are projected and observed at random orientations, and then checked against the observed SLs, retaining only those in accordance with observations (Lanzoni & Ciotti 2003). This approach is unfeasible here, because the model construction is based on numerical integration (while Lanzoni & Ciotti 2003 used the fully analytical but quite unrealistic Ferrers models), and the computational time of a Monte Carlo exploration of the parameter space would be prohibitively large. So we solved the problem as follows.

We flatten each spherical progenitor, acting on the axial ratio q and on the scale-length $R_{\rm e\,0}$ of the stellar density in Eq. (4.2), while keeping $L_{\rm r}$, Υ_* (and then M_* and $M_{\rm BH}$), and the DM halo the same. For given q and $R_{\rm e\,0}$, the circularized effective radius $R_{\rm e}$ depends on the line-of-sight (l.o.s.) direction, ranging from $R_{\rm e\,0}$ (when the model is observed face-on, hereafter FO) to $\sqrt{q}R_{\rm e\,0}$ (in the edge-on case, EO). Thus, a request for a realistic model is that $L_{\rm r}$ and $R_{\rm e}$ remain consistent with the observed Size–Luminosity relation, independently of the l.o.s. direction. In turn, also $\sigma_{\rm e8}$ will change due to the flattening, both as a consequence of the choice of q and $R_{\rm e\,0}$, and of the l.o.s. inclination.

To include all possible inclination effects, from each spherical progenitor, we build two sub-families of flat descendants, the FO-built ones and the EO-built ones. In the first sub-family, $R_{\rm e}$ is the same of the spherical progenitor when the flat model is seen FO; in the other, $R_{\rm e}$ is the same of the spherical progenitor when the flat model is seen EO. This implies that $R_{\rm e\,0}$ may vary: with the decrease of q, $R_{\rm e\,0}$ remains equal to $R_{\rm e}$ of the spherical progenitor in the FO-built case, while $R_{\rm e\,0}$ increases as $R_{\rm e}/\sqrt{q}$ in the EO-built case. Therefore, in this latter case, there is a consequent expansion (or size increase) of the galaxy, and a decrease of the galaxy scale density $\rho_0 \propto \sqrt{q}$ in Eq. (4.2). On the contrary, in the FO-built sub-family, there is a density increase as $\rho_0 \propto q^{-1}$, as the galaxy is compressed along the z-axis.

Then, we compute $\sigma_{\rm e8}$ according to the procedure described in Chapter 2, Eq. 2.15, for the range spanned by the Satoh parameter $0 \leqslant k \leqslant 1$. Since the FO and EO-built models are characterised by different structural and dynamical properties, we must check that, once observed along arbitrary inclinations, the models are still consistent with the observed SLs. For example, a FO-built model, when observed EO, will have an $R_{\rm e}$ smaller than the progenitor, while an EO-built model will have a larger $R_{\rm e}$ when observed FO. Therefore, only galaxy models that, observed along the two extreme l.o.s. directions (FO and EO), lie within the observed scatter of $R_{\rm e}$ and $\sigma_{\rm e8}$ at fixed $L_{\rm r}$ should be retained in our study. Remarkably, all the models constructed with our procedure have been found acceptable.

The effects of flattening on $\sigma_{\rm e8}$ deserve some comments. For the EO view, $\sigma_{\rm e8}$ of the EO-built models decreases for increasing flattening, due to the associated model expansion; $\sigma_{\rm e8}$ further decreases at increasing k, as more galaxy flattening is supported by ordered rotation. Also for the FO view, $\sigma_{\rm e8}$ of EO-built systems decreases, but independently of k (affecting only σ_φ, while $\sigma_{\rm R} = \sigma_{\rm z}$). In the FO-built models, one would naively expect an increase of $\sigma_{\rm e8}$ due to the density increase (and so to the gravitational potential deepening), but this is not the case: even though

less severely than for EO-built models, σ_{e8} still decreases (both for the FO and EO views). The simplest way to explain this behaviour is to consider the FO flattening of the fully analytical Ferrers ellipsoids (Binney & Tremaine 1987). As the flattening increases, the density raises, the gravitational potential well deepens, and the vertical force increases, but again the velocity dispersion drops. The physical reason, behind the mathematics (e.g., see eqs. C4-C11 in Lanzoni & Ciotti (2003)), is that stars need less vertical velocity dispersion in order to support the decreased z-axis scale-length, and so the FO view σ_{e8} decreases. σ_{e8} decreases less when observed EO, because of the decrease of R_e, that causes σ_{e8} to be computed within a smaller area around the galactic centre. Of course, if the galaxy is not fully velocity dispersion supported, the decrease of σ_{e8} for an EO view can be even larger than for the FO one, since part of the stellar kinetic energy is stored in ordered motions that do not contribute to σ_{e8}.

These general results, obtained for realistic models, about the variation of σ_{e8} in flat and rotating galaxies of fixed stellar mass, show that some caution should be exercised when using simple dynamical mass estimators based on the velocity dispersion measured in the central regions of galaxies. This point is particularly relevant for studies of the hot haloes properties, that notoriously mainly depend on the galaxy mass (Ciotti et al. 1991; Sarzi et al. 2013).

As a further test of the models, we also calculated the parameter λ_R, introduced by Emsellem et al. (2007) and related to the mean amount of stellar rotational support. Our λ_R radial profiles, even for the $k = 1$ case, are in good agreement with the profiles in the ATLAS^{3D} sample of ETGs (fig. 5 in Emsellem et al. 2011), for each galaxy ellipticity. Finally, our method of definition of the DM halo implies a constant M_h/M_* ratio within each family, but not a constant f_{DM}, that depends on q (through the variation that q imposes to ρ_*), as one can see in Fig. 4.1 for the SIS and the Einasto families. Note that f_{DM} can decrease or increase with q depending on the construction mode: the increase of the stellar density in the FO-built models results in lower f_{DM}, since the DM halo is fixed; the reverse is true for the EO-built models. Moreover, the Einasto models have always higher DM fractions than the corresponding SIS ones, due to the steepness of the SIS profile at small radii, requiring less DM to reproduce the chosen value of σ_{e8}.

4.3 The temperatures

Here we introduce a set of gas mass-weighted temperatures, equivalent to the injection and binding energies of the hot gas in ETGs. These temperatures will then serve as a tool to study the effects of galaxy flattening and rotation on the properties of the X-ray coronae.

4.3.1 The injection temperature

In the typically evolved stellar population of ETGs, the main processes responsible for the injection of gas mass, momentum and energy in the ISM are stellar winds from red/asymptotic giant branch stars, and SNIa explosions, the only ones observed in an old stellar population (e.g. Cappellaro et al. 1999). The wind material outflowing from stars leaves the stellar surface with low temperatures and low average velocities

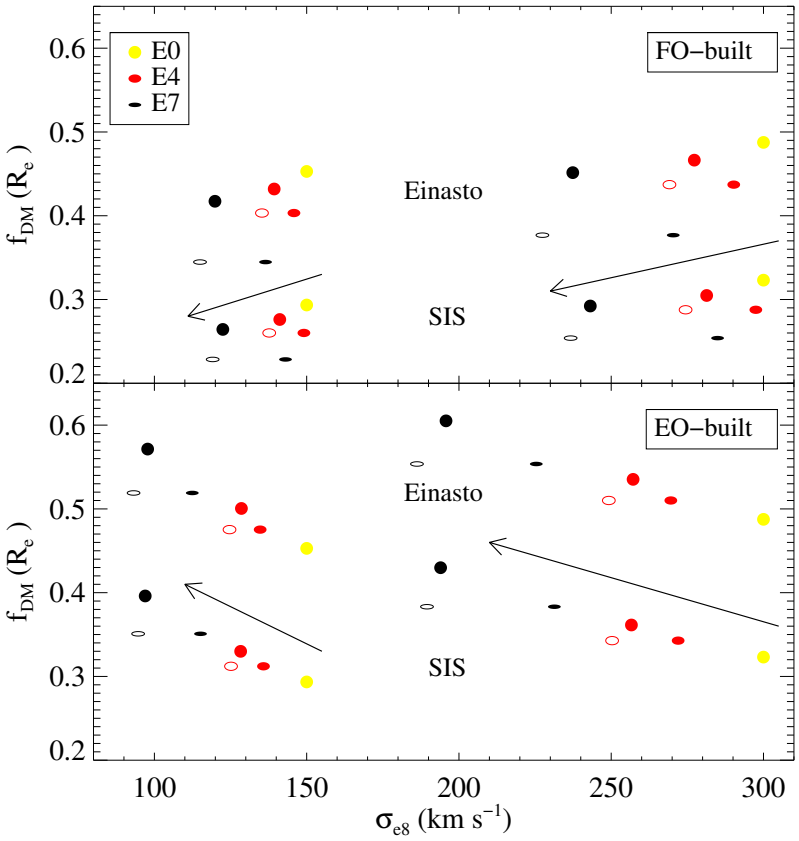

Figure 4.1: Dark matter fraction $f_{\rm DM}$ as a function of the shape parameter q for the SIS (lower symbols) and the Einasto (upper symbols) DM halo models, for two families with $\sigma_{\rm e8} = 150$ and 300 km s^{-1} for the spherical progenitors: the FO-built sub-families are in the top panel, while the EO-built ones are in bottom panel. The yellow, red, and black colours refer to the E0, E4, E7 model galaxies, respectively; symbols are filled for $k = 0$, and empty for $k = 1$. The shape of the symbols (round or elliptical) indicates the FO or the EO view of a given model. See Sections 4.2.3 and 4.2.4 for more details. The arrows indicate the trends of change of $f_{\rm DM}$ for increasing flattening, and separate the symbols of the two DM profiles.

($\sim$ few 10 km s^{-1}; Parriott & Bregman 2008), so that all its energy essentially comes from the stellar motion inside the galaxy. SNIa explosions, instead, provide mass to the ISM through their very high velocity ejecta ($\sim$ few 10^4 km s^{-1}). Thus, this material provides mass and heat to the hot haloes, via thermalisation of its energy through shocks with the ambient medium or with other ejecta, heating up to X-ray emitting temperatures.

The injection energy per unit mass due to both heating processes is $e_{\rm inj} \equiv 3k_{\rm B}T_{\rm inj}/(2\mu m_{\rm P})$, where $k_{\rm B}$ is the Boltzmann constant, $\mu = 0.62$ is the mean molecular weight for solar abundance, $m_{\rm P}$ is the proton mass, and $T_{\rm inj}$ is defined as

$$T_{\rm inj} \equiv \frac{\dot{M}_* T_* + \dot{M}_{\rm SN} T_{\rm SN}}{\dot{M}}. \tag{4.13}$$

Here T_* and $T_{\rm SN}$ are the injecta temperatures resulting from the thermalisation of their interactions with the ISM through stellar winds and SNIa respectively (see below). $\dot{M}$ is the total mass-loss rate for the entire galaxy, given by the sum of the stellar mass-loss rate $\dot{M}_*$ and of the rate of mass loss via SNIa events $\dot{M}_{\rm SN}$ ($\dot{M} = \dot{M}_* + \dot{M}_{\rm SN}$). The time evolution of the stellar mass-loss rate $\dot{M}_*$ can be calculated using single-burst stellar population synthesis models for different initial mass functions and metallicities (e.g., Maraston 2005). For example, at an age of 12 Gyr, $\dot{M}_*(M_\odot\ {\rm yr}^{-1}) \approx 2 \times 10^{-11}\, L_{\rm B}(L_{\rm B\odot})$ for the Salpeter or Kroupa IMF (e.g., Pellegrini 2012a). $\dot{M}_{\rm SN}$ is instead given by $\dot{M}_{\rm SN} = M_{\rm SN} R_{\rm SN}$, where $M_{\rm SN} = 1.4\, M_\odot$ is the mass ejected by one Type Ia supernova event and $R_{\rm SN}$ is the explosion rate. For local ETGs it is $R_{\rm SN} = 0.16(H_0/70)^2 \times 10^{-12}\, L_{\rm B}(L_{\rm B\odot})\, {\rm yr}^{-1}$, where H_0 is the Hubble constant in units of km s^{-1}Mpc^{-1} (Cappellaro et al. 1999). More recent measurements of the observed rates of supernovae in the local universe (Li et al. 2011b) give a SNIa rate in ETGs consistent with that of Cappellaro et al. (1999). For this rate, and H_0 =70 km s^{-1}Mpc^{-1}, one obtains $\dot{M}_{\rm SN} = 2.2 \times 10^{-13}\, L_{\rm B}(L_{\rm B\odot})$ $M_\odot\, {\rm yr}^{-1}$, which is ~ 80 times smaller than the $\dot{M}_*$ above for an age of 12 Gyr. Thus the main source of mass is provided by $\dot{M}_*$, and approximating $\dot{M} \simeq \dot{M}_*$, we have $T_{\rm inj} \simeq T_* + (\dot{M}_{\rm SN}/\dot{M}_*) T_{\rm SN}$.

Neglecting the internal energy and the stellar wind velocity relative to the star, T_* is the sum of two contributions, deriving from the random and the ordered stellar motions. In axisymmetric model galaxies as built here, the stellar component of the galaxy is allowed to have a rotational support, and the latter can be converted into heating of the injected gas in a variable amount. The extent of the contribution of rotational motions is not known a priori, since it depends on both the importance of the stellar ordered motions and the dynamical status of the surrounding gas already in situ (see Appendix B; see also D'Ercole et al. 2000; Negri et al. 2013). Given the complexity of the problem, hydrodynamical simulations are needed to properly calculate this heating term (as it will be done in Sections 4.5 and 4.6), but we can still obtain a simple estimate of it by making reasonable assumptions. We define the equivalent temperature of stellar motions T_* as

$$T_* = T_\sigma + \gamma_{\rm th} T_{\rm rot} \tag{4.14}$$

where

$$T_\sigma = \frac{\mu m_{\rm P}}{3k_{\rm B} M_*} \int \rho_* {\rm Tr}(\boldsymbol{\sigma}^2)\, {\rm d}V \tag{4.15}$$

is the contribution of stellar random motions,

$$T_{\rm rot} = \frac{\mu m_{\rm P}}{3k_{\rm B}M_*}\int \rho_* \, \|\mathbf{v}\|^2 \, {\rm d}V \tag{4.16}$$

is the one due to the stellar streaming motions, and $\gamma_{\rm th}$ is a parameter that regulates the degree of thermalisation of the ordered stellar motions. M_* is the stellar mass of the galaxy, $\boldsymbol{\sigma}^2$ is the velocity dispersion tensor, and $\mathbf{v} = \overline{v}_\varphi \mathbf{e}_\varphi$ is the the streaming velocity, whose only non-zero component is the azimuthal one, $\overline{v}_\varphi$ (see Chapter 2 and Appendix A). In Eqs. (4.15) and (4.16), as in the remainder of the Chapter, we assume that the gas is shed by stars with a spatial dependence that follows that of the stellar distribution ρ_*, so that the density profile of the gas injected per unit time is proportional to ρ_* (i.e. it is $\dot{\rho} = \dot{M}\rho_*/M_*$ in Eqs. B.1 − B.3 of Appendix B).

The parameter $\gamma_{\rm th}$ is defined as

$$\gamma_{\rm th} = \frac{\mu m_{\rm P}}{T_{\rm rot}3k_{\rm B}M_*}\int \rho_* \|\boldsymbol{u} - \mathbf{v}\|^2 \, {\rm d}V, \tag{4.17}$$

where $\boldsymbol{u}$ is the velocity of the pre-existing gas (see Appendix B). A simple estimate for $\gamma_{\rm th}$ is obtained when the gas velocity is proportional to $\mathbf{v}$, i.e., $\boldsymbol{u} = \alpha\mathbf{v}$, where α is some constant. In this special case, from Eqs. (4.16) and (4.17) it follows that $\gamma_{\rm th} = (\alpha - 1)^2$. When $\alpha = 1$, gas and stars rotate with the same velocity and no ordered stellar kinetic energy is thermalised, whereas for $\alpha = 0$ the gas is at rest and all the kinetic energy of the stars, including the whole of the rotational motions, is thermalised. Clearly both cases are quite extreme and unlikely, and plausibly the pre-existing gas will have a rotational velocity ranging from zero to the streaming velocity of stars, i.e., $0 \leqslant \alpha \leqslant 1$ and then $1 \geqslant \gamma_{\rm th} \geqslant 0$ (the case of a constant $\alpha > 1$, where the pre-existing gas is everywhere rotating faster than the newly injected gas is not considered). Note that, contrary to $\gamma_{\rm th}T_{\rm rot}$, T_σ is in principle exact, and can be computed a priori.

The internal plus kinetic energy of the ejecta, released during a Type Ia supernova event, is of the order of $E_{\rm SN} \simeq 10^{51}$ erg. Depending on the conditions of the environment in which the explosion occurs, the radiative losses from the expanding supernova remnant may be important, and so the amount of energy transferred to the ISM through shock heating is a fraction η of $E_{\rm SN}$. Realistic values of η for the hot and diluted ISM of ETGs are around 0.85 (e.g., Tang & Wang 2005, Thornton et al. 1998), thus

$$T_{\rm SN} = \frac{2\mu m_{\rm P}}{3k_{\rm B}}\frac{\eta E_{\rm SN}}{M_{\rm SN}}, \tag{4.18}$$

and, substituting the above expressions for $\dot{M}_{\rm SN}$ and $\dot{M}_*$, we obtain the average injection temperature

$$T_{\rm inj} = T_* + 1.7\frac{\eta}{0.85} \times 10^7 \, {\rm K}. \tag{4.19}$$

A possible additional source of heating for the gas could be provided by a central SMBH. Through its gravitational influence, it is responsible for the increase of the stellar motions within its radius of influence (of the order of a few tens of parsecs; e.g., Pellegrini (2012a)). We consider this effect here, while we neglect possible effects as radiative or mechanical feedback.

4.3.2 The temperatures related to the potential well

The gas ejected by stars can be also heated "gravitationally" by falling into the galactic potential well to the detriment of its potential energy, and by the associated adiabatic compression. When stellar mass losses accumulate, the gas density can reach high values and the cooling time can become smaller than the galactic age; if the radiative losses increase considerably, the gravitational force overwhelms the pressure gradient and eventually the gas starts inflowing toward the centre of the galaxy. Thus we can define a temperature

$$T_{\rm g}^{+} = \frac{2\mu m_{\rm P} E_{\rm g}^{+}}{3k_{\rm B}} = \frac{2\mu m_{\rm P}}{3k_{\rm B} M_*} \int \rho_* \left(\Phi - \Phi_0\right) {\rm d}V \tag{4.20}$$

where $E_{\rm g}^{+}$ is the average change in gravitational energy per unit mass of the gas flowing in through the galactic potential $\Phi(\mathbf{x})$ down to the galactic centre, and $\Phi_0 = \Phi(0)$. Note that $E_{\rm g}^{+} > 0$, having assumed as usual that $\Phi(\mathbf{x}) < 0$. However, as discussed in Pellegrini (2011), most of $E_{\rm g}^{+}$ may be radiated away, and there are conditions under which Eq. (4.20) does not apply (like the development of thermal instabilities that produce dropouts from the flow at large radii from the galactic centre). Therefore, given these uncertainties, we consider $T_{\rm g}^{+}$ just as a reference value, and keep in mind that the temperature achievable from infall can be much lower than that given by Eq. (4.20).

By analogy with $T_{\rm g}^{+}$, we can define a temperature

$$T_{\rm g}^{-} = \frac{2\mu m_{\rm P} E_{\rm g}^{-}}{3k_{\rm B}} = -\frac{2\mu m_{\rm P}}{3k_{\rm B} M_*} \int \rho_* \Phi \, {\rm d}V, \tag{4.21}$$

where $E_{\rm g}^{-}$ is the average energy necessary to extract a unit of gas mass from the galaxy, with the assumption that $\Phi(\infty) = 0$. If the gas rotates, Eq. (4.21) must be modified since, thanks to the centrifugal support, the gas is less bound. Assuming again that $\boldsymbol{u} = \alpha \mathbf{v}$, then

$$E_{\rm g}^{-}(\alpha) = -\frac{1}{M_*} \int \rho_* \left(\Phi + \frac{\alpha^2}{2} \overline{v}_{\varphi}^2\right) {\rm d}V, \tag{4.22}$$

so that $T_{\rm g}^{-}(\alpha) = T_{\rm g}^{-} - \alpha^2 T_{\rm rot}$. Note that, for a given $T_{\rm rot}$, the smallest is $\gamma_{\rm th}$ (the largest is α), the smallest is T_* (the gas is less heated), but also the lower is $T_{\rm g}^{-}$ (the gas is less bound).

When the galaxy mass distribution has a potential that diverges at small and/or large radii, as for the SIS, we assume the gas has been extracted from the galaxy when it has reached a distance of 15 $R_{\rm e}$ from the galactic centre, so that $E_{\rm g}^{-}$ and $E_{\rm g}^{+}$ do not correspond exactly to Eqs. (4.22) and (4.20). Finally, if energy losses due to cooling are present, the gas would need more than $E_{\rm g}^{-}$ to escape, but these losses are negligible for outflows that typically have a low density.

In case of gas escape, we can introduce another mass-weighted temperature by considering the enthalpy per unit mass of a perfect gas $h = \gamma k_{\rm B} T / [\mu m_{\rm P} (\gamma - 1)] = c_s^2/(\gamma - 1)$, where γ is the ratio of the specific heats and c_s is the sound speed. Building on the Bernoulli theorem, we can derive a fiducial upper limit to the temperature of outflowing gas. For a fixed galactic potential, the energy of the escaping gas can

be divided between kinetic and thermal energy with different combinations. In the extreme case in which the gas reaches infinity with a null velocity and enthalpy, and it is injected with a (subsonic) velocity $\boldsymbol{u} = \alpha \mathbf{v}$, from the Bernoulli equation $h(\mathbf{x}) + v^2(\mathbf{x})/2 + \Phi(\mathbf{x}) = 0$, we derive a characteristic gas-mass averaged escape temperature

$$T_{\rm esc}^{\rm sub} = -\frac{2\mu m_{\rm P}}{5k_{\rm B}M_*} \int \rho_* \left(\Phi + \frac{\alpha^2}{2} \overline{v}_\varphi^2 \right) {\rm d}V = \frac{3}{5} T_{\rm g}^-(\alpha), \tag{4.23}$$

for a monoatomic gas (see Pellegrini 2011 for more details). In the opposite case of an important kinetic energy of the flow, the gas temperature will be lower than $T_{\rm esc}^{\rm sub}$.

In summary, $T_{\rm g}^-$ is a temperature equivalent to the energy required to extract the gas, while $T_{\rm esc}^{\rm sub}$ is close to the temperature we expect to observe for outflowing gas. For inflowing gas, we expect to observe a temperature much lower than $T_{\rm g}^+$, since more than $\sim 0.5 E_{\rm g}^+$ is radiated away or goes into kinetic energy of the gas, or because of condensations in the gas (e.g., Sarazin & Ashe 1989). For reference, for realistic spherical models, $E_{\rm g}^+ \sim 2E_{\rm g}^-$, thus the temperature of the inflowing gas should be lower than $T_{\rm g}^-$ (Pellegrini 2011).

Finally, we mention about the relation between observed temperatures $T_{\rm X}$ and the average mass-weighted temperatures of this Section. The latter are derived under the assumption that the gas density $\rho_{\rm gas}$ follows that of the stars, which is appropriate for the continuously injected gas (e.g., for T_* and $T_{\rm inj}$), while the bulk of the hot ISM may have a different distribution; thus, mass-weighted $T_{\rm g}^-$ and $T_{\rm esc}^{\rm sub}$ referring to the whole hot gas content of an ETG may be different from those given by Eqs. (4.21) and (4.23). In general, the $\rho_{\rm gas}$ profile is shallower than that of ρ_* (e.g., Sarazin & White 1988; Fabbiano 1989), and then the gas mass-weighted $T_{\rm g}^+$ would be larger than derived with Eq. (4.20), and the mass-weighted $T_{\rm g}^-$ or $T_{\rm esc}^{\rm sub}$ would be lower than derived using Eqs. (4.21) and (4.23). For steady winds, instead, when the gas is continuously injected by stars and expelled from the galaxy, the $\rho_{\rm gas} \propto \rho_*$ assumption is a good approximation.

Another point is that the $T_{\rm X}$ values are emission-weighted averages, and will coincide with mass-weighted averages only if the entire ISM has one temperature value (e.g., Ciotti & Pellegrini 2008; Kim 2012). A single $T_{\rm X}$ value measured from the spectrum of the integrated emission will tend to be closer to the temperature of the densest region, in general the central one, thus it will be closer to the central temperature than the mass-weighted one. The temperature profiles observed with *Chandra* tend to be quite flat, except for cases where they increase outside of $\sim 0.5 R_{\rm e}$ (generally in ETGs with the largest $T_{\rm X}$), and for cases of negative temperature gradients (in ETGs with the lowest $T_{\rm X}$; Diehl & Statler 2008; Nagino & Matsushita 2009). Therefore, the largest $T_{\rm X}$ may be lower than mass-weighted averages, and the lowest $T_{\rm X}$ may be larger than them. In conclusion, the comparison of $T_{\rm X}$ and the gas content with the gas temperature and binding energy introduced in this Section (as T_* and $E_{\rm g}^-$) represents the easiest approach for a general, systematic investigation involving a wide set of galaxy models, but the warnings above should be kept in mind. Note, however, that the conclusions below remain valid when taking into account the above considerations.

Table 4.2: Summary of all parameters and temperatures.

Symbol	Meaning
q	Intrinsic axial ratio of the stellar distribution: $0.3 \leqslant q \leqslant 1$
k	Satoh parameter, controls the amount of galaxy rotation: $0 \leqslant k \leqslant 1$
$\gamma_{\rm th}$	Degree of thermalisation of the ordered stellar motions $\mathbf{v}$ (Eq. 4.17)
α	Scaling factor between the ISM velocity and the stellar streaming motions ($\boldsymbol{u} = \alpha\mathbf{v}$), with $0 \leqslant \alpha \leqslant 1$; $\gamma_{\rm th} = (\alpha - 1)^2$
$T_{\rm inj}$	Temperature equivalent of the thermalisation of the stellar motions and of the kinetic energy of SNe Ia events, for the unit mass of injected gas (Eq. 4.19)
$T_{\rm SN}$	Contribution to $T_{\rm inj}$ due to SNIa events (Eq. 4.18); it is regulated by a factor $\eta < 1$ ($\eta = 0.85$ is generally adopted)
T_*	Contribution to $T_{\rm inj}$ due to stellar motions, defined by Eq. (4.14): $T_* = T_\sigma + \gamma_{\rm th} T_{\rm rot}$
T_σ	Contribution to T_* due to stellar random motions, defined by Eq. (4.15)
$T_{\rm rot}$	Contribution to T_* due to stellar ordered motions defined by Eq. (4.16)
$T_{\rm g}^+$	Temperature equivalent of the change in gravitational energy of the injected gas, when flowing to the galactic centre (Eq. 4.20)
$T_{\rm g}^-$	Temperature equivalent of the energy required to extract the unit mass of injected gas from the galaxy (Eq. 4.21). If the injected gas rotates, then $T_{\rm g}^-(\alpha) = T_{\rm g}^- - \alpha^2 T_{\rm rot}$
$T_{\rm esc}^{\rm sub}$	Mass averaged, subsonic escape temperature for the injected gas (Eq. 4.23). It represents a fiducial upper limit to the observed temperature of outflows; $T_{\rm esc}^{\rm sub} = 3/5\, T_{\rm g}^-$

4.4 Results

Having built a large set of realistic galaxy models, consistent with the observed SLs and with DM haloes in agreement with current expectations, we can now study the effects of flattening and rotational support on the temperatures of the models, defined in Section 4.3 and summarized in Table 4.2, together with the main parameters characterizing the models. We next compare these temperatures with the observed X-ray properties of a sample of ETGs, extending to flat and rotating models the analysis carried out by Pellegrini (2011). In this Section, we take into account also the effect of α, that parametrizes the degree of thermalisation of the ordered motions.

4.4.1 The effects of shape and stellar streaming motions on the model temperatures

We explore here how T_*, $T_{\rm inj}$ and $T_{\rm g}^-$ depend on (q, k, α), i.e., galaxy flattening, rotational support, and degree of thermalisation of ordered rotation. Three values of $q = (1, 0.6, 0.3)$ are considered, that cover ETG morphologies from the spherical (E0) to the flattest ones (E7). The choice of the intermediate value $q = 0.6$ (corresponding to an E4) is motivated by the majority of ETGs having $0.55 \lesssim q \leqslant 1$ (see Fig. 4.2).

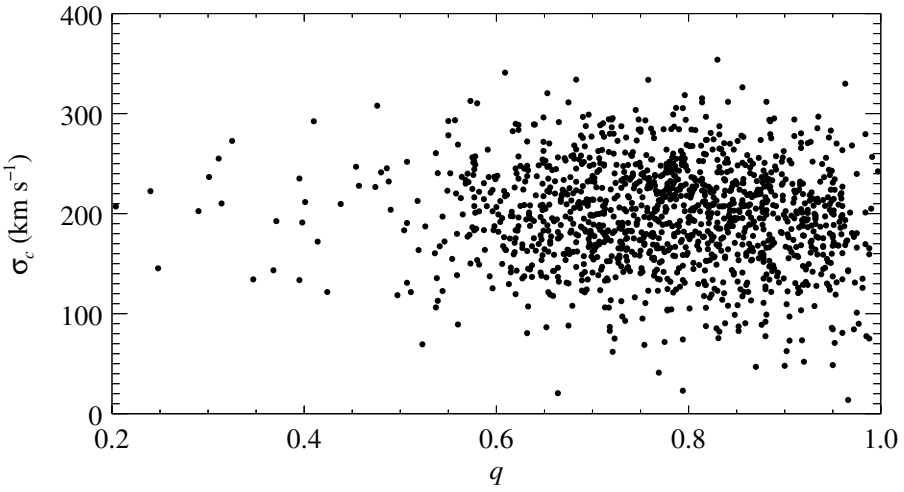

Figure 4.2: Central stellar velocity dispersion as a function of the shape parameter q for a sample of ≈ 1400 nearby ($z < 0.05$) ETGs drawn from the SDSS DR4 (data taken form Nair & Abraham 2010).

Thus, the E7 models correspond to rare objects and represent quite an extreme behaviour, whereas the most common ETGs correspond to models with q between 1 and 0.6. We also consider the two extreme values of k: fully velocity dispersion supported systems ($k = 0$), and isotropic rotators ($k = 1$); and three values of $\alpha = (0, 0.5, 1)$, in which respectively the pre-existing ISM has a null rotational velocity (all the stellar kinetic energy, including that of rotational motions, is thermalised, $\gamma_{\rm th} = 1$), or rotates with half the velocity of the stars (then $\gamma_{\rm th} = 0.25$), or has the same velocity as the stars (then no ordered stellar kinetic energy is thermalised, $\gamma_{\rm th} = 0$, see Section 4.3).

Figure 4.3 shows T_* for various descendants of spherical progenitors with $\sigma_{\rm e8} =$ 150 and 300 km s^{-1} (yellow circles), for two different DM haloes (SIS and Einasto in the left and right panels, respectively). As anticipated in Section 4.2.4, a major effect of flattening is the decrease of $\sigma_{\rm e8}$ of the descendants (with respect to the progenitor), that are then displaced on the left of their respective progenitor, in a way proportional to the flattening level [2] (arrows in Fig. 4.1, see also Figs. 4.3 and 4.4).

The trend of T_* with a pure change of shape in fully velocity dispersion supported models ($k = 0$), is due to the specific flattening procedure (see Section 4.2.4). In the FO-built sub-families (Fig. 4.3, top panels), flatter models are more concentrated than rounder ones, while in the EO-built sub-families (bottom panels), they are more extended and diluted. Thus pure flattening produces a different effect on T_*: in the FO-built cases T_* increases (as $T_{\rm g}^-$; see below), whereas in the EO-built cases T_* decreases. Therefore, we conclude that real flat galaxies can be either more

[2] In some works, instead of $\sigma_{\rm e8}$, the observations are used to measure the quantity $V_{\rm rms} = \sqrt{\sigma_{\rm P}^2 + V_{\rm P}^2}$, averaged within a central aperture (i.e., $R_{\rm e}/8$) by weighting with the surface brightness (see Chapter 2). For a chosen shape of the stellar distribution, $V_{\rm rms} = \sigma_{\rm P}$ if $k = 0$, and whenever the galaxy is seen face-on. For any view, it can be shown that, for axisymmetric stellar distributions where the Satoh k-decomposition is adopted, $V_{\rm rms}$ is independent of k; thus $V_{\rm rms,\,e8}$ has a different behaviour than $\sigma_{\rm e8}$, that is slightly lower for $k = 1$ than for $k = 0$, for the edge-on view.

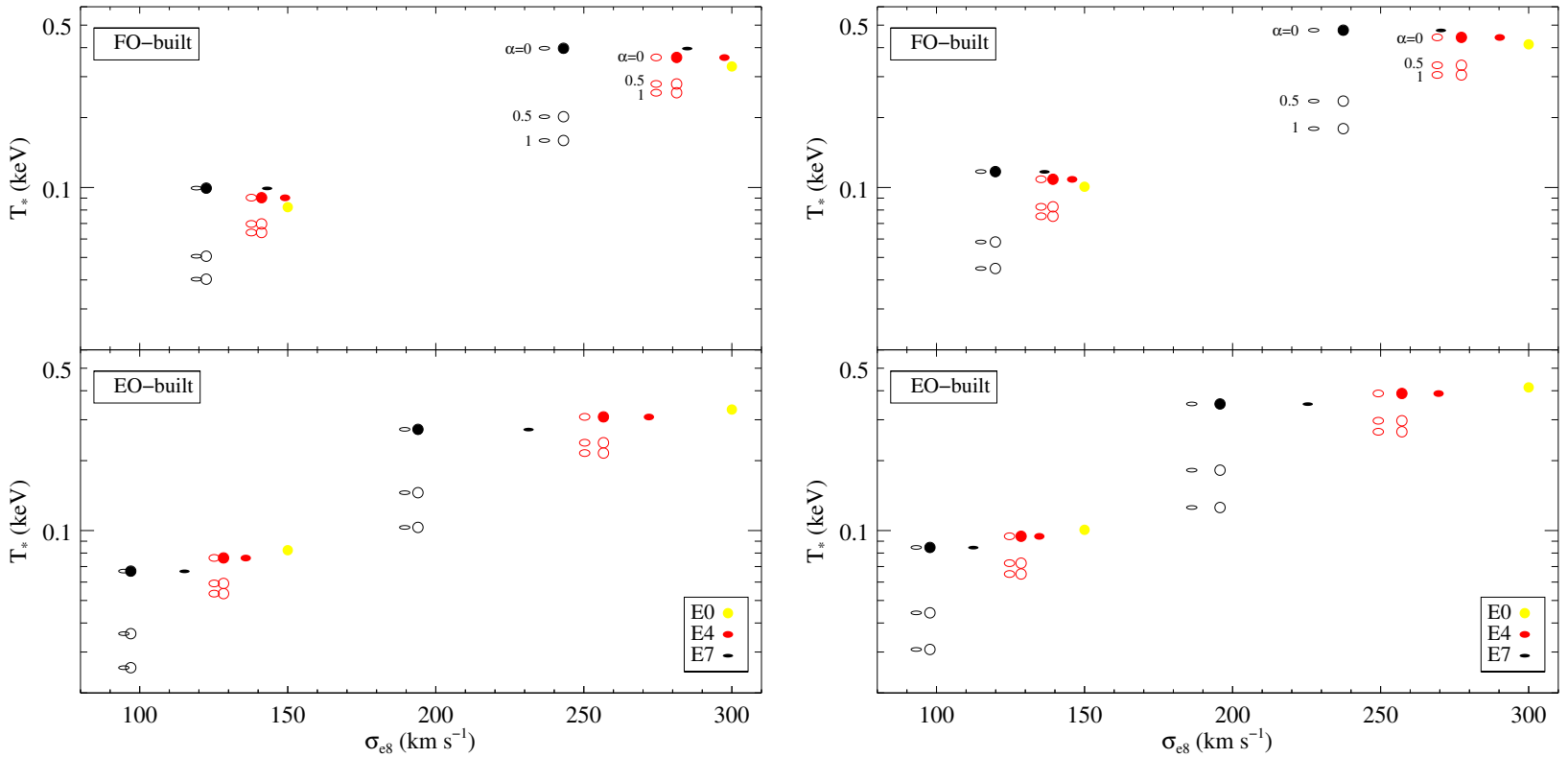

Figure 4.3: Distribution of T_* for models derived from two spherical progenitors (yellow circles) of $\sigma_{e8} = 150$ or 300 km s^{-1}, with SIS (left panel) or Einasto DM halo (right panel). Colours refer to the *intrinsic* flattening of the descendants: E4 (red) and E7 (black). At given intrinsic flattening (i.e., at fixed colour), the shape of the symbols indicates the l.o.s. inclination: FO (circle) or EO view (ellipse). Filled symbols refer to $k = 0$, empty symbols to $k = 1$. Three values of α are considered ($\alpha = 0, 0.5, 1$), as indicated for the FO-built sub-families of the σ_{e8}=300 km s^{-1} progenitor. When $k = 1$, the increase of α decreases T_* at any σ_{e8}, from the value coincident with the non-rotating case ($k = 0$) when $\alpha = 0$, down to values that are lower for larger flattenings, when $\alpha = 0.5$ and 1. In each sub-family, models with same intrinsic shape have the same T_*, independent of the FO or EO view, for fixed (k, α).

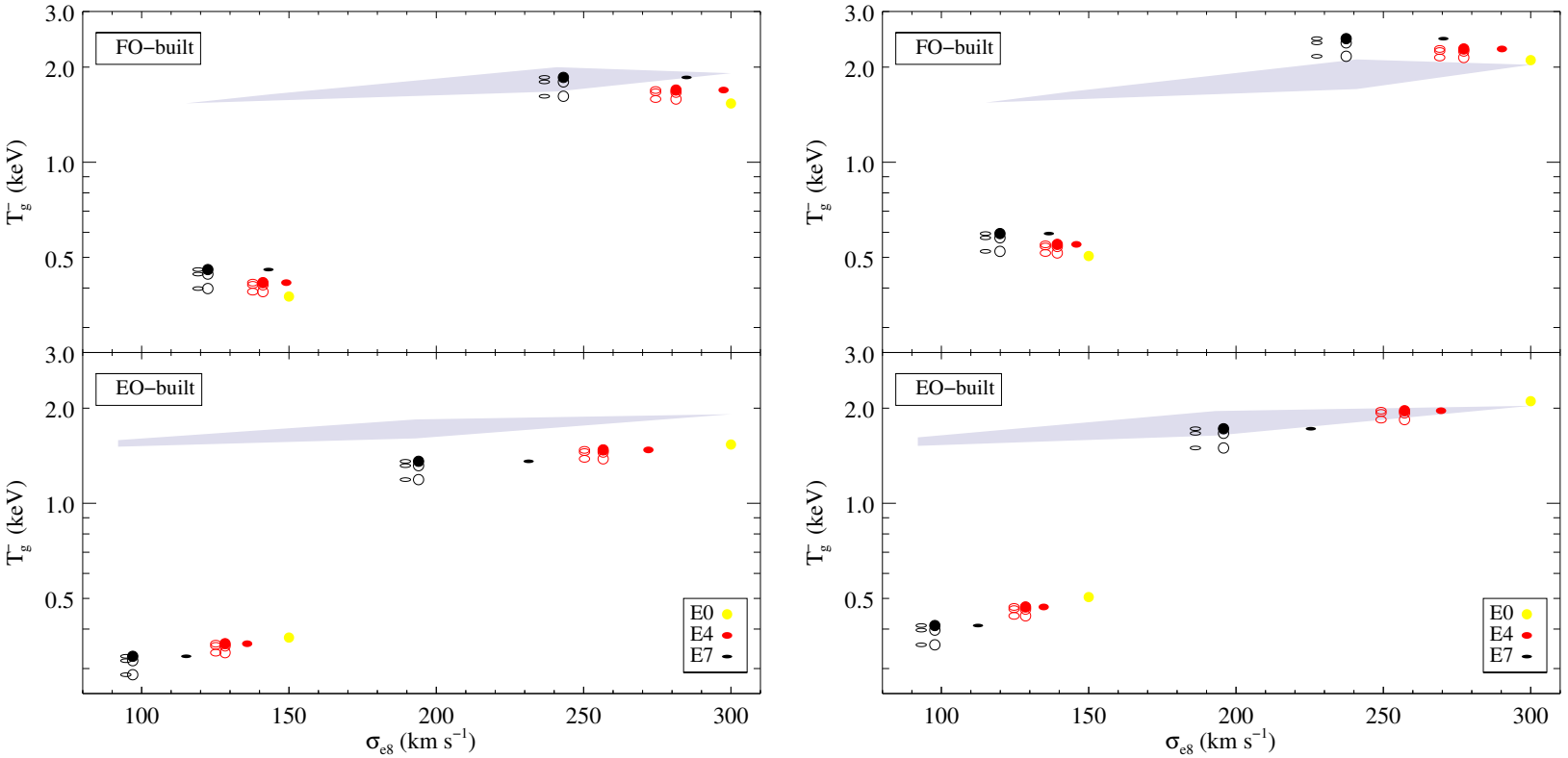

Figure 4.4: T_g^- for the same models in Fig. 4.3 (SIS and Einasto DM halo in the left and right panels, respectively); the same notation applies. The shaded area shows the range spanned by T_{inj}, considering the variations in T_* in Fig. 4.3, for $\eta = 0.85$.

Table 4.3: Observed Properties of the ETG Sample with X-ray properties for the hot gas from Chandra observations.

Name	d (Mpc)	$\log(L_K)$ ($L_{K\odot}$)	k_BT_X (keV)	L_X (10^{40}erg s^{-1})	V_{max} (km s^{-1})	σ_{e8} (km s^{-1})	V_{max}/σ_{e8}	Ref.	Type RC3	q 2MASS
(1)	(2)	(3)	(4)	(5)	(6)	(7)	(8)	(9)	(10)	(11)
NGC 720	27.6	11.31	0.54	5.06	100	241	0.41	Binney et al. 1990	E5	0.55
NGC 821	24.1	10.94	0.15	2.13×10^{-3}	120	200	0.60	Coccato et al. 2009	E6?	0.62
NGC1023	11.4	10.95	0.32	6.25×10^{-2}	250	204	1.23	Noordermeer et al. 2008	SB0	0.38
NGC1052	19.4	10.93	0.34	4.37×10^{-1}	120	215	0.56	Milone et al. 2007	E4	0.70
NGC1316	21.4	11.76	0.60	5.35	150	230	0.65	Bedregal et al. 2006	SAB0	0.72
NGC1427	23.5	10.82	0.38	5.94×10^{-2}	45	171	0.26	D'Onofrio et al. 1995	cD	–
NGC1549	19.6	11.20	0.35	3.08×10^{-1}	40	210	0.19	Longo et al. 1994	E0-1	0.90
NGC2434	21.5	10.84	0.52	7.56×10^{-1}	20	205	0.10	Carollo & Danziger 1994	E0-1	0.98
NGC2768	22.3	11.23	0.34	1.26	195	205	0.95	Proctor et al. 2009	E6	0.46
NGC3115	9.6	10.94	0.44	2.51×10^{-2}	260	239	1.09	Fisher 1997	S0	0.39
NGC3377	11.2	10.45	0.22	1.17×10^{-2}	97	144	0.67	Simien & Prugniel 2002	E5-6	0.58
NGC3379	10.5	10.87	0.25	4.69×10^{-2}	60	216	0.28	Weijmans et al. 2009	E1	0.85
NGC3384	11.5	10.75	0.25	3.50×10^{-2}	150	161	0.93	Fisher 1997	SB0	0.51
NGC3585	20.0	11.25	0.36	1.47×10^{-1}	200	198	1.01	Fisher 1997	E6	0.63
NGC3923	22.9	11.45	0.45	4.41	31	250	0.12	Norris et al. 2008	E4-5	0.64
NGC4125	23.8	11.35	0.41	3.18	150	227	0.66	Pu et al. 2010	E6 pec	0.63
NGC4261	31.6	11.43	0.66	7.02	50	300	0.17	Bender et al. 1994	E2-3	0.86
NGC4278	16.0	10.87	0.32	2.63×10^{-1}	60	252	0.24	Bender et al. 1994	E1-2	0.93
NGC4365	20.4	11.30	0.44	5.12×10^{-1}	80	245	0.33	Surma & Bender 1995	E3	0.74
NGC4374	18.3	11.37	0.63	5.95	60	292	0.21	Coccato et al. 2009	E1	0.92
NGC4382	18.4	11.41	0.40	1.19	70	187	0.37	Fisher 1997	SA0	0.67
NGC4472	16.2	11.60	0.80	18.9	73	294	0.25	Fisher et al. 1995	E2	0.81
NGC4473	15.7	10.86	0.35	1.85×10^{-1}	70	192	0.36	Emsellem et al. 2004	E5	0.54

Table 4.3 – *continued*

Name	d (Mpc)	$\log(L_K)$ ($L_{K\odot}$)	$k_B T_X$ (keV)	L_X (10^{40}erg s^{-1})	V_{max} (km s^{-1})	σ_{e8} (km s^{-1})	V_{max}/σ_{e8}	Ref.	Type RC3	q 2MASS
(1)	(2)	(3)	(4)	(5)	(6)	(7)	(8)	(9)	(10)	(11)
NGC4526	16.9	11.20	0.33	3.28×10^{-1}	246	232	1.06	Pellegrini et al. 1997	SAB0	0.43
NGC4552	15.3	11.01	0.52	2.31	17	268	0.06	Krajnović et al. 2008	E0-1	0.94
NGC4621	18.2	11.16	0.27	6.08×10^{-1}	140	225	0.62	Bender et al. 1994	E5	0.65
NGC4649	16.8	11.49	0.77	11.7	120	315	0.38	Pinkney et al. 2003	E2	0.81
NGC4697	11.7	10.92	0.33	1.91×10^{-1}	115	174	0.66	de Lorenzi et al. 2008	E6	0.63
NGC5866	15.3	10.95	0.35	2.42×10^{-1}	210	159	1.32	Neistein et al. 1999	SA0	0.42

Notes: (1) Galaxy name. (2) Distances from Boroson et al. (2011) (Tonry et al. 2001). (3) Logarithm of the K band luminosity, assuming $K_\odot = 3.33$ mag, taken from Boroson et al. (2011). (4) – (5) Hot gas temperature and the $0.3 - 8$ keV gas luminosity, from Boroson et al. (2011). (6) – (8): maximum velocity of rotation, stellar velocity dispersion, as the luminosity-weighted average within an aperture of radius $R_e/8$ (from Pellegrini 2011), and their ratio. (9) References for V_{max} in column (6). (10) Morphological type from RC3. (11) Axial ratio in the K_s band, from 2MASS.

or less bound than spherical galaxies of the same mass, depending on their mass concentration. Overall, however, the variation in T_* for both sub-families is not large: the maximum variation, from the progenitor to the E7 model, is an increase of $\sim$ 19 percent for the FO-built cases, and a decrease of $\sim$ 18 percent for the EO-built ones.

A larger effect on T_* can instead be due to the presence of significant rotational support (empty symbols in Fig. 4.3), if not thermalised. In fact, when $k = 1$, but $\alpha = 0$ ($\gamma_{\rm th} = 1$), the whole stellar kinetic energy, including the streaming one, is thermalised, and the T_* values are coincident with those of the non-rotating case (full symbols), for the same galaxy shape. In the other cases of $\alpha \neq 0$, the rotational support always acts in the sense of reducing T_*, and the flatter the shape, the larger can be the reduction. The strongest reduction of T_* is obtained for an isotropic rotator ($k = 1$) E7 model, if the gas ejected from stars retains the same stellar streaming motion ($\alpha = 1$, $\gamma_{\rm th} = 0$): for the FO-built case, T_* drops by ~ 50 percent with respect to the E0 model, and by ~ 60 percent with respect to the same E7 model with the ordered streaming motions fully thermalised ($\alpha = 0$). For the EO-built case, T_* drops by ~ 70 percent with respect to the E0 model, and by ~ 60 percent with respect to the same E7 model with $\alpha = 0$. These percentages are obviously extreme values; the T_* reduction is lower for milder flattenings, and for k and α values smaller than 1. For a fixed galaxy shape, all possible (k, α) combinations fill a sort of triangular area on the $(\sigma_{\rm e8}, T_*)$ plane, identifiable by linking the symbols of a given q (colour). Clearly, the rounder the galaxies, the weaker the effect of k and, consequently, of α variations. All the above effects are independent of the galaxy luminosity (mass), and both the $\sigma_{\rm e8} = 300$ and 150 km s^{-1} families show the same (rescaled) behaviour in the $(\sigma_{\rm e8}, T_*)$ plane.

The trends described above are independent of the specific DM halo profile: models with an Einasto DM halo (right panel) show the same pattern as those with a SIS DM halo (left panel), just with a different normalisation due to the larger total DM content (see Table 4.1). Similar results hold also for the Hernquist and NFW DM haloes.

In Fig. 4.4 we plot $T_{\rm g}^-$ for the same families in Fig. 4.3. Similarly to what happens for T_*, for fully velocity dispersion supported models, $T_{\rm g}^-$ gets larger with flattening for the FO-built sub-family (~ 21 percent), while it decreases for the more diluted EO-built models (~ 12 percent). Stellar streaming, when $\alpha > 0$, acts in the sense of making the gas less bound, due to the centrifugal support of the injected gas, and then $T_{\rm g}^-$ decreases with increasing α, at any fixed flat shape. This effect is maximum when $\alpha = 1$ and the gas rotates as the stars. However, the decrease in $T_{\rm g}^-$ due to galaxy rotation is lower than obtained for T_*: for both sub-families, $T_{\rm g}^-$ drops at most by ~ 13 percent (for the E7 models), between the two extreme cases of $\alpha = 0$ and $\alpha = 1$. This produces that, in the FO-built case, $T_{\rm g}^-$ keeps always larger than for the progenitor when q decreases, even for $k = \alpha = 1$, while T_* of rotating galaxies could become significantly lower than for the progenitor. Note that there are two compensating effects from stellar streaming when $\alpha \neq 0$: the stellar heating is lower than for $k = 0$, but the gas is also less bound. Also these results are independent of the DM halo profile, as can be judged from the right panel of Fig. 4.4, that refers to the same models of the right panel of Fig. 4.3.

Since the flatter is the galaxy, the more it can be rotationally supported (and

the more is rotationally supported, the larger is the effect of a co-rotating ISM), the effect of rotation is dependent on the degree of flattening, and thus it may prove difficult to disentangle observationally the two distinct effects due to shape and kinematics. On the theory side, we recall that a simplifying assumption made here is that $\boldsymbol{u} = \alpha \mathbf{v}$, and $\gamma_{\rm th} = (\alpha - 1)^2$, while in reality the kinematical difference between stars and pre-existing gas may be more complex, as the extent of thermalisation; only numerical simulations are able to establish what are the net effects on the gas evolution of stellar streaming motions (see Section 4.5 Negri et al. 2013, 2014a,b).

Figure 4.4 finally shows the well known fact that the contribution from SNIa dominates the gas injection energy, since $T_{\rm inj} >> T_*$. This contribution (i.e., $T_{\rm SN}$) is independent of galaxy mass, which results into lower-mass models having $T_{\rm g}^-$ far lower than $T_{\rm inj}$, and $T_{\rm g}^-$ reaching $T_{\rm inj}$ for 200 km s^{-1} $\lesssim \sigma_{\rm e8} \lesssim$ 250 km s^{-1}, depending on the DM profile. Galaxies with $\sigma_{\rm e8} \lesssim 200$ km s^{-1} consequently are more prone to an outflow, and then to have a low hot gas content, as already suggested in the past by numerical simulations and by observations (Ciotti et al. 1991; Sarazin et al. 2001; David et al. 2006; Pellegrini et al. 2007; Trinchieri et al. 2008). These findings are based on the assumption of a high thermalisation efficiency for SNIa ($\eta = 0.85$), and the quoted $\sigma_{\rm e8}$ critical values become lower for lower η values (as indicated by, e.g., Thornton et al. 1998), that decrease $T_{\rm inj}$. Variations in the DM may alter the $T_{\rm g}^-$ values, but small changes in $T_{\rm g}^-$ are found here for differences in the DM profile, and possible variations in the total DM amount cannot be very large, given the constraints from dynamical modellings within $R_{\rm e}$, and from cosmological simulations (taken into account here, Section 4.2.3). Indeed, the results for the Hernquist families are essentially identical to what we have shown for the Einasto halo, whereas for the NFW profile the trends are the same, but all the temperatures are shifted to higher values, due to their larger amounts of DM.

Finally we comment on the preliminary investigation about the role of flattening and rotation on the global energetics of the ISM in Ciotti & Pellegrini (1996). They built fully analytical axisymmetric two-component galaxy models, where the stellar and DM mass distributions were described by the MN potential-density pair. They varied the shape of both the stellar component and the DM halo from flat to spherical, and the amount of azimuthal ordered motions through the Satoh k-decomposition. Their conclusion was that, for quite round systems, flattening can have a substantial effect in reducing the binding energy of the hot gas, contrary to galaxy rotation that seemed to have a negligible role. The opposite was suggested for very flat systems. These results were confirmed by 2D hydrodynamical simulations (D'Ercole & Ciotti 1998). We stress here that the models in Ciotti & Pellegrini (1996), while capturing the main effects of flattening and rotation on the global energetics of the hot haloes of ETGs, were not tailored to reproduce in detail the observed properties of real ETGs. Our current findings, based on more realistic galaxy models, reveal a more complicated situation, where the flattening importance on the ISM status is mediated by the amount of rotation and its specific thermalisation history. Remarkably enough, however, when flattening a two-component MN model following the same procedure here adopted (constant M_*, $R_{\rm e}$ and $M_{\rm h}$), its $T_{\rm g}^-$ remains close to that of its spherical progenitor (i.e., the model moves almost parallel to the solid lines in fig. 2 in Ciotti & Pellegrini 1996).

4.4.2 Comparison with observed ETGs properties in the X-rays

Now we compare our estimates for T_* and T_g^- with observed temperatures T_X and gas content, respectively, for the Boroson et al. (2011) sample. Observed X-ray and K-band luminosities, central stellar velocity dispersions, rotation velocities, and galaxy shape are given in Tab. 4.3. Figure 4.5 shows observed (points) and model temperatures (lines) versus L_K, with T_X plotted with a different colour reflecting the ETG shape and rotational support. In order to make the comparison between models and observations more consistent, the L_K of the models have been calculated using the mean $L_K/L_V = 3.4$ of the ETGs in this sample. When comparing observed and model temperature values at fixed L_K, the mass is the same for all the models, and it should be roughly so also for the observed ETGs. At fixed L_K, then, the T_* variation due to shape and stellar streaming is obtained from all the T_* values of the descendants of a progenitor (we consider the Einasto models of Fig. 4.3), regardless of the FO or EO view. When comparing observed and model temperatures as a function of σ_{e8} instead, at any σ_{e8} the mass could be different. Figure 4.5 shows again how the effect of rotation can be potentially stronger than that of shape (as already indicated by Fig. 4.3): moderately larger or smaller T_* can be produced by flattening, depending on the way it is realised, while T_* can be much lowered by galactic rotation. Thus, at fixed L_K, the largest variation in T_* with respect to the spherical case (yellow line) does not come from a variation of shape, but is a decrease of T_* due to rotation with $\alpha = 1$ (no thermalisation).

In Fig. 4.5 all T_X are larger than T_*, yet much closer to T_* than to $T_{inj} \sim 1.5-2$ keV (see Fig. 4.4). This may be evidence of two facts: either the SNIa thermalisation η is low, or the gas flows establish themselves at a temperature close to the virial temperature[3] of the galaxy, and most of the SNIa input is spent in cooling (in gas-rich ETGs), or in lifting the gas from the potential well, and imparting bulk velocity to the outflowing gas (in gas-poorer ETGs; see Pellegrini (2011) for a quantification of these effects, and Tang et al. 2009 and Li et al. 2011a for addressing also other solutions to this problem). A combination of the two explanations may also be at place, of course. In any case, the proximity of the observed T_X values to T_* provides an empirical evidence of the importance of the study of T_* and its variations; it would not have been so, if we had found T_X to be closer to T_{inj}.

Going now into the question of whether possible effects from shape and stellar streaming are apparent on T_X, Fig. 4.5 shows a mild indication that flatter shapes and more rotationally supported ETGs tend to show a lower T_X, with respect to rounder, less rotating ETGs. This is similar to the recent result by Sarzi et al. (2013), that fast rotators seem to be confined to lower temperatures than slow rotators. Sarzi et al. (2013) suggested that in ETGs with a larger degree of rotational support, the kinetic energy associated with the stellar ordered motions may be thermalised less efficiently. As we will see in Section 4.6.2, results of hydrodynamical simulations indicate that this is the case (Negri et al. 2013, 2014a,b), but it is not the main reason for the lower observed temperatures.

We now move to consider possible effects of shape and rotation on the gas con-

[3]The integrals in the definitions of T_σ and T_{rot} (Eqs. 3 and 4) are also used to compute the total kinetic energy of the stellar motions that enters the virial theorem for the stellar component; thus the mass weighted temperature T_*, with $\gamma_{th} = 1$, is often referred to as the gas virial temperature.

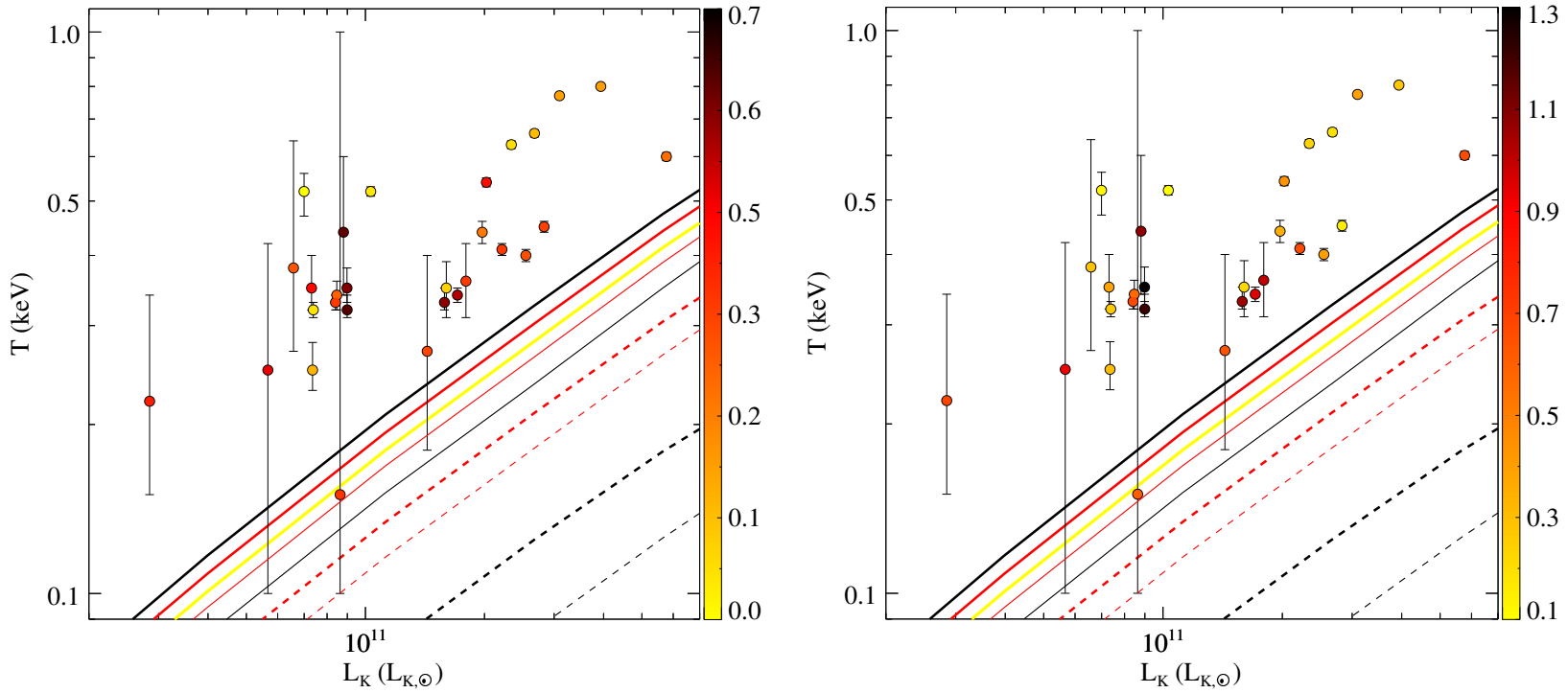

Figure 4.5: T_* (lines) for all the progenitors in Tab. 4.1 with the Einasto halo, and their descendants (with $\alpha = 0$ or $\alpha = 1$), and the observed T_X (circles), for the ETGs in the Boroson et al. (2011) sample, as a function of L_K. The yellow line refers to the progenitor ETGs, the red lines to the E4 shape, the black ones to the E7 shape; lines are solid for $k = 0$, and dashed for $k = 1$ and $\alpha = 1$. For each colour, lines representing the case of $k = 1$ and $\alpha = 0$ are coincident with the solid lines. Thick and thin lines refer to the FO and EO-built models, respectively. Left panel: the colour-coding for the observed ETGs indicates their ellipticity $\epsilon = 1 - q$, as measured in the Ks-band, from 2MASS (see Tab. 4.3), and is calibrated as for the previous figures [i.e., to be yellow for the E0 ($q = 1, \epsilon = 0$), red for the E4 ($q = 0.6, \epsilon = 0.4$), and black for the E7 ($q = 0.3, \epsilon = 0.7$); see the colour bar on the right for the ϵ of the other colours]. Right panel: the colour-coding indicates the rotational support V_{max}/σ_{e8}. Note that, for an EO view, the models of the dashed lines would have $V_{max}/\sigma_{e8} = 0.90 - 0.95$ for the E4 case, and $V_{max}/\sigma_{e8} = 1.5 - 1.6$ for the E7 case.

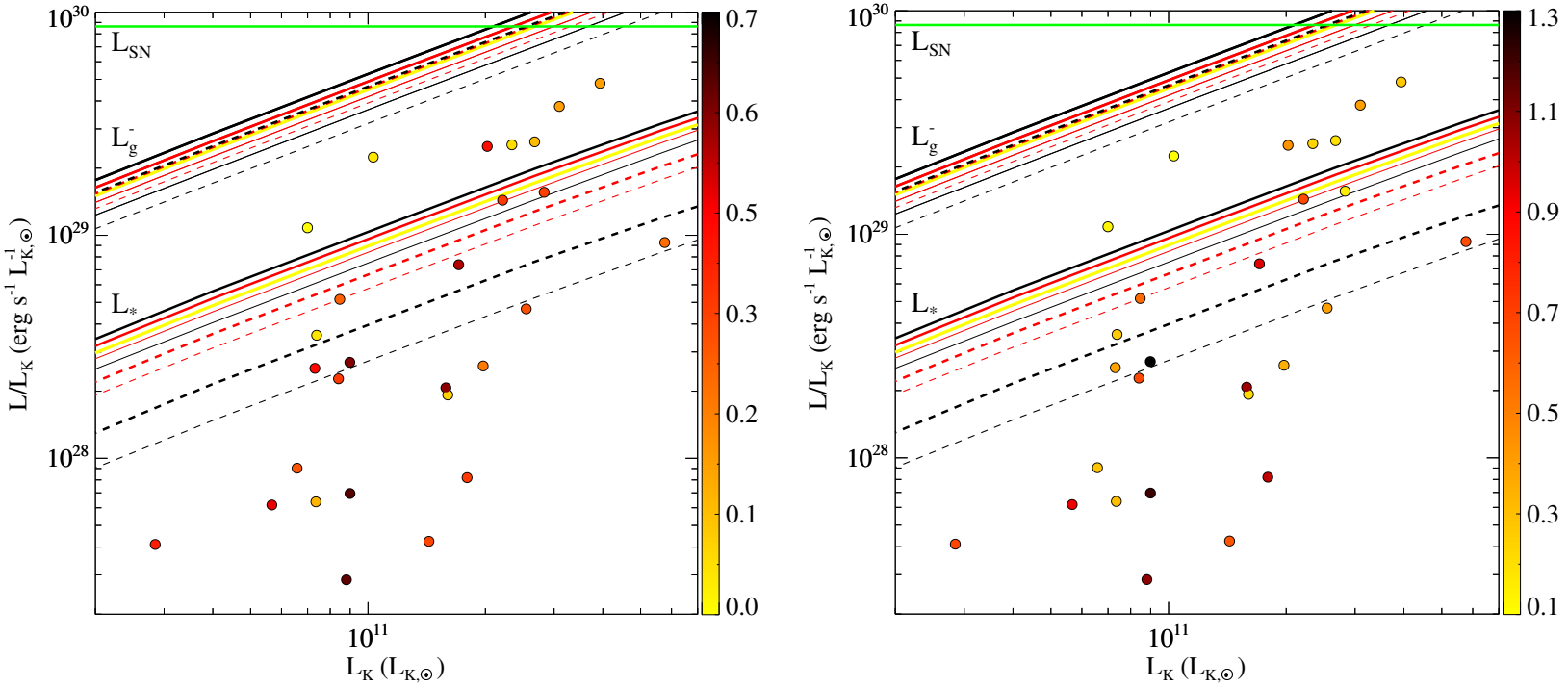

Figure 4.6: Comparison between the run of various luminosities vs. $L_{\rm K}$, for all the progenitors in Tab. 4.1 (Einasto halo case) and a selection of their descendants (only cases of $\alpha = 0, 1$), and for the observed $L_{\rm X}$ for the ETGs in the Boroson et al. (2011) sample; all quantities are normalised to $L_{\rm K}$. The lower group of lines gives $L_*/L_{\rm K}$, the upper one gives $L_{\rm g}^-/L_{\rm K}$, the horizontal line is $L_{\rm SN}/L_{\rm K}$ for $\eta = 0.85$. The yellow line refers to the progenitor ETGs, the red lines to the E4 shape, the black ones to the E7 shape; lines are solid for $k = 0$, and dashed for $k = 1$ and $\alpha = 1$, respectively. Thick and thin lines refer to the FO and EO-built models, respectively. The colour-coding for the observed ETGs indicates their ellipticity $\epsilon = 1 - q$ (left panel) and the rotational support $V_{\rm max}/\sigma_{\rm e8}$ (right panel), and is calibrated as for the previous Fig. 4.5.

tent, starting from the hypothesis that it is linked to the relative size of $T_{\rm g}^-$ and $T_{\rm inj}$. Figure 4.6 shows the observed $L_{\rm X}$ values, together with the energies (referring to the mass of gas injected in the unit time) describing the stellar heating L_*, the SNIa heating $L_{\rm SN}$, and the requirement for escape $L_{\rm g}^-$. All quantities are normalised to $L_{\rm K}$, and are computed using the expression for the stellar mass loss rate $\dot{M}_*$ and the temperatures defined in Section 4.3, such that $L_{\rm g}^- = \dot{M}_* E_{\rm g}^- = 3k_{\rm B}\dot{M}_* T_{\rm g}^-/(2\mu m_{\rm P})$, $L_* = 3k_{\rm B}\dot{M}_* T_*/(2\mu m_{\rm P})$, and $L_{\rm SN} = \eta E_{\rm SN} R_{\rm SN}$. Figure 4.6 clearly shows that flatter and more rotationally supported ETGs tend to have a lower $L_{\rm X}/L_{\rm K}$, as already known (see Section 4.1). As shown in Section 4.4.1, however, the effect of shape or rotation on $L_{\rm g}^-$ is small, so we cannot claim an important *direct* role for these two major galactic properties on determining a lower gas content and then $L_{\rm X}$. It has been suggested that a possible *indirect* effect could come from galactic rotation if it is effective in creating a gas disc, where gas cooling is triggered, the temperature is lowered, and then $L_{\rm X}$ is reduced (Brighenti & Mathews 1997). Other possibilities may be related to global instabilities of rotating flows, perhaps associated with inefficient thermalisation (Negri et al. 2014a). Note that the X-ray emissivity is also dependent on the gas temperature, and one could think that the lower $L_{\rm X}$ of flat/rotating ETGs could be due to having these preferentially a lower $T_{\rm X}$ (Fig. 4.5). This cannot be the explanation, though, because the emissivity in the 0.3-8 keV band decreases very mildly with decreasing temperature, for temperatures below a value of ~ 1 keV. Another explanation for a lower $L_{\rm X}/L_{\rm K}$ could be a lower stellar age in fast rotators: indeed, Sarzi et al. (2013) found that molecular gas and young stellar populations are detected only in fast rotators across the entire ATLAS$^{\rm 3D}$ sample, and a younger age is known to be linked to a lower $L_{\rm X}$ (Boroson et al. 2011, O'Sullivan et al. 2001). However, as we will see in detail in Section 4.6.4, the main reason for the X-ray under-luminosity of flat and rotating galaxies is related to galaxy rotation and angular momentum conservation, which make the hot gas settle in a particular configuration, and eventually lead to a lower value of $L_{\rm X}$ with respect to non-rotating galaxies.

Also, note in Fig. 4.6 how there are many ETGs with $L_{\rm X}$ lower than L_*: they do not even radiate L_*. For them, the outflow must be very important, and must have employed almost all of $L_{\rm SN}$. Numerical simulations (Ciotti et al. 1991) have already shown that $L_{\rm X}$ can be even lower than L_* during winds/outflows. Finally, as $L_{\rm g}^-$ increases and becomes closer to $L_{\rm SN}$, the ETGs below L_* disappear.

4.5 The simulations

We now move the second part of our investigation, based on hydrodynamical simulations. The theoretical analysis presented so far, indeed, can take into account neither the hydrodynamical effects due to the temporal evolution of the mass, momentum and energy sources (e.g., stellar winds and SNIa explosions), nor the ISM radiative cooling, so that hydrodynamical simulations are needed. The simulations presented in this Chapter are the result of a joint research collaboration (Negri 2014). Whilst the accurate description of the technical aspects of the numerical code ZEUS-MP2 (Stone & Norman 1992), used to run the simulations, and the specific results of the simulations are presented in Negri (2014), here we focus on the results, obtained

in the joint paper Negri et al. (2014b), that are relevant for the present study. In particular, these hydrodynamical simulations have been realised thanks to the development of our Jeans solver code (Posacki et al. 2013b), by means of which we have built the galaxy models, and all the dynamical fields necessary for the hydrodynamical equations (see Chapter 2 and Appendix B for further details). In this way, the results obtained from the simulations performed in these galaxy models are the exact numerical counterpart of the theoretical study presented in the previous Sections.

4.5.1 The galaxy models

For the simulations we built axisymmetric two-component galaxy models analogous to the ones previously analysed and described in Section 4.2. Thus, the stellar component is described by the deprojection (Mellier & Mathez 1987) of the de Vaucouleurs (1948) law, generalized for ellipsoidal axisymmetric distributions (Eqs. 4.1 and 4.2), and we restrict to the same q values of (1, 0.6, 0.3), corresponding to E0, E4 and E7 galaxies when seen edge-on. For the DM halo we adopt the NFW (Navarro et al. 1997) or the Einasto (1965) profiles.

All models belong to two different *sets*, defined by the specific profile of the DM halo. The first set is characterized by the untruncated NFW profile (Eqs. 4.8 - 4.10), while the models in the second set are embedded in the Einasto profile (Eqs. 4.4 - 4.6). In each of the two sets, we consider different *families* of models, built following the procedure described in Sections 4.2.3 and 4.2.4. Here we just recall the main steps. Each family is associated with a spherical galaxy, that we call the "progenitor". The progenitor structural parameters are determined by assigning $\sigma_{\rm e8}$ (the aperture luminosity-weighted velocity dispersion within $R_{\rm e}/8$), and then deriving the luminosity and effective radius $R_{\rm e}$ of the galaxy from the scaling laws cited above. Then, from a chosen stellar mass-to-light ratio, the stellar mass M_* is derived. Finally, the parameters of the DM halo are determined in order to reproduce the assumed $\sigma_{\rm e8}$ and fixing $M_{\rm h}/M_* \simeq 20$ (Behroozi et al. 2013). In the NFW set, these constraints produce $r_{\rm h} \simeq 2R_{\rm e}$, $22 \lesssim c \lesssim 37$, and a DM fraction $f_{\rm DM}$ within a sphere of radius $R_{\rm e}$ of $\simeq 0.6$ for the spherical progenitors. For the Einasto set we fix $n = 6$, and we find that $r_{\rm h} \simeq 20R_{\rm e}$, and $f_{\rm DM} \simeq 0.56$ for the spherical progenitor.

In each of the two sets we considered three values of $\sigma_{\rm e8}$ for the spherical progenitors, i.e., 200, 250 and 300 km s^{-1}. Therefore, each of the two sets is made of 3 families of models, for a total of 6 spherical progenitors. Table 4.4 lists all the relevant parameters characterizing the progenitors galaxy models for both sets. The flattened descendants of each progenitor with intrinsic flattening of E4 ($q = 0.6$) and E7 ($q = 0.3$), are derived as follows. We produce two flattened models for each value of q. The first flattened model is called "face-on built" (FO-built), since, when observed face-on, its $R_{\rm e}$ is the same as that of the spherical progenitor; this requires FO-built flattened models to be more and more concentrated as q decreases ($\rho_* \propto q^{-1}$). The second flattened model instead, when seen edge-on, has the same circularized $R_{\rm e}$ of the spherical progenitor, thus we call it "edge-on built" (EO-built); this property makes the EO-built models expand with decreasing q ($\rho_* \propto \sqrt{q}$). Therefore, a spherical progenitor with a given value of $\sigma_{\rm e8}$ produces four flat galaxies: two E4 models (FO and EO built), and two E7 models (FO and EO built). As a further

Table 4.4: Fundamental galaxy parameters for the NFW and Einasto sets of models.

Name	$L_{\rm B}$	$R_{\rm e}$	M_*	$M_{\rm h}$	$\sigma_{\rm e8}^{\rm NFW}$	$\sigma_{\rm e8}^{\rm EIN}$	$f_{\rm DM}^{\rm NFW}$	$f_{\rm DM}^{\rm EIN}$	c
	$(10^{11}L_{\rm B\odot})$	(kpc)	$(10^{11}M_\odot)$	$(10^{11}M_\odot)$	(km s^{-1})	(km s^{-1})			
(1)	(2)	(3)	(4)	(5)	(6)	(7)	(8)	(9)	(10)
$\rm E0^{200}$	0.27	4.09	1.25	25	200	200	0.61	0.57	37
$\rm EO4_{IS}^{200}$	0.27	4.09	1.25	25	166	166	0.63	0.59	37
$\rm EO4_{VD}^{200}$	0.27	4.09	1.25	25	179	179	0.63	0.59	37
$\rm EO7_{IS}^{200}$	0.27	4.09	1.25	25	124	124	0.66	0.62	37
$\rm EO7_{VD}^{200}$	0.27	4.09	1.25	25	148	149	0.66	0.62	37
$\rm FO4_{IS}^{200}$	0.27	4.09	1.25	25	178	179	0.59	0.55	37
$\rm FO4_{VD}^{200}$	0.27	4.09	1.25	25	191	192	0.59	0.55	37
$\rm FO7_{IS}^{200}$	0.27	4.09	1.25	25	150	151	0.57	0.53	37
$\rm FO7_{VD}^{200}$	0.27	4.09	1.25	25	178	179	0.57	0.53	37
$\rm E0^{250}$	0.65	7.04	3.35	67	250	250	0.59	0.55	28
$\rm EO4_{IS}^{250}$	0.65	7.04	3.35	67	207	208	0.62	0.57	28
$\rm EO4_{VD}^{250}$	0.65	7.04	3.35	67	223	224	0.62	0.57	28
$\rm EO7_{IS}^{250}$	0.65	7.04	3.35	67	154	155	0.66	0.61	28
$\rm EO7_{VD}^{250}$	0.65	7.04	3.35	67	184	185	0.66	0.61	28
$\rm FO4_{IS}^{250}$	0.65	7.04	3.35	67	223	224	0.57	0.53	28
$\rm FO4_{VD}^{250}$	0.65	7.04	3.35	67	240	241	0.57	0.53	28
$\rm FO7_{IS}^{250}$	0.65	7.04	3.35	67	189	190	0.56	0.51	28

Table 4.4 – *continued*

Name	$L_{\rm B}$	$R_{\rm e}$	M_*	$M_{\rm h}$	$\sigma_{\rm e8}^{\rm NFW}$	$\sigma_{\rm e8}^{\rm EIN}$	$f_{\rm DM}^{\rm NFW}$	$f_{\rm DM}^{\rm EIN}$	c
	$(10^{11}L_{\rm B\,\odot})$	(kpc)	$(10^{11}M_\odot)$	$(10^{11}M_\odot)$	(km s^{-1})	(km s^{-1})			
(1)	(2)	(3)	(4)	(5)	(6)	(7)	(8)	(9)	(10)
$\rm FO7_{VD}^{250}$	0.65	7.04	3.35	67	223	224	0.56	0.51	28
$\rm E0^{300}$	1.38	11.79	7.80	160	300	300	0.62	0.57	22
$\rm EO4_{IS}^{300}$	1.38	11.79	7.80	160	248	249	0.64	0.60	22
$\rm EO4_{VD}^{300}$	1.38	11.79	7.80	160	267	269	0.64	0.60	22
$\rm EO7_{IS}^{300}$	1.38	11.79	7.80	160	185	185	0.68	0.64	22
$\rm EO7_{VD}^{300}$	1.38	11.79	7.80	160	221	223	0.68	0.64	22
$\rm FO4_{IS}^{300}$	1.38	11.79	7.80	160	266	268	0.60	0.55	22
$\rm FO4_{VD}^{300}$	1.38	11.79	7.80	160	286	288	0.60	0.55	22
$\rm FO7_{IS}^{300}$	1.38	11.79	7.80	160	224	225	0.59	0.54	22
$\rm FO7_{VD}^{300}$	1.38	11.79	7.80	160	265	267	0.59	0.54	22

Notes: (1) Model name: E0 identifies the spherical progenitor, and the superscript is the value of $\sigma_{\rm e8}$. For the other models, the nomenclature is as follows: for example, $\rm FO4_{IS}^{200}$ means a face-on flattened E4 galaxy, obtained from the $\rm E0^{200}$ progenitor, with isotropic rotation. (2) Luminosities in the B band. (3) Effective radius (for a FO view for FO-built models, and an EO view for EO-built models). For FO-built models, the edge-on effective radius is reduced by a factor $\sqrt{q}$ (Section 4.5.1). (4) Total stellar mass. (5) Total DM mass. (6) – (7) Stellar velocity dispersion, as the luminosity-weighted average within a circular aperture of radius $R_{\rm e}/8$, for the NFW and Einasto sets, respectively; for non-spherical models, $\sigma_{\rm e8}$ is the edge-on viewed value. (8) – (9) DM fraction enclosed within a sphere of radius $R_{\rm e}$ for the NFW and Einasto sets, respectively. (10) Concentration parameter for the NFW set.

step, in order to study the effects of galaxy rotation, we assume two kinematical supports for each flattened system: one corresponding to a velocity dispersion supported galaxy (VD models), and the other one to an isotropic rotator (IS models). These two configurations are obtained by setting the Satoh parameter k equal to 0 and 1, respectively (see Eqs. 2.3 and 2.4). In the flattening procedure the DM halo is maintained fixed to that of the progenitor. Note that our flattened models are representative of ETGs since they are consistent with their observed properties. We indeed checked for models lying outside the observed scatter of the scaling laws, but our adopted flattening procedure is quite robust in producing acceptable models, so that we retained all of them.

Summarizing, from each spherical progenitor of given $\sigma_{\rm e8}$, eight flattened models are obtained (see Tab. 4.4), and we refer to this group of nine galaxy models as to a family. All models belonging to a family can be identified either by the $\sigma_{\rm e8}$ value of the spherical progenitor, or by their stellar mass M_* (or B luminosity), or DM halo mass; note however that while these last three quantities are kept constant within a family, the $\sigma_{\rm e8}$ of the descendants varies. Indeed, the modification of stellar structure involves a change in the stellar kinematics, and so in the value of $\sigma_{\rm e8}$; in particular, for our models $\sigma_{\rm e8}$ decreases for increasing flattening (see Section 4.2.4 for a comprehensive discussion). Note that $\sigma_{\rm e8}$ depends on the line-of-sight direction for non-spherical models; when quoting $\sigma_{\rm e8}$ for the latter models, in the following, we refer to the edge-on projection.

4.5.2 The contribution of stellar kinematics to the ISM energetics

When studying the effect of flattening and ordered rotation on the hot ISM temperature and content, analytical studies based on global energetics arguments, such as the one presented in the first part of this Chapter (see also Ciotti & Pellegrini 1996, Pellegrini 2011, Posacki et al. 2013b), showed that different and competitive effects should be taken into account. Some of the expectations have been confirmed by past numerical studies, even though the galaxy models adopted were not tailored on realistic elliptical galaxies, but more on S0/Sa (D'Ercole & Ciotti 1998; Negri et al. 2014a). In any case, such studies showed that different physical phenomena can be important as a function of the galaxy mass and potential well depth (i.e., whether the ISM is outflowing or inflowing).

In order to compare the results of the numerical simulations with the global energetic estimates, the following quantities are also computed by the hydrodynamical code. The first is the thermalisation of stellar random motions, providing an energy input per unit time to the ISM of

$$L_\sigma \equiv \frac{1}{2}\int \dot\rho\, \mathrm{Tr}(\boldsymbol{\sigma}^2)\, \mathrm{d}V. \tag{4.24}$$

Note that while the contribution from stellar random motions is fully independent of the ISM velocity field (see Eq. (B.3)), the thermalisation of the stellar ordered (streaming) motion depends on the relative motion between stars ($\mathbf{v}$) and ISM ($\boldsymbol{u}$)

$$\begin{aligned} L_{\rm v} &\equiv \frac{1}{2}\int \dot\rho\, \|\mathbf{v}-\boldsymbol{u}\|^2\, \mathrm{d}V \\ &= \frac{1}{2}\int \dot\rho (u_R^2+u_z^2)\, \mathrm{d}V + \frac{1}{2}\int \dot\rho (\overline{v}_\varphi - u_\varphi)^2\, \mathrm{d}V = L_{\rm m} + L_\varphi, \end{aligned} \tag{4.25}$$

so that, at variance with L_σ, it cannot be predicted a priori from the knowledge of the galaxy structure and kinematics. We recall that in our galaxy models $\mathbf{v} = \overline{v}_\varphi \mathbf{e}_\varphi$, and L_m and L_φ are respectively the energy input rate due to the ISM velocity in the meridional plane (R, z), and to the *relative* velocity of stars and the ISM in the azimuthal direction.

As in Section 4.3.1, we parametrize the thermalised fraction of the available kinetic energy due to stellar streaming with

$$\gamma_\mathrm{th} \equiv \frac{L_\mathrm{v}}{L_\mathrm{rot}}, \tag{4.26}$$

where

$$L_\mathrm{rot} \equiv \frac{1}{2} \int \dot{\rho} \, \|\mathbf{v}\|^2 \, \mathrm{d}V \tag{4.27}$$

is the energy input per unit time that would be injected in a galaxy with an ISM at rest (i.e., $\boldsymbol{u} = 0$), due to thermalisation stellar streaming motions. Note that Eq. (4.26) is equivalent to Eq. (4.17). Note also that γ_th is undefined (formally, it diverges) for VD supported models, and can be very large for slow rotators and/or for gas flows with large velocities in the meridional plane (as in the case of galactic winds). Using these definitions, the total energy supplied to the ISM due to stellar motions can be written as

$$L_* \equiv L_\sigma + L_\mathrm{v} = L_\sigma + \gamma_\mathrm{th} L_\mathrm{rot}. \tag{4.28}$$

All the luminosities defined above can be converted into the equivalent temperatures T_σ and T_rot, already defined in Section 4.3 (see Eqs. 4.15 and 4.16) and computable a priori, with the addition of two new temperatures, T_m and T_φ, which can be computed only from the output of the simulations. These temperatures are related by the following relations

$$T_* = T_\sigma + \gamma_\mathrm{th} T_\mathrm{rot}; \quad \gamma_\mathrm{th} T_\mathrm{rot} = T_\mathrm{m} + T_\varphi. \tag{4.29}$$

Finally and most importantly, from the simulations output we calculate the X-ray emission in the 0.3–8 keV *Chandra* band

$$L_\mathrm{X} = \int \varepsilon_\mathrm{X} dV, \tag{4.30}$$

and the X-ray emission weighted temperature as

$$T_\mathrm{X} = \frac{\int T \varepsilon_\mathrm{X} dV}{L_\mathrm{X}}, \tag{4.31}$$

where ε_X is the thermal emissivity in the energy range 0.3–8 keV of a hot, collisionally ionized plasma, obtained by the spectral fitting package XSPEC[4] (spectral model APEC, Smith et al. 2001), and the volume integrals are performed over the whole computational mesh. We recall that ε_X scales proportionally to the second power of the ISM density and is almost independent of the ISM temperature in the 0.3–8 keV energy range.

[4] http://heasarc.nasa.gov/xanadu/xspec/.

4.6 Results

While the hydrodynamical evolution of the simulations does not concern the scope of the present thesis and is accurately described in Negri et al. (2014b), here we just present the main differences between the hydrodynamical evolutions of representative VD and IS models, which are necessary for the understanding and the explanation of the results we found about the thermalisation parameter $\gamma_{\rm th}$, and the global properties $T_{\rm X}$ and $L_{\rm X}$ of the models. The final properties of all models, obtained at $t = 13$ Gyr, are given in Tables 4.5 and 4.6.

4.6.1 Hydrodynamics

The hydrodynamical evolution of the majority of the models can be summarized by describing three representative models. Here, without loss of generality, we choose three models of the EO-built sub-family with $\sigma_{\rm e8} = 250$ km s^{-1} of the NFW set: the spherical progenitor (E0^{250}), and its two more flattened descendants, i.e. the velocity dispersion supported E7 model (EO7$^{250}_{\rm VD}$), and the corresponding E7 isotropic rotator (EO7$^{250}_{\rm IS}$). For a detailed description of the hydrodynamical evolution of all models see Negri et al. (2014b); Negri (2014).

All the ISM physical quantities of the E0^{250} model evolve while being stratified on a spherical shape, as a consequence of the galaxy spherical symmetry. Shortly after the beginning of the simulation, a decoupled flow is established ($t \simeq 2.4$ Gyr), with an inflow in a round central region surrounded by an outflowing atmosphere. In the inflow region cold gas accumulates, due to the lack of rotational support, and form a cold core at the very centre. As time increases both the inflow and the outflow regions decrease, leading to the formation of a hot atmosphere approximately isothermal ($T \simeq 9 \times 10^6$ K) in nearly hydrostatic equilibrium. As a consequence, $T_{\rm X}$ steadily increases in pace with the time evolution of mass sources and specific heating (Fig. 4.7, solid green line) and reaches the maximum value for the whole sub-family.

The ISM evolution of the velocity dispersion supported EO7$^{250}_{\rm VD}$ model presents important similarities with the spherical progenitor. This is due to the absence of angular momentum, and to the fact that the weight of the spherical DM halo makes the total gravitational potential much rounder than the associated stellar density distribution. Therefore, the major differences between the E0^{250} progenitor and the EO7$^{250}_{\rm VD}$ model are the different spatial regions where the gas is injected, and the different velocity dispersion field of the stars. In particular, the edge-on flattening makes the stellar gravitational potential to become shallower, so that the stellar motions (and the relative heating) are lower with respect to the progenitor. Even in this case, at early times the flow is kinematically decoupled, with an equatorial outflow due to the concentrated heating on the equatorial plane, and a polar accretion along the z-axis. As in the spherical progenitor, a dense, cold core forms in the galaxy centre, surrounded by a hot atmosphere ($T \simeq 5 \times 10^6$ K). However, due to the weaker gravitational field, the EO7$^{250}_{\rm VD}$ model loses more gas and retains a less dense hot atmosphere with respect to the spherical progenitor (Fig. 4.8, black solid line), resulting in a lower $T_{\rm X}$ (Fig. 4.7, black solid line). Note that the lower heating due to the lower stellar motions partially contributes to the lowering of $T_{\rm X}$, so that

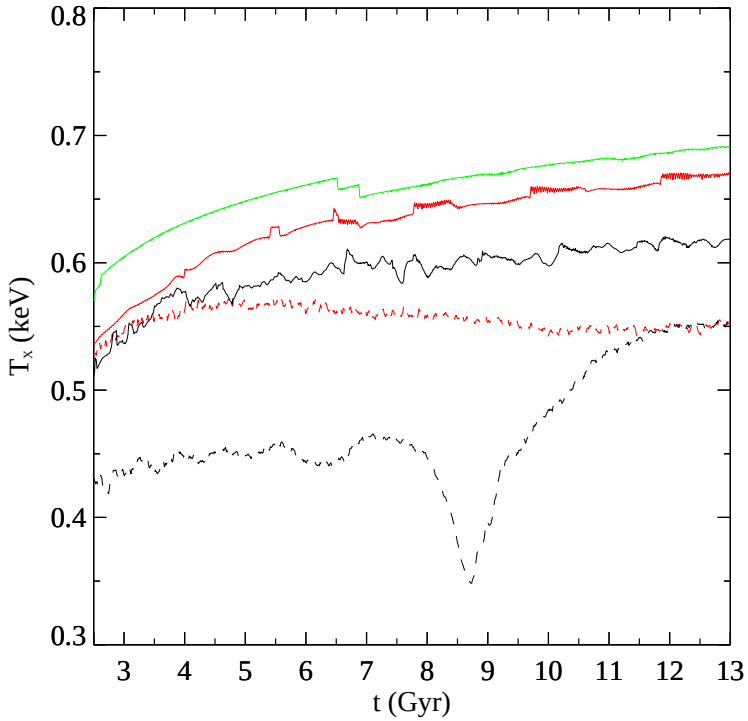

Figure 4.7: Time evolution of the X-ray luminosity $L_{\rm X}$ and X-ray emission weighted temperature $T_{\rm X}$ for the sub-family derived from the E0^{250} model with the NFW halo. The red and black lines report the evolution of the VD models (solid), and of the IS models (dashed). The colours map the flattening: green, red and black correspond to the E0, E4 and E7 galaxies, respectively.

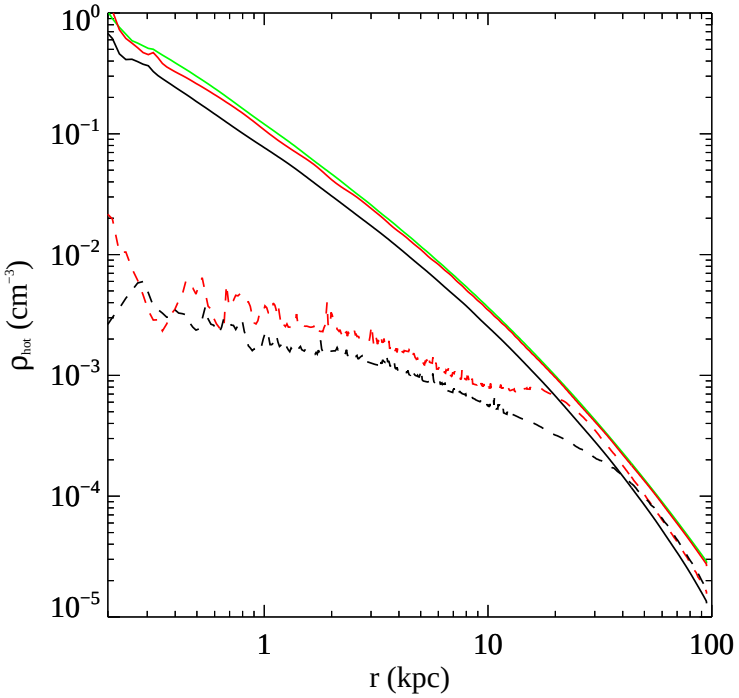

Figure 4.8: Angle-averaged profile of the hot ISM density at $t = 13$ Gyr for the same models as in Fig. 4.7. Solid lines refer to VD models, dashed lines refer to IS models.

it is a consequence of both hydrodynamical and energetic effects (see Sections 4.6.2 and 4.6.3 for a detailed discussion).

The main characteristic of the isotropic rotator $EO7^{250}_{IS}$ model is the formation, due to angular momentum conservation, of a rotationally supported, thin and dense cold disc, which grows in size during galaxy evolution, reaching a final size of $\simeq$ 10 kpc. The disc increases its mass due to the cooling ISM in the central regions that collapses onto it. In this way a hot and low-density region forms above and below the disc that cannot be replenished by the inflowing gas, which is supported by angular momentum. This hot and rarefied zone secularly increases in size along with the cold disc, due to the combination of the centrifugal barrier, that keeps the centre at low density, and the secular increase of the specific heating, which produces the growth of the heating region, roughly extending as the cold thin disc. As a consequence, T_X is the lowest of the three models $E0^{250}$, $EO7^{250}_{VD}$ and $EO7^{250}_{IS}$ (Fig. 4.7, black dashed line), since the galaxy regions which more contribute to computation of T_X (see Eq. 4.31) are the external ones, where the ISM is denser but at a lower temperature. A further marginal contribution to the lowering of T_X comes from the lower heating associated with stellar motions (see Sections 4.6.2 and 4.6.3). Besides the formation of the cold disc, another important difference between $EO7^{250}_{IS}$ and $EO7^{250}_{VD}$ concerns the ISM kinematics outside the equatorial plane. In the case of the $EO7^{250}_{IS}$ galaxy model, starting from $t \simeq 8$ Gyr the meridional velocity field develops a very complex pattern of vortexes above and below the equatorial plane. These vortexes contribute to the ISM heating in a way proportional to T_m

(see Table 4.5). The cold mass accreted at the centre is now much smaller than in the previous two models, but a similar amount is distributed in the cold disc.

As mentioned above, the evolutions of the three models described so far are representative of the majority of the models, so that, for example, the less flattened $\mathrm{EO4}^{250}_{\mathrm{VD}}$ and $\mathrm{EO4}^{250}_{\mathrm{IS}}$ models behave analogously, even if less prominently due to the milder flattening.

The main features of the family with the spherical progenitor of $\sigma_{\mathrm{e8}} = 250$ km s^{-1} are maintained in the $\sigma_{\mathrm{e8}} = 300$ km s^{-1} family. In particular, independently of the DM halo profile, increasing σ_{e8}, T_{X} increases. This is expected because more massive models can retain more and hotter gas independently of the flattening and kinematical support. In more massive models T_{X} is less fluctuating with time, the outflow velocities of the galaxy outskirts are lower, and the complicated meridional circulation in the rotating models is reduced.

The situation is quite different for the families with low mass progenitors ($\sigma_{\mathrm{e8}} = 200$ km s^{-1}). These are the only cases where a transition to a global wind can be induced by a change of shape or by rotation, in accordance with the energetic analysis of Section 4.4 (see also Ciotti & Pellegrini 1996; Posacki et al. 2013b). This is especially true for the less concentrated Einasto models. In these global wind cases, T_{X} keeps larger than expected from the trend defined by non-wind models due to the reduced cooling, and to the thermalisation of the meridional motions (see Section 4.6.3 for a detailed discussion).

The sensitivity of the flow phase for low-mass models near the transition to the outflow is shown for example by the $\mathrm{EO7}^{200}_{\mathrm{VD}}$ model with the NFW halo, that experiences two quite distinct evolutionary phases. At the beginning, a significant equatorial degassing is apparent, coincident with the strong heating in that region. As time increases, the velocity field in the outflow region decreases and gas cooling becomes more and more important. However, after $\simeq 9$ Gyr, the secular increase of the specific heating, coupled with the shallow potential well, induces again higher and higher velocities and the gas temperature increases again. Its associated counterpart, the $\mathrm{EO7}^{200}_{\mathrm{IS}}$ model, is instead in a permanent wind phase from the beginning, thus showing the additional effect of rotation in flattened, low-mass galaxies.

4.6.2 The thermalisation parameter

Thanks to the hydrodynamical simulations it is possible to compute the thermalisation parameter γ_{th}, defined in Sections 4.3 and 4.5.2 (Posacki et al. 2013b), for which only reasonably assumed values have been possible to adopt in the theoretical analysis of Section 4.4. This is a global parameter that helps to quantify the heating of the ISM due to stellar ordered motions (see Appendix B). From Eqs. (4.25)-(4.27) it is easy to see that, in principle, γ_{th} can attain large values, even larger than unity, if the gas meridional motions are important, since the stellar streaming motions are only in the azimuthal direction. Thus, in this case, it is useful to define the azimuthal thermalisation parameter as $\gamma^{\varphi}_{\mathrm{th}} \equiv L_{\varphi}/L_{\mathrm{rot}}$, which is able to properly quantify the net effect of heating due to stellar streaming. Note that, in the analysis of Section 4.4, the possible presence of ISM meridional motions could not be taken into account without arbitrary assumptions, so that $\gamma_{\mathrm{th}} = \gamma^{\varphi}_{\mathrm{th}} \leqslant 1$.

For all galaxy models we find that $\gamma^{\varphi}_{\mathrm{th}}$ is small ($\gamma^{\varphi}_{\mathrm{th}} \simeq 0.05 - 0.28$, except for

one case with $\gamma_{\rm th}^{\varphi} = 0.37$, see Tables 4.5 and 4.6), with a mild trend for lower values of $\gamma_{\rm th}^{\varphi}$ in high-$\sigma_{\rm e8}$ galaxies, implying that the ISM almost co-rotates with the stellar population everywhere. This supports the adequacy of the low $\gamma_{\rm th}$ values ($\gamma_{\rm th} = 0; 0.25$) adopted in the theoretical analysis of Section 4.4. We also find that $\gamma_{\rm th} \simeq \gamma_{\rm th}^{\varphi}$ for medium-high mass galaxy models (i.e., with progenitors of $\sigma_{\rm e} = 250 - 300\,{\rm km\ s^{-1}}$), reflecting the fact that there are not significant ISM velocities in the meridional plane (i.e., $T_{\rm m}$ is very low). In low-rotation, low-mass systems, instead, $\gamma_{\rm th}$ is fully dominated by high velocity galactic winds and exceeds unity, $T_{\rm m}$ becomes important, and so $\gamma_{\rm th} \gg \gamma_{\rm th}^{\varphi}$.

One could be tempted to interpret the lack of thermalisation of a significant fraction of ordered motions in all the IS models as the reason for the lower $T_{\rm X}$ of the IS models with respect to their VD counterparts (Fig. 4.7, black and red dashed lines vs. the solid lines). However, even if this effect certainly contributes, it is not the main reason for the lower $T_{\rm X}$ in rotating models. Indeed, we found that artificially adding the "missing" thermalisation to the equations of hydrodynamics in dedicated test simulations of rotating models leads only to a negligible increase in $T_{\rm X}$, showing that also other effects contribute to the low $T_{\rm X}$ (see Section 4.6.3).

4.6.3 The X-ray emission weighted temperature $T_{\rm X}$

We now move to describe the properties of the 0.3–8 keV luminosity weighted ISM temperature $T_{\rm X}$ for the whole set of galaxy models, as they would be observed at an age of 13 Gyr. The distribution of the $T_{\rm X}$ values for all models is given in Fig. 4.9, as a function of $\sigma_{\rm e8}$, $M_{\rm hot}$ and $L_{\rm B}$.

In general $T_{\rm X}$ increases with $\sigma_{\rm e8}$, a natural consequence of the deeper potential well associated with larger $\sigma_{\rm e8}$. This leads to faster stellar (random and ordered) velocities, with the consequent larger energy input from thermalisation of the stellar motions. In addition, in a deeper potential the hot gas is retained at a larger $T_{\rm X}$. The temperature range spanned by the models agrees well with that of real ETGs, and the observed trend of $T_{\rm X}$ with $\sigma_{\rm e8}$ is reproduced (e.g., see Fig. 6 in Boroson et al. 2011, who measured $T_{\rm X}$ of the pure gaseous component for a sample of 30 ETGs). At high $\sigma_{\rm e8}$, the observed $T_{\rm X}$ values span a narrower range than in our models, likely because the models include very flat and highly rotating ETGs that are missing in the observed sample. Interestingly, instead, the low-$\sigma_{\rm e8}$ end of the observed $T_{\rm X} - \sigma_{\rm e8}$ relation shows an increase of dispersion in the $T_{\rm X}$ values, and a hint for a flattening of the relation with respect to the trend shown at larger $\sigma_{\rm e8}$. These features are shown also by our models: at low $\sigma_{\rm e8}$ the trend of $T_{\rm X}$ flattens for NFW models, and the scatter around it increases considerably for the Einasto models.

This is explained by the transition to global winds in flattened and rotating low-mass galaxies (as discussed at the end of Section 4.6.1), which leads to a reduction in $L_{\rm X}$ and an increase of $T_{\rm X}$ with respect to the trend defined by more massive ETGs, or ETGs of similar mass but not in wind. The change in the relationship is due to the thermalisation of the resulting meridional flows (while the thermalisation of galaxy rotation remains negligible, see Section 4.6.2), and to the lower cooling. For example, the $\rm EO4^{200}_{VD}$ and $\rm EO4^{200}_{IS}$ models in the Einasto set, have high $T_{\rm X}$ as a consequence of the transition to the wind phase.

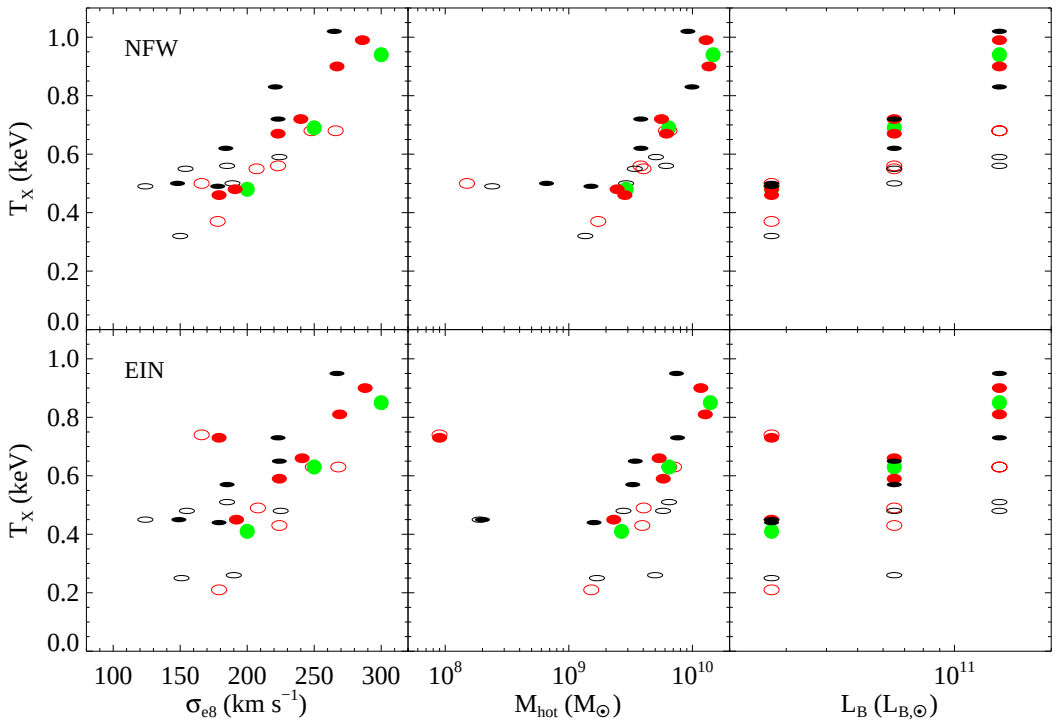

Figure 4.9: ISM emission weighted temperature $T_{\rm X}$ in the 0.3–8 keV band at 13 Gyr for all the models in the NFW (top panels) and in the Einasto (bottom panels) sets as a function of $\sigma_{\rm e8}$, of the hot ($T > 10^6$ K) ISM mass, and of the galaxy blue optical luminosity. Spherical progenitors (green circles) with $\sigma_{\rm e8} = (200, 250, 300)$ have been considered. The green, red and black colours refer to the E0, E4 and E7 models respectively. Filled and empty symbols indicate the fully velocity dispersion supported VD models, and the isotropic rotators IS models, respectively.

Table 4.5: Simulations results for the NFW set at $t = 13$ Gyr.

Name	$M_{\rm esc}$	$M_{\rm gas}$	$M_{\rm hot}$	$L_{\rm X}$	$T_{\rm X}$	T_*	T_σ	$T_{\rm v}$	$T_{\rm m}$	$\gamma_{\rm th}$	$\gamma_{\rm th}^{\varphi}$
	$(10^9 M_\odot)$	$(10^9 M_\odot)$	$(10^9 M_\odot)$	$(10^{40}$ erg s$^{-1})$	(keV)	(keV)	(keV)	(keV)	(keV)		
(1)	(2)	(3)	(4)	(5)	(6)	(7)	(8)	(9)	(10)	(11)	(12)
$\mathrm{E0}^{200}$	3.2	8.9	2.91	2.06	0.48	0.26	0.26	1.7E-3	1.7E-3	–	–
$\mathrm{EO4}^{200}_{\rm IS}$	9.8	2.4	0.15	8.29E-4	0.50	0.40	0.17	0.24	0.21	2.62	0.25
$\mathrm{EO4}^{200}_{\rm VD}$	4.5	7.5	2.84	1.99	0.46	0.26	0.26	1.5E-3	1.5E-3	–	–
$\mathrm{EO7}^{200}_{\rm IS}$	10.3	1.8	0.24	1.95E-3	0.49	0.29	0.08	0.22	0.18	1.24	0.22
$\mathrm{EO7}^{200}_{\rm VD}$	9.4	2.8	0.66	1.89E-2	0.50	0.33	0.25	7.8E-2	7.8E-2	–	–
$\mathrm{FO4}^{200}_{\rm IS}$	3.3	8.8	1.73	0.45	0.37	0.21	0.18	2.9E-2	9.0E-3	0.31	0.21
$\mathrm{FO4}^{200}_{\rm VD}$	2.9	9.2	2.46	2.21	0.48	0.27	0.27	3.7E-3	3.7E-3	–	–
$\mathrm{FO7}^{200}_{\rm IS}$	3.4	8.7	1.36	0.25	0.32	0.12	0.09	2.9E-2	1.1E-2	0.15	0.10
$\mathrm{FO7}^{200}_{\rm VD}$	4.0	8.1	1.51	1.82	0.49	0.28	0.28	2.0E-3	2.0E-3	–	–
$\mathrm{E0}^{250}$	5.1	27.5	6.43	11.1	0.69	0.42	0.42	1.2E-3	1.2E-3	–	–
$\mathrm{EO4}^{250}_{\rm IS}$	8.3	23.8	4.02	0.76	0.55	0.29	0.27	1.8E-2	3.1E-3	0.13	0.10
$\mathrm{EO4}^{250}_{\rm VD}$	6.9	25.2	6.17	9.50	0.67	0.42	0.41	1.5E-3	1.5E-3	–	–
$\mathrm{EO7}^{250}_{\rm IS}$	11.4	19.7	3.42	0.33	0.55	0.18	0.13	5.5E-2	4.9E-3	0.20	0.18
$\mathrm{EO7}^{250}_{\rm VD}$	12.5	18.7	3.83	4.87	0.62	0.41	0.40	1.8E-3	1.8E-3	–	–
$\mathrm{FO4}^{250}_{\rm IS}$	6.5	26.2	3.80	0.87	0.56	0.30	0.29	1.9E-2	3.9E-3	0.13	0.10
$\mathrm{FO4}^{250}_{\rm VD}$	5.2	27.4	5.62	11.1	0.72	0.43	0.43	1.6E-3	1.6E-3	–	–
$\mathrm{FO7}^{250}_{\rm IS}$	6.4	26.0	2.91	0.43	0.50	0.19	0.15	3.7E-2	7.9E-3	0.13	0.10

Table 4.5 – *continued*

Name	$M_{\rm esc}$	$M_{\rm gas}$	$M_{\rm hot}$	$L_{\rm X}$	$T_{\rm X}$	T_*	T_σ	$T_{\rm v}$	$T_{\rm m}$	$\gamma_{\rm th}$	$\gamma_{\rm th}^{\varphi}$
	$(10^9 M_\odot)$	$(10^9 M_\odot)$	$(10^9 M_\odot)$	$(10^{40}$ erg s$^{-1})$	(keV)	(keV)	(keV)	(keV)	(keV)		
(1)	(2)	(3)	(4)	(5)	(6)	(7)	(8)	(9)	(10)	(11)	(12)
$\rm FO7_{VD}^{250}$	7.4	25.3	3.82	10.3	0.72	0.45	0.45	1.7E-3	1.7E-3	–	–
$\rm E0^{300}$	7.6	64.7	14.70	43.3	0.94	0.65	0.65	1.0E-3	1.0E-3	–	–
$\rm EO4_{IS}^{300}$	14.1	56.0	6.52	1.34	0.68	0.43	0.42	1.5E-2	1.9E-3	0.07	0.06
$\rm EO4_{VD}^{300}$	10.5	59.9	13.61	37.7	0.90	0.63	0.63	1.2E-3	1.2E-3	–	–
$\rm EO7_{IS}^{300}$	15.9	50.2	6.13	1.04	0.56	0.23	0.20	2.3E-2	1.5E-3	0.06	0.05
$\rm EO7_{VD}^{300}$	17.8	48.8	9.92	25.0	0.83	0.62	0.62	1.2E-3	1.2E-3	–	–
$\rm FO4_{IS}^{300}$	11.9	60.9	6.11	1.35	0.68	0.45	0.43	1.7E-2	4.0E-3	0.08	0.06
$\rm FO4_{VD}^{300}$	8.5	64.3	12.91	41.7	0.99	0.65	0.65	1.5E-3	1.5E-3	–	–
$\rm FO7_{IS}^{300}$	11.1	61.8	5.07	0.90	0.59	0.25	0.23	2.7E-2	4.0E-3	0.06	0.05
$\rm FO7_{VD}^{300}$	12.7	60.4	9.19	36.7	1.02	0.67	0.67	1.6E-3	1.6E-3	–	–

Notes: (1) Name of the model. (2) – (3) Total ISM mass escaped from and retained within the numerical grid at $t = 13$ Gyr, respectively. (4) – (6) ISM mass with $T > 10^6$ K, ISM X-ray luminosity in the 0.3–8 keV band, and ISM X-ray emission weighted temperature in the same band, at $t = 13$ Gyr. (7) – (10) Thermalization temperatures of stellar motions at $t = 13$ Gyr, defined accordingly to Eqs. (4.29) and (4.15). By construction, $T_* = T_\sigma + T_{\rm v}$; for rotating models $T_{\rm v} = \gamma_{\rm th} T_{\rm rot}$ and $T_\varphi = T_{\rm v} - T_{\rm m} = \gamma_{\rm th}^{\varphi} T_{\rm rot}$, while for velocity dispersion supported models $T_{\rm v} = T_{\rm m}$ (see Section 4.5.2). (11) – (12) Thermalization parameter as defined in Eq. (4.26), and its azimuthal component $\gamma_{\rm th}^{\varphi} = L_\varphi / L_{\rm rot}$ (see Eq. 4.25), at $t = 13$ Gyr.

Table 4.6: Simulations results for the Einasto set at $t = 13$ Gyr.

Name	$M_{\rm esc}$	$M_{\rm gas}$	$M_{\rm hot}$	$L_{\rm X}$	$T_{\rm X}$	T_*	T_σ	$T_{\rm v}$	$T_{\rm m}$	$\gamma_{\rm th}$	$\gamma_{\rm th}^{\varphi}$
	$(10^9 M_\odot)$	$(10^9 M_\odot)$	$(10^9 M_\odot)$	$(10^{40}$ erg s$^{-1})$	(keV)	(keV)	(keV)	(keV)	(keV)		
(1)	(2)	(3)	(4)	(5)	(6)	(7)	(8)	(9)	(10)	(11)	(12)
$\mathrm{E0}^{200}$	3.9	8.2	2.67	1.89	0.41	0.24	0.24	3.7E-3	3.7E-3	–	–
$\mathrm{EO4}^{200}_{\rm IS}$	12.1	0.1	0.09	5.25E-4	0.74	0.49	0.15	0.34	0.31	4.34	0.28
$\mathrm{EO4}^{200}_{\rm VD}$	12.1	0.1	0.09	5.51-4	0.73	0.54	0.23	0.31	0.31	–	–
$\mathrm{EO7}^{200}_{\rm IS}$	12.0	0.2	0.19	1.25E-3	0.45	0.34	0.07	0.27	0.24	1.79	0.14
$\mathrm{EO7}^{200}_{\rm VD}$	11.3	0.9	0.20	1.56E-3	0.45	0.42	0.22	0.20	0.20	–	–
$\mathrm{FO4}^{200}_{\rm IS}$	6.0	5.7	1.52	0.97	0.21	0.21	0.16	5.2E-2	2.1E-2	0.63	0.37
$\mathrm{FO4}^{200}_{\rm VD}$	3.6	8.5	2.31	1.94	0.45	0.25	0.25	2.1E-3	2.1E-3	–	–
$\mathrm{FO7}^{200}_{\rm IS}$	3.9	8.2	1.69	0.16	0.25	0.14	0.09	4.8E-2	3.0E-2	0.28	0.11
$\mathrm{FO7}^{200}_{\rm VD}$	4.9	7.3	1.60	2.10	0.44	0.26	0.26	2.8E-3	2.8E-3	–	–
$\mathrm{E0}^{250}$	6.6	26.0	6.47	10.1	0.63	0.37	0.37	1.4E-3	1.4E-3	–	–
$\mathrm{EO4}^{250}_{\rm IS}$	10.3	21.8	4.03	1.01	0.49	0.26	0.24	1.8E-2	3.4E-3	0.15	0.12
$\mathrm{EO4}^{250}_{\rm VD}$	9.2	22.9	5.81	7.90	0.59	0.36	0.36	1.9E-3	1.9E-3	–	–
$\mathrm{EO7}^{250}_{\rm IS}$	14.2	16.9	2.77	0.25	0.48	0.18	0.11	6.2E-2	9.4E-3	0.27	0.26
$\mathrm{EO7}^{250}_{\rm VD}$	16.0	15.2	3.29	2.86	0.57	0.35	0.34	3.2E-3	3.2E-3	–	–
$\mathrm{FO4}^{250}_{\rm IS}$	8.1	24.5	3.93	1.46	0.43	0.27	0.26	1.7E-2	3.8E-3	0.13	0.10
$\mathrm{FO4}^{250}_{\rm VD}$	6.9	25.8	5.38	9.79	0.66	0.38	0.38	2.0E-3	2.0E-3	–	–
$\mathrm{FO7}^{250}_{\rm IS}$	8.0	24.4	4.99	4.64	0.26	0.17	0.14	2.9E-2	1.1E-2	0.11	0.07

Table 4.6 – *continued*

Name	$M_{\rm esc}$	$M_{\rm gas}$	$M_{\rm hot}$	$L_{\rm X}$	$T_{\rm X}$	T_*	T_σ	$T_{\rm v}$	$T_{\rm m}$	$\gamma_{\rm th}$	$\gamma_{\rm th}^{\varphi}$
	$(10^9 M_\odot)$	$(10^9 M_\odot)$	$(10^9 M_\odot)$	$(10^{40}$ erg s$^{-1})$	(keV)	(keV)	(keV)	(keV)	(keV)		
(1)	(2)	(3)	(4)	(5)	(6)	(7)	(8)	(9)	(10)	(11)	(12)
$\rm FO7^{250}_{VD}$	9.5	23.3	3.45	7.95	0.65	0.40	0.40	2.0E-3	2.0E-3	–	–
$\rm E0^{300}$	9.6	62.7	13.97	39.9	0.85	0.56	0.56	1.0E-3	1.0E-3	–	–
$\rm EO4^{300}_{IS}$	17.2	53.2	7.10	1.57	0.63	0.38	0.36	1.5E-2	1.6E-3	0.09	0.08
$\rm EO4^{300}_{VD}$	13.0	57.5	12.71	33.2	0.81	0.54	0.54	1.4E-3	1.4E-3	–	–
$\rm EO7^{300}_{IS}$	20.3	45.6	6.47	1.27	0.51	0.20	0.18	2.6E-2	2.2E-3	0.08	0.07
$\rm EO7^{300}_{VD}$	23.5	43.2	7.58	18.3	0.73	0.52	0.52	1.8E-3	1.8E-3	–	–
$\rm FO4^{300}_{IS}$	14.5	58.0	6.50	1.45	0.63	0.40	0.38	1.8E-2	3.6E-3	0.10	0.08
$\rm FO4^{300}_{VD}$	11.1	61.8	11.70	37.8	0.90	0.57	0.57	1.7E-3	1.7E-3	–	–
$\rm FO7^{300}_{IS}$	14.1	56.6	5.79	1.35	0.48	0.23	0.21	2.5E-2	3.5E-3	0.07	0.06
$\rm FO7^{300}_{VD}$	16.9	56.3	7.43	31.1	0.95	0.60	0.59	1.8E-3	1.8E-3	–	–

Notes: all quantities are as in Table 4.5

The middle panels of Fig. 4.9 show the T_X distribution as a function of M_{hot}. In the NFW set, there is a sequence of T_X values clearly visible at $M_{hot} > 2 \times 10^9 M_\odot$, with VD models hotter than the corresponding IS models. However, the three models with the smallest amount of hot ISM ($M_{hot} < 10^9 M_\odot$) have higher temperatures than one would expect extrapolating the T_X sequence to very low values of M_{hot}, as a consequence of the transition to the wind phase. A change in the trend is even more visible in the low mass Einasto models, where the stronger tendency to establish a global wind leads to an *increase* of T_X at very low M_{hot}, reaching values even higher than in VD models with large X-ray haloes. In conclusion, at medium-high σ_{e8}, T_X of VD models tends to remain above that of rotating models; at low σ_{e8}, in addition to the cooler branch of rotating models, another hotter branch of IS and VD models appears, made by models in wind.

Finally, the right panels of Fig. 4.9 show again how T_X of IS models is systematically lower with respect to that of VD ones of same L_B, with the exception of those in the wind phase. As for L_X, T_X of VD models is dominated by the dense central luminous regions. In IS models, instead, the central region is hotter than in VD models, but it is also at a lower density, so that its contribution to T_X is marginal, and T_X is more affected by colder ($T \simeq 2 \times 10^6$ K) and denser gas located in the outer regions. Thus, the main reason of the lower T_X in IS models of medium-high mass is not galaxy shape, but the importance of galaxy rotation, that drives the hydrodynamical evolution (Section 4.6.1). From the Jeans equations, the more a galaxy is flat, the more it can be rotating; thus the E7 IS models are cooler than their VD counterparts, and by a larger amount than for the analogous E4 pair, due to the stronger rotation in the E7 models.

A "zoom" on the specific effects of flattening and rotation is given in Fig. 4.10, where we plot, separately for each σ_e, and for FO- and EO-built families, the L_X values of all the models in Fig. 4.9. The additional symbols (crosses) represent T_σ (see Eq. 4.15), thus they give the temperatures associated with the thermalisation of all stellar velocities for VD models (solid crosses), and only to the random part of the stellar velocities for IS models (empty crosses). We recall that the values of T_σ depend only on the galaxy structure (and are calculated without the need of running simulations, as in the analysis of Section 4.4), and do not contain contributions from gas cooling and SNIa heating. The simulations show that the values of T_* (Eq. 4.29) are almost coincident with those of T_σ in the medium-high σ_{e8} models (i.e., models in a slow inflow where γ_{th} is very small, see Tables 4.5 and 4.6). The low-σ_{e8} wind models, instead, have $T_* > T_\sigma$, and the temperature difference is due to thermalisation of the strong meridional motions developed in the wind phase ($T_* \simeq T_\sigma + T_m$, while T_φ remains very small). In Fig. 4.10 it is even more apparent than in Fig. 4.9 how VD models are in general hotter than their rotating counterparts, due to the above discussed hydrodynamical effects. In addition, the T_X difference between VD and IS models increases with galaxy flattening, and it is larger for the more massive and FO-built models, and decreases for smaller and EO-built models. Exceptions are found in the low-σ_{e8} EO-built models, as a consequence of the transition to global wind induced by flattening and rotation.

Two interesting considerations can be made by comparing T_X resulting from the simulations with the temperatures T_* and T_σ associated with the thermalisation of stellar motions. The first is that T_X of all models is higher than T_* and T_σ, as some-

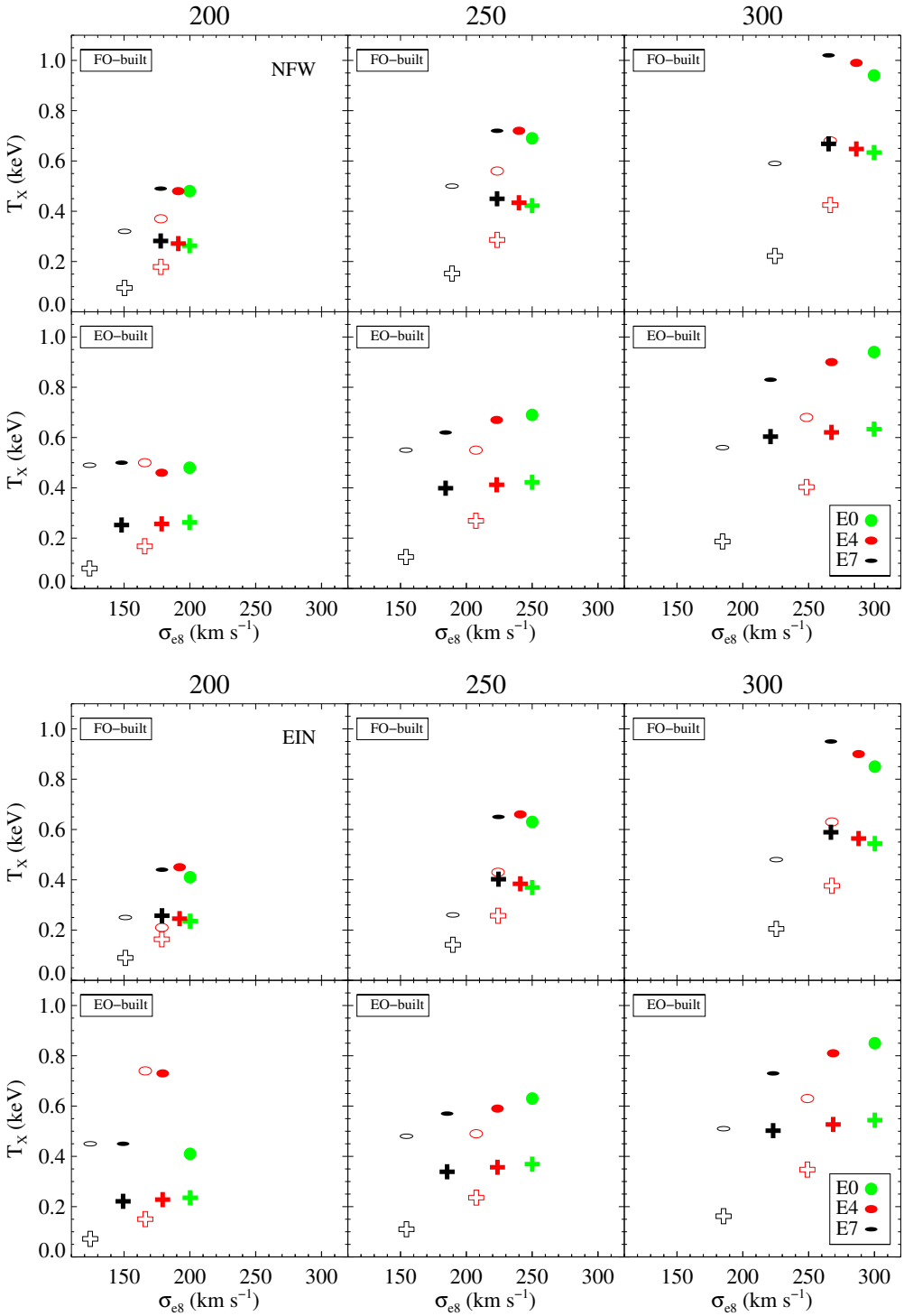

Figure 4.10: The emission weighted ISM temperature T_X in the 0.3–8 keV band at 13 Gyr for the models in the NFW (top six panels) and in the Einasto (bottom six panels) sets as a function of σ_{e8}. Different columns show the results for the families obtained from the spherical progenitors with $\sigma_{e8} = (200, 250, 300)$ km s^{-1}, and refer to model flattened according to the edge-on or face-on procedure. The notation for the symbols is the same as in Fig. 4.9. Crosses show the values of T_σ calculated according to Eq. (4.15). For the relation of T_σ with T_* and T_X, see the Sections 4.3 and 4.5.2.

what expected due to the additional heating contributions (e.g., from SNIa) to the gas, and to the relatively small radiative losses (we recall that $T_{\rm X}$ is computed from the hot, low-density gas only). The second consideration is that, notwithstanding the missing SNIa heating and cooling terms in T_σ, the *trend* of $T_{\rm X}$ with galaxy flattening and rotation is remarkably the same as that of T_σ for all models, with the exception of the global wind, low-$\sigma_{\rm e8}$ models. Thus T_σ, except for wind cases, is a good proxy for T_*, and a robust indicator of the trend of $T_{\rm X}$ with galaxy properties (shape and internal kinematics), supporting the importance of theoretical analyses as the one in Section 4.4. As a final comment, we note that, in general, at fixed $\sigma_{\rm e8}$, Einasto models tend to be slightly colder than the NFW models, both in $T_{\rm X}$ and T_σ, due to the different DM profile.

4.6.4 The X-ray ISM luminosity $L_{\rm X}$

The second important diagnostic explored is the 0.3–8 keV luminosity $L_{\rm X}$. Here we just summarize the main properties of the models, commenting the results of Section 4.4 about the gravitational temperature estimates in light of the hydrodynamical results; for a detailed description of these last see Negri (2014); Negri et al. (2014b).

In medium to large $\sigma_{\rm e8}$ models, $L_{\rm X}$ on average increases with $\sigma_{\rm e8}$ (similarly to the $T_{\rm g}^-$ trend in Fig. 4.4 of Section 4.4), however presenting at each $\sigma_{\rm e8}$ a significant spread in $L_{\rm X}$, consistent with observations (Boroson et al. 2011). At fixed stellar mass M_*, round progenitors are found at high $L_{\rm X}$, while the dispersion is associated with a mix of flattening and rotation effects. In particular, $L_{\rm X}$ of the VD models is higher than that of IS ones by up to a factor of $\simeq 40$. The largest difference occurs for the more massive and flatter models, and it is much larger than the $L_{\rm X}$ variation between a spherical progenitor and its most flattened VD version. Indeed, $L_{\rm X}$ of VD models of identical M_* with different flattening lies in a narrow range, analogously to the $T_{\rm g}^-$ values found in Section 4.4. The same behaviour occurs also among IS models with the same M_*. This indicates that, at fixed M_* and fixed internal kinematics, $L_{\rm X}$ is only marginally sensitive to even large variations of the flattening degree of the stellar component, as already suggested by Fig. 4.4. However, Fig. 4.4 was not able to explain the observed $L_{\rm X}$ difference between roundish galaxies and their flatter and rotating counterparts.

Conversely, the most interesting feature of the models that emerges from the simulation is a clear $L_{\rm X}$ difference between VD and flattened IS models of similar $\sigma_{\rm e8}$, with rotating models characterised by a strong X-ray under-luminosity. As described in the previous Sections, this is an hydrodynamical effect driven by the presence of angular momentum, which causes rotating galaxies with medium to large $\sigma_{\rm e8}$ to develop a different flow evolution, where the gas is prevented from accumulating in the central regions by the centrifugal barrier, leading to the creation of a very hot, low density atmosphere in the centre, and eventually resulting in a lower total $L_{\rm X}$. Furthermore, IS models have also a lower $M_{\rm hot}$ than VD models. This is due to the presence of recurrent cooling episodes driven by rotation (that further contribute to the lowering of $L_{\rm X}$), and not to escaping ISM (except for the models with the lowest $\sigma_{\rm e8}$). All these hydrodynamical effects were obviously not possible to predict and take into account in the theoretical energetic analysis of Section 4.4. In VD

models, instead, the ISM flows directly toward the central galactic regions, where a steep density profile is created. This difference in the hot gas density distribution, already showed in Fig. 4.8, is a major reason for the systematic difference of $L_{\rm X}$, and it nicely explains the lower $L_{\rm X}$ observed for fast rotators than for slow rotators in the ATLAS sample (Sarzi et al. 2013).

The models with the $\sigma_{\rm e8} = 200$ km s^{-1} progenitor, instead, behave differently from the rest of the models. This is especially true for the EO flattening, when the galaxy potential well becomes shallower, and thus energetic effects of flattening and rotation are larger than for the FO flattening. For example, the EO7$^{200}_{\rm VD}$ model drops to low $L_{\rm X}$, at variance with the FO7$^{200}_{\rm VD}$ model; this drop happens also for the Einasto EO4$^{200}_{\rm VD}$ model. In the NFW case, a further reduction in $L_{\rm X}$ is attained when introducing rotation in the EO7$^{200}_{\rm IS}$ model, in accordance with Ciotti & Pellegrini (1996) and Posacki et al. (2013b), where thermalisation of ordered motions does not take place. A transition to a very low $L_{\rm X}$ value is also obtained for the NFW EO4$^{200}_{\rm IS}$ model: here the only addition of rotation causes the degassing of the galaxy and a very lower value of $L_{\rm X}$ with respect to the VD counterpart. These findings point out the high sensitivity of the flow phase to (even small) changes in the mass profile (e.g., flattening or mass concentration) and in the stellar kinematics (e.g., rotation) at low galactic masses, for which then it is difficult to predict systematic trends in $L_{\rm X}$. We stress that the VD and IS models are characterized, by construction, by the same gravitational potential, so that the difference in $L_{\rm X}$ is only due to galactic rotation.

Thus, it seems that, for low $\sigma_{\rm e8}$ galaxies, energetic effects might be more important in determining the X-ray properties of ETGs, while hydrodynamical ones prevail in medium-high $\sigma_{\rm e8}$ galaxies.

4.7 Summary and conclusions

In this Chapter we investigated the relationship between the temperature and content of the hot X-ray emitting haloes of ETGs and their galactic shape and rotational support. The main focus of this work is the explanation of long-standing and more recently observed trends of $L_{\rm X}$ and $T_{\rm X}$ with galaxy shape and rotation (as well as, of course, with fundamental galaxy properties as stellar velocity dispersion and optical luminosity). This work is an extension of previous similar studies (Ciotti & Pellegrini 1996; Pellegrini et al. 1997; D'Ercole & Ciotti 1998; Pellegrini 2011), and is based on a twofold approach consisting of a theoretical and a numerical analysis.

In the first theoretical part (Posacki et al. 2013b), by means of our Jeans solver code (Chapter 2), we built a large set of axisymmetric three-component (stars, DM halo, SMBH) galaxy models, representative of observed ETGs. We varied the degree of flattening and rotational support of the stellar component, in order to establish what is the dependence of the temperature and binding energy of the injected gas on the observed galaxy shape and internal kinematics. For the injected gas, we defined the equivalent temperature of stellar motions as $T_* = T_\sigma + \gamma_{\rm th} T_{\rm rot}$, where the parameter $\gamma_{\rm th}$ takes into account how much of the ordered rotation of the galaxy is eventually thermalised by the stellar mass losses. We considered the simplified case in which the pre-existing gas velocity is proportional to the stellar streaming velocity. When pre-existing gas and stars rotate with the same velocity, no ordered

stellar kinetic energy is thermalised ($\gamma_{\rm th} = 0$); when the gas is at rest, all the kinetic energy due to stellar streaming is thermalised ($\gamma_{\rm th} = 1$). We also defined the temperature $T_{\rm g}^-$ equivalent to the binding energy for the injected gas. Our main results are as follows:

- Flatter models can be either more or less concentrated than rounder ones of the same mass and same circularized $R_{\rm e}$, depending on how they are built. If $R_{\rm e}$ is kept constant for a FO view, flatter models are more concentrated and bounded than the round counterpart; the opposite is true if $R_{\rm e}$ is kept constant for an EO view. As a consequence, the effect of a pure change of shape is an increase of T_* and $T_{\rm g}^-$ in the first way of flattening, and a decrease in the second one. Overall, however, the variation in T_* for both cases is mild, within ~ 20 percent even for the maximum degree of flattening (the E7 model). Similarly, $T_{\rm g}^-$ gets larger by at most ~ 20 percent, and decreases by at most ~ 12 percent.

- A more significant effect on T_* can be due to the amount of rotational support. The isotropic rotator case is investigated here ($k = 1$). If $\gamma_{\rm th} = 1$, the whole stellar kinetic energy, including the streaming one, is thermalised, and T_* coincides with that of the non-rotating case, for the same galaxy shape. If $\gamma_{\rm th} < 1$, T_* is instead always reduced, and the larger so the flatter is the shape. The strongest reduction is obtained for the E7 models when $\gamma_{\rm th} = 0$, and then T_* can drop by $50 - 70$ percent with respect to the E0 models. Thus, *the presence of stellar streaming, when not thermalised, acts always in the sense of decreasing T_*, and the size of this decrease depends on the relative motion between pre-existing gas and stars.* Clearly, the flatter the galaxies, the stronger can be the rotational support, and, consequently its potential effect on T_*. Thus the effect of rotation is dependent on the degree of flattening, and, as a minimum, it requires a flat shape as a premise.

- Since stellar streaming acts in the sense of making the gas less bound due to the centrifugal support, at any fixed galaxy shape and rotational support $T_{\rm g}^-$ decreases in proportion to how the velocity field of the ISM is close to that of the stars. However, this decrease is lower than that produced on T_*: $T_{\rm g}^-$ drops at most by ~ 13 percent (for the E7 models), between the two extreme cases of ISM at rest and gas rotating as the stars. Note then two compensating effects from stellar streaming when $\gamma_{\rm th} < 1$: T_* is lower than for a non-rotating galaxy, but the gas is also less bound.

- All the above trends and effects are independent of the galaxy luminosity (mass), and DM halo shape. Only the normalization of T_* and $T_{\rm g}^-$ changes, if the DM halo mass changes (e.g., it increases from the SIS to the Einasto to the Hernquist to the NFW halo models).

The comparison of the above results with observed $T_{\rm X}$ and $L_{\rm X}$ for the ETGs in the *Chandra* sample of Boroson et al. (2011) shows that:

- All observed $T_{\rm X}$ are larger than T_*, but much closer to T_* than to $T_{\rm SN}$. T_* ranges between 0.1 and 0.4 keV, for 150 km s^{-1} $\lesssim \sigma_{\rm e8} \lesssim$ 300 km s^{-1} (the

lower end being possibly even lower, depending on the effects of rotation), while $T_{\rm SN} \approx 1.5$ keV (for a thermalisation parameter $\eta = 0.85$), so that the contribution from SNIa dominates the gas injection energy ($T_{\rm inj} \sim 1.5-2$ keV), that is then practically insensitive to changes in T_* due to the galaxy shape or kinematics. The proximity of the observed $T_{\rm X}$ values to T_* indicates that η may be lower, and/or that the gas tends to establish itself at a temperature close to the virial temperature, in all flow phases. In any case, this proximity provides an empirical confirmation of the relevance of a study of T_* and its variations.

- For 200 km s^{-1} $\lesssim \sigma_{\rm e8} \lesssim$ 250 km s^{-1}, $T_{\rm g}^-$ becomes larger than $T_{\rm inj}$, and inflows in these galaxies can become important. These $\sigma_{\rm e8}$ values could be lower if $\eta <$ 0.85, and if the DM amount is larger than assumed here. Galaxies with $\sigma_{\rm e8} \lesssim$ 200 km s^{-1} ($L_{\rm K} \lesssim 2 \times 10^{11} L_{\rm K\odot}$), instead have a high probability of hosting an outflow, and then a low hot gas content, as confirmed by observations of $L_{\rm X}/L_{\rm K}$ vs. $L_{\rm K}$. The ratio $L_{\rm X}/L_{\rm K}$ seems to be lower also for a flatter shape and larger rotation. However, the effect of shape or rotation on $T_{\rm g}^-$ is small, thus, from the energetic point of view, these two major galactic properties are not expected to play a major role in determining the gas content.

- We find a mild indication that, at fixed $L_{\rm K}$, flatter shapes and more rotationally supported ETGs show a lower $T_{\rm X}$, with respect to rounder, less rotating ETGs (similarly to what found by Sarzi et al. 2013). This tendency can be explained by the effects predicted here on T_* due to flattening and rotation. Since, for a fixed galaxy mass, a decrease of T_* due to rotation is predicted to be potentially stronger than produced by shape without rotation, *not thermalised* stellar streaming might be a more efficient cause of the lower $T_{\rm X}$.

In the second numerical part of the investigation, outcome of a joint research collaboration (Negri et al. 2014b), we performed a large suite of high-resolution 2D hydrodynamical simulations, to study the effects of galaxy shape and stellar kinematics on the evolution of the X-ray emitting gaseous haloes of ETGs. Realistic galaxy models are built with our Jeans solver code, that allows for a full generality in the choice of axisymmetric galaxy shape and of the stellar and DM profiles, which can be tailored to reproduce observational constraints. Stellar motions in the azimuthal direction are split among velocity dispersion and ordered rotation by using the Satoh (1980) decomposition. In particular, we explored two extreme kinematical configurations, the fully velocity dispersion supported system and the isotropic rotator, in order to encompass all the possible behaviours occurring in nature. Of course, the VD configuration applies only to a minor fraction of the flat galaxy population (e.g., Emsellem et al. 2011). On the other hand, IS models approximate only to some extent the dynamical structure of flat and fast rotating galaxies, since the latter are more generally characterized by a varying degree of anisotropy in the meridional plane with intrinsic flattening (Cappellari et al. 2007). The source of gas is provided by secular evolution of the stellar population (stellar winds from ageing stars and SNIa ejecta). Heating terms account for SNIa events and thermalisation of stellar motions.

Evidences from our theoretical analysis (Posacki et al. 2013b), and from previous

exploratory theoretical (Ciotti & Pellegrini 1996) and numerical works (D'Ercole & Ciotti 1998; Negri et al. 2014a,b), seem to point toward a cooperation of flattening and rotation in establishing the final X-ray temperature and luminosity of the ISM. However which of the two is the driving parameter, and what is the involved physical *mechanism*, had not been clarified yet. From the present numerical investigation, we conclude that more than one physical effect is at play, and that the relative importance of flattening and rotation changes as a function of galaxy mass. Summarizing our findings, we discuss separately first the results about the ISM X-ray emission-weighted temperature $T_{\rm X}$ and then the X-ray luminosity $L_{\rm X}$.

- The variation of $T_{\rm X}$ due to a change of shape and internal kinematics is different for low and high mass galaxies. $T_{\rm X}$ does not change appreciably adding flattening and rotation to low mass progenitors that are in the global wind phase. Due to their low density and high meridional velocities, global winds are generally hotter than what expected by extrapolation of the $T_{\rm X}$ of more massive systems. Adding flattening and rotation to ETGs energetically near to host a global wind leads to a transition to a wind phase, with the consequent increase of $T_{\rm X}$.

- In the medium-high mass galaxies a change of shape produces small changes in $T_{\rm X}$. Adding rotation, instead, results in a much lower $T_{\rm X}$. This is because angular momentum conservation leads to the formation of a massive centrifugally supported cold disc and to a lower density of the hot ISM in the central regions above and below the equatorial plane, with respect to VD models. Then, the external, and colder, regions weight more in the computation of $T_{\rm X}$.

- Overall, for medium-high mass galaxies, $T_{\rm X}$ increases with galaxy mass, independently of the specific DM halo profile. In general, in the Einasto haloes the hot gas is systematically cooler and with a larger scatter in $T_{\rm X}$, than in the NFW DM haloes of comparable mass.

- In rotating models the ISM almost co-rotates with the stars (i.e., $\gamma^{\varphi}_{\rm th} \lesssim 0.25$ as adopted in Posacki et al. 2013b), and so there is a corresponding reduction of the thermalisation of the galaxy streaming velocity. At the same time the rotating ISM is less bound, due to the centrifugal support.

- With the exception of low mass galaxies in the wind phase, T_σ (the temperature associated with the thermalisation of the stellar velocity dispersion, Eq. 4.15) is a good proxy for T_*, the true thermalisation temperature of stellar motions, as computed from the simulations; for wind models instead $T_* > T_\sigma$. In general $T_{\rm X} > T_*$, but the dependence of $T_{\rm X}$ on galaxy mass and shape in no wind galaxies is outstandingly reproduced by that of T_σ (see Fig. 4.10), a quantity that can be computed without resorting to numerical simulations.

The main results concerning $L_{\rm X}$ can be summarized as follows:

- In case of galaxies energetically near to the onset of a galactic wind (i.e., for ETGs with $\sigma_{\rm e8} \approx 200\,{\rm km\ s^{-1}}$), flattening and rotation contribute significantly to induce a wind, in agreement with the energetic expectations discussed in

Ciotti & Pellegrini (1996) and Posacki et al. (2013b), with the consequent sharp decrease of $L_{\rm X}$. The transition to a global wind is favoured respectively by the facts that flattening can reduce the depth of the potential well, and that in rotating systems the ISM and the stellar component almost corotate; this reduces (in absolute value) the effective potential experienced by the ISM.

- In models with $\sigma_{\rm e8} > 200$ km s^{-1}, galaxy shape variations, in absence of rotation, have only a minor impact on the values of $L_{\rm X}$. Indeed, fully velocity dispersion supported flattened models have $L_{\rm X}$ similar to or just lower than that of their spherical progenitors, in agreement with the energetic expectations of our theoretical analysis (Posacki et al. 2013b).

- In flat galaxies with $\sigma_{\rm e8} > 200$ km s^{-1}, rotation reduces significantly $L_{\rm X}$. Not only the thermalisation parameter is low and part of the heating due to stellar motions is missing with respect to the corresponding VD model, but rotation acts also on the hydrodynamics of the gas flow: conservation of angular momentum of the ISM injected at large radii favours gas cooling through the formation of rotating discs of cold gas, reducing the amount of hot gas in the central regions and then $L_{\rm X}$. In conclusion, galaxy flattening has an important, though *indirect* effect for medium-to-high mass galaxies, in the sense that only flattened systems can host significant rotation of the stellar component.

Chapter 5

The stellar initial mass function of ETGs

Posacki S., Cappellari M., Treu T., Pellegrini S., Ciotti L., 2014, MNRAS, in press (arXiv:1407.5633)

In this Chapter we present an investigation about the shape of the IMF of ETGs, based on a joint lensing and dynamical analysis, and on stellar population synthesis models, for a sample of 55 lens ETGs identified by the Sloan Lens ACS (SLACS) Survey. The work here presented has been published in Posacki et al. (2014).

5.1 Introduction

The stellar IMF describes the mass distribution of the stellar population originated in a single star formation burst, at the time of birth. It gives us information about the relative importance of low and high mass stars, hence its form directly affects the amount of stellar ejecta and their chemical composition, the mass distribution of stellar remnants, and the stellar mass-to-light ratio of the population. The study of the shape of the IMF also gives us direct insights into the physics of star formation, and it is crucial for the estimate of galaxy stellar masses starting from the observed luminosity. Thus the knowledge of the IMF is fundamental in many fields of astrophysics that study the formation and evolution of stellar systems.

Several direct measurements of star counts of resolved stellar populations in the solar neighbourhood have shown that the IMF can be parametrized by a power law mass distribution $dN/dM \propto M^{-s}$, characterized by a Salpeter (1955) slope $s \simeq 2.35$ for $M \gtrsim 0.5M_{\odot}$, and by a change toward flatter slopes for $M \lesssim 0.5M_{\odot}$ (Kroupa 2001; Chabrier 2003). This holds in different environments throughout the Milky Way (Kroupa 2002; Bastian et al. 2010), but whether this is true for all galaxies is still ongoing debate. Stellar counts down to very low stellar masses (i.e., in the mass range of major uncertainty given the intrinsic difficulty of measurements) is not feasible in distant external galaxies, so that, in order to study the extragalactic IMF, people use alternative methods based, for example, on ionized gas emission, redshift evolution of the tilt and normalization of the Fundamental Plane, strength of IMF-sensitive spectral features, gas kinematics, gravitational lensing and stellar dynamics (see Cappellari et al. 2013a for a more detailed review). Among these indirect methods, it is widely used to constrain the IMF shape by estimating galaxy stellar masses from dynamical models and comparing them with the predictions of stellar population synthesis models, that rely on an assumed IMF shape. Note that this method does not directly measure the shape of the IMF, but its overall mass normalization: each IMF shape results in a different M_*/L, that is converted in a different stellar mass, once the luminosity is measured. In the last decade a number of works based on this method have agreed that spiral galaxies are inconsistent with a Salpeter normalization over the whole mass range, and that they need a lighter overall normalization similar to Kroupa or Chabrier, like the Milky Way (Bell & de Jong 2001; Kassin et al. 2006; Bershady et al. 2011; Brewer et al. 2012). The same result also appears to be valid for at least some ETGs (Cappellari et al. 2006; Ferreras et al. 2008; Dutton et al. 2011; Thomas et al. 2011; Brewer et al. 2014; Zepf et al. 2014), thus showing no evidence of a departure from a universal stellar IMF.

In contrast, however, there are numerous works carried out on ETG samples that point out evidences of a dynamical mass excess over the predictions of stellar population models with fixed IMF. This excess increases with galaxy mass and it can be explained either (i) by an IMF normalization that increases from a Kroupa/Chabrier one at low masses, up to a Salpeter normalization for the more massive galaxies, implying a systematic variation of the IMF (e.g., Renzini & Ciotti 1993), or (ii) by an increase of the DM fraction as function of galaxy mass due to a non-universal DM halo profile (Padmanabhan et al. 2004; Cappellari et al. 2006; Grillo et al. 2009; Thomas et al. 2009; Tortora et al. 2009; Auger et al. 2010; Graves & Faber 2010; Schulz et al. 2010; Treu et al. 2010; Barnabè et al. 2011; Dutton et al. 2012; Tortora

et al. 2013). This method, based on the comparison between galaxy stellar masses computed from dynamical and stellar population synthesis models, is indeed subject to degeneracies in the dynamical modelling, which are related to the assumptions for the luminous and DM density profiles, and for the velocity dispersion anisotropy. For example, given the uncertainties related to the knowledge of DM halo distributions in galaxies, general forms for the DM profile can be adopted for the dynamical modelling, like the generalized NFW profile, where the inner slope is allowed to be a free parameter. Allowing this results in a degeneracy between stellar mass and inner slope, in the sense that steeper inner slopes require less stellar mass to reproduce the same observed stellar velocity dispersion. However, the degeneracies can be reduced by additional constraints derived, for example, from gravitational lensing analysis or integral field spectroscopy observations.

An example is given by the results of the SLACS group: Treu et al. (2010) analysed 56 lens ETGs belonging to the SLACS sample by building dynamical models tuned to reproduce the SDSS-measured velocity dispersion σ_* and the total projected mass within the Einstein radius. They adopted two-component spherical isotropic dynamical models with self-similar Hernquist (1990) profiles to describe the stellar density, and a NFW (Navarro et al. 1997) DM density distribution with fixed slope and scale radius. Treu et al. (2010) found that bottom-heavy IMFs such as Salpeter are strongly preferred over light-weight IMFs such as Kroupa/Chabrier for the most massive ETGs, assuming standard NFW DM density profiles. This result was then strengthened by Auger et al. (2010) who included adiabatic contraction and weak-lensing constraints in the modelling, and found that only Salpeter-like IMF are consistent with the observed properties of their ETG sample. Note the SLACS sample is an effectively velocity dispersion selected sample, so that it is composed of high σ galaxies (see Section 5.2 and references therein).

Another remarkable example is the work of Cappellari et al. (2012, 2013b,a) on the volume-limited, nearly mass selected ATLAS^{3D}sample of 260 ETGs. They constructed detailed axisymmetric dynamical models, which allow for orbital anisotropy and reproduce in detail both the galaxy images and the high-quality integral-field stellar kinematics out to about one effective radius R_e. Given the tighter constraints with respect to previous analogous studies, their models were well-suited to explore different DM density profiles, and they find that a non-universal IMF is always required under all halo assumptions, due to the low DM mass contribution within R_e. Their study, based on an unprecedented large sample of ETGs spanning a wide range in galaxy mass, found a systematic trend in IMF normalization varying from Kroupa/Chabrier up to Salpeter or heavier for increasing velocity dispersion.

Finally other works, based on IMF-sensitive spectral features, that are completely independent of dynamical modelling assumptions, find a steepening IMF with increasing velocity dispersion and [Mg/Fe], with massive ETGs requiring bottom-heavy, dwarf-rich IMF (van Dokkum & Conroy 2010, 2011; Conroy & van Dokkum 2012; Spiniello et al. 2012, 2014; Ferreras et al. 2013). Thus, there seems to be a systematic dependence of the IMF on galaxy properties, indicating that high mass ETGs prefer on average a Salpeter normalization, while low mass galaxies are consistent with a lighter normalization, similar to Kroupa or Chabrier. However, quantitative consistency between the dynamical and spectral synthesis approach has not been achieved yet (e.g., Smith 2014; McDermid et al. 2014).

In this Chapter we revisit the analysis of Treu et al. (2010) in order to investigate the effects of a more detailed modelling of the stellar component. The spherical models of Treu et al. (2010) indeed provide only a crude approximation to the observed galaxy surface brightness, which shows evidence for disks and it is known to vary systematically with galaxy mass (Caon et al. 1993). To address this potential bias, here we construct models which allow for axisymmetry and can reproduce the observed galaxy surface brightness in detail, in an essentially non-parametric way. Moreover, differently from Treu et al. (2010), our stellar population synthesis models are built via full spectrum fitting of SDSS spectra, and not by means of multicolour photometry. An approach closely related to the one illustrated in this work, was employed also by Barnabè et al. (2013) in their analysis of two SLACS ETGs, where they also exploited X-Shooter spatially-resolved kinematic data in order to put constraints on these systems' IMFs.

Finally, our analysis is similar to that performed by Cappellari et al. (2013b), therefore this allows us also to combine the SLACS and the ATLAS^{3D}samples, obtaining a larger and homogeneously analysed sample of ETGs. Remarkably, due to their selection criteria the two samples are complementary, so that the combined sample is fairly representative of ETGs, extending from low to very high velocity dispersions (or stellar masses). Another attempt to compare similar previous works was made by Dutton et al. (2013a), even though it is not as homogeneous as this.

The Chapter is organized as follows. In Section 5.2 we briefly summarize the sample and data we used, while in Section 5.3 we describe our dynamical and stellar population synthesis models. The main results are presented in Section 5.4, and Section 5.5 summarizes the conclusions. All magnitudes are in the AB photometric system, and a standard concordance cosmology is assumed, i.e. $h = 0.7$, $\Omega_m = 0.3$ and $\Omega_\Lambda = 0.7$.

5.2 Sample and data

The subsample of galaxies analysed in this work is extracted from the SLACS sample studied in Treu et al. (2010). The SLACS sample is composed of massive ETGs, that were spectroscopically selected from the SDSS database for being gravitational lenses (Bolton et al. 2006). In particular, the SLACS sample consists of galaxies with very high σ for two main reasons: (i) the lensing cross section scales approximately with σ^4, and (ii) the SDSS is a flux-limited sample, so that high-luminosity, and therefore high σ, galaxies are overrepresented because they are visible over a larger volume (Hyde & Bernardi 2009). Thus, the SLACS sample is effectively σ-selected (Auger et al. 2010; Ruff et al. 2011). Several studies have shown that the SLACS sample is indistinguishable from a σ-selected sample of non-lens ETGs (Bolton et al. 2006; Treu et al. 2006, 2009).

We selected our SLACS subsample by requiring the availability of *HST* photometry in the I-band, since it is expected to better trace the luminous mass, being less affected by the presence of dust. In this way, we obtained a subsample of 55 galaxies that span a redshift range of $0.06 \lesssim z \lesssim 0.36$. Our data consist of $HST/\mathrm{ACS}/F814W$ images (Auger et al. 2009), and SDSS optical spectra taken from data release ten (DR10, Ahn et al. 2014). SDSS spectra cover the wavelength range $3800 - 9200$ Å, with a spectral resolution of ~ 2.76 Å FWHM, which corre-

sponds to an intrinsic dispersion $\sigma_{\rm int} \sim 85\,{\rm km\ s^{-1}}$ at 3800 Å and $\sigma_{\rm int} \sim 50\,{\rm km\ s^{-1}}$ at 9000 Å.

5.3 The galaxy models

In order to study the mass normalization of the IMF for our sample of 55 ETGs, we compare the stellar mass-to-light ratios M_*/L determined from two different and independent diagnostics of galaxy stellar mass. The first method relies on gravitational lensing and stellar kinematics, it involves the construction of dynamical models, and so it is sensitive to galaxy mass structure and stellar dynamics assumptions (Section 5.3.1). Here we try to reduce the unavoidable degeneracies generating from the assumption of a particular stellar profile, by using a parametrization which allows for a large number of free parameters. This approach is able to reproduce the galaxy surface brightness images in detail, adding new parameters until the difference between the model and the image becomes negligible. The second approach is instead based on stellar population synthesis models, it assumes an IMF, and returns an estimate of M_*/L by means of spectral fitting; the reliability of this method depends mostly on the goodness of the stellar templates (Section 5.3.2).

5.3.1 The dynamical modelling

5.3.1.1 The mass structure

The mass structure of our galaxy models consists of three components: an axisymmetric stellar distribution, a spherical DM halo, and a central SMBH. The stellar component is accurately modelled with the aid of I-band *HST* images on which we performed a Multi-Gaussian Expansion axisymmetric parametrization (Emsellem et al. 1994, see also Bendinelli 1991; Bendinelli et al. 1993) that fits the galaxy surface brightness distribution. In particular, we used the MGE_FIT_SECTORS software package of Cappellari (2002)[1], where the MGE formalism and the fitting algorithm are fully described (a brief description of the properties of the MGE method is present in Appendix C). Given the nature of our sample, the galaxy images are characterized by the presence of several gravitational arches or rings that we properly mask in order to obtain a better fit. We impose the surface brightness profile of the MGE model to decrease as R^{-4} at large radii, so as to limit the inclusion of spurious light from nearby galaxies. All the model gaussians are convolved with a gaussian point spread function with a dispersion of 0.04 arcsec, as befitting for ACS. We also use some prescriptions for the gaussians' axial ratio: in the limits of obtaining a good fit of the surface brightness, we force 1) the flattest gaussian to have the highest axial ratio, and 2) the gaussians' axial ratio range to be the smallest possible. In this way, we both avoid an artificial restriction of the range of the possible inclination angles for which the model can be deprojected (see Cappellari 2002, Section 2.2.2), and we 'regularize' the model, preventing significant variations of the axial ratio, as physically plausible. These assumptions are needed because the deprojection, to obtain the intrinsic stellar luminosity density from the observed surface brightness, is mathematically non-unique (Rybicki 1987; Gerhard & Binney 1996).

[1] Available at `http://purl.org/cappellari/software`

Moreover, some of the galaxies have been observed only once so that we remove the presence of cosmic rays using the LA_COSMIC software of van Dokkum (2001)[2]. The model flux is corrected for foreground galactic extinction following Schlafly & Finkbeiner (2011), as given by the NASA/IPAC Extragalactic Database (NED), and the apparent I-band magnitude m_I is computed, assuming $M_{\odot\, I} = 4.57$[3]. Then, by means of SDSS spectra, we perform a k-correction following Hogg et al. (2002), and we transform all observed magnitudes to consistent V and r-band rest-frame magnitudes, M_V and M_r respectively, assuming the redshift values reported in Table 5.1. This correction was necessary due to the non-negligible redshift range spanned by the galaxies, and the choice of the photometric bands is motivated by the possibility to compare our results with the SLACS and ATLAS^{3D}ones, that have been obtained in these bands. Then, assuming $M_{\odot\, r} = 4.64$ (Blanton & Roweis 2007), we normalized the model gaussians in units of $L_{\odot\, r}\,\mathrm{pc}^{-2}$, so that now the MGE model has the right units and format to be used for the dynamical modelling (see Section 5.3.1.2). The central regions of the MGE models for all the 55 galaxies are shown in Fig. 5.1 and Table 5.1 reports their magnitudes. Images covering a wider spatial range of the MGE models, together with all their parameters, are illustrated in Appendix C.

As a sanity check, we compared our m_I with the ones reported by Bolton et al. (2008): their magnitudes were calculated, starting from the same data, by fitting two-dimensional ellipsoidal de Vaucouleurs (1948) luminosity profiles, and are the result of the full (not truncated) analytic integral of the best fitting de Vaucouleurs model. We find that the two sets of magnitudes agree with an rms scatter of 0.08 mag, but our m_I are systematically higher by 0.18 mag, implying fluxes underestimated by 18 per cent. This is likely due to the fact that SLACS magnitudes are extrapolated to infinite radii, while ours are limited to the observed photons. Finally, in Fig. 5.2 we compared our M_V with the magnitudes calculated by Auger et al. (2009) in the same band, and found they are consistent with an rms scatter of 0.07 mag, which implies an error of 5 per cent in the luminosity; we assume the same error also for M_r.

For what concerns the DM halo density distribution, we adopt the NFW (Navarro et al. 1997) profile for two main reasons. The first is imposed by the few observational constraints at our disposal (see Section 5.3.1.3), which prevent us from exploring a more flexible DM halo profile, since the addition of further parameters to the models would make the problem completely undetermined. Thus, our results are valid under the assumption that the NFW profile is reliable in providing fair estimates for the DM fraction. The second reason is that one of the motivations of this study is to investigate the possible bias introduced by Treu et al. (2010) with the use of spherical isotropic Hernquist models to describe the stellar components of the SLACS sample, that is apparently composed of non spherical galaxies (see Fig.5.1). Thus, in order to disentangle the effects produced by this approximation, we make use of the same DM density profile adopted by Treu et al. (2010), that is the untruncated NFW profile

$$\rho_{\mathrm{h}}(r) = \frac{\rho_{\mathrm{crit}}\ \delta_{\mathrm{c}} r_{\mathrm{h}}}{r\,(1 + r/r_{\mathrm{h}})^2}, \tag{5.1}$$

[2]Available at `http://www.astro.yale.edu/dokkum/lacosmic/`

[3]Taken from `http://mips.as.arizona.edu/~cnaw/sun.html`

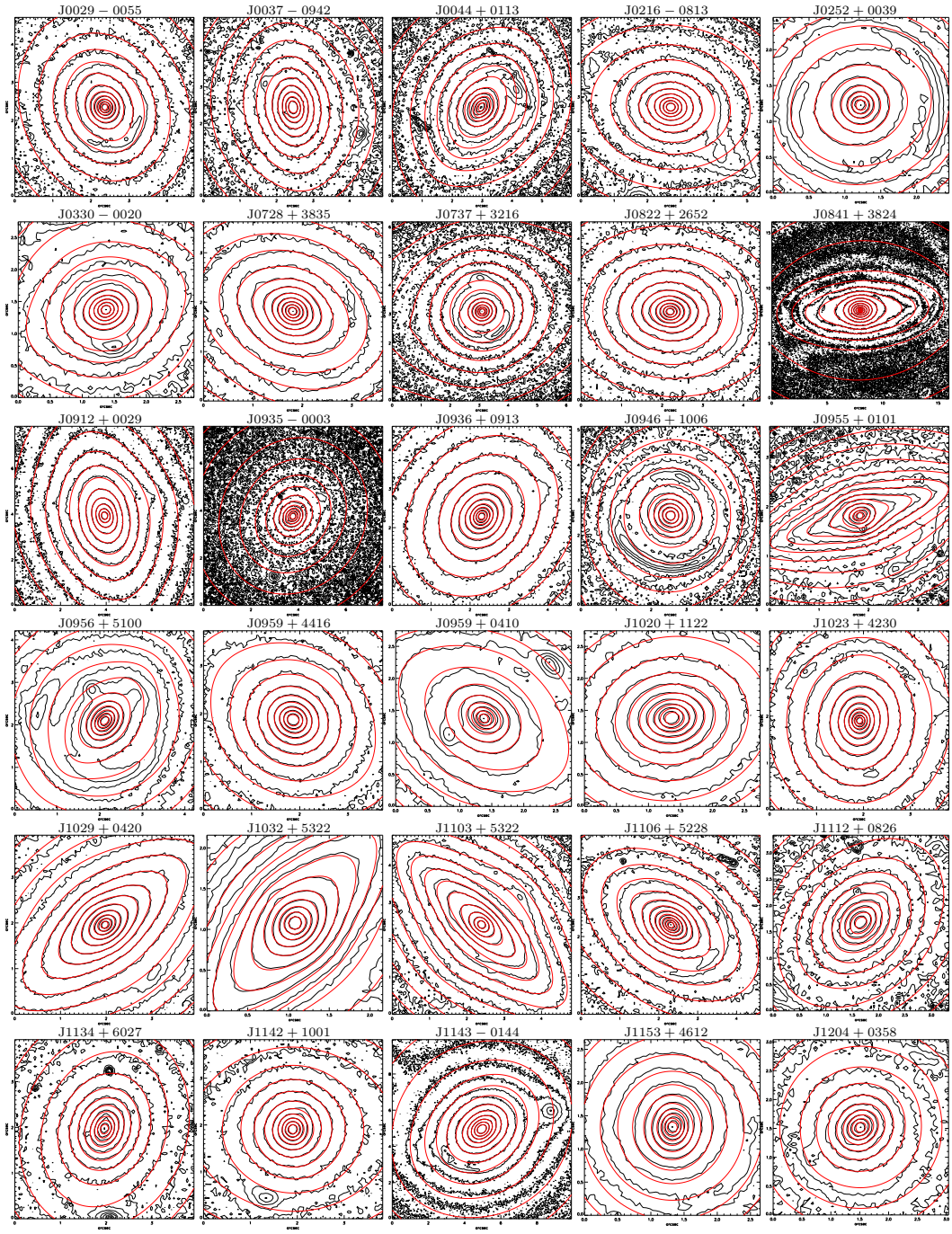

Figure 5.1: Contour maps of the central regions ($\sim 0.5\,R_{\rm e}$) of the WFC/$F814W$ (I-band) images of the 55 galaxies (black). The contours of the MGE surface brightness, convolved with the proper PSF, are superimposed in red.

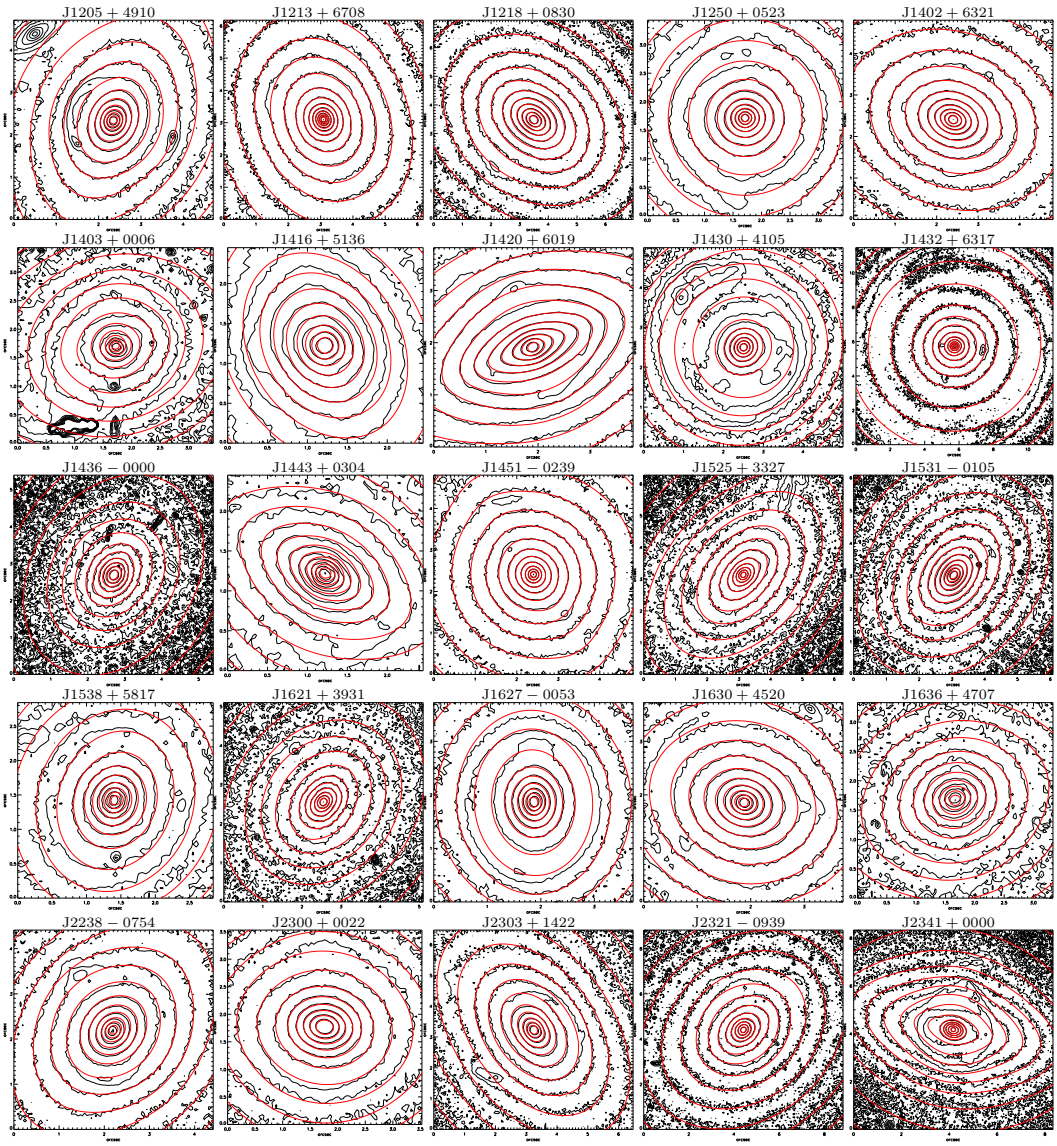

Figure 5.1: – *continued*

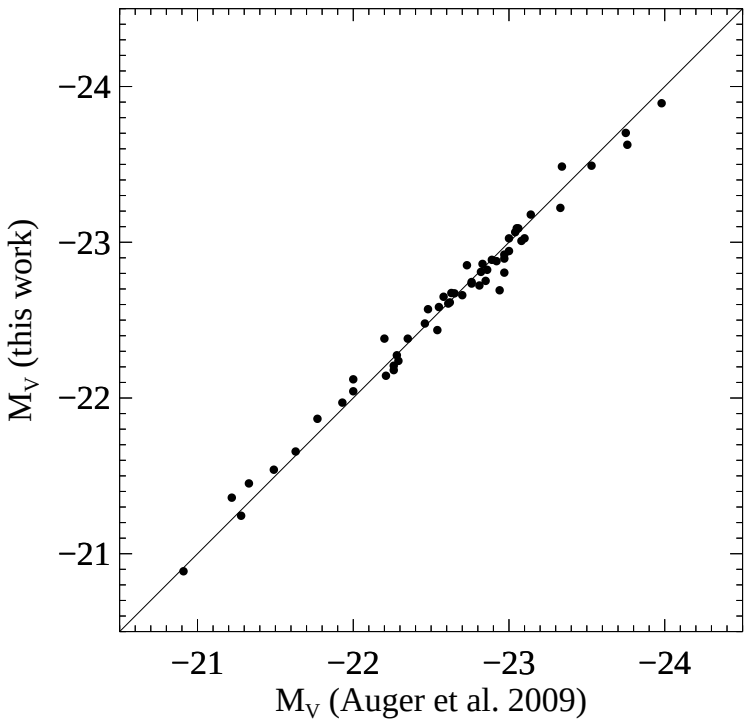

Figure 5.2: V-band absolute magnitudes for the SLACS sample, computed here and in Auger et al. (2009).

Table 5.1: Properties and JAM models parameters of the 55 galaxy SLACS subsample.

Name	z	σ_* [km s^{-1}]	$R_{\rm EIN}$ [kpc]	$\log M_{\rm EIN}$ [$M_\odot$]	m_I [mag]	M_V [mag]	M_r [mag]	$\log R_{\rm e}^{\rm maj}$ [arcsec]	$\log R_{\rm e}$ [arcsec]
(1)	(2)	(3)	(4)	(5)	(6)	(7)	(8)	(9)	(10)
J0029–0055	0.2270	229 ± 18	3.48	11.08	17.16	-22.67	-22.79	2.017	1.830
J0037–0942	0.1955	279 ± 14	4.95	11.47	16.35	-23.09	-23.20	2.016	1.763
J0044+0113	0.1196	266 ± 13	1.72	10.96	15.83	-22.38	-22.48	2.216	1.923
J0216–0813	0.3317	333 ± 23	5.53	11.69	17.12	-23.70	-23.85	2.050	1.831
J0252+0039	0.2803	164 ± 12	4.40	11.25	18.15	-22.24	-22.35	0.950	0.878
J0330–0020	0.3507	212 ± 21	5.45	11.40	18.21	-22.75	-22.93	1.076	0.941
J0728+3835	0.2058	214 ± 11	4.21	11.30	16.83	-22.73	-22.84	1.567	1.348
J0737+3216	0.3223	338 ± 17	4.66	11.46	17.25	-23.49	-23.64	1.829	1.738
J0822+2652	0.2414	259 ± 15	4.45	11.38	17.10	-22.89	-23.00	1.644	1.458
J0841+3824	0.1159	225 ± 11	2.96	11.12	15.23	-22.86	-22.99	6.743	4.672
J0912+0029	0.1642	326 ± 16	4.58	11.60	15.77	-23.22	-23.34	3.034	2.452
J0935–0003	0.3475	396 ± 35	4.26	11.60	17.05	-23.89	-24.05	2.744	2.551
J0936+0913	0.1897	243 ± 12	3.45	11.17	16.62	-22.74	-22.86	1.876	1.691
J0946+1006	0.2219	263 ± 21	4.95	11.46	17.18	-22.58	-22.70	1.760	1.722
J0955+0101	0.1109	192 ± 13	1.83	10.83	17.04	-20.89	-21.02	1.549	0.840
J0956+5100	0.2405	334 ± 17	5.05	11.57	16.82	-23.18	-23.28	1.756	1.572
J0959+4416	0.2369	244 ± 19	3.61	11.23	17.12	-22.82	-22.93	1.500	1.381
J0959+0410	0.1260	197 ± 13	2.24	10.88	17.05	-21.24	-21.37	1.249	1.009
J1020+1122	0.2822	282 ± 18	5.12	11.54	17.47	-22.94	-23.05	1.156	1.037
J1023+4230	0.1912	242 ± 15	4.50	11.37	16.89	-22.48	-22.60	1.480	1.383
J1029+0420	0.1045	210 ± 11	1.92	10.78	16.24	-21.66	-21.77	1.771	1.193
J1032+5322	0.1334	296 ± 15	2.44	11.05	17.12	-21.36	-21.47	1.004	0.659
J1103+5322	0.1582	196 ± 12	2.78	10.98	16.63	-22.27	-22.39	1.927	1.217

Table 5.1 – *continued*

Name	z	σ_* [km s^{-1}]	$R_{\rm EIN}$ [kpc]	$\log M_{\rm EIN}$ [$M_\odot$]	m_I [mag]	M_V [mag]	M_r [mag]	$\log R_{\rm e}^{\rm maj}$ [arcsec]	$\log R_{\rm e}$ [arcsec]
(1)	(2)	(3)	(4)	(5)	(6)	(7)	(8)	(9)	(10)
J1106+5228	0.0955	262 ± 13	2.17	10.96	15.55	-22.12	-22.23	2.036	1.609
J1112+0826	0.2730	320 ± 20	6.19	11.65	17.41	-22.90	-23.02	1.160	1.010
J1134+6027	0.1528	239 ± 12	2.93	11.10	16.43	-22.38	-22.50	2.147	1.935
J1142+1001	0.2218	221 ± 22	3.52	11.22	17.13	-22.65	-22.76	1.779	1.640
J1143-0144	0.1060	269 ± 13	3.27	11.29	15.15	-22.72	-22.84	3.493	3.133
J1153+4612	0.1797	226 ± 15	3.18	11.05	17.25	-21.97	-22.08	1.037	1.029
J1204+0358	0.1644	267 ± 17	3.68	11.24	16.94	-22.04	-22.16	1.241	1.229
J1205+4910	0.2150	281 ± 14	4.27	11.40	16.81	-22.88	-23.00	1.977	1.706
J1213+6708	0.1229	292 ± 15	3.13	11.16	15.70	-22.57	-22.69	2.969	2.604
J1218+0830	0.1350	219 ± 11	3.47	11.21	15.89	-22.61	-22.72	2.739	2.414
J1250+0523	0.2318	252 ± 14	4.18	11.26	16.88	-23.01	-23.11	1.297	1.290
J1402+6321	0.2046	267 ± 17	4.53	11.46	16.52	-23.02	-23.14	2.251	1.997
J1403+0006	0.1888	213 ± 17	2.62	10.98	17.19	-22.14	-22.26	1.131	1.041
J1416+5136	0.2987	240 ± 25	6.08	11.56	17.71	-22.85	-22.97	1.227	1.082
J1420+6019	0.0629	205 ± 10	1.26	10.59	15.19	-21.54	-21.65	2.048	1.575
J1430+4105	0.2850	322 ± 32	6.53	11.73	16.96	-23.49	-23.58	1.728	1.668
J1432+6317	0.1230	199 ± 10	2.78	11.05	15.44	-22.80	-22.93	3.751	3.724
J1436–0000	0.2852	224 ± 17	4.80	11.36	17.41	-23.03	-23.13	1.776	1.587
J1443+0304	0.1338	209 ± 11	1.93	10.78	17.02	-21.45	-21.57	1.230	0.984
J1451–0239	0.1254	223 ± 14	2.33	10.92	16.08	-22.21	-22.33	2.167	2.010
J1525+3327	0.3583	264 ± 26	6.55	11.68	17.39	-23.63	-23.79	2.180	1.773
J1531–0105	0.1596	279 ± 14	4.71	11.43	15.95	-22.92	-23.04	2.573	2.201
J1538+5817	0.1428	189 ± 12	2.50	10.95	16.78	-21.87	-21.98	1.384	1.270
J1621+3931	0.2449	236 ± 20	4.97	11.47	16.95	-23.09	-23.22	1.908	1.698

Table 5.1 – *continued*

Name	z	σ_* [km s^{-1}]	$R_{\rm EIN}$ [kpc]	$\log M_{\rm EIN}$ [$M_\odot$]	m_I [mag]	M_V [mag]	M_r [mag]	$\log R_{\rm e}^{\rm maj}$ [arcsec]	$\log R_{\rm e}$ [arcsec]
(1)	(2)	(3)	(4)	(5)	(6)	(7)	(8)	(9)	(10)
J1627–0053	0.2076	290 ± 15	4.18	11.36	16.92	-22.66	-22.78	1.660	1.514
J1630+4520	0.2479	276 ± 16	6.91	11.69	17.00	-23.06	-23.18	1.537	1.394
J1636+4707	0.2282	231 ± 15	3.96	11.25	17.17	-22.67	-22.78	1.402	1.272
J2238–0754	0.1371	198 ± 11	3.08	11.11	16.33	-22.18	-22.30	1.963	1.748
J2300+0022	0.2285	279 ± 17	4.51	11.47	17.22	-22.61	-22.73	1.410	1.298
J2303+1422	0.1553	255 ± 16	4.35	11.42	16.07	-22.69	-22.83	2.591	2.108
J2321–0939	0.0819	249 ± 12	2.47	11.08	14.82	-22.44	-22.56	3.316	2.963
J2341+0000	0.1860	207 ± 13	4.50	11.35	16.48	-22.81	-22.94	2.661	2.078

Notes: (1) Galaxy name. (2) – (3) Galaxy redshift and SDSS-measured stellar velocity dispersion within the spectroscopic aperture of diameter 3 arcsec, both taken from Treu et al. (2010) their Table 1. (4) – (5) Einstein radius and total projected mass within a cylinder of radius equal to $R_{\rm EIN}$, taken from Auger et al. (2009), their Table 4. (6) I-band apparent magnitude ($F814W$) derived from the MGE model (1σ random error of 0.06 mag). (7) – (8) V and r-band absolute magnitudes (1σ random error of 0.05 mag). (9) Major axis of the isophote containing half of the analytic total light of the MGE models (1σ error of 10 per cent or 0.041 dex). (10) Circularized effective radius $R_{\rm e} = \sqrt{A_{\rm e}/\pi}$ where $A_{\rm e}$ is the area of the effective isophote containing half of the analytic total light of the MGE models (same error as $R_{\rm e}^{\rm maj}$.

with fixed $r_{\rm h} = 30$ kpc. We then perform a one-dimensional MGE fit to Eq. (5.1) in order to recover the DM surface density in units of $M_\odot$ pc^{-2}, and add the DM halo to the dynamical modelling (Section5.3.1.2).

Finally, we apply a similar procedure for the SMBH, parametrizing it with a single gaussian with a dispersion of 0.01 arcsec. The SMBH mass is chosen adopting the $M_{\rm BH} - \sigma_{\rm e}$ relation of Gültekin et al. (2009) for elliptical galaxies, where, for each galaxy, $\sigma_{\rm e}$ (i.e., the luminosity averaged stellar velocity dispersion within $R_{\rm e}$) is computed starting from σ_* (the SDSS-measured velocity dispersion, luminosity-averaged within a circular aperture of radius 1.5 arcsec) and using the conversion formula in eq. (1) of Cappellari et al. (2006), thus accounting for aperture correction.

5.3.1.2 The stellar kinematics

The model velocity fields are computed using the Jeans anisotropic MGE (JAM) modelling method of Cappellari (2008), which can be applied to an axisymmetric stellar distribution, described by a three-integral DF. This method assumes a velocity ellipsoid aligned with the cylindrical coordinates (R, z, φ), and a constant vertical anisotropy parametrized by $\beta_z = 1 - \sigma_z^2/\sigma_R^2$.

Indeed, Cappellari et al. (2007) modelled integral-field observations for a sample of 25 ETGs, using orbit-based three-integral axisymmetric models, and measured the shape and orientation of the velocity ellipsoid at every position within the meridional plane (within $R_{\rm e}$). They found that for the fast-rotator galaxies the axial ratio of the ellipsoids varies gradually as a function of the polar angle, in such a way that the ellipsoid has nearly the same oblate shape on both the equatorial plane and the symmetry axis. Thus, to first order the global anisotropy of the galaxies can be described as a simple flattening of the velocity ellipsoid in the z-direction ($\sigma_z^2 < \sigma_R^2$). Conversely, note that the dynamical models used in Chapter 4, built with our Jeans solver code (Chapter 2), are always semi-isotropic models (i.e., $\sigma_z^2 = \sigma_R^2$) since they are based on a two-integral DF, and they become isotropic ($\sigma_z^2 = \sigma_R^2 = \sigma_\varphi^2$) for a particular choice of the Satoh parameter ($k = 1$). However, the implementation of the vertical anisotropy in our code would be straightforward.

For our models we fix $\beta_z = 0.2$, which has been found to be representative of local ETGs (Cappellari et al. 2007). However, relaxing this assumption, and considering isotropic models ($\beta_z = 0$) as done in Treu et al. (2010), negligibly affects our results. Moreover, for simplicity we assume a spatially constant M_*/L, even if recent studies found evidences for a IMF dependence on galactocentric distance (e.g., Martín-Navarro et al. 2014; Pastorello et al. 2014). These evidences do not make our results invalid, since this assumption simply implies that our measured M_*/L represents a mean value in the observed region (which typically has size $r \lesssim R_{\rm e}$), as already done by Cappellari et al. (2013b). This does not exclude, for example, that the IMF might be universal in the outer disc components and vary only within bulges or spheroids (see e.g., Dutton et al. 2013b).

The main ingredients of the dynamical modelling are the galaxy surface brightness in units of $L_\odot$ pc^{-2}, and the galaxy surface density of the total mass distribution in units of $M_\odot$ pc^{-2}. This last is the sum of the three components (stars, DM and SMBH) obtained as described in Section 5.3.1.1, where the stellar one is multiplied by a stellar mass-to-light ratio $(M_*/L)_{\rm dyn}$ that is the quantity we want to retrieve (as

will be explained in Section 5.3.1.3). Then the only free parameters left are β_z and the inclination angle i, whose values have to be provided or assumed. Indeed, once the MGE parametrization of the surface brightness profile is obtained, the MGE parametrization of the intrinsic light profile can be easily and analytically recovered for a choice of the inclination angle i. Here we adopt $i = 60°$, i.e., the average inclination for random orientations, and, whenever the axial ratio of the gaussians does not allow deprojection for this inclination, we adopt the minimum inclination permitted. Note that a significant error in the adopted value of i would produce errors smaller that 10 per cent on the retrieved mass-to-light ratio, if the observed axial ratio is $q < 0.7$ (see Cappellari et al. 2006 Fig. 4 for a detailed discussion). Given these inputs, with the JAM[1] method we are able to directly compute the projected second velocity moment along the line-of-sight (LOS) $V_{\rm rms}$, with a single numerical quadrature. Finally, in order to compare $V_{\rm rms}$ with σ_*, we convolve it with a gaussian PSF with a FWHM of 1.5 arcsec, as typical for SDSS observations, and then we compute a luminosity-weighted average inside the 3 arcsec diameter SDSS fiber.

5.3.1.3 Inferring the parameters of the dynamical models

For each galaxy in the sample we built a set of galaxy models, whose mass structure and kinematical configuration have been already described in Sections 5.3.1.1 and 5.3.1.2, respectively. We then use two observationally derived quantities to constrain the best model: the SDSS-measured aperture stellar velocity dispersion σ_*, provided by the SDSS database, and the total projected mass $M_{\rm EIN}$ enclosed within the Einstein ring of radius $R_{\rm EIN}$, calculated by Auger et al. (2009). These quantities are reproduced in Table 5.1 with their errors; for $M_{\rm EIN}$ we adopt an error of 5 per cent.

Within a set, the models have the same values for $(M_{\rm BH}, i, \beta_{\rm z})$, and they differ only in the mass normalization of the two main components: the stellar population and the DM halo. In practice, we choose a sufficiently wide range within which the r-band stellar mass-to-light ratio $(M_*/L)_{\rm dyn}$ is allowed to vary, and we multiply the MGE model surface density by $(M_*/L)_{\rm dyn}$; in this way we convert the MGE model into a mass density. Analogously, we choose a range for the DM mass normalization by using the parameter $f_{\rm DM}$, i.e., the DM fraction within a sphere of radius equal to one effective radius $R_{\rm e}$; obviously $0 \leq f_{\rm DM} \leq 1$. We then build a model for each couple of values $((M_*/L)_{\rm dyn}, f_{\rm DM})$, and we choose the best-fitting model by means of chi-squared minimization on the two observables $(\sigma_*, M_{\rm EIN})$. The chi-square maps for the whole sample (Fig. 5.3) show some degeneracy between $f_{\rm DM}$ and $(M_*/L)_{\rm dyn}$. In general, the DM fraction is very low ($f_{\rm DM} \lesssim 0.4$) and for nearly half of the sample it tends to zero, probably due to systematics. Few galaxies are indeed scarcely reproduced by the NFW profile here adopted, probably due to systematic errors associated with σ_*, or to difficulties in the retrieval of the MGE parametrization because of strong lens disturbances, or to the lensing analysis. Table 5.2 shows the best-fitting $(M_*/L)_{\rm dyn}$ and $f_{\rm DM}$, and reports the associated typical errors. These are the median values of the 1σ errors, computed projecting the white areas in Fig. 5.3 in the allowed region of the parameters.

Isotropic models (not shown here) result overall in lower $f_{\rm DM}$ and higher $(M_*/L)_{\rm dyn}$, which do not affect any of our results. The dynamical contribution of the SMBH

Table 5.2: Mass-to-light ratios and $f_{\rm DM}$ of the models for the 55 galaxy SLACS subsample

Name	$\log(M/L)_{\rm MFL}$ $[M_\odot/L_{\odot r}]$	$\log(M_*/L)_{\rm dyn}$ $[M_\odot/L_{\odot r}]$	$\log(M_*/L)_{\rm Salp}$ $[M_\odot/L_{\odot r}]$	$f_{\rm DM}$
(1)	(2)	(3)	(4)	(5)
J0029–0055	0.693	0.609	0.610	< 0.207
J0037–0942	0.665	0.648	0.615	0.036
J0044+0113	0.771	0.708	0.642	< 0.174
J0216–0813	0.747	0.737	0.635	< 0.401
J0252+0039	0.439	-0.178	0.646	0.804
J0330–0020	0.487	0.279	0.557	0.350
J0728+3835	0.491	0.331	0.598	0.416
J0737+3216	0.819	0.662	0.572	< 0.061
J0822+2652	0.681	0.665	0.531	0.041
J0841+3824	0.688	0.672	0.724	0.079
J0912+0029	0.872	0.848	0.728	< 0.174
J0935–0003	0.923	0.784	0.545	< 0.511
J0936+0913	0.640	0.611	0.600	< 0.123
J0946+1006	0.871	0.824	0.632	0.137
J0955+0101	0.858	0.846	0.640	< 0.246
J0956+5100	0.826	0.765	0.646	< 0.070
J0959+4416	0.631	0.609	0.524	0.003
J0959+0410	0.777	0.763	0.661	0.024
J1020+1122	0.662	0.595	0.634	0.194
J1023+4230	0.674	0.578	0.662	0.256
J1029+0420	0.672	0.581	0.637	< 0.044
J1032+5322	1.004	0.804	0.670	< 0.009

Table 5.2 – *continued*

Name	$\log(M/L)_{\rm MFL}$ $[M_\odot/L_{\odot\,r}]$	$\log(M_*/L)_{\rm dyn}$ $[M_\odot/L_{\odot\,r}]$	$\log(M_*/L)_{\rm Salp}$ $[M_\odot/L_{\odot\,r}]$	$f_{\rm DM}$
(1)	(2)	(3)	(4)	(5)
J1103+5322	0.599	0.539	0.690	< 0.246
J1106+5228	0.668	0.593	0.680	< 0.027
J1112+0826	0.793	0.783	0.625	0.001
J1134+6027	0.714	0.698	0.677	0.001
J1142+1001	0.624	0.437	0.665	0.338
J1143-0144	0.754	0.734	0.713	0.060
J1153+4612	0.678	0.656	0.658	0.001
J1204+0358	0.835	0.805	0.677	< 0.065
J1205+4910	0.785	0.751	0.667	< 0.086
J1213+6708	0.817	0.717	0.684	< 0.022
J1218+0830	0.640	0.555	0.667	0.294
J1250+0523	0.548	0.509	0.522	< 0.078
J1402+6321	0.706	0.620	0.661	0.256
J1403+0006	0.656	0.607	0.468	< 0.180
J1416+5136	0.612	0.458	0.575	0.265
J1420+6019	0.596	0.513	0.649	< 0.055
J1430+4105	0.774	0.755	0.640	0.044
J1432+6317	0.569	-0.112	0.658	0.862
J1436–0000	0.588	0.440	0.652	0.338
J1443+0304	0.686	0.647	0.594	< 0.040
J1451–0239	0.679	0.635	0.579	< 0.146
J1525+3327	0.622	0.433	0.612	0.478
J1531–0105	0.728	0.720	0.706	< 0.103
J1538+5817	0.577	0.429	0.671	0.256

Table 5.2 – *continued*

Name	$\log(M/L)_{\rm MFL}$ $[M_\odot/L_{\odot\,r}]$	$\log(M_*/L)_{\rm dyn}$ $[M_\odot/L_{\odot\,r}]$	$\log(M_*/L)_{\rm Salp}$ $[M_\odot/L_{\odot\,r}]$	$f_{\rm DM}$
(1)	(2)	(3)	(4)	(5)
J1621+3931	0.571	0.365	0.629	0.431
J1627–0053	0.830	0.766	0.653	< 0.065
J1630+4520	0.671	0.555	0.685	0.275
J1636+4707	0.620	0.608	0.639	0.030
J2238–0754	0.621	0.461	0.631	0.375
J2300+0022	0.804	0.754	0.661	0.115
J2303+1422	0.779	0.744	0.691	0.147
J2321–0939	0.709	0.700	0.657	0.001
J2341+0000	0.616	0.219	0.470	0.676

Notes: (1) Galaxy name. (2) Total mass-to-light ratio of the mass-follows-light dynamical models (Section 5.3.1) in the r-band (1σ error of 14 per cent or 0.056 dex). (3) – (4) r-band stellar mass-to light ratios derived from the dynamical and the stellar population synthesis models, respectively (Sections 5.3.1 and 5.3.2). The 1σ error in $(M_*/L)_{\rm dyn}$ is 28 per cent (0.106 dex), and 7 per cent (0.03 dex) for $(M_*/L)_{\rm Salp}$. (5) DM fraction enclosed within a sphere of radius $R_{\rm e}$, derived from the dynamical models (1σ error of 0.16).

is irrelevant, since removing it from the modelling results in a negligible increase of $(M_*/L)_{\rm dyn}$: the percentage variation has a median value of 1 per cent for the whole sample, and is always smaller than 7 per cent.

Finally, we also built another set of dynamical models where the total mass distribution follows that of the light (mass-follows-light models). These are less sophisticated dynamical models that are constrained only using σ_*, and whose best-fitting mass-to-light ratios are reported in Table 5.2 as $(M/L)_{\rm MFL}$. The associated typical error is reported in Table 5.2. It is computed propagating the errors in σ_* and in the JAM modelling (6 per cent, as evaluated in Cappellari et al. 2006 from a wider exploration of dynamical modelling approaches), and adopting the median value for all the galaxies.

5.3.2 The stellar population synthesis modelling

Our stellar population synthesis models are performed applying a full-spectrum fitting approach to SDSS spectra, and using a selection of the simple stellar population (SSP) models of Vazdekis et al. (2010)[4], which are based on the MILES stellar spectral library (Sánchez-Blázquez et al. 2006), and cover the wavelength range $3540 - 7410$ Å at 2.50 Å (FWHM) spectral resolution. In particular, we adopt the Salpeter (1955) IMF as reference, and we select the MILES SSP models with age $t \geqslant 1$ Gyr and metallicity $-1.71 \leqslant [M/H] \leqslant 0.22$: this leads to a total of 156 SSPs with 26 logarithmically-spaced ages, and metallicity values $[M/H] = [-1.71, -1.31, -0.71, -0.40, 0.00, 0.22]$. For each galaxy then, the spectral fitting is allowed to use only SSPs with age not greater than the age of the Universe at the galaxy redshift, reducing the number of SSP templates to $N < 156$. The full-spectrum fitting is performed with the PPXF software[1], which implements the Penalized Pixel-Fitting method of Cappellari & Emsellem (2004), and, for each galaxy, returns the best fitting matrix of weights w (to be multiplied by the SSP templates). Then, the stellar mass-to-light ratio in the r-band associated with the population model is

$$(M_*/L)_{\rm Salp} = \frac{\sum_{j=1}^{N} w_j \, M_j^{\rm nogas}}{\sum_{j=1}^{N} w_j \, L_{j,\,r}}, \tag{5.2}$$

where $M_j^{\rm nogas}$ and $L_{j,\,r}$ are the stellar mass (including neutron stars and black holes, but excluding the gas lost by the stars during stellar evolution) and the r-band luminosity of the j-th SSP, respectively. In general, for these unregularized fits, we find that $N \leqslant 5$, and in most of the cases $N = 2$ with the older and more metal rich SSP having $w \simeq 1$.

The spectral fitting has been performed also using the ppxf keyword REGUL: in this way the fitting procedure is forced to apply a linear regularization to the weights (see equation 18.5.10 of Press et al. 1992), obtaining a smoother solution than the unregularized fit. The regularized solution is as statistically good as the unregularized one, being still consistent with the observations, but it is more physically plausible and representative of the galaxy population since it reduces the scatter in the retrieved population parameters (i.e., age and metallicity) of the solution. The regularized $(M_*/L)_{\rm Salp}$ slightly underestimate the unregularized ones by 0.02

[4] Available at `http://miles.iac.es/`

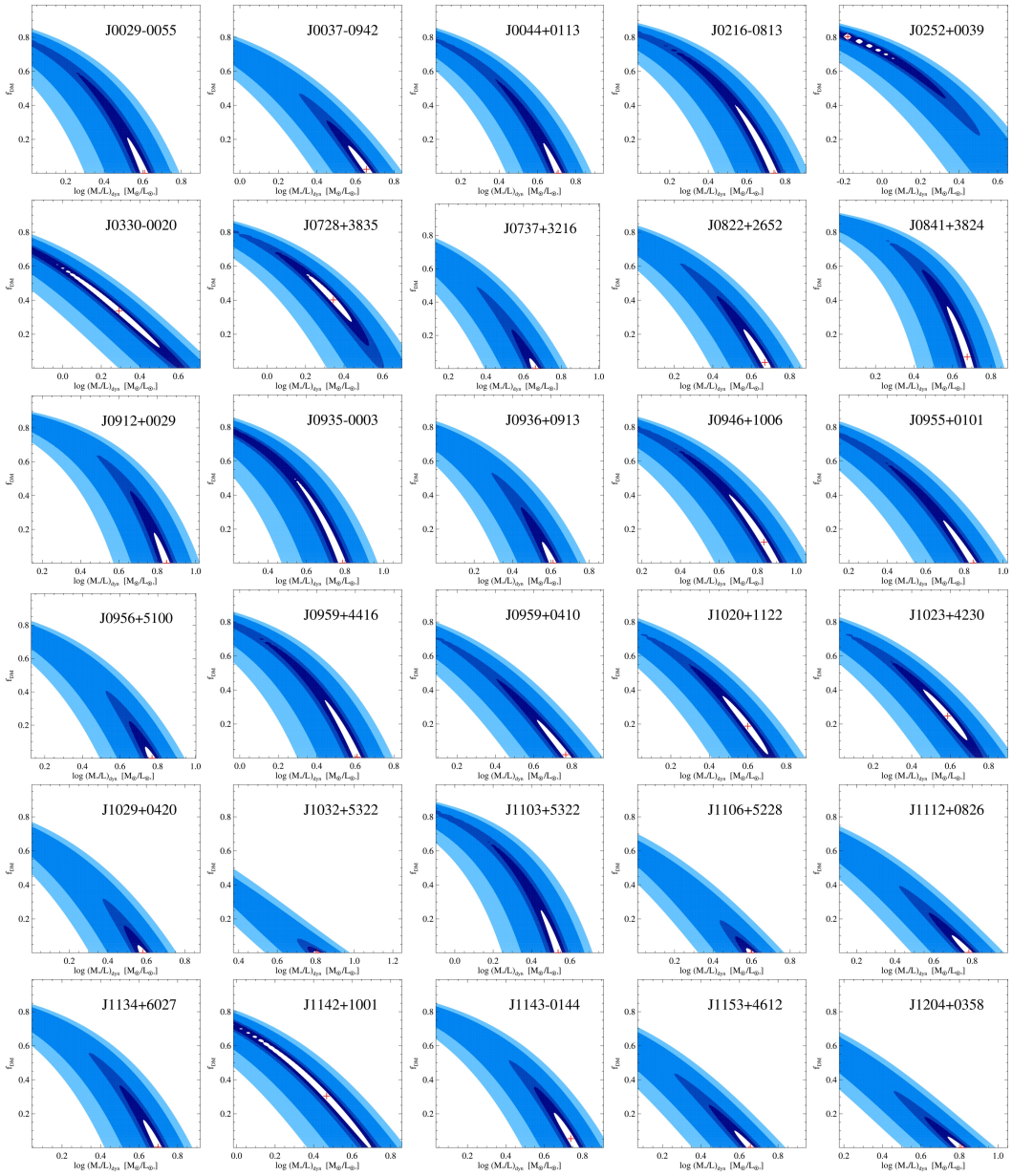

Figure 5.3: $\Delta\chi^2$ contour maps obtained from the dynamical models, as a function of the DM fraction $f_{\rm DM}$ (vertical axis) and r-band stellar mass-to light ratio $(M_*/L)_{\rm dyn}$ (horizontal axis). The red cross locates the minimum chi-square value. The $1, 2, 3\,\sigma$ confidence levels for 1 degree of freedom ($\Delta\chi^2 = 1, 4, 9$) are shown in white, dark blue and light blue, respectively.

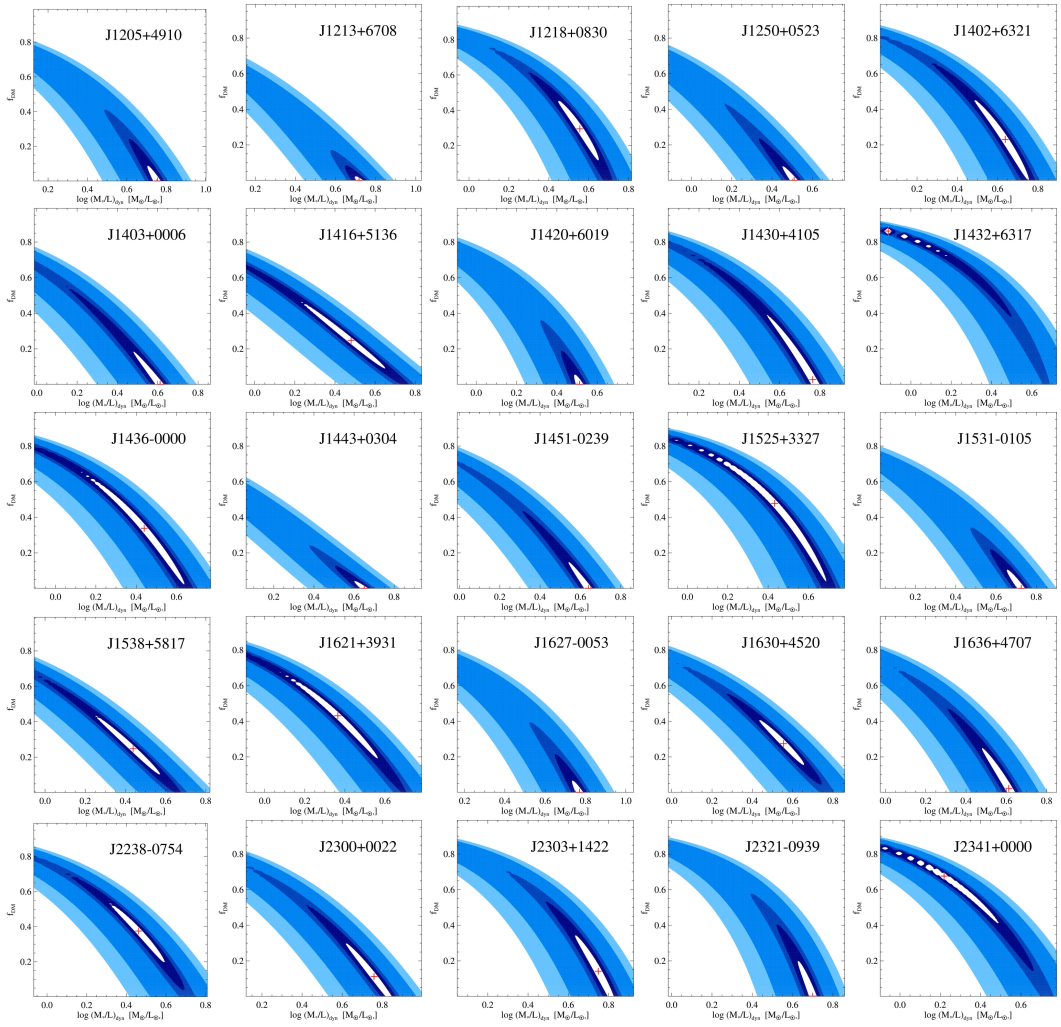

Figure 5.3: – *continued*

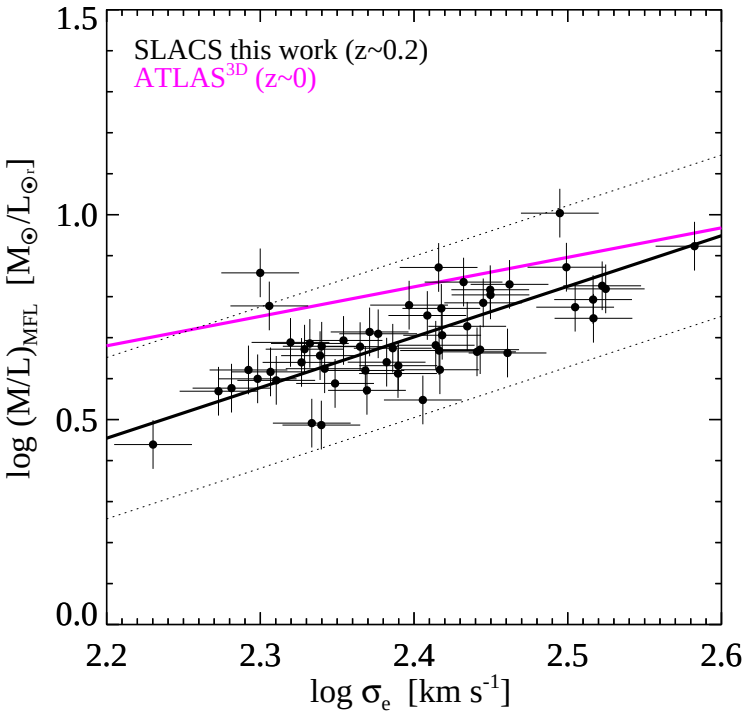

Figure 5.4: r-band mass-to-light ratios of the mass-follows-light dynamical models for the SLACS sample, as a function of σ_e, and their best-fitting relation (black line). The magenta line is the best-fitting relation for the ATLAS^{3D}sample (Cappellari et al. 2013b). The values of σ_e are computed as described at the end of Section 5.3.1.1. Our best-fitting relation is obtained with LTS_LINEFIT, and the dotted lines mark the 3σ bands (enclosing 99.7% of the values for a Gaussian distribution). Outliers deviating more than 3σ from the best-fitting relation were automatically excluded from the fit (i.e., points beyond the dotted lines).

dex, with an rms scatter of 0.014 dex; this would imply errors of 7 per cent in the individual $(M_*/L)_{\rm Salp}$. Finally we find that our results are robust against plausible variations of the REGUL parameter, so that here we present the results obtained with the regularized solutions. In both fits we make use of a 10-th degree multiplicative Legendre polynomial to correct the continuum shape for calibration effects and to account for possible intrinsic dust absorption. The best-fitting $(M_*/L)_{\rm Salp}$ are reported in Table 5.2 for each galaxy.

5.4 Results

Here we present our main results regarding the mass-to-light ratios we derived and their correlation with the stellar velocity dispersion ($M/L - \sigma$ relation), and we focus mostly on the implications concerning the IMF normalization.

5.4.1 Mass-follows-light models

We recall that these models have a total mass profile that follows that of the light, and are tuned to reproduce only the galaxy surface brightness and the SDSS-measured aperture velocity dispersion. Figure 5.4 shows the mass-to-light ratios $(M/L)_{\rm MFL}$ we derived for these dynamical models as a function of $\sigma_{\rm e}$, and the black line is the $M/L-\sigma_{\rm e}$ relation we obtained for the SLACS sample. The relation is of the form

$$\log(M/L)_r = (1.24 \pm 0.14) \times \log\left(\frac{\sigma_{\rm e}}{200\,{\rm km\ s^{-1}}}\right) + (0.58 \pm 0.02), \qquad (5.3)$$

and has an rms scatter of 0.08 dex. The best-fitting relation has been obtained using the LTS_LINEFIT routine[1] of Cappellari et al. (2013b), which allows and fits for intrinsic scatter, and robustly manages the presence of outliers. In the fit we consider a typical error of 6 per cent for $\sigma_{\rm e}$, and we quadratically co-added JAM modelling errors of 14 per cent, plus distance errors, plus 5 per cent errors for our photometry. When compared with previous similar estimates for different samples of ETGs, local and not (e.g., Cappellari et al. 2006; van der Marel & van Dokkum 2007; Cappellari et al. 2013b), our relation is slightly steeper. For example, analogous mass-follows-light models have been built also for the ATLAS$^{\rm 3D}$(Cappellari et al. 2013b) and SAURON samples (Cappellari et al. 2006), leading to $M/L-\sigma_{\rm e}$ relations shallower than our, and with higher zero-points (e.g., see the magenta line in Fig. 5.4). The ATLAS$^{\rm 3D}$sample consists of local galaxies, while the SLACS galaxies reside at higher redshifts (the median redshift for the SLACS sample is $z \simeq 0.2$), so that their stellar populations are younger on average, resulting in lower stellar mass-to-light ratios. Indeed the offset between the two samples can be accounted just by considering passive evolution. For reference, a solar metallicity ($[Z/H] = 0$) passively evolving stellar population varies its M/L_r by ~ 0.10 dex from an age of 11 Gyr to 14 Gyr ($z \sim 0.2$ to $z = 0$, assuming it formed at $z_{\rm form} = \infty$), according to the models of Maraston (2005). This value provides a lower limit to the expected passive M/L_r variation we should observe.

A possible explanation for the steeper slope, instead, could be provided by indications that the $M/L-\sigma_{\rm e}$ relation might steepen at the high $\sigma_{\rm e}$ end (Zaritsky et al. 2006). In fact, the SLACS sample consists mostly of high velocity dispersion galaxies ($200\,{\rm km\ s^{-1}} \lesssim \sigma_{\rm e} \lesssim 400\,{\rm km\ s^{-1}}$) due to its selection criteria, while for example the volume limited ATLAS$^{\rm 3D}$sample extends from high-intermediate $\sigma_{\rm e}$ galaxies to very low $\sigma_{\rm e}$ systems ($50\,{\rm km\ s^{-1}} \lesssim \sigma_{\rm e} \lesssim 250\,{\rm km\ s^{-1}}$). Thus the two relations shown in Fig. 5.4 have been obtained sampling different ranges in velocity dispersion, that barely intersect each other.

5.4.2 Dependency of the IMF normalization on velocity dispersion

Figure 5.5 shows the two sets of stellar mass-to-light ratios obtained from our dynamical and stellar population synthesis models, one against the other. Note that, at variance with $(M/L)_{\rm MFL}$, the dynamical mass-to-light ratios $(M_*/L)_{\rm dyn}$ here shown are purely stellar, since a NFW DM halo has been included in the modelling, so that they can be directly compared with $(M_*/L)_{\rm Salp}$. Thus, if for example the IMF of ETGs is universal and Salpeter-like, $(M_*/L)_{\rm dyn}$ should be very similar

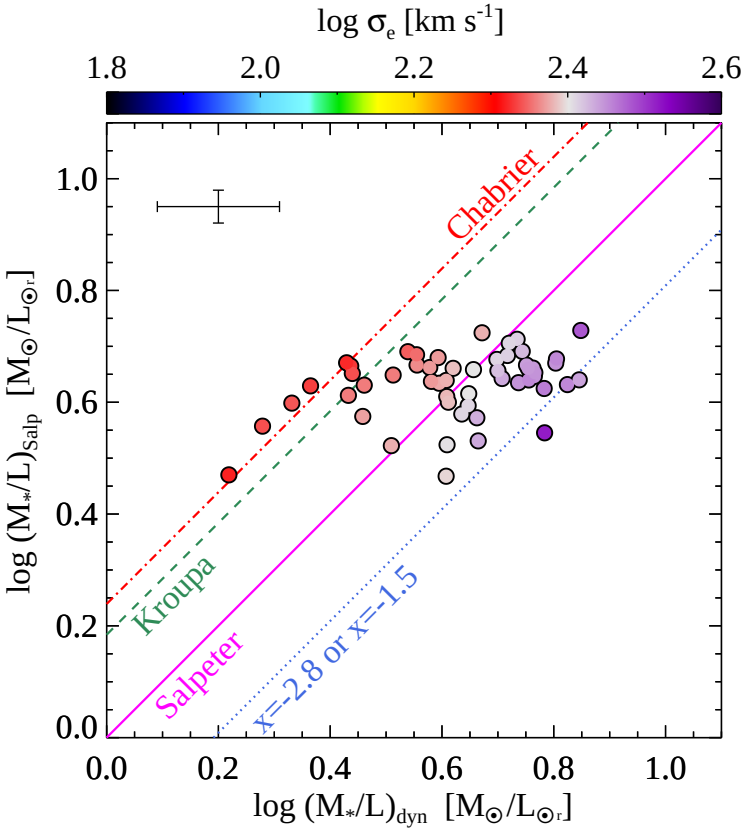

Figure 5.5: The stellar mass-to-light ratios $(M_*/L)_{\rm Salp}$ for a Salpeter IMF (Section 5.3.2) are shown as a function of the dynamical stellar mass-to-light ratios $(M_*/L)_{\rm dyn}$ (Section 5.3.1), both derived in the r-band. The colours of the symbols code the galaxy velocity dispersion: in place of the individual $\sigma_{\rm e}$ values, here we show the two-dimensional LOESS smoothed $\sigma_{\rm e}$ values (see the top colour bar). A representative error bar is shown at the top-left. Two galaxies resulting in too high and unrealistic DM fractions (J0252+0039 and J1432+6317) have been excluded from the plot. The diagonal lines are computed from the Vazdekis et al. (2010) models for a population with solar metallicity.

to $(M_*/L)_{\rm Salp}$, which has been calculated under this assumption (i.e., all galaxies should lie close to the magenta line, with some scatter). If otherwise ETGs have a lighter IMF, like Chabrier or Kroupa, one would expect to find that $(M_*/L)_{\rm Salp}$ systematically overestimates $(M_*/L)_{\rm dyn}$ by the same percentage, for the whole sample. The situation apparent in Fig. 5.5 is somewhat different: galaxies do not lie near one of the lines representing different IMFs, but are distributed across all of them. The scatter is significant compared to the typical error, and reveals that some galaxies are actually more properly represented by a lighter or a heavier IMF normalization. This suggests a variation of the IMF for ETGs, that seems also to correlate with the galaxy velocity dispersion, with low-$\sigma_{\rm e}$ galaxies being consistent with a Chabrier or Kroupa-like IMF, while medium and high-$\sigma_{\rm e}$ galaxies agree with a Salpeter or heavier IMF. Note that our results are equally consistent with both a bottom heavy and top heavy IMF trend (as considered by Weidner et al. 2013), since the approach we use does not constrain the shape of the IMF directly, but only the overall mass normalization. In Fig. 5.5 each galaxy is coloured according to its LOESS-smoothed value of $\sigma_{\rm e}$, as done in Cappellari et al. (2013a) (their fig. 11). Applying the LOESS[1] method (Cleveland 1979), we evaluated mean values of $\sigma_{\rm e}$ that are the result of an average over the neighbouring galaxies, weighted with the relative distances. In this way, one aims to reconstruct the average values characterizing the underlying galaxy population, i.e., the values one should expect to obtain when disposing of much larger galaxy samples.

Another way of seeing this variation is by looking at the IMF mismatch parameter $\alpha \equiv (M_*/L)_{\rm dyn}/(M_*/L)_{\rm Salp}$. Figure 5.6 shows the logarithm of α as a function of σ_*, as already done in Treu et al. (2010) (see their fig. 4, central panel). Here, the red points refer to the values obtained by Treu et al. (2010), while our results are shown in black, and the solid lines are the respective best-fitting relations. Note that the dynamical models of Treu et al. (2010) consist of spherical isotropic models, with a stellar component following a Hernquist (1990) profile. Moreover their stellar population synthesis models were built using multicolour *HST* photometry, while ours are based on full-spectrum fitting. Regardless of the very different approaches adopted, we find that the two works produce essentially the same result pointing toward an IMF variation, with high-σ_* galaxies being consistent on average with a Salpeter normalization. Our relation is

$$\log\alpha = (1.3 \pm 0.23) \times \log\left(\frac{\sigma_*}{200\,{\rm km\ s^{-1}}}\right) - (0.14 \pm 0.03), \tag{5.4}$$

with an rms scatter of 0.1 dex; in the fit we consider a median error of 6 per cent for σ_*, and we quadratically co-added the dynamical modelling errors of 28 per cent, plus distance errors, plus population models errors of 7 per cent, plus 5 per cent errors for our photometry. Our relation is very similar to that reported in Treu et al. (2010). However, inspecting Fig. 5.6 a difference must be noted: our dynamical modelling produces a weaker correlation, in the sense that our points are more scattered in the $(\log\alpha, \sigma_*)$ plane with respect to the points of Treu et al. (2010). This is reasonably due to the use of a more flexible parametrization of the light profiles. Indeed, given its nature, the SLACS sample is likely to include also compact galaxies, and using a density profile with a fixed internal slope (like the Hernquist profile) to fit all the galaxies might artificially produce some correlation, by overestimating the stellar

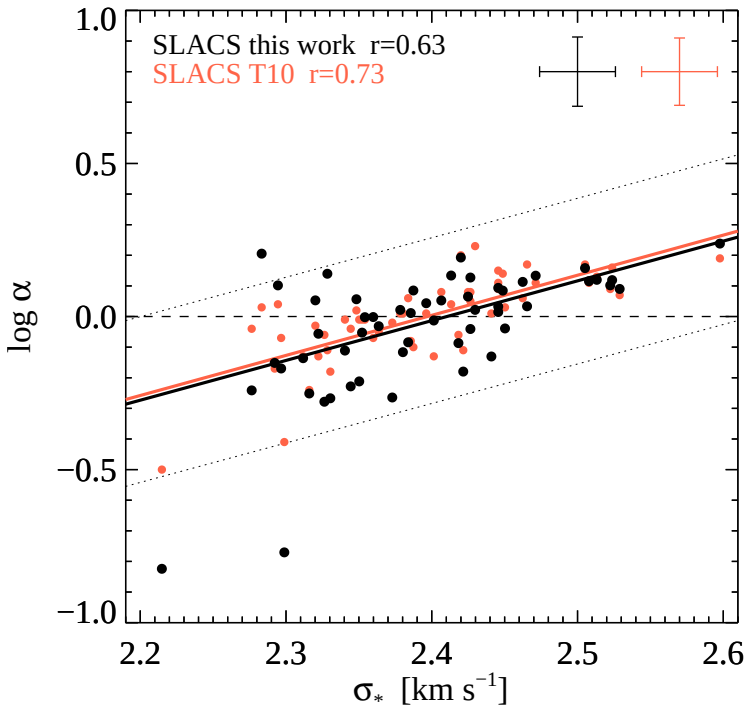

Figure 5.6: IMF mismatch parameter α as a function of σ_* for the SLACS sample. Red points are taken from Treu et al. (2010), as well as their best-fitting relation represented by the red line. Black points refer to the values computed in this work. The black line is our best-fitting relation obtained with LTS_LINEFIT, and the dotted lines mark the 3σ bands (enclosing 99.7% of the values for a Gaussian distribution). Outliers deviating more than 3σ from the best-fitting relation were automatically excluded from the fit (i.e., points beyond the dotted lines). The value of the linear correlation coefficient r is also reported. Representative error bars are shown at the top-right: for the data of Treu et al. (2010) we compute the median error.

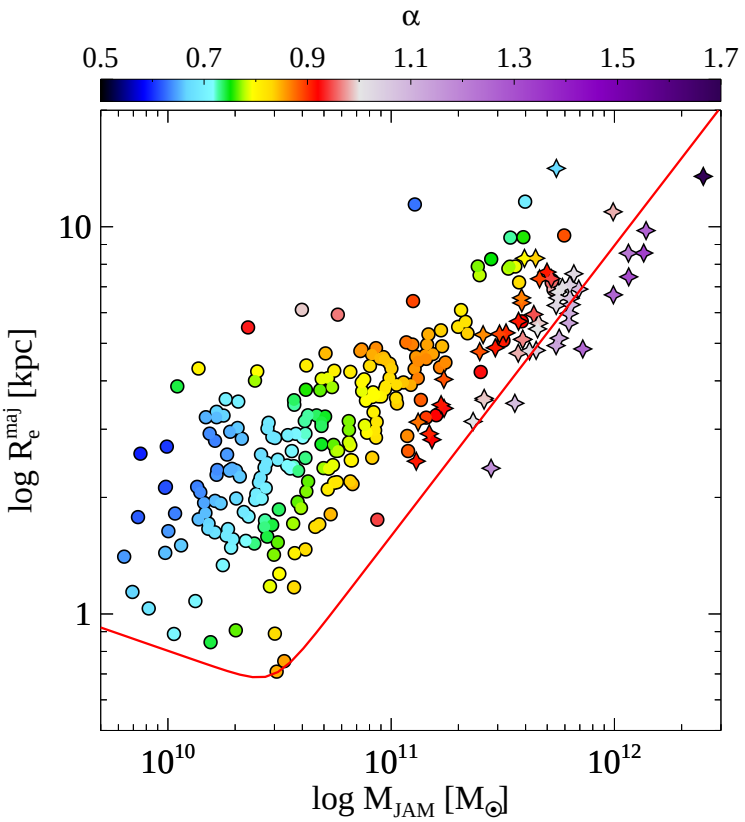

Figure 5.7: R_e^{maj}, the major axis of the isophotes containing half of the analytic total light of the MGE models, is shown as function of M_{JAM}, the total mass of the mass-follows-light models (i.e. $M_{JAM} = (M/L)_{MFL} \times L_r$), for the SLACS (stars) and ATLAS^{3D}samples (circles). The colours of the symbols code the ratio $\alpha = (M_*/L)_{dyn}/(M_*/L)_{Salp}$: in place of the individual α values, here we show the two-dimensional LOESS smoothed α values (see the top colour bar). The red line shows the zone of exclusion relation given by equation (4) of Cappellari et al. (2013a), for the ATLAS^{3D}sample.

mass in the high-σ_e compact galaxies. Figure 5.7 illustrates the type of galaxies that are in the σ-selected SLACS sample (stars), compared to the volume-selected ATLAS^{3D}sample (circles): it can be noticed that they are quite massive and dense, since they fill the lower envelope of the galaxy distribution in the (R_e^{maj}, M_{JAM}) at the high mass end (i.e., with the smaller R_e^{maj} for $M_{JAM} > 10^{11} M_\odot$).

Finally, the analysis we conducted on the SLACS sample is analogous to the one performed on the ATLAS^{3D}sample, both in terms of the dynamical and stellar population approach. This allows us to directly compare the respective results, and merge the two samples homogeneously analysed to infer some global insights on the IMF of ETGs. Fig. 5.8 shows the IMF mismatch parameter as a function of σ_e for the two samples (i.e., SLACS in black and ATLAS^{3D}in magenta). Here, notwithstanding the heterogeneity of the samples in terms of selection criteria, galaxy redshift and mass range, one can immediately appreciate how the black points seem to follow the same relation of the magenta points, but extending to higher σ_e values. Indeed, the

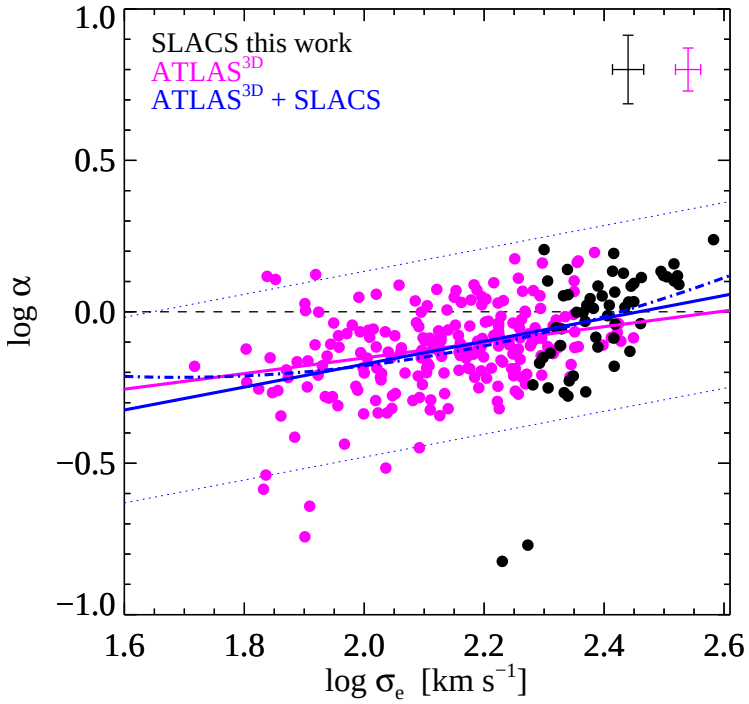

Figure 5.8: The IMF mismatch parameter α is shown as a function of σ_e for the SLACS (black) and the ATLAS^{3D}sample (magenta). The magenta solid line is the best-fitting relation for the subset of the whole ATLAS^{3D}sample made of 223 galaxies with the stellar absorption line-strength index Hβ < 2.3 Å, taken from Cappellari et al. (2013a). The blue solid line is the best-fitting relation for the two samples put together, obtained with LTS_LINEFIT, and the blue dotted lines mark the 3σ bands (enclosing 99.7% of the values for a Gaussian distribution). Outliers deviating more than 3σ from the best-fitting relation were automatically excluded from the fit (i.e., points beyond the dotted lines). The blue dot-dashed line is a parabolic fit to both samples together, performed with the MPFITFUN routine. Representative error bars are shown at the top-right: for the data of Cappellari et al. (2013a) we compute the median error.

magenta solid line, representing the best-fitting relation for the ATLAS^{3D}sample, is only slightly shallower that the blue solid line, obtained by fitting both samples together; in particular, we find for the whole sample SLACS + ATLAS^{3D}

$$\log \alpha = (0.38 \pm 0.04) \times \log \left(\frac{\sigma_e}{200\,\mathrm{km\ s^{-1}}} \right) + (-0.06 \pm 0.01), \tag{5.5}$$

with an rms scatter of 0.12 dex. The similarity of the two best-fitting relations is even more remarkable when comparing them with the steeper relation we find for the SLACS sample alone (Eq. 5.4). Note that the steepness of the slope in Eq. 5.4 is not due to the fact that α is fitted as a function of σ_* instead of σ_e, since we find a very similar result also for σ_e (slightly steeper). This shows that the slope of the $\alpha - \sigma_e$ relation is very sensitive to the σ_e range, with a considerable increase for $\sigma_e \gtrsim 250\,\mathrm{km\ s^{-1}}$, and suggests that the relation is not a simple single power law. In this scenario, the steepness of the $\alpha - \sigma_e$ correlation, found by Treu et al. (2010) and confirmed here, for the ETGs of the SLACS sample is a natural consequence of the velocity dispersion selection nature of the SLACS sample. We then try to fit a parabola to the whole sample SLACS + ATLAS^{3D}, obtaining

$$\begin{aligned} \log \alpha =& (0.40 \pm 0.15) \times \log \left(\frac{\sigma_e}{200\,\mathrm{km\ s^{-1}}} \right)^2 + \\ & (0.49 \pm 0.05) \times \log \left(\frac{\sigma_e}{200\,\mathrm{km\ s^{-1}}} \right) + (-0.07 \pm 0.01), \end{aligned} \tag{5.6}$$

with an rms scatter of 0.12 dex.

Thus, by homogeneously studying ETGs collected over a very wide and unprecedented range of σ_e and M_*, we have provided a comprehensive insight about the IMF normalizaton for this morphological type of galaxies, showing that the IMF gets heavier for increasing σ_e, and becomes Salpeter-like at $\sigma_e \simeq 250\,\mathrm{km\ s^{-1}}$. The issue of the IMF variability for the ATLAS^{3D}sample has also been studied by Tortora et al. (2014) within the MOND framework, obtaining results consistent with the ones from Newtonian dynamics plus DM.

5.5 Discussion and Conclusions

In this work we studied the mass normalization of the IMF of ETGs, exploiting information derived from gravitational lensing, stellar dynamics and stellar population synthesis models, and making use of high-quality photometric and spectroscopic data. We selected 55 ETGs belonging to the SLACS sample and constructed dynamical and stellar population synthesis models for each galaxy. Our dynamical models are built solving the Jeans axisymmetric anisotropic equations with the JAM method of Cappellari (2008); they reproduce in detail the *HST* galaxy images and are constrained using the SDSS-measured velocity dispersion and the mass within the Einstein radius. Our stellar population synthesis models are computed with the full-spectrum fitting technique and are based on the SSP models of Vazdekis et al. (2010). We derived accurate estimates of stellar mass-to-light ratios from the two sets of models, $(M_*/L)_{\mathrm{dyn}}$ and $(M_*/L)_{\mathrm{Salp}}$ respectively.

From the comparison of the two estimates of stellar mass-to-light ratios, we find a trend of IMF with velocity dispersion, where, on average, the IMF normalization smoothly varies from Kroupa/Chabrier for galaxies with $\sigma_e \sim 90\,\mathrm{km\ s^{-1}}$, up to a bottom-heavy Salpeter-like IMF for galaxies with $\sigma_e \sim 270\,\mathrm{km\ s^{-1}}$ (Fig. 5.5). This change of IMF normalization as a function of σ_e is significant beyond the extent of the error estimates in the stellar the mass-to-light ratios, and thus suggests an intrinsic systematic variation of the stellar IMF for ETGs.

With our accurate and realistic modelling of the stellar profiles, our analysis provides an improvement over the study of Treu et al. (2010), conducted on the same ETG sample. Notwithstanding the different and independent approaches adopted, we confirm their finding of a steep correlation between the IMF mismatch parameter $\alpha = (M_*/L)_{\rm dyn}/(M_*/L)_{\rm Salp}$ and the galaxy velocity dispersion (Fig. 5.6); however our relation has a slightly lower correlation coefficient, presumably due to relaxing the restrictive assumption of a fixed stellar density profile to fit the whole galaxy sample.

We also built mass-follows-light dynamical models and computed total mass-to-light ratios $(M/L)_{\rm MFL}$ for them. We find a $(M/L)_{\rm MFL} - \sigma_e$ correlation steeper than previous analogous estimates for different local ETG samples (e.g., the $(M/L)_{\rm MFL} - \sigma_e$ relation for the 260 ETGs ATLAS$^{\rm 3D}$sample), and with a lower zero-point (Fig. 5.4). The SLACS sample resides at higher redshift and is likely to include galaxies with younger stellar populations; indeed the offset in the zero-points can be accounted for by passive evolution between $z \sim 0.2$ and $z = 0$. The different slope instead could be an effect of the different σ_e range spanned by the samples, in accordance with Zaritsky et al. (2006) that suggests a steepening this relation as a function of σ_e. Note that the slope of the $(M/L)_{\rm MFL} - \sigma_e$ relation gives an upper limit to any systematic increase of the IMF mass normalization with σ_e.

Finally, as an important outcome of analysing the SLACS galaxies with a procedure that is homogeneous with that adopted for the ATLAS$^{\rm 3D}$galaxies (Cappellari et al. 2013a), we could merge the two samples. In this way, we explored the behaviour of ETGs in the $\alpha - \sigma_e$ plane with the largest sample ever, where ETGs of all σ_e values from $50\,\mathrm{km\ s^{-1}}$ to $\sim 350\,\mathrm{km\ s^{-1}}$ are well represented. We found that the volume-limited ATLAS$^{\rm 3D}$sample and the velocity dispersion selected SLACS galaxies smoothly merge in a unique shallower relation in the (α, σ_e) plane (Fig. 5.8). From this comprehensive analysis, we find that the $\alpha - \sigma_e$ relation might not be linear, and that the slope inferred depends on the range of σ_e covered by the galaxies. This is significantly different for the ATLAS$^{\rm 3D}$(volume selected) and SLACS sample (velocity dispersion selected).

Chapter 6

Conclusions

Dynamical models of galaxies are a powerful tool to study and understand several astrophysical problems related to galaxy formation and evolution. In this thesis we concentrated on a particular type of dynamical models, that are widely used in literature, and are based on the solution of the Jeans equations. We developed a numerical Jeans solver code able to build state-of-the-art axisymmetric galaxy models, which allow for a full generality in the choice of galaxy shape and of the stellar and DM profiles, multiple mass components, different kinematical configurations, and can be tailored to reproduce observational constraints.

In particular, we focused our attention on the family of ETGs, and we exploited these models to address two of the main issues in the field of research of ETGs, which are currently matter of great interest for the astronomical community.

The first topic concerns the hot and X-ray emitting gaseous coronae that surround ETGs. The main goal is to explain why flat and rotating galaxies generally exhibit haloes with lower gas temperatures $T_{\rm X}$ and luminosities $L_{\rm X}$ with respect to rounder and velocity dispersion supported systems. The bulk of the mass of these haloes is produced by stellar winds, and is heated up to X-ray temperatures by SNIa explosions and by the thermalisation of stellar motions, so that a tight relation links stellar motions and the energetics of the hot gas. Thus, in this thesis, we studied the effects that galaxy shape and rotation can produce on the gas energy budget and content by means of a twofold analysis, based both on theoretical energy estimates and on hydrodynamical simulations. In order to perform a general and systematic investigation able to explore the wide ranges of the involved driving parameters, we built a large set of axisymmetric galaxy models, which are representative of observed ETGs, and have variable degrees of flattening and rotational support of the stellar component, and different DM density profiles.

For these models we computed the equivalent temperature of stellar motions $T_* = T_\sigma + \gamma_{\rm th} T_{\rm rot}$, where the parameter $\gamma_{\rm th}$ takes into account how much of the ordered rotation of the galaxy is eventually thermalised by the stellar mass losses, and the temperature equivalent of the energy required for the gas escape $T_{\rm g}^-$. In particular, different degrees of thermalisation of the ordered rotational field of the galaxy ($\gamma_{\rm th}$) are considered. We find that T_* and $T_{\rm g}^-$ can vary only mildly due to a pure change of shape. Galaxy rotation instead, when not thermalised, can lead to a large decrease of T_*, and this effect can be larger in flatter galaxies that can be more rotationally supported. In light of these results, the observed trend of a lower $T_{\rm X}$ in

flatter and more rotating galaxies could be explained by the lack of thermalisation of the whole stellar kinetic energy.

Then, as a natural extension of the theoretical analysis, in order to take into account the hydrodynamical effects due to the temporal evolution of the mass, momentum and energy sources (e.g., stellar winds and SNIa explosions), and the ISM radiative cooling, we performed high-resolution 2D hydrodynamical simulations, outcome of a joint research collaboration (Negri et al. 2014b). The simulations have been carried out for a large set of ETGs models, built with our Jeans solver code that provides all the dynamical fields necessary for the hydrodynamical equations. The models span the same wide parameter spaces previously explored, so that the results obtained from the simulations are the exact numerical counterpart of the theoretical analysis described above.

We find that, in general, the heating contribution from thermalization of the ordered motions is negligible (i.e., $\gamma_{\rm th} \ll 1$ and so $T_* \simeq T_\sigma$) because the rotation field of the ISM in rotating galaxies is very similar to that of the stars. This implies that, in rotating galaxies, the heating provided to the gas by stellar motions is lower than in dynamically hot systems. In general, the final X-ray temperature $T_{\rm X}$ are larger than the corresponding T_* values, but the qualitative dependence of $T_{\rm X}$ on galaxy mass and shape is very well reproduced by that of T_*, and hence T_σ, which can be computed without resorting to numerical simulations. The relative importance of flattening and rotation in determining the final $T_{\rm X}$ is a function of the galactic mass. Flattening and rotation in low mass galaxies favour the establishment of global winds: this almost depletes the galaxy of gas, leaving it with a small amount of very hot gas, heated to high values of $T_{\rm X}$ due to the thermalisation of the established strong meridional motions. In medium-to-high mass galaxies, flattening and rotation are not sufficient to induce global winds. In these cases, in accordance with observations and the predictions of our theoretical analysis, rotating models have lower $T_{\rm X}$ values than velocity dispersion supported objects. However, the difference in $T_{\rm X}$ is only partially due to the lower T_* of rotating models, since the main agent is the conservation of angular momentum, which deeply affects the nature of the gas flows in rotating models. This causes the creation of a hot gas atmosphere that has both a shallower density profile and a lower total gas mass, that eventually results in a reduction of $T_{\rm X}$. Thus, we conclude that the X-ray coolness and underluminosity of flat and rotating galaxies are major effects of galaxy rotation. However, they cannot be definitively disentangled from galaxy flattening effects, since highly rotating galaxies are generally quite flattened.

A future development of the present work, that could add precious information to this scenario, would consist in the construction of galaxy models that are specifically tailored to reproduce particular observed ETGs (e.g., NGC4649), for which constraints are available in the optical and in the X-rays. This could allow to run more targeted simulations.

The second addressed topic concerns the stellar IMF of ETGs. In this thesis we studied the IMF mass normalization for 55 lens ETGs belonging to the SLACS sample, by means of an analysis which combines three independent diagnostics of mass: stellar dynamics, gravitational lensing, and stellar populations synthesis models. In particular, we constructed two-component axisymmetric dynamical models based on the Jeans equations, which allow for orbital anisotropy, and re-

produce in detail the observed *HST* photometry. The galaxy models are further constrained by the total projected mass within the Einstein radius and the stellar velocity dispersion (σ) within the SDSS fibers. Assuming a DM halo slope $\rho_{\rm h} \propto r^{-1}$, we computed the best-fitting dynamically-derived stellar mass-to-light ratios $(M_*/L)_{\rm dyn}$. We then built stellar population synthesis models via full spectrum fitting of SDSS spectra, and derived the best fitting stellar mass-to-light ratios $(M_*/L)_{\rm Salp}$ for an assumed Salpeter IMF. From the comparison of $(M_*/L)_{\rm dyn}$ and $(M_*/L)_{\rm Salp}$, derived in independent manners, we infer the mass normalization of the IMF. Our results confirm the previous analysis by the SLACS team that the mass normalization of the IMF of high σ galaxies is consistent on average with a Salpeter slope. Most importantly, our study allows for a fully consistent and homogeneously carried out study of the trend between IMF and σ for both the SLACS and ATLAS$^{\rm 3D}$samples. The two samples explore quite different σ ranges, and are highly complementary, the first being essentially σ selected, and the latter volume-limited and nearly mass selected. We find that the two samples merge smoothly into a single trend of the form $\log\alpha = (0.38 \pm 0.04) \times \log(\sigma_{\rm e}/200\,{\rm km\ s^{-1}}) + (-0.06 \pm 0.01)$, where $\alpha = (M_*/L)_{\rm dyn}/(M_*/L)_{\rm Salp}$ and $\sigma_{\rm e}$ is the luminosity averaged σ within one effective radius $R_{\rm e}$. This is consistent with a systematic variation of the IMF normalization from Kroupa to Salpeter in the interval $\sigma_{\rm e} \approx 90 - 270\,{\rm km\ s^{-1}}$.

Future improvements of this study would be possible adding further observational constraints, like integral-field spectroscopic observations, which are already available for 14 of the 55 galaxies here analysed. This could allow to add the DM halo density slope as a free parameter in the dynamical modelling and constrain it, thus deriving more general conclusions on the IMF mass normalization of these galaxies.

Appendix A

The Jeans equations

In this Appendix we introduce the phase space distribution function and we show the derivation of the Jeans equations starting from the Collisionless Boltzmann equation.

A.1 The phase-space distribution function

Consider a system made up of N stars. If N is a large number and if the system is collisionless (i.e. we follow the system evolution to times smaller than the two-body relaxation time t_{2b}) we are allowed to describe it in a continuous way instead of a discrete one, as the system intrinsically is.

So we can introduce the phase-space distribution function $f(\mathbf{x}, \mathbf{v}, t)$ that describes at any time the dynamical state of the N-body system. Its domain is the extended one-particle phase-space $\gamma \times \Re$, i.e. the Cartesian product between the one-particle phase-space $\gamma = \Re^3 \times \Re^3$ and the time interval.

The DF is a real-valued non-negative function defined by

$$\begin{aligned} f &: \gamma \times \Re \mapsto \Re^+ \cup 0 \\ \int_{\Re^3} f(\mathbf{x}, \mathbf{v}, t)\ \mathrm{d}^3\mathbf{v} &= n(\mathbf{x}, t), \end{aligned} \tag{A.1}$$

where $n(\mathbf{x}, t)$ is the (continuous) number density distribution of the discrete N-body system. Given this definition, it follows that the number of stars that, at time t, have positions in the volume $\mathrm{d}^3\mathbf{x}$ centred on $\mathbf{x}$ and velocities included in the range $\mathrm{d}^3\mathbf{v}$ centred on $\mathbf{v}$ is

$$dN = f(\mathbf{x}, \mathbf{v}, t)\ \mathrm{d}^3\mathbf{v}\, \mathrm{d}^3\mathbf{x}. \tag{A.2}$$

Now it can be easily deduced that the total number of stars N of the system is the integral of dN over the whole phase-space γ

$$N = \int_{\Re^3} n(\mathbf{x}, t)\, \mathrm{d}^3\mathbf{x} = \int_{\gamma} f(\mathbf{x}, \mathbf{v}, t)\ \mathrm{d}^3\mathbf{v}\, \mathrm{d}^3\mathbf{x}. \tag{A.3}$$

Thus f is also called phase-space density and it gives, at any time t, a full description of the state of any collisionless system specifying the number of stars in each point of the phase-space. Therefore the DF is somehow related to a continuous probability density function; more precisely the quantity $f(\mathbf{x}, \mathbf{v}, t)\ \mathrm{d}^3\mathbf{v}\, \mathrm{d}^3\mathbf{x}$ represents the probability of finding any star, at time t, in the volume $\mathrm{d}^3\mathbf{v}\, \mathrm{d}^3\mathbf{x}$ around the phase-space point $(\mathbf{x}, \mathbf{v})$.

The DF of a collisionless system satisfies the Collisionless Boltzmann equation (CBE) that can be written as

$$\frac{\partial f}{\partial t} + \mathbf{v} \cdot \frac{\partial f}{\partial \mathbf{x}} - \frac{\partial \Phi_{\mathrm{T}}}{\partial \mathbf{x}} \cdot \frac{\partial f}{\partial \mathbf{v}} = 0, \tag{A.4}$$

where Φ_{T} is the total gravitational potential of the system, comprehensive of the stellar system self-gravity and of its interaction with a possible DM halo. The CBE describes the evolution of the DF in the collisionless regime.

From the DF we can derive macroscopic functions that describe the continuous system and are related to observable quantities: they are f-weighted means over the velocity space of the corresponding microscopic functions. From a physical point of view, the most interesting macroscopic functions are the first and second-order velocity moments and they are defined as

$$\overline{v}_i(\mathbf{x}, t) \equiv \frac{1}{n(\mathbf{x}, t)} \int_{\Re^3} v_i f\, \mathrm{d}^3\mathbf{v}, \tag{A.5}$$

$$\overline{v_i v_j}(\mathbf{x},t) \equiv \frac{1}{n(\mathbf{x},t)} \int_{\Re^3} v_i v_j f \, \mathrm{d}^3\mathbf{v}, \tag{A.6}$$

$$\sigma_{ij}^2(\mathbf{x},t) \equiv \frac{1}{n(\mathbf{x},t)} \int_{\Re^3} (v_i - \overline{v}_i)(v_j - \overline{v}_j) f \, \mathrm{d}^3\mathbf{v}, \tag{A.7}$$

for $i, j = 1, 2, 3$ denoting two generic coordinates in the configuration space. The line over the expressions means that we are calculating a mean weighted with the phase-space distribution function. The first function is the i-component of the mean stellar velocity and it is called streaming velocity; the third function is the ij-component of the symmetric velocity dispersion tensor and represents the random velocities of stars about their mean velocity.

From the three definitions above we have that

$$\sigma_{ii}^2 = \overline{(v_i - \overline{v}_i)^2}, \tag{A.8}$$

and it's easy to prove that

$$\sigma_{ij}^2 = \overline{v_i v_j} - \overline{v}_i \overline{v}_j. \tag{A.9}$$

Due to its symmetry, it is possible to choose an orthogonal matrix in which the tensor σ^2 is diagonal and, in this way, we obtain the velocity ellipsoid, i.e. an ellipsoid whose semi-axes are directed along the basis vectors and have lengths σ_{ii}^2, for $i = 1, 2, 3$. Due to the spectral theorem, since $\sigma^2(\mathbf{x}, t)$ is symmetric, it can be diagonalised through an orthogonal matrix $A(\mathbf{x}, t)$ that changes the reference system in which the tensor is described.

Thus, in this new reference system $\sigma^2(\mathbf{x}, t)$ is diagonal and, due to equation (A.8), its three eigenvalues are positive so that they can be geometrically interpreted as the semi-axis lengths of an ellipsoid, the velocity dispersion ellipsoid that is defined in each point of the stellar system. In particular, inside the stellar system, the velocity dispersion ellipsoid will in principle have a different diagonalising matrix A and different semi-axis lengths from place to place and in time.

If the velocity dispersion ellipsoid is everywhere a sphere (i.e. $\forall \mathbf{x}$ the three eigenvalues coincide) the velocity dispersion tensor is said to be isotropic and we can write it as

$$\sigma_{ij}^2(\mathbf{x},t) = \sigma^2(\mathbf{x},t)\delta_{ij}, \tag{A.10}$$

else it is called anisotropic.

A.2 The Jeans equations

In order to derive the Jeans equations here we follow the same procedure as in Binney & Tremaine (2008). Eq. (A.4) can be integrated in the velocity space obtaining

$$\int \frac{\partial f}{\partial t} \, \mathrm{d}^3\mathbf{v} + \int v_i \frac{\partial f}{\partial x_i} \, \mathrm{d}^3\mathbf{v} - \frac{\partial \Phi_\mathrm{T}}{\partial x_i} \int \frac{\partial f}{\partial v_i} \, \mathrm{d}^3\mathbf{v} = 0, \tag{A.11}$$

where we have used the Einstein summation convention. Since the velocity range of the integration domain does not depend on time, the temporal derivative in the first term can be taken out of the integral. The same holds for the spatial derivative in

the second term because v_i is independent of x_i. Moreover, applying the divergence theorem on the third term makes it vanish, given that $f(\mathbf{x}, \mathbf{v}, t) = 0$ for sufficiently large $|\mathbf{v}|$, i.e., there are no stars that move infinitely fast. Thus, using Eqs. (A.1) and (A.5) we have that

$$\frac{\partial n}{\partial t} + \frac{\partial (n\overline{v}_i)}{\partial x_i} = 0, \tag{A.12}$$

that is the equation of continuity for n. We now multiply eq. (A.4) by v_j and integrate over all velocities, obtaining

$$\frac{\partial}{\partial t} \int f v_j \, \mathrm{d}^3\mathbf{v} + \int v_i v_j \frac{\partial f}{\partial x_i} \, \mathrm{d}^3\mathbf{v} - \frac{\partial \Phi_\mathrm{T}}{\partial x_i} \int v_j \frac{\partial f}{\partial v_i} \, \mathrm{d}^3\mathbf{v} = 0. \tag{A.13}$$

Assuming again that f vanishes for large $|\mathbf{v}|$, and applying the divergence theorem to the third term, this becomes

$$\int v_j \frac{\partial f}{\partial v_i} \, \mathrm{d}^3\mathbf{v} = -\int f \frac{\partial v_j}{\partial v_i} \, \mathrm{d}^3\mathbf{v} = -\int \delta_{ij} f \, \mathrm{d}^3\mathbf{v} = -\delta_{ij} n. \tag{A.14}$$

Thus Eq. (A.13) may be rewritten

$$\frac{\partial (n\overline{v}_j)}{\partial t} + \frac{\partial (n\overline{v_i v_j})}{\partial x_i} + n\frac{\partial \Phi_\mathrm{T}}{\partial x_j} = 0. \tag{A.15}$$

Subtracting Eq. (A.12) multiplied by $\overline{v}_j$ from the above equation transforms it in

$$n\frac{\partial \overline{v}_j}{\partial t} - \overline{v}_j \frac{\partial (n\overline{v}_i)}{\partial x_i} + \frac{\partial (n\overline{v_i v_j})}{\partial x_i} = -n\frac{\partial \Phi_\mathrm{T}}{\partial x_j}. \tag{A.16}$$

Then, substituting Eq. (A.9) in the third term, we have

$$n\frac{\partial \overline{v}_j}{\partial t} + n\overline{v}_i \frac{\partial \overline{v}_j}{\partial x_i} = -n\frac{\partial \Phi_\mathrm{T}}{\partial x_j} - \frac{\partial (n\sigma_{ij}^2)}{\partial x_i}, \tag{A.17}$$

that is an analog of Euler's equation for fluids, where in place of the mass density there is the number density, and the fluid velocity is replaced by the mean stellar velocity. The second term on the right hand side of Eq. (A.17) is similar to the pressure force but, more exactly, it is a stress tensor that describes an anisotropic pressure. Since Eqs. (A.12) and (A.17) were first applied to stellar dynamics by Jeans (1919), we call them the Jeans equations, even if they were originally derived by Maxwell (but he already has a set of equations named after him).

The Jeans equations are very useful since they provide us a theoretical tool to interpret directly observable quantities, such as the streaming velocity and velocity dispersion, relating them to other interesting but directly inaccessible quantities, like the potential and the density field of a given galaxy. However, they are four equations in nine unknowns so they constitute an infinite set of equations, that can be closed by making some more or less arbitrary assumptions.

For example, if we consider a spherical and time-independent system with a DF of the form $f = f(H, \mathbf{L})$, where H is the Hamiltonian and $\mathbf{L}$ is the angular momentum vector, the Jeans equations are simplified and become

$$\frac{\mathrm{d}(n\sigma_r^2)}{\mathrm{d}r} + n\left(\frac{2\sigma_r^2 - \sigma_\theta^2 - \sigma_\varphi^2}{r}\right) = -n\frac{\mathrm{d}\Phi_\mathrm{T}}{\mathrm{d}r}, \tag{A.18}$$

where (r, θ, φ) are the spherical coordinates.

Another example is given for an axisymmetric system in a steady state with a DF of the form $f = f(H, L_z)$, where L_z is the vertical component of the angular momentum and (R, z, φ) are the cylindrical coordinates. In this case we have that $\sigma_z = \sigma_R \equiv \sigma$, and the Jeans equations are

$$\frac{\partial(n\sigma^2)}{\partial z} = -n\frac{\partial \Phi_{\mathrm{T}}}{\partial z} \tag{A.19}$$

and

$$\frac{\partial(n\sigma^2)}{\partial R} - n\frac{\overline{v_\varphi^2} - \sigma^2}{R} = -n\frac{\partial \Phi_{\mathrm{T}}}{\partial R}. \tag{A.20}$$

Appendix B

The equations of fluid dynamics

Here we report the fluid equations in the presence of source terms, necessary to understand the relation between the stellar dynamical configuration of a galaxy and the energy provided to its ISM by its evolving stellar population. The stellar velocity fields are indeed a major ingredient of the energy budget of the hot X-ray haloes of ETGs, thoroughly studied in Chapter 4.

B.1 The fluid equations in the presence of source terms

The equations of fluid dynamics in the presence of different sources of mass, momentum and energy, under the simplifying assumption of isotropy of the mass losses, can be written in Lagrangian formalism (D'Ercole et al. 2000; Posacki 2011) as

$$\frac{D\rho}{Dt} + \rho(\nabla \cdot \boldsymbol{u}) = \dot{\rho}, \tag{B.1}$$

$$\rho\frac{D\boldsymbol{u}}{Dt} = -\nabla p - \rho\nabla\Phi_{\rm tot} + \dot{\rho}(\mathbf{v} - \boldsymbol{u}), \tag{B.2}$$

$$\frac{DE}{Dt} + (E+p)\nabla\cdot\boldsymbol{u} = \sum_i \dot{\rho}_i\left[e_i + \frac{u_{{\rm s},\,i}^2}{2}\right] + \frac{\dot{\rho}}{2}\left[\|\boldsymbol{u}-\mathbf{v}\|^2 + {\rm Tr}(\boldsymbol{\sigma}^2)\right] - \mathscr{L}, \tag{B.3}$$

where ρ, $\boldsymbol{u}$, E, p are respectively the ISM mass density, velocity, internal energy density and pressure. $\Phi_{\rm tot}$ is the total gravitational potential (comprehensive of all possible mass components, e.g., gas, stars, DM, black hole). $\dot{\rho}(\mathbf{x},t) = \sum_i \dot{\rho}_i$ is the total mass return per unit time and volume, due to different sources (e.g., stellar winds and SNIa events) associated with the stellar population with streaming velocity $\mathbf{v}(\mathbf{x},t)$ and velocity dispersion tensor $\boldsymbol{\sigma}^2(\mathbf{x},t)$. $e_i(\mathbf{x},t)$ is the internal energy return per unit mass and time of the i-th source field, and $u_{{\rm s},\,i}(\mathbf{x},t)$ is the modulus of the relative velocity of the material injected by the i-th source field with respect to the source star. Finally, $\mathscr{L}$ are the bolometric radiative losses per unit time and volume.

For example, in applications as the one in Chapter 4, $\dot{\rho}$ is represented by the sum of stellar winds and SNIa explosions ejecta, so that $\dot{\rho} \equiv \dot{\rho}_* + \dot{\rho}_{\rm SN}$. In Chapter 4 the $\boldsymbol{\sigma}^2(\mathbf{x},t)$ and $\mathbf{v}(\mathbf{x},t)$ velocity fields are computed for realistic ETGs galaxy models by means of the Jeans solver code described in Chapter 2. As often done in similar works, in Chapter 4 we neglect e_* and $u_{{\rm s},*}$, being them significantly smaller than the contribution of ${\rm Tr}(\boldsymbol{\sigma}^2)$. In general, the opposite holds instead for SNIa events, where $\dot{\rho}_{\rm SN}{\rm Tr}(\boldsymbol{\sigma}^2)$ is negligible with respect to the energy injection due to the SNIa explosions. However, in Chapter 4, we take into account also the contribution $\dot{\rho}_{\rm SN}{\rm Tr}(\boldsymbol{\sigma}^2)$ and we adopt a velocity of the SNIa ejecta $u_s \simeq 8.5\times10^3$ km s^{-1}, corresponding to 10^{51} erg associated with an ejecta of 1.4 $M_\odot$.

Appendix C

The Multi-Gaussian Expansion models

In this Appendix we briefly introduce the Multi-Gaussian Expansion technique, that has been applied to I-band *HST* images of the SLACS galaxies to fit their surface brightness distributions and model their stellar components (see Chapter 5). We then present the images and the structural parameters of the axisymmetric MGE models we built.

C.1 The MGE method

The MGE method (Emsellem et al. 1994) consists of a series expansion of galaxy images using two-dimensional Gaussian functions. The use of Gaussians has important advantages since, for example, both convolutions and de-projections can be performed analytically in a simple and efficient way. This allows, e.g., to take seeing or PSF effects into account, and to derive the intrinsic stellar luminosity density from the observed galaxy photometry for a given choice of the inclination angle. Furthermore, expressing the density in MGE form allows many other dynamical and photometric quantities to be evaluated easily and accurately (Emsellem et al. 1994). For example, the MGE potential can be computed with a single integration, as opposed to the two that are required when the intrinsic density is stratified on similar triaxial ellipsoids, and three in the general case. In the case of axisymmetric MGE dynamical models based on a two-integral phase space distribution function, the velocity moments predicted from the Jeans equations, already projected onto the sky, can be expressed with only a double integration. The even part of the distribution function can also be easily retrieved from an MGE density distribution via the Hunter & Qian (1993) formalism (Cappellari 2002). Finally, the possibility to add as many gaussians as needed without adding complexity gives a high versatility to the MGE parametrization, making it one of the few simple parametrizations that are general enough to reproduce the surface brightness of realistic multi-component objects (e.g., spirals with multiple disks).

The MGE parametrization has been used for the modelling of a number of galaxies (Emsellem et al. 1994; Emsellem 1995; Emsellem et al. 1996, 1999; van den Bosch et al. 1998; van den Bosch & Emsellem 1998; Cretton & van den Bosch 1999), and, in particular, it has been extensively used for the modelling of the ATLAS^{3D} sample of ETGs (Cappellari et al. 2013b). For a detailed description of the MGE formalism, and of the fitting algorithm of the MGE_FIT_SECTORS software package used in Chapter 5, we cross-refer to Cappellari (2002) and references therein.

C.2 The MGE models

Figure C.1 shows in black the contour maps of the WFC/$F814W$ (I-band) images of the SLACS sample over a region extending out to $\sim 6\,R_{\rm e}$, where $R_{\rm e}$ is the half-light radius in the V-band. The red contours superimposed to the image are the MGE surface brightness fits, convolved with the proper PSF. For each galaxy, the parameters of the best-fitting MGE parametrizations of the projected light are presented in Table C.1.

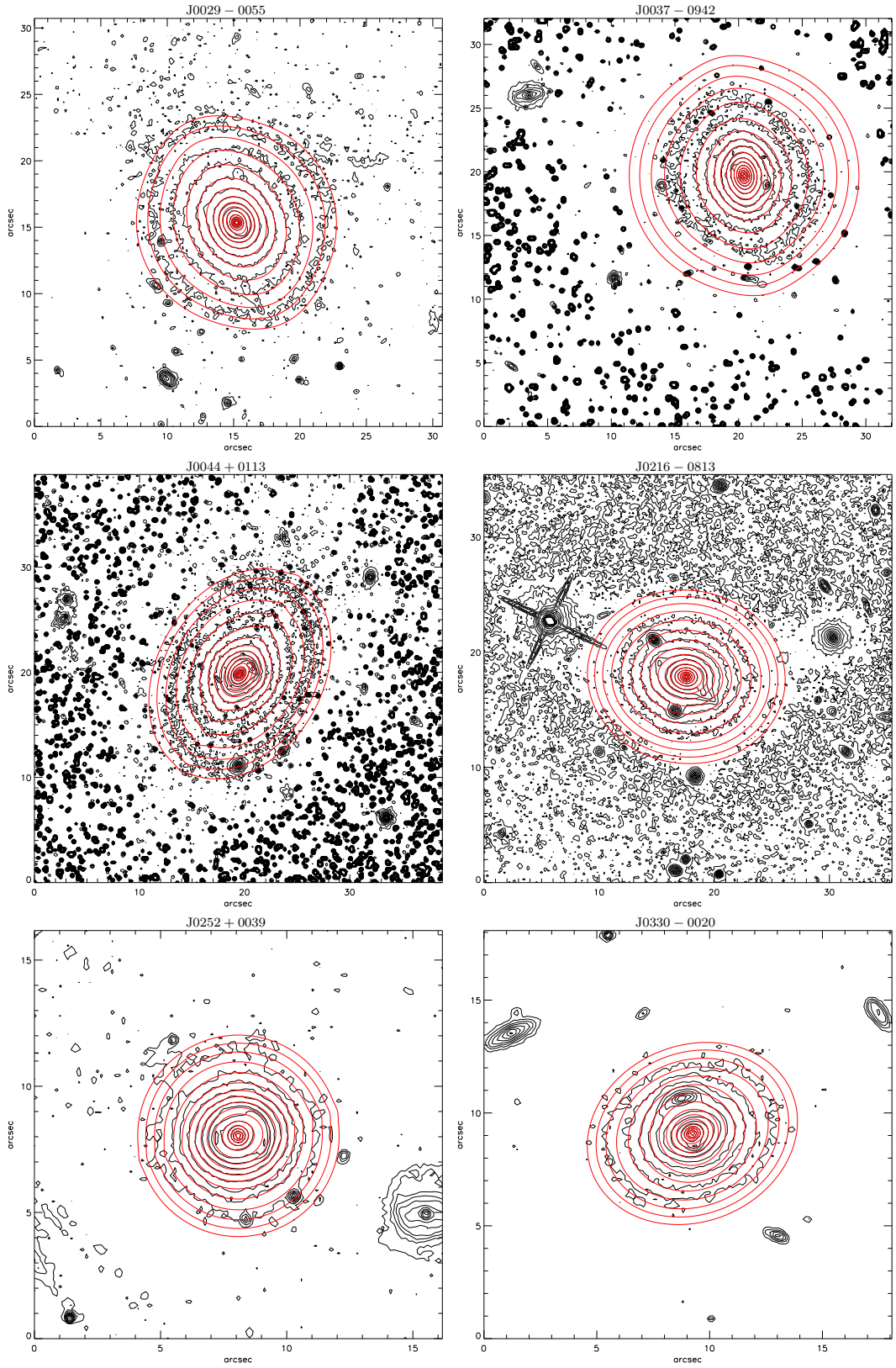

Figure C.1: Contour maps of the WFC/$F814W$ (I-band) images for the 55 SLACS galaxies (black). The contours of the MGE surface brightness, convolved with the proper PSF, are superimposed in red.

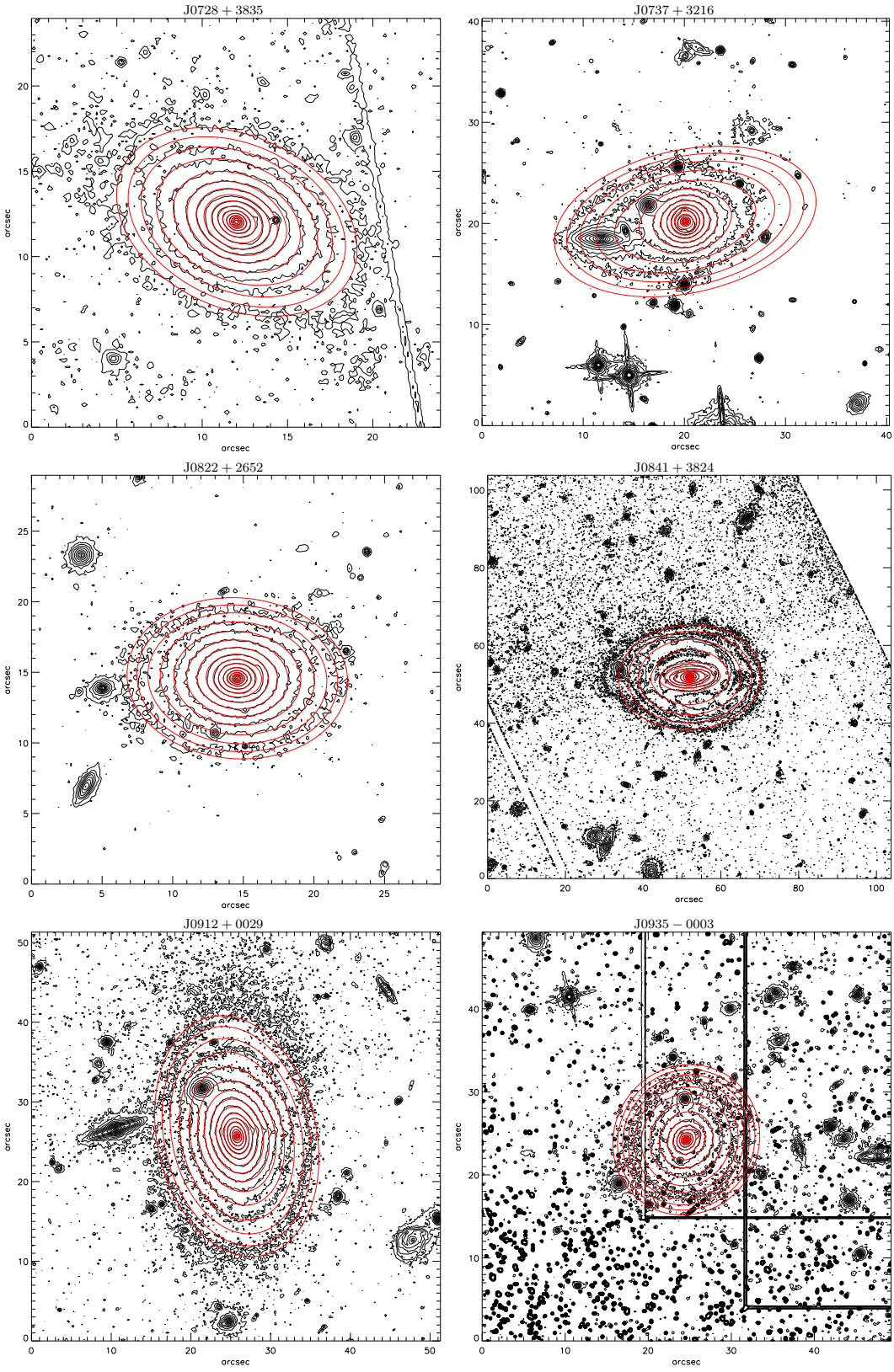

Figure C.1: – *continued*

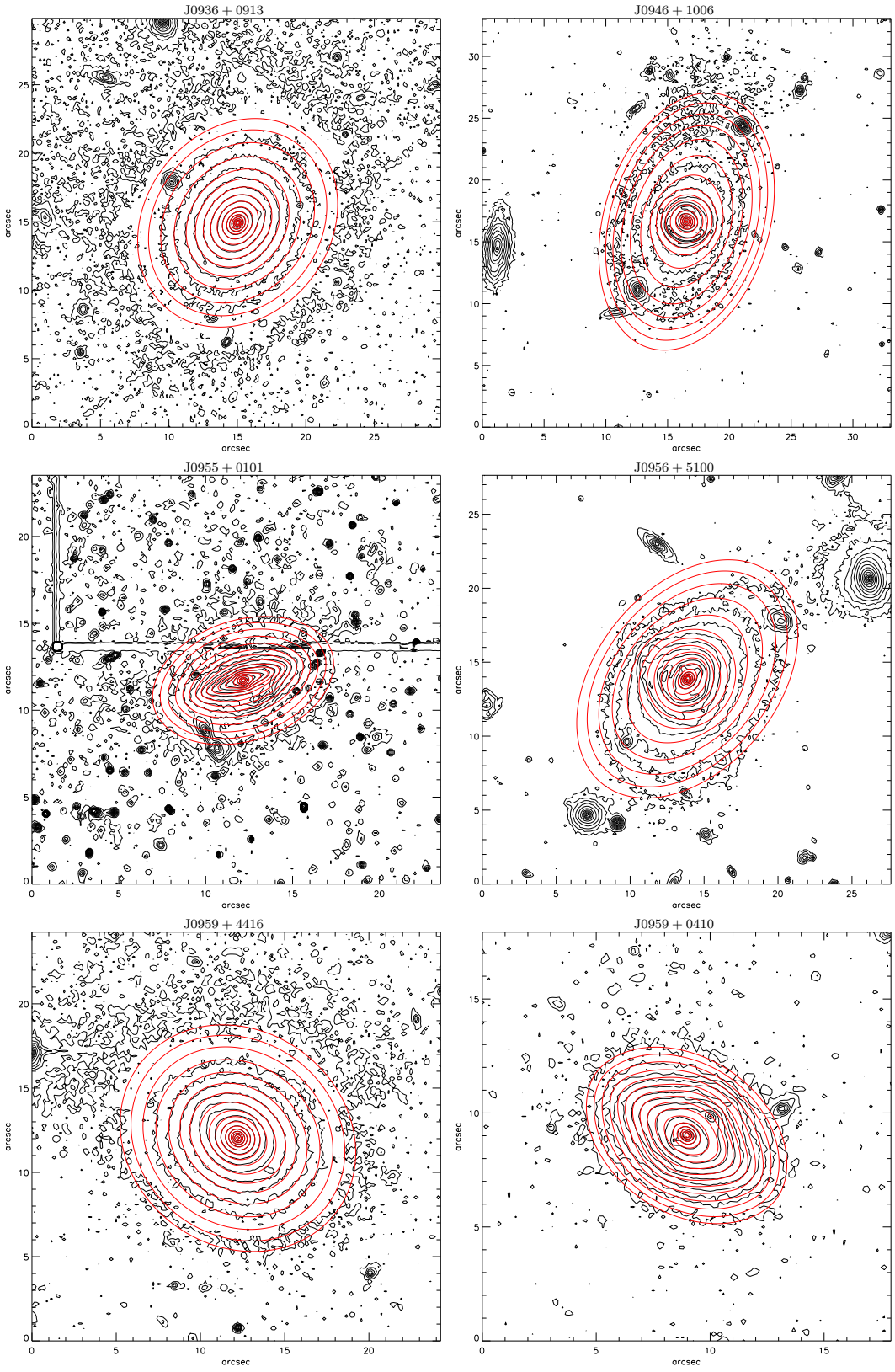

Figure C.1: – *continued*

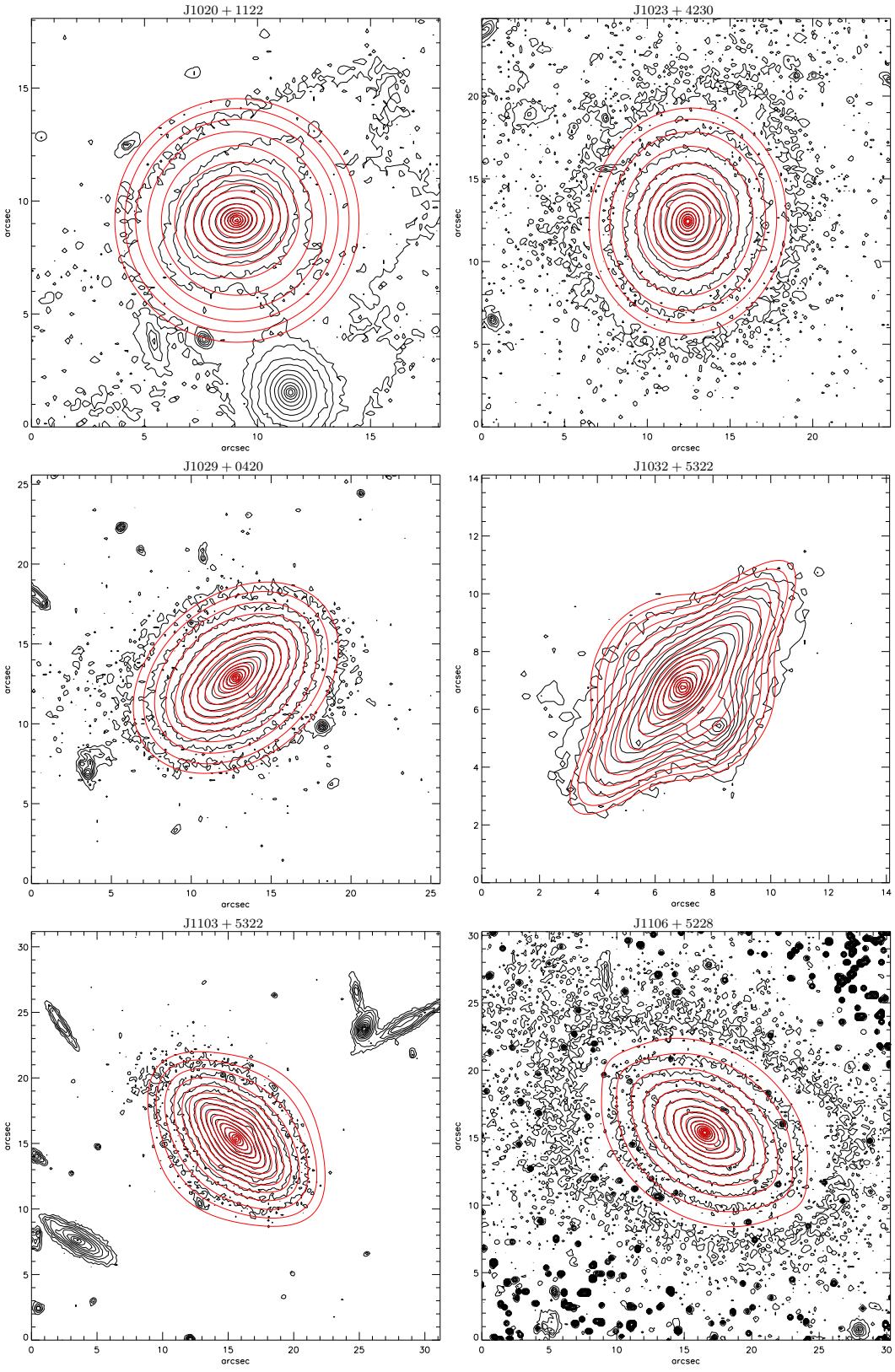

Figure C.1: – *continued*

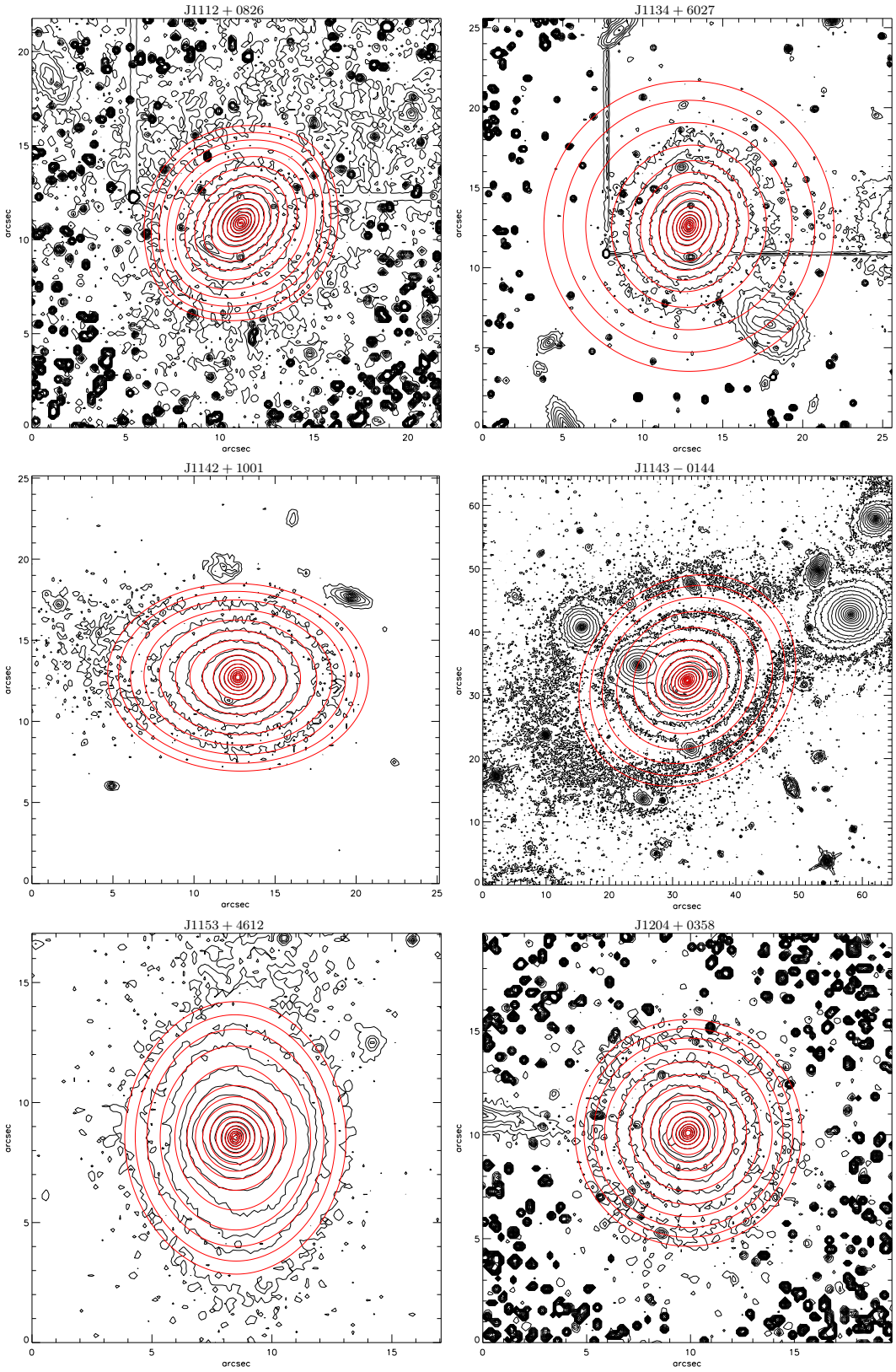

Figure C.1: – *continued*

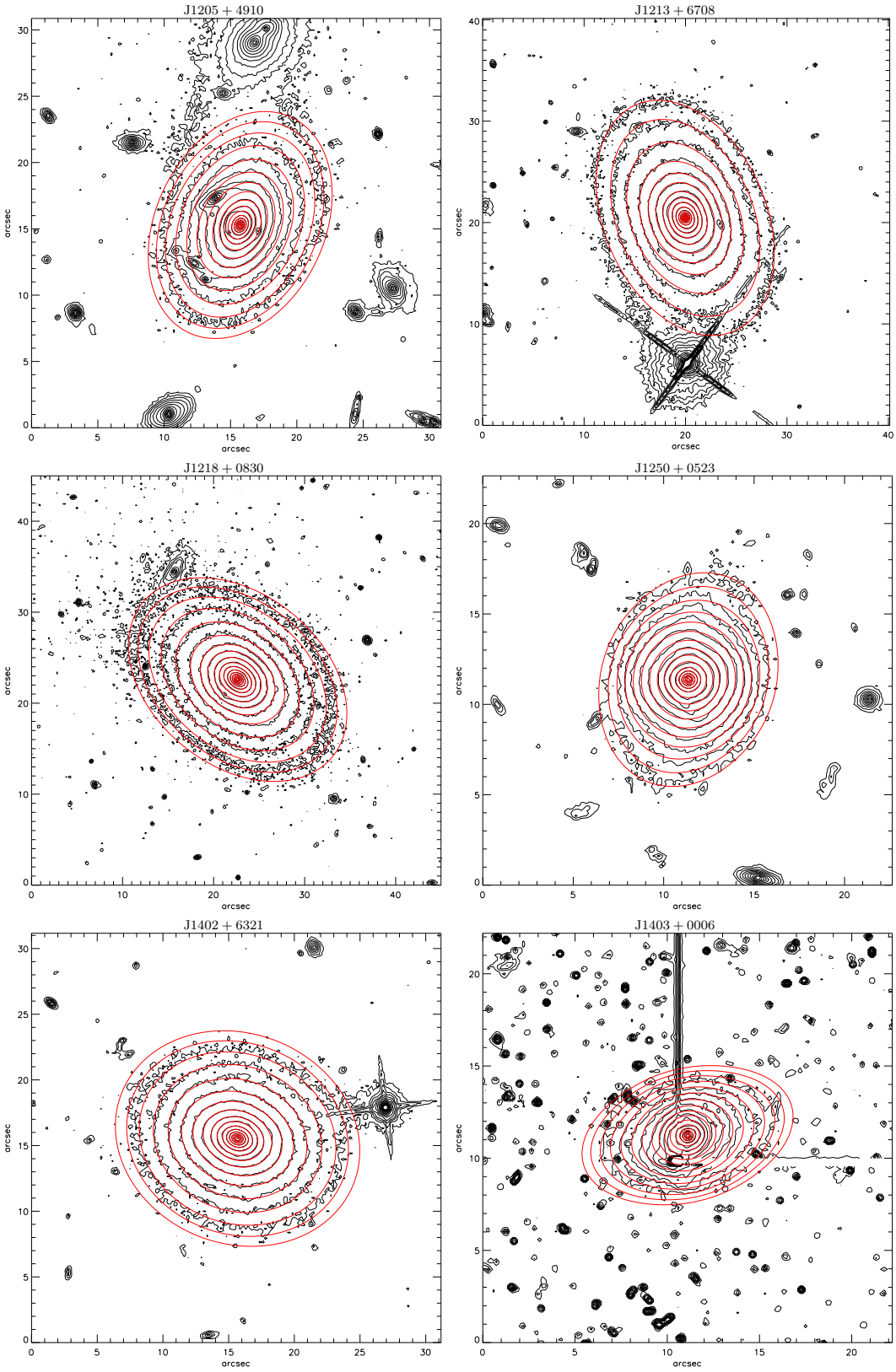

Figure C.1: – *continued*

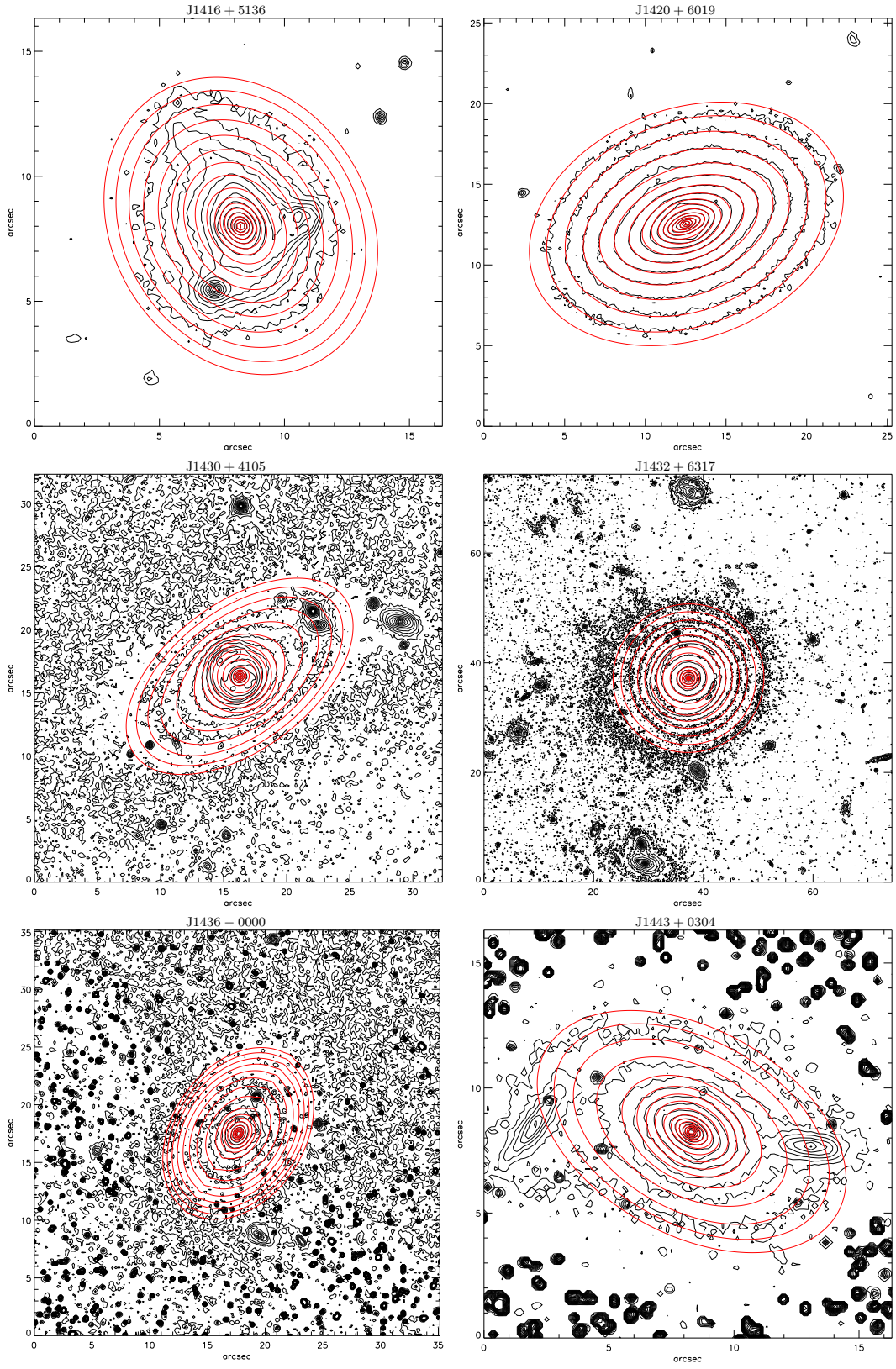

Figure C.1: – *continued*

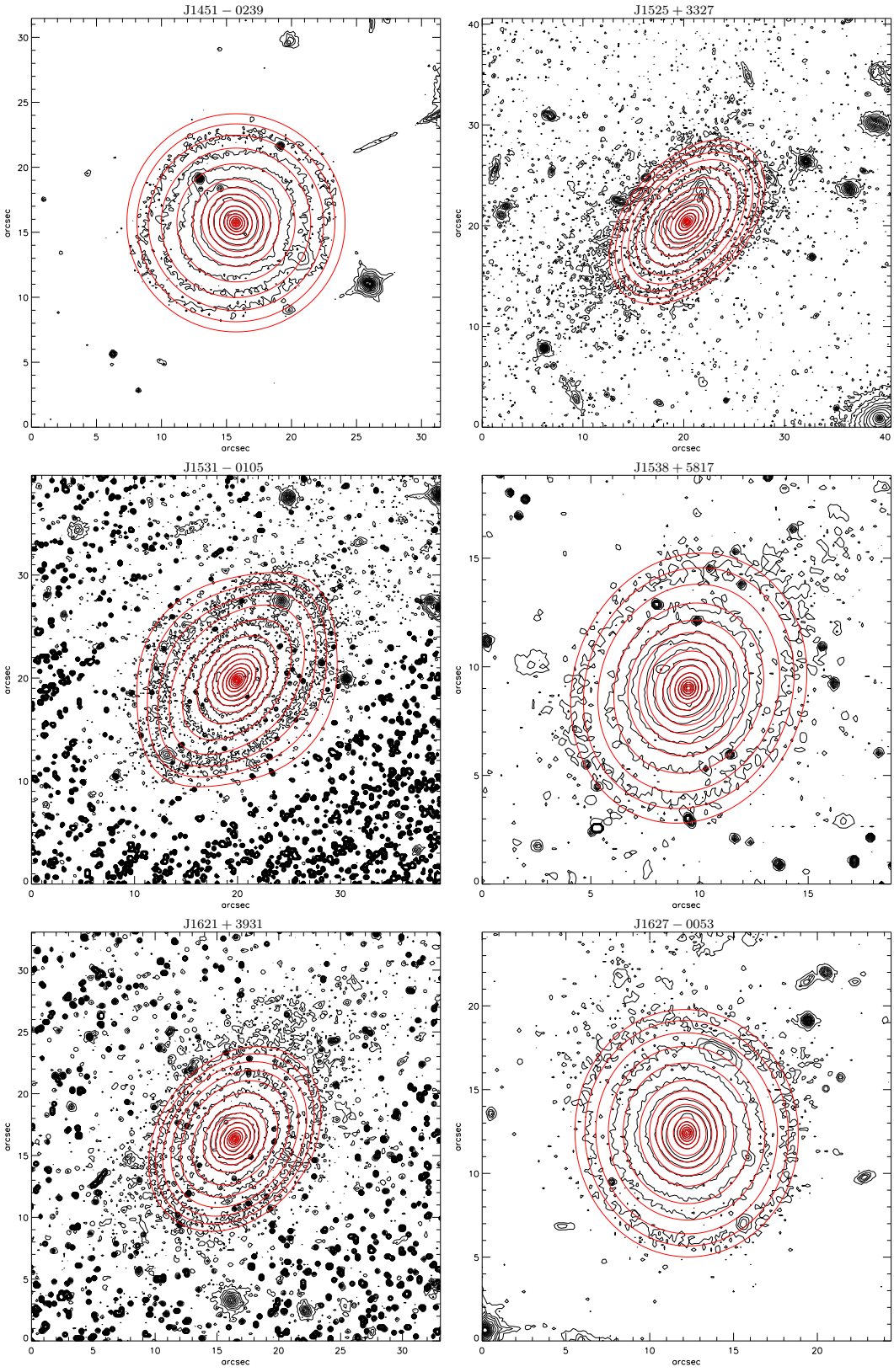

Figure C.1: – *continued*

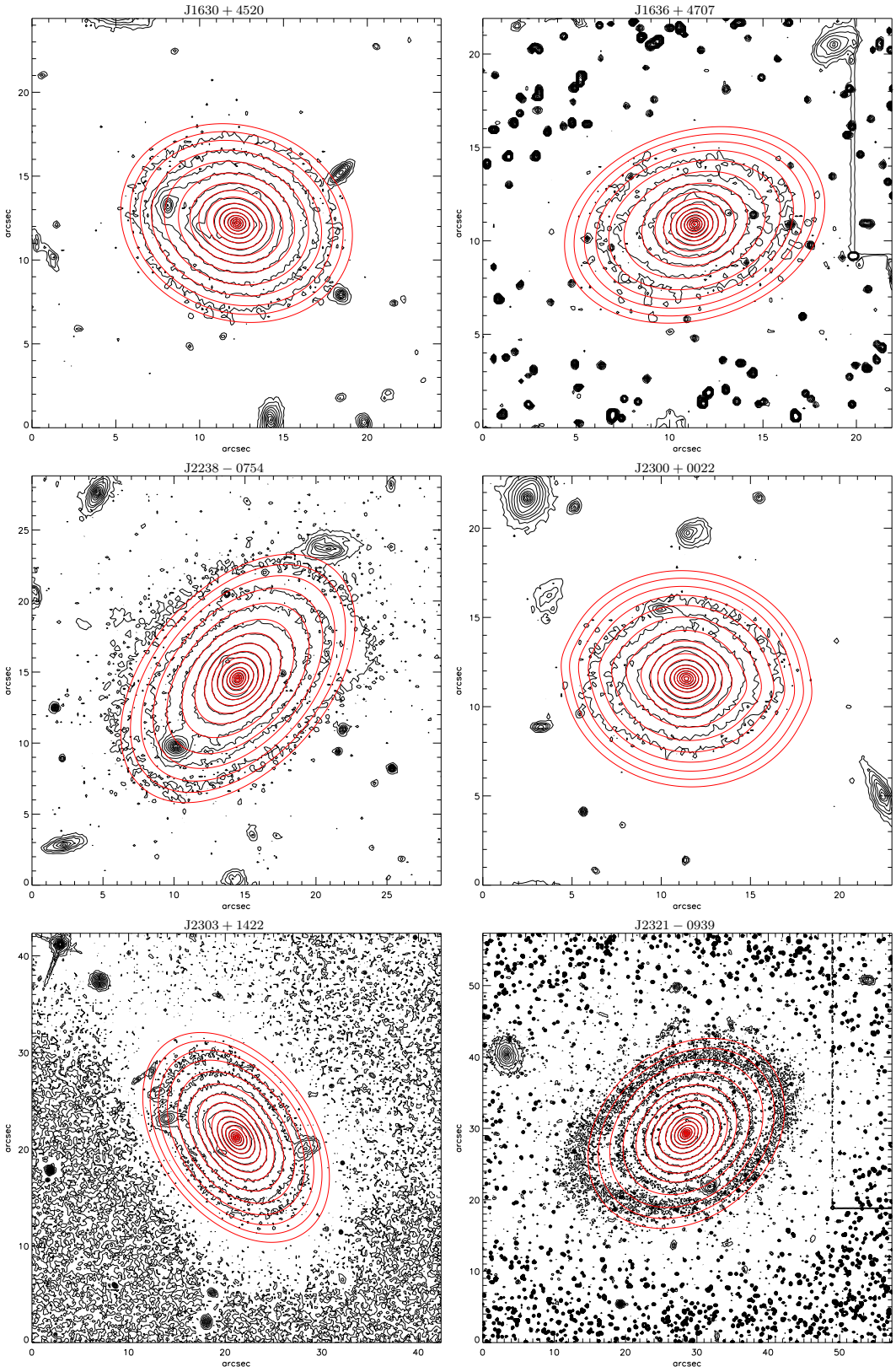

Figure C.1: – *continued*

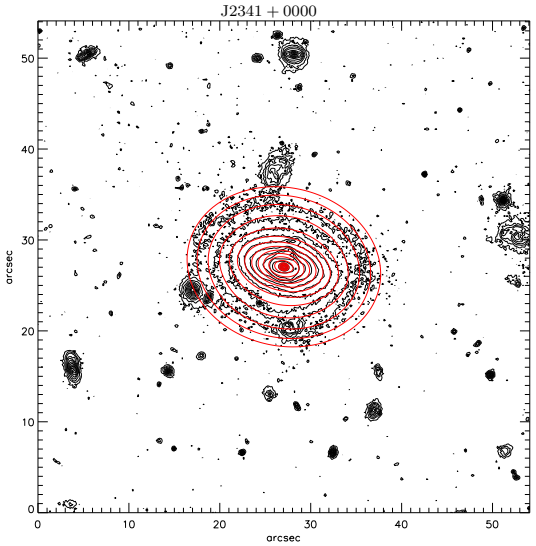

Figure C.1: – *continued*

Table C.1: MGE parameters for the de-convolved r-band surface brightness.

$\log I_i$ $[L_{\odot\,r}\,\mathrm{pc}^{-2}]$	$\log \sigma_i$ [arcsec]	q_i	$\log I_i$ $[L_{\odot\,r}\,\mathrm{pc}^{-2}]$	$\log \sigma_i$ [arcsec]	q_i	$\log I_i$ $[L_{\odot\,r}\,\mathrm{pc}^{-2}]$	$\log \sigma_i$ [arcsec]	q_i
J0029–0055			J0037–0942			J0044+0113		
3.895	–1.532	0.922	3.124	–1.323	0.891	3.552	–1.264	0.693
3.700	–1.050	0.941	3.442	–0.924	0.693	3.735	–0.786	0.567
3.372	–0.684	0.903	3.494	–0.773	0.693	3.507	–0.565	0.820
2.714	–0.183	0.792	3.355	–0.496	0.693	2.549	–0.209	0.554
1.902	–0.076	0.941	3.068	–0.212	0.693	2.871	–0.113	0.842
2.081	0.174	0.792	2.225	0.127	0.891	2.422	0.193	0.842
1.677	0.570	0.838	2.356	0.152	0.693	1.521	0.304	0.297
			1.833	0.593	0.891	1.018	0.658	0.297
						1.820	0.658	0.758
J0216–0813			J0252+0039			J0330–0020		
3.392	–1.532	0.842	4.005	–1.532	0.941	4.247	–1.532	0.787
3.536	–1.006	0.842	3.462	–1.078	0.941	3.215	–1.094	0.745
3.454	–0.762	0.842	3.240	–0.724	0.941	3.670	–0.925	0.829
3.183	–0.450	0.794	2.199	–0.143	0.652	3.028	–0.601	0.842
2.718	–0.126	0.792	2.684	–0.136	0.941	2.679	–0.406	0.743
2.377	0.171	0.792	1.834	0.212	0.941	2.529	–0.111	0.743
1.935	0.531	0.842				1.976	–0.055	0.842
						1.949	0.300	0.835
J0728+3835			J0737+3216			J0822+2652		
4.156	–1.532	0.845	3.631	–1.532	0.941	3.935	–1.532	0.792
3.811	–1.069	0.852	3.778	–1.119	0.982	3.676	–1.074	0.792
3.583	–0.790	0.838	3.474	–0.700	0.900	3.536	–0.796	0.792
3.125	–0.521	0.941	2.880	–0.188	0.990	3.173	–0.470	0.743
2.670	–0.303	0.512	2.317	0.142	0.842	2.713	–0.118	0.792
2.698	–0.044	0.746	1.815	0.552	0.842	2.186	0.177	0.759
2.089	0.183	0.792				1.791	0.528	0.743
1.484	0.541	0.495						
1.568	0.541	0.804						
J0841+3824			J0912+0029			J0935–0003		
4.318	–1.532	0.760	3.349	–1.433	0.801	3.459	–1.162	0.862
3.810	–0.996	0.990	3.464	–0.917	0.870	3.499	–0.848	0.822
3.056	–0.551	0.531	3.097	–0.629	0.732	3.276	–0.570	0.823
3.296	–0.423	0.792	3.172	–0.410	0.727	2.819	–0.247	0.862
2.878	–0.142	0.848	2.520	–0.092	0.565	2.371	0.058	0.862
2.202	0.278	0.446	2.680	0.029	0.597	2.129	0.532	0.862
2.249	0.493	0.446	2.329	0.047	0.941			
1.598	0.937	0.798	2.120	0.392	0.841			
			2.053	0.427	0.443			
			1.584	0.826	0.657			
J0936+0913			J0946+1006			J0955+0101		
4.075	–1.532	0.822	3.338	–1.532	0.990	4.135	–1.532	0.720
3.780	–1.019	0.818	3.374	–0.940	0.990	3.634	–1.064	0.599
3.437	–0.800	0.826	3.250	–0.568	0.990	3.286	–0.772	0.842
3.233	–0.506	0.828	2.587	–0.023	0.990	2.841	–0.520	0.842
2.574	–0.270	0.842	1.475	0.287	0.743	2.878	–0.036	0.248
2.467	–0.060	0.792	1.642	0.585	0.743	2.459	0.116	0.411
2.342	0.198	0.817				1.324	0.396	0.842
1.706	0.584	0.833				1.630	0.396	0.442

Table C.1: – *continued*

$\log I_i$ $[L_{\odot\,r}\,\mathrm{pc}^{-2}]$	$\log \sigma_i$ [arcsec]	q_i	$\log I_i$ $[L_{\odot\,r}\,\mathrm{pc}^{-2}]$	$\log \sigma_i$ [arcsec]	q_i	$\log I_i$ $[L_{\odot\,r}\,\mathrm{pc}^{-2}]$	$\log \sigma_i$ [arcsec]	q_i
J0956+5100			J0959+4416			J0959+0410		
3.818	–1.532	0.743	3.272	–1.253	0.941	4.098	–1.532	0.801
3.827	–1.025	0.743	3.593	–1.018	0.941	3.523	–1.123	0.857
3.496	–0.751	0.743	3.429	–0.748	0.877	3.466	–0.866	0.746
3.236	–0.504	0.743	3.079	–0.492	0.892	3.062	–0.525	0.847
2.679	–0.024	0.743	2.726	–0.185	0.941	2.582	–0.025	0.891
2.353	0.040	0.941	1.756	0.178	0.492	2.273	0.142	0.383
1.760	0.268	0.743	2.136	0.184	0.879	1.852	0.299	0.714
1.791	0.579	0.743	1.676	0.507	0.865			
J1020+1122			J1023+4230			J1029+0420		
3.731	–1.413	0.792	4.322	–1.532	0.866	4.279	–1.532	0.736
3.811	–0.967	0.792	3.781	–1.026	0.891	3.788	–0.998	0.758
3.444	–0.656	0.792	3.230	–0.754	0.842	3.493	–0.715	0.714
2.989	–0.374	0.792	3.149	–0.517	0.842	3.125	–0.454	0.821
2.656	–0.033	0.803	2.668	–0.179	0.842	2.962	–0.195	0.396
1.930	0.348	0.990	2.446	0.074	0.891	2.065	0.075	0.891
			1.766	0.490	0.883	2.622	0.094	0.396
						2.198	0.299	0.504
						1.411	0.517	0.513
						1.502	0.517	0.891
J1032+5322			J1103+5322			J1106+5228		
4.256	–1.532	0.827	3.779	–1.532	0.744	4.608	–1.532	0.644
3.805	–0.991	0.842	3.501	–1.012	0.812	3.928	–0.975	0.743
3.450	–0.660	0.812	3.369	–0.622	0.677	3.734	–0.961	0.545
2.745	–0.298	0.813	3.057	–0.083	0.347	3.710	–0.741	0.743
2.789	–0.038	0.297	2.228	0.020	0.842	2.948	–0.580	0.545
2.327	0.188	0.348	2.441	0.234	0.347	3.459	–0.482	0.743
1.288	0.390	0.842	1.918	0.312	0.574	2.785	–0.240	0.545
1.577	0.390	0.297	1.369	0.555	0.447	2.941	–0.020	0.626
			1.314	0.555	0.842	1.996	0.279	0.743
						2.211	0.350	0.545
						1.787	0.678	0.723
J1112+0826			J1134+6027			J1142+1001		
3.734	–1.240	0.792	4.047	–1.532	0.743	3.710	–1.532	0.990
3.535	–0.763	0.743	3.784	–0.920	0.743	3.692	–1.059	0.990
3.070	–0.630	0.743	3.346	–0.597	0.743	3.403	–0.771	0.990
3.099	–0.368	0.743	3.045	–0.348	0.820	2.928	–0.495	0.990
2.689	–0.072	0.755	2.387	0.012	0.743	2.690	–0.221	0.990
2.142	0.325	0.792	2.218	0.226	0.879	2.105	0.176	0.771
			1.522	0.674	0.891	1.812	0.527	0.743
J1143–0144			J1153+4612			J1204+0358		
3.350	–0.792	0.832	4.166	–1.532	0.842	4.089	–1.532	0.891
3.507	–0.515	0.743	3.857	–1.027	0.842	3.766	–0.950	0.891
3.213	–0.228	0.743	3.353	–0.742	0.842	3.275	–0.614	0.891
2.732	0.156	0.753	2.869	–0.527	0.842	2.778	–0.347	0.936
2.095	0.436	0.891	2.637	–0.381	0.990	2.533	–0.038	0.990
1.507	0.919	0.813	2.588	–0.112	0.990	1.992	0.345	0.990
			1.852	0.391	0.842			

Table C.1: – *continued*

$\log I_i$ $[L_{\odot\,r}\,\mathrm{pc}^{-2}]$	$\log \sigma_i$ [arcsec]	q_i	$\log I_i$ $[L_{\odot\,r}\,\mathrm{pc}^{-2}]$	$\log \sigma_i$ [arcsec]	q_i	$\log I_i$ $[L_{\odot\,r}\,\mathrm{pc}^{-2}]$	$\log \sigma_i$ [arcsec]	q_i
J1205+4910			J1213+6708			J1218+0830		
3.819	–1.532	0.842	4.345	–1.532	0.857	3.347	–1.532	0.792
3.386	–1.139	0.842	4.110	–1.052	0.822	3.260	–1.031	0.792
3.678	–0.921	0.842	3.635	–0.729	0.891	3.383	–0.805	0.792
3.134	–0.628	0.842	3.170	–0.424	0.880	3.267	–0.542	0.693
2.923	–0.433	0.693	2.744	–0.007	0.779	3.024	–0.317	0.728
2.732	–0.157	0.842	2.147	0.301	0.799	2.668	–0.075	0.693
2.371	0.195	0.693	1.702	0.417	0.693	2.453	0.175	0.792
1.732	0.589	0.693	1.647	0.805	0.693	1.807	0.475	0.720
0.827	0.589	0.842				1.530	0.801	0.707
J1250+0523			J1402+6321			J1403+0006		
4.417	–1.532	0.990	3.875	–1.532	0.792	4.177	–1.532	0.891
3.871	–0.994	0.990	3.316	–1.058	0.842	3.638	–1.054	0.891
3.400	–0.591	0.990	3.537	–0.858	0.743	3.283	–0.680	0.891
2.818	–0.157	0.990	3.267	–0.603	0.743	1.979	–0.250	0.693
2.416	0.154	0.990	3.013	–0.368	0.743	2.899	–0.197	0.891
1.675	0.503	0.772	2.707	–0.059	0.796	2.197	0.174	0.709
			2.193	0.263	0.766	1.790	0.384	0.693
			1.751	0.619	0.842			
J1416+5136			J1420+6019			J1430+4105		
3.661	–1.531	0.973	4.194	–1.532	0.743	3.902	–1.532	0.936
3.656	–1.039	0.990	3.936	–0.983	0.743	3.709	–0.998	0.941
3.296	–0.732	0.956	3.486	–0.671	0.743	3.404	–0.595	0.932
3.111	–0.352	0.794	3.384	–0.501	0.396	2.820	0.071	0.941
2.389	0.070	0.743	3.471	–0.219	0.396	1.707	0.652	0.594
1.664	0.427	0.743	3.024	–0.050	0.743			
1.090	0.427	0.990	2.435	0.172	0.396			
			2.176	0.299	0.743			
			2.031	0.452	0.436			
			1.851	0.683	0.716			
J1432+6317			J1436–0000			J1443+0304		
3.914	–1.532	0.976	3.317	–1.532	0.792	4.369	–1.532	0.792
3.634	–0.994	0.974	3.227	–1.094	0.812	3.773	–1.045	0.990
3.350	–0.678	0.978	3.502	–0.783	0.772	3.462	–1.037	0.594
2.912	–0.358	0.907	3.125	–0.446	0.772	3.298	–0.774	0.594
2.732	–0.003	0.953	2.136	–0.054	0.772	3.194	–0.556	0.638
2.182	0.503	0.990	2.434	–0.028	0.812	2.738	–0.299	0.594
0.158	0.811	0.396	1.991	0.458	0.772	2.064	–0.039	0.990
1.435	0.811	0.990				2.453	–0.022	0.594
						1.748	0.449	0.594
						1.009	0.449	0.990
J1451–0239			J1525+3327			J1531–0105		
4.236	–1.532	0.952	3.969	–1.532	0.770	3.782	–1.532	0.718
3.756	–1.024	0.984	3.635	–1.030	0.792	3.753	–0.949	0.743
3.378	–0.645	0.921	3.279	–0.703	0.747	3.444	–0.699	0.693
2.936	–0.349	0.951	2.854	–0.469	0.594	3.216	–0.480	0.693
2.613	–0.074	0.990	2.801	–0.186	0.594	2.997	–0.280	0.693
1.716	0.186	0.297	2.559	0.130	0.671	2.605	–0.033	0.693
2.202	0.213	0.990	1.944	0.574	0.606	2.473	0.201	0.743
1.690	0.621	0.990				1.836	0.709	0.693

Table C.1: – *continued*

$\log I_i$ $[L_{\odot\,r}\,\mathrm{pc}^{-2}]$	$\log \sigma_i$ [arcsec]	q_i	$\log I_i$ $[L_{\odot\,r}\,\mathrm{pc}^{-2}]$	$\log \sigma_i$ [arcsec]	q_i	$\log I_i$ $[L_{\odot\,r}\,\mathrm{pc}^{-2}]$	$\log \sigma_i$ [arcsec]	q_i
J1538+5817			J1621+3931			J1627–0053		
4.324	–1.532	0.862	3.815	–1.443	0.767	3.864	–1.532	0.817
3.785	–0.991	0.862	3.546	–1.101	0.792	3.417	–1.144	0.792
3.393	–0.620	0.862	3.537	–0.910	0.743	3.627	–0.937	0.843
2.765	–0.212	0.822	3.339	–0.591	0.743	3.381	–0.572	0.827
2.432	0.070	0.852	2.884	–0.364	0.743	2.724	–0.085	0.792
1.751	0.475	0.853	2.712	0.003	0.792	2.172	0.125	0.941
			1.993	0.519	0.755	1.730	0.517	0.926
J1630+4520			J1636+4707			J2238–0754		
3.925	–1.532	0.831	3.922	–1.532	0.896	3.998	–1.532	0.733
3.796	–1.044	0.832	3.595	–0.991	0.941	3.668	–0.925	0.823
3.443	–0.648	0.831	3.334	–0.680	0.852	2.853	–0.668	0.644
2.917	–0.309	0.842	2.954	–0.422	0.941	3.234	–0.524	0.891
2.185	–0.164	0.684	2.365	–0.274	0.743	2.431	–0.279	0.644
2.441	0.019	0.842	2.358	–0.129	0.941	2.713	–0.072	0.891
2.104	0.152	0.842	2.280	0.030	0.743	2.145	0.257	0.644
1.865	0.478	0.842	1.965	0.447	0.743	1.797	0.627	0.644
J2300+0022			J2303+1422			J2321–0939		
2.876	–1.364	0.773	3.356	–1.202	0.743	3.920	–1.532	0.842
3.405	–0.982	0.843	3.555	–0.816	0.743	3.682	–0.950	0.842
3.280	–0.710	0.703	3.276	–0.440	0.698	3.656	–0.632	0.842
3.227	–0.513	0.833	2.804	–0.023	0.685	3.199	–0.289	0.743
2.342	–0.218	0.702	2.328	0.309	0.644	2.920	0.030	0.800
2.456	–0.067	0.990	1.774	0.693	0.646	1.896	0.254	0.743
2.036	0.031	0.693				2.434	0.422	0.805
1.567	0.424	0.990				1.724	0.846	0.776
1.692	0.424	0.693						
J2341+0000								
3.973	–1.523	0.754						
3.427	–0.766	0.716						
3.365	–0.652	0.792						
2.432	–0.128	0.495						
2.458	0.036	0.792						
2.311	0.325	0.495						
1.548	0.369	0.792						
1.525	0.697	0.792						

Notes: Column 1: Logarithm of the Gaussian amplitude. Column 2: Logarithm of the Gaussian width. Column 3: Axial ratio of the Gaussian.

Bibliography

Abazajian K. N. et al., 2009, ApJS, 182, 543

Ahn C. P. et al., 2014, ApJS, 211, 17

An J. H., Evans N. W., 2006, ApJ, 642, 752

Auger M. W., Treu T., Bolton A. S., Gavazzi R., Koopmans L. V. E., Marshall P. J., Bundy K., Moustakas L. A., 2009, ApJ, 705, 1099

Auger M. W., Treu T., Gavazzi R., Bolton A. S., Koopmans L. V. E., Marshall P. J., 2010, ApJ, 721, L163

Bacon R. et al., 2001, MNRAS, 326, 23

Barnabè M., Ciotti L., Fraternali F., Sancisi R., 2006, A&A, 446, 61

Barnabè M., Czoske O., Koopmans L. V. E., Treu T., Bolton A. S., 2011, MNRAS, 415, 2215

Barnabè M., Spiniello C., Koopmans L. V. E., Trager S. C., Czoske O., Treu T., 2013, MNRAS, 436, 253

Bastian N., Covey K. R., Meyer M. R., 2010, ARA&A, 48, 339

Bedregal A. G., Aragón-Salamanca A., Merrifield M. R., Milvang-Jensen B., 2006, MNRAS, 371, 1912

Behroozi P. S., Wechsler R. H., Conroy C., 2013, ApJ, 770, 57

Bell E. F., de Jong R. S., 2001, ApJ, 550, 212

Bender R., Burstein D., Faber S. M., 1992, ApJ, 399, 462

Bender R., Saglia R. P., Gerhard O. E., 1994, MNRAS, 269, 785

Bendinelli O., 1991, ApJ, 366, 599

Bendinelli O., Ciotti L., Parmeggiani G., 1993, A&A, 279, 668

Bershady M. A., Martinsson T. P. K., Verheijen M. A. W., Westfall K. B., Andersen D. R., Swaters R. A., 2011, ApJ, 739, L47

Bertin G., 2000, Dynamics of Galaxies. Cambridge Univ. Press, Cambridge, UK

Bertin G., Stiavelli M., 1984, A&A, 137, 26

Binney J., 1981, MNRAS, 196, 455

Binney J., 2014, MNRAS, 440, 787

Binney J., Mamon G. A., 1982, MNRAS, 200, 361

Binney J., Tremaine S., 1987, Galactic dynamics. Princeton Univ. Press, Princeton, NJ

Binney J., Tremaine S., 2008, Galactic Dynamics: Second Edition. Princeton Univ. Press, Princeton, NJ

Binney J. J., Davies R. L., Illingworth G. D., 1990, ApJ, 361, 78

Blanton M. R., Roweis S., 2007, AJ, 133, 734

Bolton A. S., Burles S., Koopmans L. V. E., Treu T., Gavazzi R., Moustakas L. A., Wayth R., Schlegel D. J., 2008, ApJ, 682, 964

Bolton A. S., Burles S., Koopmans L. V. E., Treu T., Moustakas L. A., 2006, ApJ, 638, 703

Boroson B., Kim D. W., Fabbiano G., 2011, ApJ, 729, 12

Brewer B. J. et al., 2012, MNRAS, 422, 3574

Brewer B. J., Marshall P. J., Auger M. W., Treu T., Dutton A. A., Barnabè M., 2014, MNRAS, 437, 1950

Brighenti F., Mathews W. G., 1997, ApJ, 490, 592

Caon N., Capaccioli M., D'Onofrio M., 1993, MNRAS, 265, 1013

Cappellari M., 2002, MNRAS, 333, 400

Cappellari M., 2008, MNRAS, 390, 71

Cappellari M. et al., 2006, MNRAS, 366, 1126

Cappellari M., Emsellem E., 2004, PASP, 116, 138

Cappellari M. et al., 2007, MNRAS, 379, 418

Cappellari M. et al., 2011a, MNRAS, 413, 813

Cappellari M. et al., 2011b, MNRAS, 416, 1680

Cappellari M. et al., 2012, Nature, 484, 485

Cappellari M. et al., 2013a, MNRAS, 432, 1862

Cappellari M. et al., 2013b, MNRAS, 432, 1709

Cappellaro E., Evans R., Turatto M., 1999, A&A, 351, 459

Carollo C. M., Danziger I. J., 1994, MNRAS, 270, 523

Carollo C. M., de Zeeuw P. T., van der Marel R. P., 1995, MNRAS, 276, 1131

Chabrier G., 2003, PASP, 115, 763

Ciotti L., 1996, ApJ, 471, 68

Ciotti L., 1999, ApJ, 520, 574

Ciotti L., Bertin G., 2005, A&A, 437, 419

Ciotti L., D'Ercole A., Pellegrini S., Renzini A., 1991, ApJ, 376, 380

Ciotti L., Giampieri G., 2007, MNRAS, 376, 1162

Ciotti L., Lanzoni B., 1997, A&A, 321, 724

Ciotti L., Lanzoni B., Renzini A., 1996, MNRAS, 282, 1

Ciotti L., Morganti L., 2009, MNRAS, 393, 179

Ciotti L., Morganti L., 2010a, MNRAS, 401, 1091

Ciotti L., Morganti L., 2010b, MNRAS, 408, 1070

Ciotti L., Morganti L., de Zeeuw P. T., 2009, MNRAS, 393, 491

Ciotti L., Pellegrini S., 1992, MNRAS, 255, 561

Ciotti L., Pellegrini S., 1996, MNRAS, 279, 240

Ciotti L., Pellegrini S., 2008, MNRAS, 387, 902

Cleveland W. S., 1979, JASA, 74, 829

Coccato L. et al., 2009, MNRAS, 394, 1249

Conroy C., van Dokkum P. G., 2012, ApJ, 760, 71

Cretton N., van den Bosch F. C., 1999, ApJ, 514, 704

Cuddeford P., 1991, MNRAS, 253, 414

David L. P., Jones C., Forman W., Vargas I. M., Nulsen P., 2006, ApJ, 653, 207

de Lorenzi F., Gerhard O., Saglia R. P., Sambhus N., Debattista V. P., Pannella M., Méndez R. H., 2008, MNRAS, 385, 1729

de Vaucouleurs G., 1948, Annales d'Astrophysique, 11, 247

de Zeeuw P. T., Evans N. W., Schwarzschild M., 1996, MNRAS, 280, 903

Dehnen W., 1993, MNRAS, 265, 250

Dejonghe H., 1984, A&A, 133, 225

Dejonghe H., 1986, Phys. Rep., 133, 217

D'Ercole A., Ciotti L., 1998, ApJ, 494, 535

D'Ercole A., Recchi S., Ciotti L., 2000, ApJ, 533, 799

Desroches L.-B., Quataert E., Ma C.-P., West A. A., 2007, MNRAS, 377, 402

Diehl S., Statler T. S., 2008, ApJ, 687, 986

Donas J. et al., 2007, ApJS, 173, 597

D'Onofrio M., Zaggia S. R., Longo G., Caon N., Capaccioli M., 1995, A&A, 296, 319

Dutton A. A. et al., 2011, MNRAS, 416, 322

Dutton A. A., Macciò A. V., Mendel J. T., Simard L., 2013a, MNRAS, 432, 2496

Dutton A. A., Mendel J. T., Simard L., 2012, MNRAS, 422, L33

Dutton A. A. et al., 2013b, MNRAS, 428, 3183

Eddington A. S., 1916, MNRAS, 76, 572

Einasto J., 1965, Trudy Astrofizicheskogo Instituta Alma-Ata, 5, 87

Emsellem E., 1995, A&A, 303, 673

Emsellem E., Bacon R., Monnet G., Poulain P., 1996, A&A, 312, 777

Emsellem E. et al., 2011, MNRAS, 414, 888

Emsellem E. et al., 2007, MNRAS, 379, 401

Emsellem E. et al., 2004, MNRAS, 352, 721

Emsellem E., Dejonghe H., Bacon R., 1999, MNRAS, 303, 495

Emsellem E., Monnet G., Bacon R., Nieto J.-L., 1994, A&A, 285, 739

Eskridge P. B., Fabbiano G., Kim D.-W., 1995, ApJS, 97, 141

Evans N. W., 1993, MNRAS, 260, 191

Evans N. W., 1994, MNRAS, 267, 333

Evans N. W., Bowden A., 2014, MNRAS, 443, 2

Evans N. W., de Zeeuw P. T., 1994, MNRAS, 271, 202

Evans N. W., de Zeeuw P. T., Lynden-Bell D., 1990, MNRAS, 244, 111

Evans N. W., Williams A. A., 2014, MNRAS, 443, 791

Fabbiano G., 1989, ARA&A, 27, 87

Ferrarese L., Merritt D., 2000, ApJ, 539, L9

Ferreras I., La Barbera F., de la Rosa I. G., Vazdekis A., de Carvalho R. R., Falcón-Barroso J., Ricciardelli E., 2013, MNRAS, 429, L15

Ferreras I., Saha P., Burles S., 2008, MNRAS, 383, 857

Fisher D., 1997, AJ, 113, 950

Fisher D., Franx M., Illingworth G., 1995, ApJ, 448, 119

Gao L., Navarro J. F., Cole S., Frenk C. S., White S. D. M., Springel V., Jenkins A., Neto A. F., 2008, MNRAS, 387, 536

Gebhardt K. et al., 2000, ApJ, 539, L13

Gerhard O., Kronawitter A., Saglia R. P., Bender R., 2001, AJ, 121, 1936

Gerhard O. E., 1991, MNRAS, 250, 812

Gerhard O. E., Binney J. J., 1996, MNRAS, 279, 993

Graves G. J., Faber S. M., 2010, ApJ, 717, 803

Grillo C., Gobat R., Lombardi M., Rosati P., 2009, A&A, 501, 461

Gültekin K. et al., 2009, ApJ, 698, 198

Hernquist L., 1990, ApJ, 356, 359

Hogg D. W., Baldry I. K., Blanton M. R., Eisenstein D. J., 2002, preprint (arXiv:0210394)

Hunter C., Qian E., 1993, MNRAS, 262, 401

Hyde J. B., Bernardi M., 2009, MNRAS, 394, 1978

Jaffe W., 1983, MNRAS, 202, 995

Jeans J. H., 1919, Royal Society of London Philosophical Transactions Series A, 218, 157

Kassin S. A., de Jong R. S., Weiner B. J., 2006, ApJ, 643, 804

Kim D.-W., 2012, in Hot Interstellar Matter in Elliptical Galaxies, Astrophysics and Space Science Library, Vol. 378, pp. 121–162, Kim, D.–W. and Pellegrini, S., eds

King I., Gilmore G., van der Kruit P. C., eds., 1990, The Milky Way As Galaxy

King I. R., 1966, AJ, 71, 64

Krajnović D. et al., 2008, MNRAS, 390, 93

Kroupa P., 2001, MNRAS, 322, 231

Kroupa P., 2002, Science, 295, 82

Kuzmin G. G., 1956, AZh, 33, 27

Lanzoni B., Ciotti L., 2003, A&A, 404, 819

Li J.-T., Wang Q. D., Li Z., Chen Y., 2011a, ApJ, 737, 41

Li W., Chornock R., Leaman J., Filippenko A. V., Poznanski D., Wang X., Ganeshalingam M., Mannucci F., 2011b, MNRAS, 412, 1473

Łokas E. L., Mamon G. A., 2001, MNRAS, 321, 155

Longo G., Zaggia S. R., Busarello G., Richter G., 1994, A&AS, 105, 433

Magorrian J. et al., 1998, AJ, 115, 2285

Maraston C., 2005, MNRAS, 362, 799

Martín-Navarro I., La Barbera F., Vazdekis A., Falcón-Barroso J., Ferreras I., 2014, arXiv:1404.6533

Mathews W. G., Baker J. C., 1971, ApJ, 170, 241

Mathews W. G., Brighenti F., 2003, ARAA, 41, 191

McDermid R. M. et al., 2014, ApJ, 792, L37

Mellier Y., Mathez G., 1987, A&A, 175, 1

Merritt D., 1985, AJ, 90, 1027

Merritt D., Ferrarese L., 2001, ApJ, 547, 140

Merritt D., Graham A. W., Moore B., Diemand J., Terzić B., 2006, AJ, 132, 2685

Michie R. W., 1963, MNRAS, 126, 499

Milone A. D. C., Rickes M. G., Pastoriza M. G., 2007, A&A, 469, 89

Miyamoto M., Nagai R., 1975, PASJ, 27, 533

Nagai R., Miyamoto M., 1976, PASJ, 28, 1

Nagino R., Matsushita K., 2009, A&A, 501, 157

Nair P. B., Abraham R. G., 2010, ApJS, 186, 427

Napolitano N. R. et al., 2009, MNRAS, 393, 329

Narayanan D., Davé R., 2013, MNRAS, 436, 2892

Navarro J. F., Frenk C. S., White S. D. M., 1997, ApJ, 490, 493

Navarro J. F. et al., 2004, MNRAS, 349, 1039

Navarro J. F. et al., 2010, MNRAS, 402, 21

Negri A., 2014, Hydrodynamical simulations of early-type galaxies: effects of galaxy shape and stellar dynamics on hot coronae, PhD Thesis, University of Bologna, Unpublished

Negri A., Ciotti L., Pellegrini S., 2014a, MNRAS, 439, 823

Negri A., Pellegrini S., Ciotti L., 2013, Mem. Soc. Astron. Italiana, 84, 762

Negri A., Posacki S., Pellegrini S., Ciotti L., 2014b, MNRAS, 445, 1351

Neistein E., Maoz D., Rix H.-W., Tonry J. L., 1999, AJ, 117, 2666

Noordermeer E. et al., 2008, MNRAS, 384, 943

Norris M. A. et al., 2008, MNRAS, 385, 40

Osipkov L. P., 1979, Pisma v Astronomicheskii Zhurnal, 5, 77

O'Sullivan E., Forbes D. A., Ponman T. J., 2001, MNRAS, 324, 420

Padmanabhan N. et al., 2004, New Astr., 9, 329

Parriott J. R., Bregman J. N., 2008, ApJ, 681, 1215

Pastorello N., Forbes D. A., Foster C., Brodie J. P., Usher C., Romanowsky A. J., Strader J., Arnold J. A., 2014, MNRAS, 442, 1003

Pellegrini S., 1999, A&A, 351, 487

Pellegrini S., 2011, ApJ, 738, 57

Pellegrini S., 2012a, in Hot Interstellar Matter in Elliptical Galaxies, Astrophysics and Space Science Library, Vol. 378, pp. 21–54, Kim, D.–W. and Pellegrini, S., eds

Pellegrini S., 2012b, in Hot Interstellar Matter in Elliptical Galaxies, ASSL, Vol. 378, pp. 21–54, Kim, D.–W. and Pellegrini, S., eds

Pellegrini S., Baldi A., Kim D. W., Fabbiano G., Soria R., Siemiginowska A., Elvis M., 2007, ApJ, 667, 731

Pellegrini S., Held E. V., Ciotti L., 1997, MNRAS, 288, 1

Perryman M. A. C. et al., 2001, A&A, 369, 339

Perryman M. A. C. et al., 1997, A&A, 323, L49

Pinkney J. et al., 2003, ApJ, 596, 903

Plummer H. C., 1911, MNRAS, 71, 460

Posacki S., 2011, Gas Flows in Galaxies: Treatment of Sources and Sinks from First Principles, Master Thesis, University of Bologna, Unpublished

Posacki S., Cappellari M., Treu T., Pellegrini S., Ciotti L., 2014, arXiv:1407.5633

Posacki S., Pellegrini S., Ciotti L., 2013a, Mem. Soc. Astron. Italiana, 84, 766

Posacki S., Pellegrini S., Ciotti L., 2013b, MNRAS, 433, 2259

Press W. H., Teukolsky S. A., Vetterling W. T., Flannery B. P., 1992, Numerical recipes in FORTRAN. The art of scientific computing

Proctor R. N., Forbes D. A., Romanowsky A. J., Brodie J. P., Strader J., Spolaor M., Mendel J. T., Spitler L., 2009, MNRAS, 398, 91

Pu S. B., Saglia R. P., Fabricius M. H., Thomas J., Bender R., Han Z., 2010, A&A, 516, A4

Renzini A., Ciotti L., 1993, ApJ, 416, L49

Retana-Montenegro E., van Hese E., Gentile G., Baes M., Frutos-Alfaro F., 2012, A&A, 540, A70

Ruff A. J., Gavazzi R., Marshall P. J., Treu T., Auger M. W., Brault F., 2011, ApJ, 727, 96

Rybicki G. B., 1987, in IAU Symposium, Vol. 127, Structure and Dynamics of Elliptical Galaxies, de Zeeuw P. T., ed., p. 397

Salpeter E. E., 1955, ApJ, 121, 161

Sánchez-Blázquez P. et al., 2006, MNRAS, 371, 703

Sarazin C. L., Ashe G. A., 1989, ApJ, 345, 22

Sarazin C. L., Irwin J. A., Bregman J. N., 2001, ApJ, 556, 533

Sarazin C. L., White, III R. E., 1987, ApJ, 320, 32

Sarazin C. L., White, III R. E., 1988, ApJ, 331, 102

Sarzi M. et al., 2013, MNRAS, 432, 1845

Sarzi M. et al., 2010, MNRAS, 402, 2187

Satoh C., 1980, PASJ, 32, 41

Schlafly E. F., Finkbeiner D. P., 2011, ApJ, 737, 103

Schulz A. E., Mandelbaum R., Padmanabhan N., 2010, MNRAS, 408, 1463

Schwarzschild M., 1979, ApJ, 232, 236

Simien F., Prugniel P., 2002, A&A, 384, 371

Smet C. O., Posacki S., Ciotti L., 2014, MNRAS, submitted

Smith R. J., 2014, MNRAS, 443, L69

Smith R. K., Brickhouse N. S., Liedahl D. A., Raymond J. C., 2001, ApJ, 556, L91

Spiniello C., Trager S., Koopmans L. V. E., Conroy C., 2014, MNRAS, 438, 1483

Spiniello C., Trager S. C., Koopmans L. V. E., Chen Y. P., 2012, ApJ, 753, L32

Steinmetz M. et al., 2006, AJ, 132, 1645

Stone J. M., Norman M. L., 1992, ApJS, 80, 753

Surma P., Bender R., 1995, A&A, 298, 405

Tang S., Wang Q. D., 2005, ApJ, 628, 205

Tang S., Wang Q. D., Mac Low M.-M., Joung M. R., 2009, MNRAS, 398, 1468

Thomas J., Saglia R. P., Bender R., Thomas D., Gebhardt K., Magorrian J., Corsini E. M., Wegner G., 2005, MNRAS, 360, 1355

Thomas J., Saglia R. P., Bender R., Thomas D., Gebhardt K., Magorrian J., Corsini E. M., Wegner G., 2009, ApJ, 691, 770

Thomas J. et al., 2011, MNRAS, 415, 545

Thornton K., Gaudlitz M., Janka H.-T., Steinmetz M., 1998, ApJ, 500, 95

Tonry J. L., Dressler A., Blakeslee J. P., Ajhar E. A., Fletcher A. B., Luppino G. A., Metzger M. R., Moore C. B., 2001, ApJ, 546, 681

Toomre A., 1982, ApJ, 259, 535

Tortora C., Napolitano N. R., Romanowsky A. J., Capaccioli M., Covone G., 2009, MNRAS, 396, 1132

Tortora C., Romanowsky A. J., Cardone V. F., Napolitano N. R., Jetzer P., 2014, MNRAS, 438, L46

Tortora C., Romanowsky A. J., Napolitano N. R., 2013, ApJ, 765, 8

Tremaine S., Richstone D. O., Byun Y.-I., Dressler A., Faber S. M., Grillmair C., Kormendy J., Lauer T. R., 1994, AJ, 107, 634

Trenti M., Bertin G., 2005, A&A, 429, 161

Treu T., Auger M. W., Koopmans L. V. E., Gavazzi R., Marshall P. J., Bolton A. S., 2010, ApJ, 709, 1195

Treu T., Gavazzi R., Gorecki A., Marshall P. J., Koopmans L. V. E., Bolton A. S., Moustakas L. A., Burles S., 2009, ApJ, 690, 670

Treu T., Koopmans L. V., Bolton A. S., Burles S., Moustakas L. A., 2006, ApJ, 640, 662

Treu T., Koopmans L. V. E., 2004, ApJ, 611, 739

Trinchieri G. et al., 2008, ApJ, 688, 1000

van den Bosch F. C., Emsellem E., 1998, MNRAS, 298, 267

van den Bosch F. C., Jaffe W., van der Marel R. P., 1998, MNRAS, 293, 343

van der Marel R. P., van Dokkum P. G., 2007, ApJ, 668, 756

van Dokkum P. G., 2001, PASP, 113, 1420

van Dokkum P. G., Conroy C., 2010, Nature, 468, 940

van Dokkum P. G., Conroy C., 2011, ApJ, 735, L13

Van Hese E., Baes M., Dejonghe H., 2009, ApJ, 690, 1280

Vazdekis A., Sánchez-Blázquez P., Falcón-Barroso J., Cenarro A. J., Beasley M. A., Cardiel N., Gorgas J., Peletier R. F., 2010, MNRAS, 404, 1639

Weidner C., Kroupa P., Pflamm-Altenburg J., Vazdekis A., 2013, MNRAS, 436, 3309

Weijmans A.-M. et al., 2009, MNRAS, 398, 561

Williams A. A., Evans N. W., Bowden A. D., 2014, MNRAS, 442, 1405

Wilson C. P., 1975, AJ, 80, 175

Zaritsky D., Gonzalez A. H., Zabludoff A. I., 2006, ApJ, 638, 725

Zepf S. E., Maccarone T. J., Kundu A., Gonzalez A. H., Lehmer B., Maraston C., 2014, in American Astronomical Society Meeting Abstracts, Vol. 223, American Astronomical Society Meeting Abstracts 223, p. 455.01

Zhao H., 1996, MNRAS, 278, 488